Monopile foundations under complex cyclic lateral loading

Iona A. Richards
St. Peter's College
University of Oxford

A thesis submitted for the degree of
Doctor of Philosophy

Trinity 2019

Abstract

Monopile foundations under complex cyclic lateral loading

Iona A. Richards

St Peter's College, University of Oxford

A thesis submitted for the degree of *Doctor of Philosophy*

Trinity 2019

The vast majority of offshore wind turbines are supported on monopile foundations. These foundations experience lateral loading which is both cyclic and complex: continuously varying in amplitude, direction, frequency and eccentricity with the environmental and turbine operation conditions. The effect of cyclic loading on the accumulated rotation (ratcheting), strength and stiffness of the foundation must be considered, while advanced structural dynamic modelling requires prediction of the cyclic hysteretic response. However, there are currently no commonly accepted design methods for predicting the cyclic response of monopile foundations, particularly under the complex loading to which they are exposed.

This thesis explores the response of monopile foundations to cyclic lateral loading through laboratory-scale physical modelling in dry sand, principally at $1g$. The development of novel laboratory apparatus allows the application of complex, continuously varying cyclic loading. Regular, unidirectional tests complement previous studies and explore the impact of load amplitude and asymmetry in detail. Regular, multidirectional tests provide novel insight into the response to loading with multiple direction components. And irregular, multi-amplitude and multidirectional tests reveal the response to realistic loading, highlighting the dominance of large load events. Throughout, the monopile response is characterised in terms of ratcheting, evolution of hysteresis loop shape and the post-cyclic reloading response. Behaviour in very loose and dense sand is found to be qualitatively similar.

A complementary study using centrifuge modelling explores the impact of stress-level on the monopile response, to establish the relevance of $1g$ modelling and inform comparison of monopile responses observed at different stress-levels. Qualitatively similar behaviour is observed at multiple stress-levels, although the rate of ratcheting and stiffening reduce with increasing stress-level.

Together, the physical modelling results inform the design of monopile foundations under cyclic lateral loading. In particular, the results facilitate demonstration and development of numerical models in the *Hyperplastic Accelerated Ratcheting Model* (HARM) framework, which can capture ratcheting and evolution of the hysteretic response, and can respond to arbitrary loading. Models in the HARM framework are shown to capture key features of the response to complex — irregular, multi-amplitude and multidirectional — cyclic loading in dry sand of various densities and at multiple stress-levels. The results build confidence in the application of models in the HARM framework for full-scale monopile design.

Acknowledgements

First and foremost, I would like to thank my supervisors Byron Byrne and Guy Houlsby. This thesis would not have been possible without their careful guidance and enthusiasm. In particular, I thank Guy for patiently accommodating many an impromptu meeting, and Byron for the encouragement over many years, from my time at Catz as an undergraduate. Special thanks also go to Clive Baker. From machining bespoke components to advising on the intricacies of lifting equipment, Clive's technical expertise, support and good humour facilitated all aspects of the experimental work at Oxford.

It has been a pleasure to be part of the Civil Engineering Group at Oxford, surrounded by so many cheerful, helpful people. In particular, my gratitude goes to Christelle Abadie, whose support and generous advice was invaluable in the development of this project, and to Toby Balaam for numerous fruitful discussions, particularly regarding our cyclic definitions work. I am also grateful to Tom Adcock and Mark McAllister for facilitating access to wave loading data from the DeRisk project, and providing much-appreciated technical input. For advice and assistance in the lab and beyond, I thank Jonathan White, Russell Mayall, Brian Sheil and Ross McAdam; and for all the help with purchasing, I thank Alison May. Special thanks must also go to the REMS contingent and the ever-evolving Wallis room lunch group, for all the laughs, and to the civil climbing group, for the support on and off the wall.

At UWA, I am very grateful to Fraser Bransby and Christophe Gaudin for supporting my visit in 2018, and for many insightful discussions. The experimental work at UWA would not have been possible without the support of the excellent technical team, led by John Breen; thank you all for going the extra mile. I am also grateful to Manuel Herduin for allowing me to use his laboratory apparatus, and to Juliano Nietiedt for the assistance in the laboratory (as well as all the lifts to the office). I must also thank everyone at UWA who made me so welcome, and especially those who showed me a little of Western Australia.

Beyond the Jenkin building (Oxford) and the IOMRC (Perth), I thank Liz and Nigel for providing a home-from-home during my visits to Cranfield, Em and Freddie for the adventures, and Renée for all the support. Fearghus, thanks for being my (often rather distant) rock. Finally, I thank my parents and Al for, ultimately, making this possible.

Contents

Nomenclature

Greek alphabet variables

	Empirical value in dilatancy expressions (Bolton, 1986; Bolton, 1987)
α	Internal variables (hyperplasticity) Ratcheting power-law exponent
α_r	Ratcheting strain (HARM)
β	Scalar hardening parameter (HARM) Secant stiffness power-law exponent
γ	Energy loss power-law exponent Shear strain
γ'	Soil effective unit weight
ε	Strain (may represent pile rotation θ or pile displacement u for macro pile response)
ε_a	Axial strain
ζ_b	Cyclic load magnitude characterisation $\zeta_b = \sigma_e/\sigma_R$
ζ_c	Cyclic load asymmetry characterisation $\zeta_c = \sigma_r/\sigma_e$
η	Energy loss factor Pile aspect ratio Stress-dependent stiffness exponent
θ	Pile rotation
κ	Increase in surface strengths K_m (HARM evolution functions)
κ_g^*	Parameter for evolution of K_m (HARM evolution functions)
κ_m^*	Parameter for evolution of K_m (HARM evolution functions)
λ	Plastic multiplier (plasticity)
ξ	Damping ratio (structural dynamics)
ρ_κ	Parameter for evolution of K_m (HARM evolution functions)
τ	Shear stress
σ	Stress (may represent moment M or horizontal load H applied to pile for macro pile response)
σ'	Vertical effective stress
σ'_c	Effective confining stress

σ'_{REF}	Reference vertical effective stress $\sigma'_{REF} = 0.7L\gamma'$
ϕ'	Angle of friction
ϕ'_c	Critical angle of friction
ϕ'_p	Peak angle of friction
Φ	Half internal spread angle (fan-type loading) Standard deviation of wrapped normal spreading distribution (wave loading, e.g. Adcock and Taylor, 2009)
χ	Generalised stress (hyperplasticity)
$\bar{\chi}$	Dissipative generalised stress (hyperplasticity)
ψ'	Angle of dilation
ω	Angular velocity (centrifuge)

Latin alphabet variables

a_n	Point on cyclic response at mean stress on loading (cyclic definitions)
A	Area beneath backbone curve (HARM evolution functions) Ratcheting power-law coefficient
b_n	Point on cyclic response at mean stress on unloading (cyclic definitions)
B	Secant stiffness power-law coefficient
B_L	Secant stiffness logarithmic coefficient
c	Constraint (hyperplasticity)
c_v	Coefficient of consolidation
C	Energy loss power-law coefficient
d	Dissipation function (hyperplasticity) Pile pivot point depth
d_{10}, d_{30}, d_{50}, d_{60}	Soil particle sizes
D	Parameter for backbone correction (HARM calibration) Pile outside diameter
D_R	Relative density (%)
D_t	Tank diameter
e	Error in process variable (control) Soil void ratio
$\tilde{e}$	Dimensionless loading eccentricity
e_n	Point on cyclic response at extreme stress (cyclic definitions)
E	Parameter for backbone correction (HARM calibration) Young's modulus
E_E	Elastic energy (per cycle)
E_H	Hysteretic energy loss (per cycle)

E_i	Initial stiffness (monotonic response)
E_pI_p	Pile bending stiffness
E_{SL}	Soil's Young's modulus
f	Frequency Helmholtz free energy function (hyperplasticity) Ratio of prototype-scale to laboratory-scale parameter
f_0	Natural frequency (structural dynamics)
f_L	Data logging frequency
F	Friction (in displacement transducers)
F_{β^*}	Factor (HARM evolution functions)
F_E	Excitation force (structural dynamics)
F_T	Transmitted force (structural dynamics)
g	Acceleration due to gravity Gibbs free energy (hyperplasticity)
G_{MAX}	Maximum shear modulus
G_S	Soil specific gravity
h	Drop height (sand raining) Pile loading eccentricity
h_t	Tank depth
H	Horizontal load applied to pile Surface modulus (kinematic hardening model)
H_B	Horizontal response at pile base (PISA monotonic method)
k	Secant stiffness
k_{MAX}	Maximum stiffness (not secant)
K	Gain (control) Surface strength (kinematic hardening model)
K_b, K_c	Empirical functions for secant stiffening
K_p	Rankine's passive earth pressure coefficient
K_R	Pile relative stiffness (Poulos and Hull, 1989)
l_i	Magnitude of linkage vector $\mathbf{L}_i$ (kinematics)
L	Pile embedded length
$\mathbf{L}_i$	Linkage vector (kinematics)
m	Distributed moment soil reaction (PISA monotonic method) Pile mass Surface index (kinematic hardening model)
m_{kg}	Parameter for evolution of K_m (HARM evolution functions)
m_{km}	Parameter for evolution of K_m (HARM evolution functions)
m_r	Parameter for evolution of R (HARM evolution functions)

m_s	Parameter for evolution of R (HARM evolution functions)
m_σ	Power-law exponent for variation of T_b with ζ_b
M	Maximum number of surfaces (kinematic hardening model) Moment applied to pile (at mudline)
M_B	Moment response at pile base (PISA monotonic method)
n	Cycle number Experimental g-level Number of transducers aligned with loading direction
N	Maximum cycle number
p	Distributed lateral soil reaction (*p-y* and PISA monotonic methods)
p'	Mean effective stress
p_a	Atmospheric pressure
P	Normalised excess pore pressure (Li *et al.*, 2019)
P_c	Monotonic conic function parameter
$\mathbf{P}_i$	Coordinates of pivot point on pile (kinematics)
P_j	Monotonic Jeanjean parameter
P_p	Monotonic power-law parameter
q	Deviator stress
q_c	CPT cone resistance
Q	Empirical value in dilatancy expression (Bolton, 1986) Flow rate (sand raining)
r_n	Point on cyclic response at reversal stress (cyclic definitions)
R	Empirical value in dilatancy expression (Bolton, 1986) Ratcheting parameter (HARM)
R_0	Parameter for evolution of R (HARM evolution functions)
R_a	Pile roughness
R_e	Centrifuge effective radius
R_n	Normalised roughness (R_a/d_{50})
R_R^*	Parameter for R (HARM evolution functions)
$\mathbf{s}$	Pile pose (kinematics)
t	Pile wall thickness Time
t_p	Wave loading period
$\hat{\mathbf{T}}$	Transformation matrix (kinematics)
T_b, T_c	Empirical functions for ratcheting response
T_d	Derivative time (control)
T_i	Integral time (control)

$\mathbf{T}_i$	Coordinates of pivot point on transducer (kinematics)
$\mathbf{T}_i^R$	Coordinates of pivot point on retracted transducer (kinematics)
T_p	Normalised wave loading period (Li *et al.*, 2019)
u	Controller output (control) Excess pore pressure Pile displacement (at load application point)
V	Vertical (axial) force on pile
$\mathbf{V}$	Vector of linkage lengths (kinematics)
W	Work done on pile-soil system
y	Lateral pile displacement (*p-y* and PISA monotonic methods) Yield surface (hyperplasticity)
z	Vertical pile displacement

Common subscripts, superscripts, prefixes and diacritics

$\dot{X}$	Time derivative of X
$\bar{X}$	Mean value of X
$\tilde{X}$	Dimensionless parameter (Leblanc *et al.*, 2010a)
ΔX	Accumulated value of X (ε, u or θ relative to monotonic response)
X^*	Indication of special case of X Specific value of X (HARM evolution functions)
X_0	Initial value of X
X_{AV}	Average value of X
X_c	Common value of X
X_{CYC}	Cyclic amplitude of X
X_e	Error value Experimentally-determined value Extreme value of X (cyclic definitions)
X_H	Relating to horizontal load H
X_i	Indicating parameter is defined in both the x- and y-direction General index
X_l	Value of X on cyclic loading
X_L	At laboratory-scale
X_m	Surface index (kinematic hardening model)
X_{m0}	Value of X at σ_e on cycle $n = 0$
X_M	Relating to moment M
X_{MAX}	Maximum value of X
X_{MIN}	Minimum value of X

X_n	Value of X at cycle n
X_p	Peak value of X
X_P	At prototype-scale
X_r	Parameter corresponding to ratcheting (hyperplasticity) Reversal value of X (cyclic definitions)
X_{r0}	Value of X at onset of reloading
X_R	Reference value of X
X_u	Relating to pile displacement u Value of X on cyclic unloading
X_x	Relating to x direction
X_y	Relating to y direction

Test name abbreviations

L	Very loose sand (OU)
D	Dense sand (OU)
1G	$1g$ (UWA)
9G	$9g$ (UWA)
80G	$80g$ (UWA)
M	Monotonic loading
TW	Two-way unidirectional cyclic loading ($\zeta_c = -1$)
OW	One-way unidirectional cyclic loading ($\zeta_c = 0$)
PT	Partial two-way unidirectional cyclic loading ($-1 \leq \zeta_c \leq 0$)
PO	Partial one-way unidirectional cyclic loading ($0 \leq \zeta_c \leq 1$)
SP	Multidirectional spiral loading
T	T-shaped multidirectional cyclic loading
L	L-shaped multidirectional cyclic loading
TH	High amplitude T-shaped cyclic loading
F	Fan-type multidirectional cyclic loading
UD	Unidirectional irregular storm loading
MD	Multidirectional irregular storm loading

Other common abbreviations

CPT	Cone Penetration Test
FE	Finite Element
FLS	Fatigue Limit State

HARM	Hyperplastic Accelerated Ratcheting Model
OU	Oxford University
OWT	Offshore Wind Turbine
RNA	Rotor Nacelle Assembly
SF	Superfine (silica sand)
SLS	Serviceability Limit State
ULS	Ultimate Limit State
UWA	The University of Western Australia
YLB	Yellow Leighton Buzzard (sand)

Publications

Richards, I. A., Byrne, B. W. and Houlsby G. T. (2018). "Physical modelling of monopile foundations under variable cyclic lateral loading". *Proceedings of the 9th International Conference on Physical Modelling in Geotechnics (ICPMG)*. London, UK, pp. 737–742.

Richards, I. A., Houlsby G. T. and Byrne, B. W. (2019). "Exploring the response of a monopile to storm loading". *Proceedings of Coastal Structures 2019*. Hannover, Germany.

Richards, I. A., Byrne, B. W. and Houlsby G. T. (2019). "Monopile rotation under complex cyclic lateral loading in sand". *Géotechnique (Ahead of Print)*. DOI: 10.1680/jgeot.18.p.302.

Richards, I. A., Bransby, M. F., Byrne, B. W., Gaudin, C. and Houlsby G. T. (2019). "The effect of stress-level on the response of a model monopile to cyclic lateral loading in sand". *Submitted*.

Chapter 1

Introduction

1.1 Application

1.1.1 Offshore wind power

The historic Paris Agreement (United Nations, 2015), signed by 196 countries, has the long-term goal of limiting the global average temperature rise to below $2°$ above pre-industrial levels, and to pursue efforts to limit the increase to $1.5°$. To achieve this goal, countries have pledged to reach "net-zero" emissions by the second half of the century. An urgent, global transition from fossil-fuels to renewable energy is therefore necessary (EWEA, 2015).

Offshore wind power is playing a significant role in this energy transition. Figure 1.1 shows how offshore wind installations in Europe have grown significantly over the last decade. The UK currently has the largest offshore wind capacity with over 8 GW installed (Wind Europe, 2019), supplying almost 10% of the UK electricity demand (Renewable UK, 2019). Growth of the industry is expected to continue worldwide, with 70 GW installed capacity expected in Europe by 2030 (Wind Europe, 2017), and markets in China, Japan, Taiwan and the USA expected to grow rapidly. Indeed, IEA (2017) suggests that offshore wind could represent 4.5% of the global electricity output by 2050.

Compared to onshore wind, offshore wind takes advantage of higher and more consistent wind speeds offshore. With fewer logistical and planning constraints, larger wind farms made up of bigger, more efficient turbines can also be developed. Offshore Wind Turbines (OWTs) have grown in size significantly over the last decade, as shown in

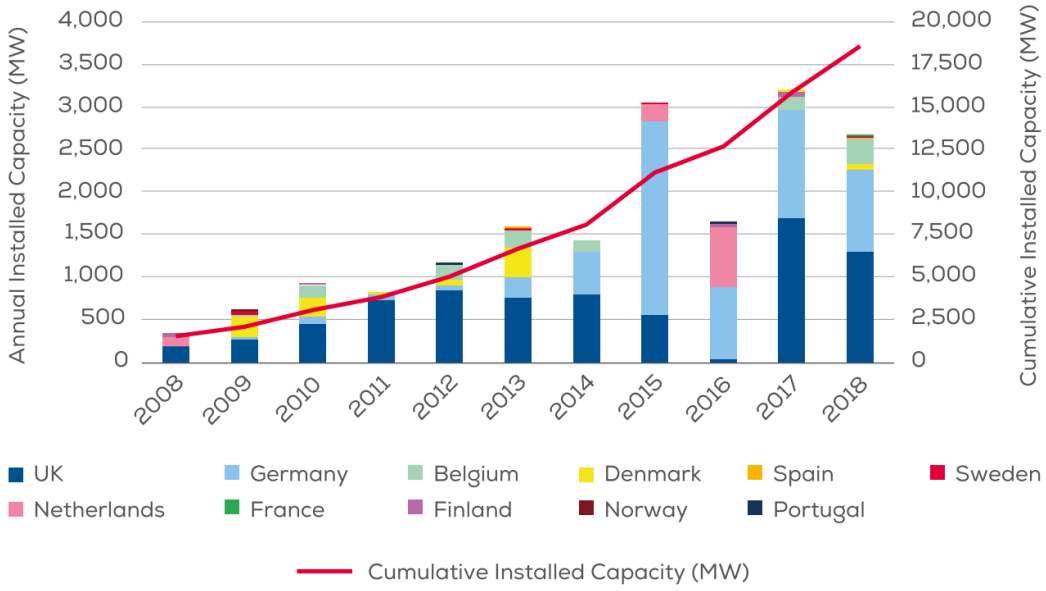

Figure 1.1: Annual offshore wind installations by country and cumulative capacity (Wind Europe, 2019)

Figure 1.2. This trend is expected to continue, with a 12 MW capacity turbine with 220 m rotor diameter already in the late stages of development (GE Renewable Energy, 2019).

The growth of the offshore wind industry has been coupled with a significant reduction in the cost. Economies of scale have been realised as farms and turbines have increased in size, and greater wind speeds have been exploited by developing further offshore, typically in deeper water (Wind Europe, 2018). Technological advancements, including in foundation design, have also contributed to cost-reduction. In the UK, the cost of offshore wind has reduced by 50% since 2015, and is now cheaper than new gas or nuclear power (Renewable UK, 2019). Meanwhile, in Germany and the Netherlands the latest offshore wind auctions were won at "zero-subsidy" (Windpower, 2019).

1.1.2 Offshore wind turbine support structures

The components of an OWT required for electricity generation and control operations are contained within the Rotor Nacelle Assembly (RNA), which is almost universally supported atop a tubular steel tower. However, there is some variation in the choice of support structure (and foundation) for the RNA and tower beneath the water-level. Figure 1.3 illustrates a number of possible support structures for OWTs: monopiles,

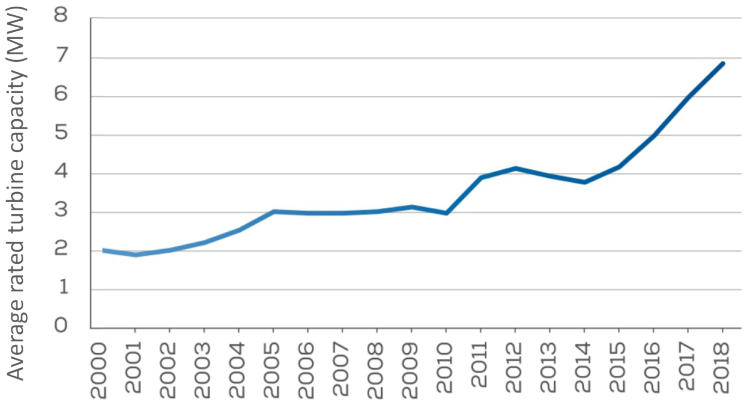

Figure 1.2: Yearly average of newly installed offshore wind turbine rated capacities in Europe (modified from Wind Europe, 2019)

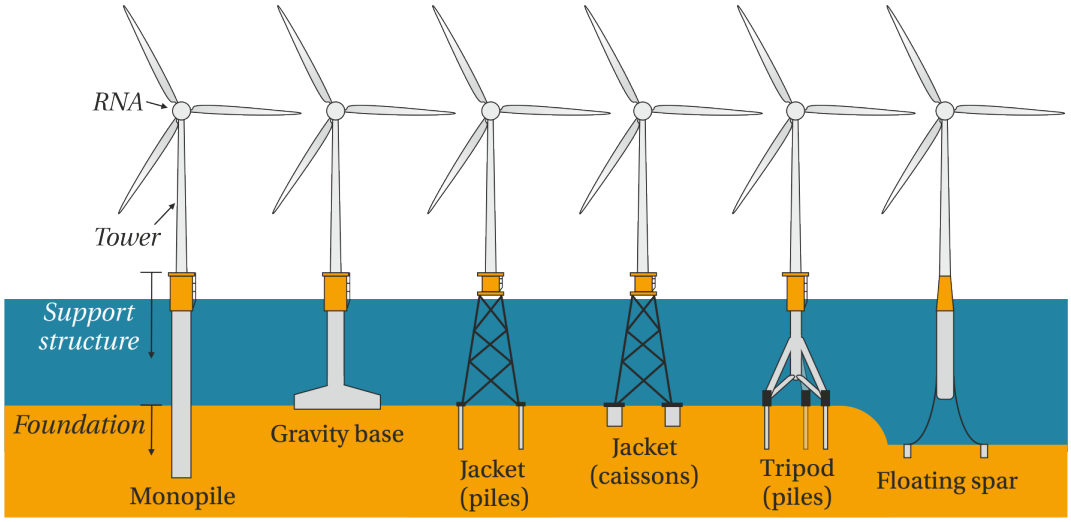

Figure 1.3: Illustration of possible support structures for OWTs

gravity bases, jacket structures on either piles or caissons, tripods and floating spar-type structures.

The vast majority of OWTs are supported on monopiles — large-diameter open-ended steel piles. In Europe, monopiles represent 81.5% of installed OWT support structures, while jackets, gravity bases, tripod foundations and floating structures represent 8%, 6%, 4% and 0.3% of installed structures respectively (Wind Europe, 2019). With support structures accounting for approximately 20% of capital expenditure for an offshore wind farm (EWEA, 2009), their selection and design is critical.

The current prevalence of monopiles is explained by their simple design, established supply chain and robust installation procedures (typically impact driven). Although

initially considered to be a solution only for shallow water sites, the proven performance of these foundations, coupled with ongoing optimisation of their design, has made monopiles an attractive option for turbines of increased size and farms in deeper water. The dominance of the monopile is expected to continue, although the market-share of alternative grounded support structures may increase as offshore wind expands outside of Europe, where different soil conditions and environmental loading exist. Meanwhile, floating OWTs present an opportunity for development of offshore wind in deeper water (> 50 m) (IRENA, 2017).

Figure 1.4 illustrates a monopile foundation and highlights key dimensions: embedded length L and diameter D. The monopile wall thickness t, which may vary along the pile length, is also a key dimension. Modern monopiles have diameters up to 8 m (Sørensen *et al.*, 2017) with length (L) to diameter (D) ratios (L/D) of $3-6$ (Sørensen *et al.*, 2017; Schroeder *et al.*, 2015) and wall thicknesses around 100 mm (Schroeder *et al.*, 2015). The next generation of monopiles might be 10 m in diameter. Monopiles are typically connected to the tower with a transition piece located at the water-level, while scour protection is typically installed to minimise erosion at the seabed. Figure 1.5 shows a fabricated monopile before installation.

1.2 Design of monopile foundations

1.2.1 Loading

Lateral loading dominates the design of monopile foundations for OWTs, in contrast with the design of piles for conventional applications (*e.g.* supporting offshore jacket structures or high-rise buildings onshore), where axial loading is the key concern. A combination of wind, waves, current and turbine operation loads act on the OWT structure. These loads, which also interact with the dynamic response of the structure, result in combined moment (M) and horizontal loading (H) on the monopile foundation, as indicated in Figure 1.6. All load components vary temporally and spatially; waves are usually the dominant cyclic component with a frequency of around 0.1 Hz. The combined loading experienced by the monopile is therefore cyclic and

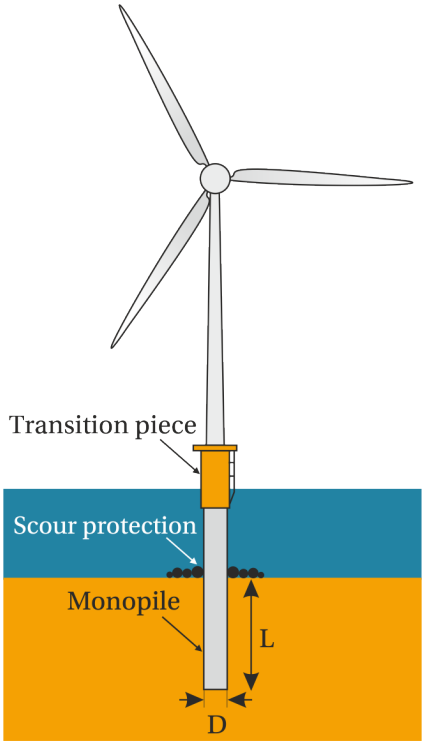

Figure 1.4: Schematic of an OWT on a monopile foundation

Figure 1.5: Fabricated monopile for Veja Mate offshore wind farm ($D = 7.8$ m) (Windindustrie in Deutschland, 2016)

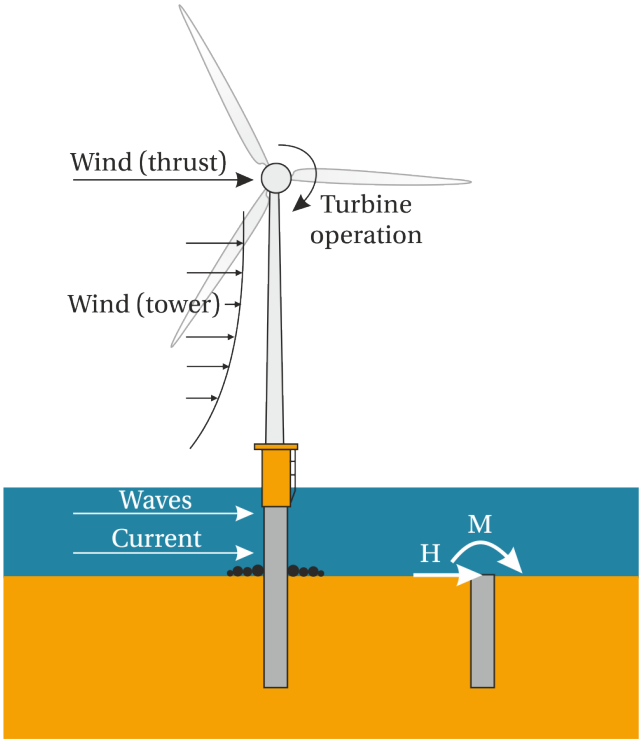

Figure 1.6: Schematic indicating lateral loading on an OWT on a monopile foundation

Limit state	Moment amplitude $/M_{ULS}$	No. of cycles N
Ultimate Limit State (ULS)	1.00	1
Serviceability Limit State (SLS)	0.64	10^2
Fatigue Limit State (FLS)	0.39	10^7

Table 1.1: Example distribution of cyclic load amplitudes experienced by monopile foundation over lifetime (Leblanc *et al.*, 2010b)

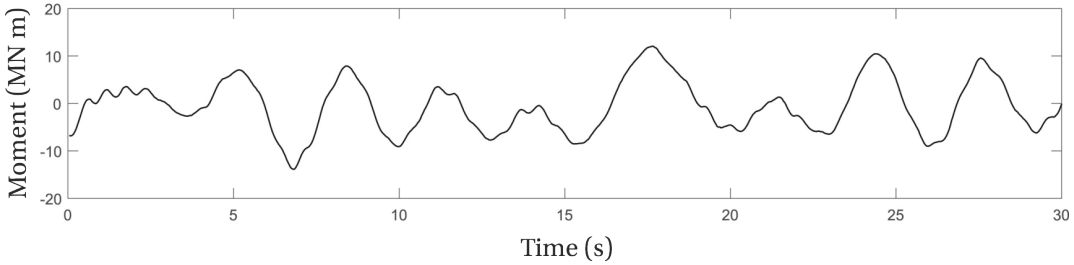

Figure 1.7: Example 30 second moment loading on an OWT monopile in the North Sea in idling conditions (derived from strain measurements at mudline) (Page *et al.*, 2019)

complex: continuously varying in amplitude, direction, frequency and eccentricity (M/H).

An example distribution of approximate cyclic moment amplitudes experienced by a monopile foundation (relative to the *Ultimate Limit State* (ULS) design moment M_{ULS}) is presented in Table 1.1 (following Leblanc *et al.*, 2010b). The distribution highlights the variation in load amplitude and the small number of larger-amplitude load cycles experienced over the foundation lifetime. Meanwhile, Figure 1.7 shows the moment loading experienced at the mudline of an OWT monopile (in a single direction) over 30 seconds, in idling conditions (Page *et al.*, 2019). This measured data shows the type of irregular, multi-amplitude cyclic loading monopiles experience in the field.

Figure 1.8 presents the significant spatial variation of wind and waves for an example site offshore the Netherlands. Although the spatial variation of loading is site-specific, all sites are exposed to multidirectional environmental loading. Wind-wave misalignment also occurs as weather systems change direction (Van Vledder, 2013). Figure 1.9 shows, for a site in the Irish Sea, recorded wind-wave misalignment of up to approximately $90°$.

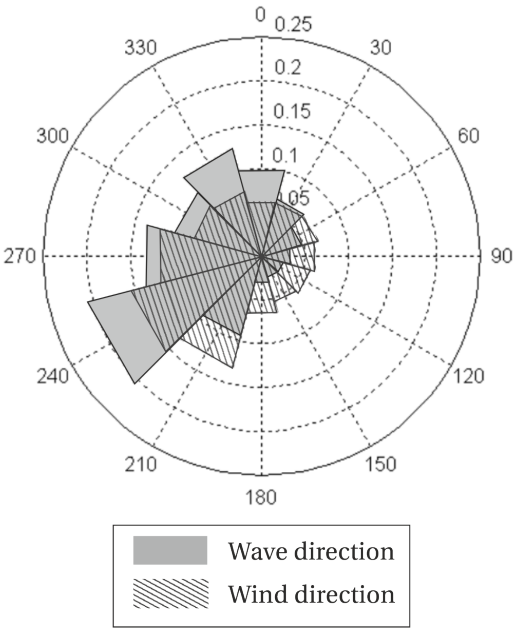

Figure 1.8: Frequency of occurrence of wave direction and wind direction for a site offshore the Netherlands (Bierbooms, 2003)

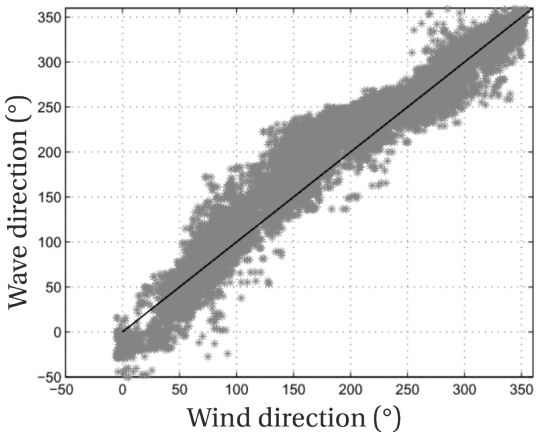

Figure 1.9: Example wind-wave misalignment at Walney Offshore Wind Farm in the Irish Sea (Koukoura, 2014)

1.2.2 Illustrative monopile response

Monopile foundations exhibit a non-linear response under lateral loading. Figure 1.10a illustrates a typical monopile response under continuously increasing (monotonic) loading. From the monotonic response, the initial (maximum) stiffness k_{MAX} and the ultimate response at large loads are of interest. The ultimate response is often defined at a reference rotation or displacement.

Under cyclic loading, monopiles may accumulate pile displacement u and/or pile rotation θ, and the shape of the hysteresis loop may evolve; both behaviours are of concern in monopile design. Figure 1.10b illustrates a typical response of a monopile in sand to simplified (unidirectional, regular) biased cyclic loading to demonstrate ratcheting (the accumulation of u and/or θ) and evolution of the hysteresis loop shape, which may be characterised in terms of stiffness and energy dissipation metrics. As discussed in Section 1.2.1, monopiles in the field are exposed to complex cyclic loading. The response that might be expected under example irregular, multi-amplitude loading is illustrated in Figure 1.10c.

The illustrative responses in Figure 1.10 are presented arbitrarily in terms of either

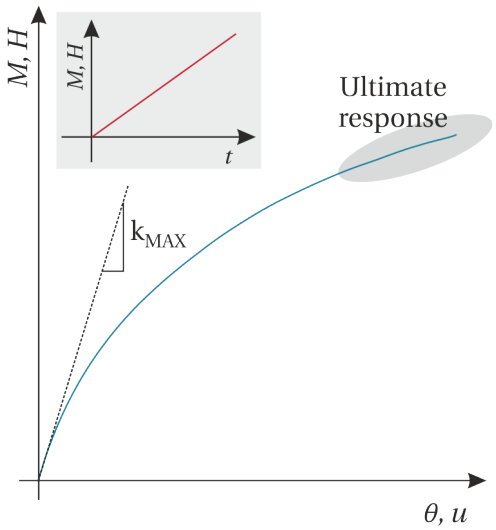

(a) Monotonic loading

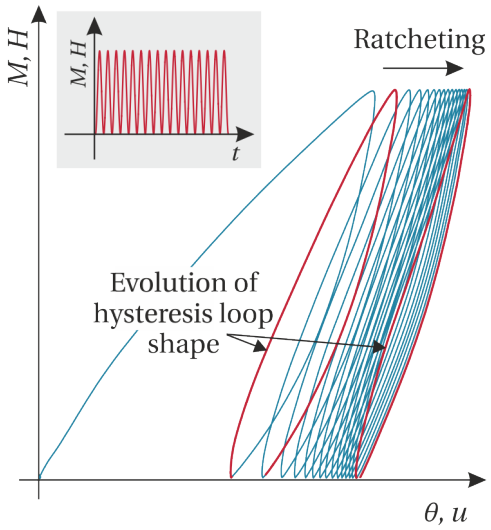

(b) Regular cyclic loading

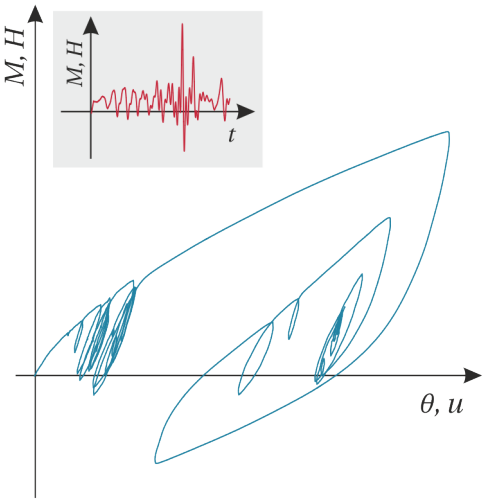

(c) Irregular multi-amplitude cyclic loading

Figure 1.10: Illustration of typical monopile response in sand under various types of unidirectional lateral loading

moment-rotation ($M-\theta$) or horizontal load-displacement ($H-u$). Both work-conjugate pairs have been used to present results in previous work, and both pairs are used in this thesis. An approximate relationship between the responses can be obtained by considering the total work rate for a rigid monopile under lateral loading:

$$\dot{W} = H^* \dot{u}^* = H\dot{u} + M\dot{\theta} \tag{1.1}$$

Where Figure 1.11 illustrates the terms. Assuming a small rotation angle, the total work

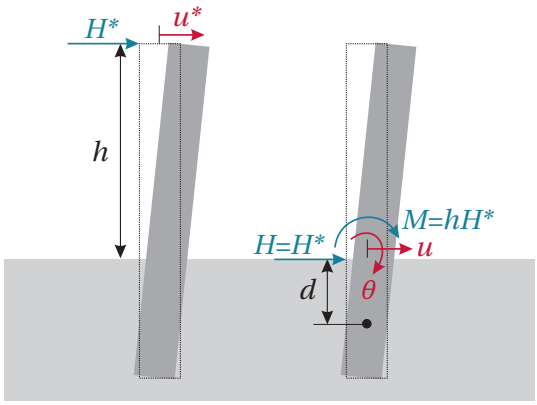

Figure 1.11: Illustration of moment M, rotation θ, horizontal load H and displacement u for rigid monopile under lateral loading

rate can be expressed in terms of either $H^* - u^*$ or $M - \theta$ as:

$$\dot{W} = H^*\dot{u}^* \approx M\dot{\theta}\left(\frac{d+h}{h}\right) \tag{1.2}$$

Where h is the loading eccentricity and d is the depth of the point of pile rotation, which is expected to remain approximately constant (Abadie, 2015). With $d \approx 0.7L$ (Abadie, 2015) and *e.g.* $h = 2.5L$, the total work rate is approximately 28% greater than that suggested by responses presented in $M - \theta$ space.

1.2.3 Design requirements

Rotation criteria

The response to lateral loading is a crucial element of monopile design. The response is typically specified in terms of rotation at the mudline, rather than in terms of pile displacement. The DNVGL-ST-0126 standard *Support structures for wind turbines* specifies the calculation of monopile rotation under both ULS and *Serviceability Limit State* (SLS) conditions (DNV GL, 2016): the maximum rotation response under ULS conditions shall be determined (7.6.2.5), as well as the permanent (long-term) rotation under SLS conditions (7.6.2.7). DNVGL-ST-0126 also stipulates that the effects of cyclic loading on the strength and stiffness under ULS and SLS conditions should be assessed (7.4.4.4), and that the effects of pore-pressure build-up under cyclic loading should be considered (7.4.4.2).

Monopile rotation under ULS conditions may be estimated with a monotonic design method (discussed in Section 1.2.4) which is able to capture the ultimate response of

the foundation, as illustrated in Figure 1.10a. The ultimate response may be defined as at yield, or using a rotation (or displacement) criteria if yield is expected at excessively large rotations, as is often the case for piles in sand. A ULS criteria of $2°$ pile rotation or $0.1D$ displacement at the mudline appears to be conventional (*e.g.* Byrne *et al.*, 2017).

To predict permanent accumulated monopile rotation under SLS conditions — where loading is cyclic — and to estimate the effect of cyclic loading on the SLS and ULS response, cyclic design methods are required. DNVGL-ST-0126 suggests that the allowable permanent accumulated rotation of the monopile under SLS conditions might be $0.25°$. However, it also states that these tolerances are typically derived from visual requirements or requirements for turbine operation, and are therefore expected to be project-specific.

Dynamic criteria

The monopile's dynamic response is important, as it determines the dynamic response of the combined OWT structure, and hence the structural fatigue damage (*e.g.* Aasen *et al.*, 2017). Indeed, many monopile designs may be dominated by dynamic considerations. DNVGL-ST-0126 specifies the evaluation of dynamic load effects using an integrated analysis of the OWT structure which includes the response of the foundation (7.4.5.1).

To minimise dynamic load effects, the OWT structure's natural frequencies must avoid excitation at i) wind loading frequencies (although these are typically very low), ii) wave loading frequencies, iii) rotor frequencies (1P), and iv) blade-passing frequencies (3P). Monopile structures are typically designed as *soft-stiff* structures, with the natural frequency of the first tower bending mode (f_0) in the narrow band between the 1P and 3P excitation frequencies, as indicated in Figure 1.12. As turbines increase in size the rotor frequency (1P) reduces, increasing the intersection of the *soft-stiff* frequency band and the wave frequency distribution. Non-negligible excitation from wave loading may therefore occur, the effects of which can be minimised with the addition of active damping (*e.g.* Brodersen *et al.*, 2017).

The dynamic response may be quantified in terms of stiffness and energy dissipation. Monopile stiffness impacts the OWT structure's natural frequencies, while

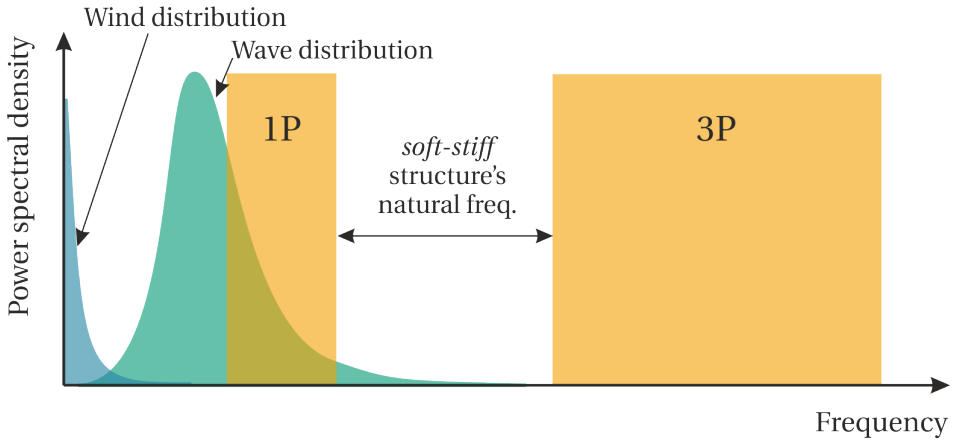

Figure 1.12: Typical frequency spectrum for dynamic loads on an OWT structure (after Bhattacharya, 2014)

monopile energy dissipation contributes to the total structural dissipation, which moderates dynamic load amplification and will inform the requirement for any active damping. In an integrated dynamic analysis the monopile response is often represented by a series of non-linear soil reaction curves, which capture an initial stiffness k_{MAX} (employing *e.g.* the *p-y* method or PISA method, discussed in Section 1.2.4). However, when implemented directly as non-linear springs, these representations neglect energy dissipation. Single-element (macro) models may also be used to represent the monopile response. Spring models, which include lateral, rotational and potentially cross-coupling components (*e.g.* Arany *et al.*, 2016), may be employed with or without dissipation. Macro plasticity models have also been developed, which are able to capture the non-linear foundation response including dissipation (Page *et al.*, 2018).

Additional considerations

Pile driveability is an essential design requirement. As monopiles increase in size to support larger turbines in deeper water, larger hydraulic hammers are required and significant noise pollution is generated, often requiring noise-mitigation. Buckling during driving can also be a concern (*e.g.* Randolph, 2018). Alternative installation methods for so-called XL monopiles include vibratory installation systems (Carbon

Trust, 2014) and systems which drive the monopile with water rather than steel rams (Carbon Trust, 2019).

The effect of scour is an important design consideration, and the installation of preventative scour protection is now commonplace. The influence of scour and scour protection on the structure's natural frequency and lateral response should be considered (Mayall, 2019).

Another important consideration is the ability of the supply chain to fabricate, handle and transport the monopiles. Indeed, these practical considerations present a very significant challenge as monopiles increase in size.

1.2.4 Monotonic design

Monotonic design methods allow prediction of the rotation (and displacement) response under ULS conditions and are often a pre-requisite for cyclic design methods. Also, the initial stiffness predicted by the monotonic response (k_{MAX}) is often a key parameter for assessment of the structure's fatigue life through integrated dynamic analyses.

Monotonic design of piles under lateral loading has conventionally been conducted using the *p-y* method, where the monopile is modelled as an elastic beam and the distributed lateral response of the soil is represented by a series of independent non-linear springs, defined by *p-y* curves (Reese and Van Impe, 2011). The *p-y* curves for cohesionless soil presented in design standards (*e.g.* DNV GL, 2016; API, 2011) originate from the work of Reese *et al.* (1974) based on field tests conducted by Cox *et al.* (1974), and employ a continuously differentiable function proposed by Murchison and O'Neill (1984). However, the standard *p-y* method and the conventional *p-y* curves — developed for slender, small-diameter piles — have been found to be deficient for the design of large-diameter monopiles with $L/D < 6$ (Alderlieste *et al.*, 2011; Doherty and Gavin, 2012). Indeed, DNVGL-ST-0126 cautions against the use of the conventional *p-y* curves for piles with $D > 1$ m, without validation by *e.g.* FE analysis (F.2.4.1).

Recent work as part of the *Pile Soil Analysis* (PISA) project has developed a new design methodology for monopiles under monotonic lateral loading (*e.g.* Burd *et al.*, 2019). Like the *p-y* method, the PISA design model is a one-dimensional (1D)

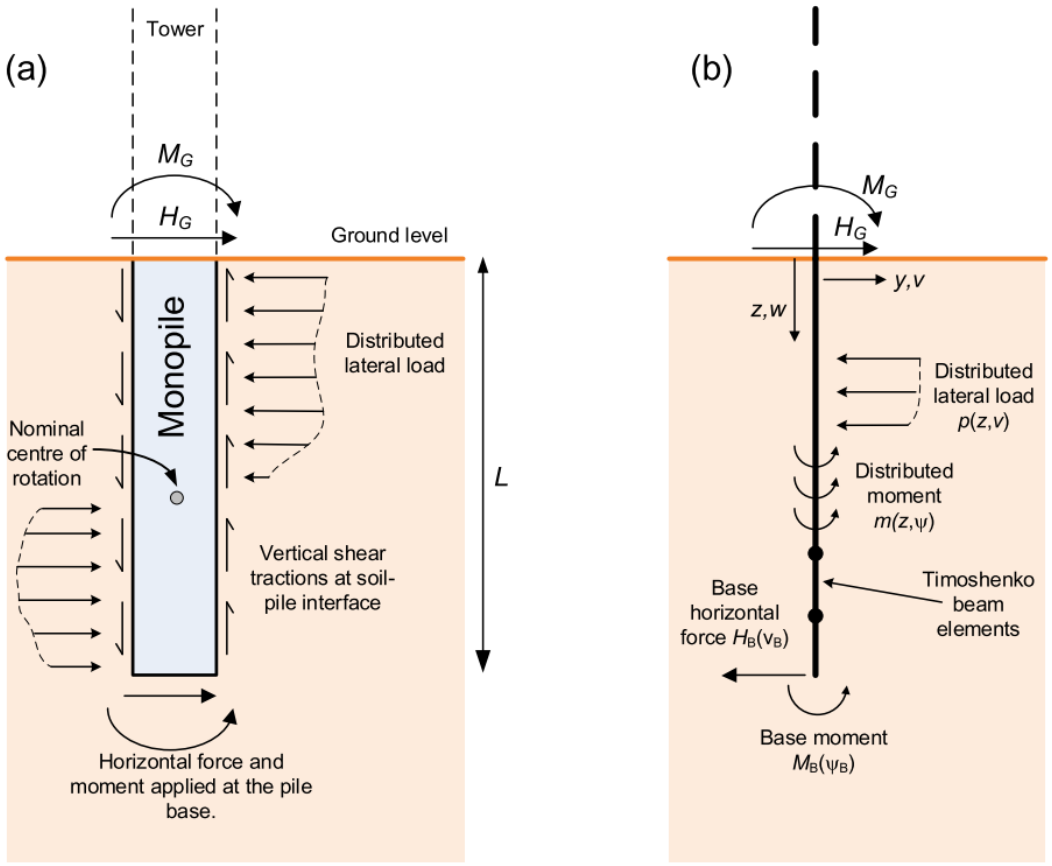

Figure 1.13: Illustration of PISA design model (a) idealisation of the soil reaction components acting on the pile (b) 1D finite element implementation of the model showing soil reactions (Burd *et al.*, 2019)

representation of the pile-soil system with the soil response represented by independent non-linear springs. However, the PISA design model includes distributed moment m and horizontal H_B and moment M_B responses at the pile base, alongside the distributed lateral response p, as indicated in Figure 1.13. These additional soil reaction components (m, H_B, M_B) become increasingly significant as L/D is reduced (Byrne *et al.*, 2015). Four-parameter conic functions are used to define the soil reactions within the PISA design model. Parameters for an exemplar sand are presented by Burd *et al.* (2019), but the intention is that the parameters are calibrated to site-specific 3D finite element (FE) analyses for application in different soil conditions.

Although it is practical to perform a limited number of 3D FE computations for

calibration of a design tool to a site, there is a significant advantage in performing the majority of the design calculations with faster 1D models, particularly when location-specific designs are required across perhaps 100 turbine locations. The PISA design method allows for improved prediction of the monotonic response with a fast 1D model, and has contributed to optimised design and significant capital expenditure savings, as demonstrated by Manceau *et al.* (2019).

1.2.5 Cyclic design

While monotonic design methods allow prediction of the ULS response and the initial stiffness k_{MAX} for some dynamic calculations, cyclic design methods are necessary to predict the following three aspects of the monopile response:

1. Permanent monopile rotation (ratcheting) under SLS conditions.

2. The effects of cyclic loading on the strength and stiffness under SLS and ULS conditions.

3. The hysteretic response under cyclic loading for advanced dynamic modelling.

Cyclic design methods should be able to perform under realistic (irregular, multi-amplitude and multidirectional) cyclic loading conditions, and similar to monotonic design methods, they should be fast, given the vast number of design calculations necessary across a wind farm.

The conventional *p-y* curves presented in *e.g.* DNVGL-ST-0126 include empirical coefficients which reduce the *p-y* curve capacity under cyclic loading by a constant factor (Reese *et al.*, 1974). Long and Vanneste (1994) also modified static *p-y* curves to account for cyclic loading, as a function of cycle number n instead. However, both these methods are based on limited tests on slender piles, with relatively few cycles (packets with $N < 100$) of high-amplitude cyclic loading applied (Cox *et al.*, 1974; Little and Briaud, 1988). Moreover, the degraded curves obtained with these *cyclic degradation* approaches bear no resemblance to the continuous pile response observed under cyclic loading.

Figure 1.14 compares the response of a (model-scale) monopile in (dry) sand to 100 cycles of loading with the type of responses that may be obtained using the cyclic degradation approaches presented by Long and Vanneste (1994) and Reese *et al.* (1974) (where it is assumed that the macro response of the foundation reflects the constituent *p-y* responses). Although the cyclic degradation approach of Long and Vanneste (1994) has the ability to predict the rotation response at peak load after n cycles (an idealised prediction is shown in Figure 1.14), neither approach can predict the permanent pile rotation on unloading or the hysteretic response, the evolution of which is indicative of the impact of cyclic loading on the foundation's strength and stiffness. It is also unclear how these methods can be adapted for multi-amplitude and multidirectional loading.

No further guidance is provided for cyclic design in standards such as DNVGL-ST-0126, and indeed no commonly accepted design methods currently exist for predicting the response of monopile foundations to cyclic lateral loading. This disparity between the requirements for design and the available design methods has motivated much research in this area over the last decade, as summarised in Section 1.3. Progress has been made in understanding the monopile response to regular (constant amplitude), unidirectional cyclic lateral loading and a number of design methods have been proposed, principally for predicting the permanent rotation response under SLS conditions. However, few studies have explored the monopile response under irregular, multi-amplitude and multidirectional loading, and few design methods are able to capture all aspects of the cyclic response necessary for design.

Cyclic design becomes increasingly important as conservatism in ULS design is reduced (Manceau *et al.*, 2019) and OWT structures become exposed to greater cyclic wave loading at sites with more demanding environmental conditions. Predicting the permanent rotation under SLS loading and the effect of cyclic loading on the response is also increasingly important as turbines near the end of their design life and lifetime extension is considered.

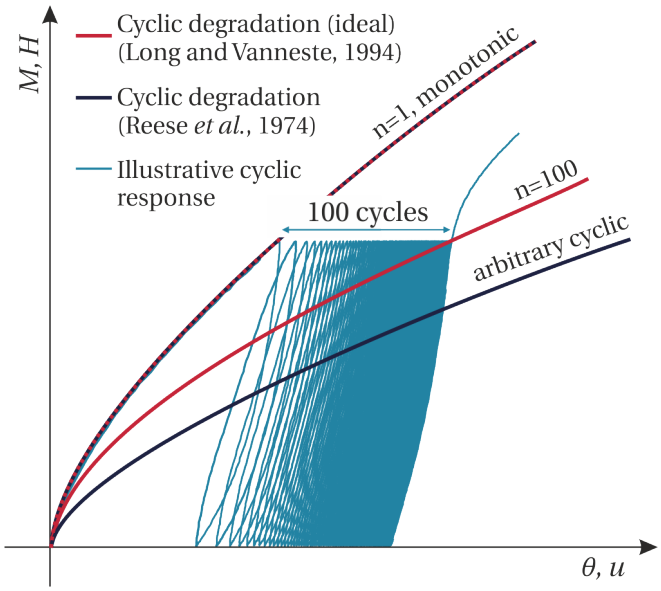

Figure 1.14: Comparison of typical response to unidirectional cyclic loading in drained sand with responses that may be obtained with cyclic degradation approaches

1.3 Relevant research contributions

This thesis focuses on the response of monopiles in sand. As such, this summary of relevant research contributions is also generally restricted to sand.

1.3.1 Physical modelling

Many recent studies have explored the response of monopiles in sand to cyclic loading through small-scale physical modelling, to gain insight into the monopile response and ultimately inform cyclic design. The response of rigid piles with low L/D ratios has been explored at both $1g$ (*e.g.* Leblanc *et al.*, 2010a) and in the centrifuge at elevated stress-levels (*e.g.* Klinkvort and Hededal, 2013); Table 1.2 summarises a selection of these studies. All reported studies have explored the cyclic response in dry or drained (water-saturated) sand. Although numerical modelling has demonstrated that partial drainage and accumulation of pore pressure may be expected for large-diameter monopiles, particularly under large-amplitude cyclic loading (Li *et al.*, 2019; Peralta *et al.*, 2017), important insights can be gained from physical modelling which isolates aspects of the full-scale problem. Physical modelling of pore pressure accumulation under representative cyclic loading would be of great value, but would require a viscous pore fluid to capture the drainage response (*e.g.* Dewoolkar *et al.*, 1999).

Key reference	g-level	Sand properties	Pile L/D	Max. cycles N	ζ_b	ζ_c
Li *et al.* (2010)	$100g$	Dry, dense	5	1000	N/A	0
Leblanc *et al.* (2010)	$1g$	Dry, loose & dense	4.5	65000	0.2–0.5	-1.0–0.5
Cuéllar *et al.* (2012)	$1g$	Saturated[i], dense	~ 4	5000000	$0.2, 0.3$	$< 0, 0$
Klinkvort and Hededal (2013)	$16g$–$75g$	Saturated[i], dense	6	10000	0.08–0.3	-1.0–0.5
Nicolai and Ibsen (2014)	$1g$	Saturated[i], dense	5	50000	0.1–0.4	-0.9–0
Rudolph et al.[ii] (2014)	$1g$, $200g$	Saturated[i] & dry, dense	5	30000	N/A	0
Abadie *et al.* (2019)	$1g$	Dry, very loose	4.7	100000	0.2–0.7	-0.6–0.5
Arshad and O'Kelly (2017)	$1g$	Dry, dense	10	6000	0.3–0.4	-1.0–0.5
Truong *et al.* (2019)	$60g$, $250g$	Dry & saturated[i], dense	6, 11.4	1500	0.4–1.0	-1.1–0.7

[i] Water-saturated.
[ii] Multidirectional cyclic loading applied, all other studies apply unidirectional loading only.

Table 1.2: Selection of relevant physical modelling studies in sand

Regular, unidirectional cyclic loading

The majority of studies have focused on understanding the permanent rotation (or displacement) response of monopiles under regular, unidirectional cyclic loading, as illustrated in Figure 1.10b. Cyclic loading is typically characterised in terms of parameters ζ_b (Leblanc *et al.*, 2010a) and ζ_c (Long and Vanneste, 1994; Leblanc *et al.*, 2010a), which are defined here in terms of maximum and minimum applied moments M_{MAX}, M_{MIN} across a cycle:

$$\zeta_b = \frac{M_{MAX}}{M_R} \tag{1.3}$$

$$\zeta_c = \frac{M_{MIN}}{M_{MAX}} \tag{1.4}$$

These parameters could equally be defined in terms of maximum and minimum horizontal loads H_{MAX}, H_{MIN}. Load asymmetry is defined by parameter ζ_c, with descriptions summarised in Table 1.3, while cyclic load amplitude is together defined

Constant loading	$\zeta_c = 1$
1-way loading	$\zeta_c = 0$
2-way loading	$\zeta_c = -1$
Partial 2-way loading	$-1 < \zeta_c < 0$
Partial 1-way loading	$0 < \zeta_c < 1$

Table 1.3: Load asymmetry descriptions

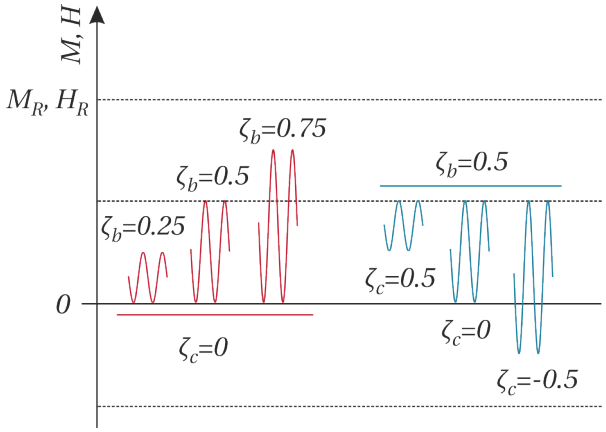

Figure 1.15: Characterisation of cyclic loading in terms of ζ_b and ζ_c (after Leblanc *et al.*, 2010a)

by ζ_b and ζ_c, as illustrated in Figure 1.15. Definition of an (arbitrary) reference load M_R is also required, which varies between studies, in general.

Permanent rotation (or displacement) has been found to accumulate as a power-law (Leblanc *et al.*, 2010a; Klinkvort and Hededal, 2013; Nicolai and Ibsen, 2014; Abadie *et al.*, 2019b; Truong *et al.*, 2019) or logarithmically (Li *et al.*, 2010) with cycle number. Consistent ratcheting behaviour was also observed during large-scale ($D = 0.762$ m, $D = 2.0$ m) cyclic loading tests performed in dense marine sand as part of the PISA project (Beuckelaers, 2017). Ratcheting increases significantly with load amplitude (characterised by ζ_b for constant ζ_c), while load asymmetry (characterised by ζ_c) has also been found to impact the ratcheting response (Leblanc *et al.*, 2010a; Klinkvort and Hededal, 2013; Nicolai and Ibsen, 2014; Truong *et al.*, 2019). Most studies have focused on understanding the macro rotation (or displacement) response of the monopile, although Truong *et al.* (2019) was also able to observe evolution of the distribution of pile displacement and variation in residual (locked-in) net lateral stresses during cyclic loading, using strain gauges on the pile surface.

Some previous studies have also explored the evolution of secant stiffness per cycle, which helps quantify the impact of cyclic loading on the foundation's strength, stiffness and dynamic response. Leblanc *et al.* (2010a) and Klinkvort and Hededal (2013) found secant stiffness to evolve logarithmically with cycle number under a range of loading conditions, while Abadie *et al.* (2019b) observed a faster increase in secant stiffness for the first 50 cycles, and a logarithmic trend thereafter. Abadie *et al.* (2019b) also explored evolution of the initial (maximum) stiffness with cyclic loading, but found no variation over up to 100000 cycles.

The hysteretic response under cyclic loading has been reported in various studies (*e.g.* Niemann *et al.*, 2018; Beuckelaers, 2017), but Abadie *et al.* (2019b) and Abadie (2015) specifically explored the symmetric hysteretic response to demonstrate approximate adherence to the extended Masing rules (Masing, 1926; Pyke, 1979), which have important implications for numerical modelling. Abadie *et al.* (2019b) and Abadie (2015) also report an exponential decrease in per-cycle energy dissipation with cyclic loading (in very loose sand), which is relevant for dynamic design.

Multi-amplitude cyclic loading

A few studies have applied successive packets of regular cyclic loading at different amplitudes, as illustrated in Figure 1.16a, to explore the response to multi-amplitude cyclic loading (Leblanc *et al.*, 2010b; Abadie *et al.*, 2019b). These studies showed behaviour consistent with that observed under constant amplitude cyclic loading and demonstrated a modest impact of packet order. They also emphasised the disproportionately large contribution to ratcheting made by the larger load cycles, given the non-linearity of the monopile response. Exploration of the response to irregular multi-amplitude loading, representative of that experienced by monopiles in the field, would complement these packeted multi-amplitude studies.

Multi-amplitude tests involving regular cycling followed by application of a large monotonic load, as illustrated in Figure 1.16b, have also been conducted to explore the effect of cyclic loading on the ultimate response (Nicolai and Ibsen, 2014; Nicolai *et al.*, 2017b; Abadie *et al.*, 2019b; Truong *et al.*, 2019). In general, the post-cyclic responses were found to re-join or exceed the monotonic response, at odds with the

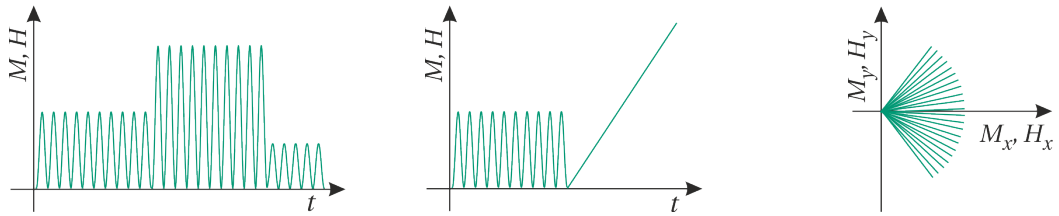

(a) Regular, multi-amplitude packeted cyclic loading

(b) Regular cyclic loading followed by reload

(c) Regular, fan-type multidirectional loading

Figure 1.16: Illustration of multi-amplitude and multidirectional loading applied in previous physical modelling studies

cyclic degradation approaches. The results also suggest that it may be necessary to consider the interaction of cyclic loading with the ULS response to accurately predict pile rotation at peak load. Nicolai *et al.* (2017b) were able to quantify the observed increase in monopile capacity in terms of cycle number and loading characteristics, given that their tests reached yield.

Multidirectional cyclic loading

A limited number of studies have explored the response of monopiles to multidirectional cyclic lateral loading. Peralta (2010) applied successive packets of regular cyclic loading at 0°, 90°, 180°, *etc.* The pile was observed to move in the direction of the applied load regardless of the loading history, and some hardening (reduction of displacement) was observed with application of successive load packets.

The studies of Dührkop and Grabe (2008), Rudolph and Grabe (2013), Rudolph *et al.* (2014b), and Rudolph *et al.* (2014a) involved application of more representative loading, with the cyclic loading direction varying continuously in a fan-type shape, across a specific spread angle, as illustrated in Figure 1.16c. These studies reveal the important result that multidirectional cyclic loading can lead to greater ratcheting than equivalent unidirectional loading, although there is inconsistency in the most damaging spread angle observed across the studies (Rudolph *et al.*, 2014a). The impact of multidirectionality on secant stiffness and energy dissipation has not been explored.

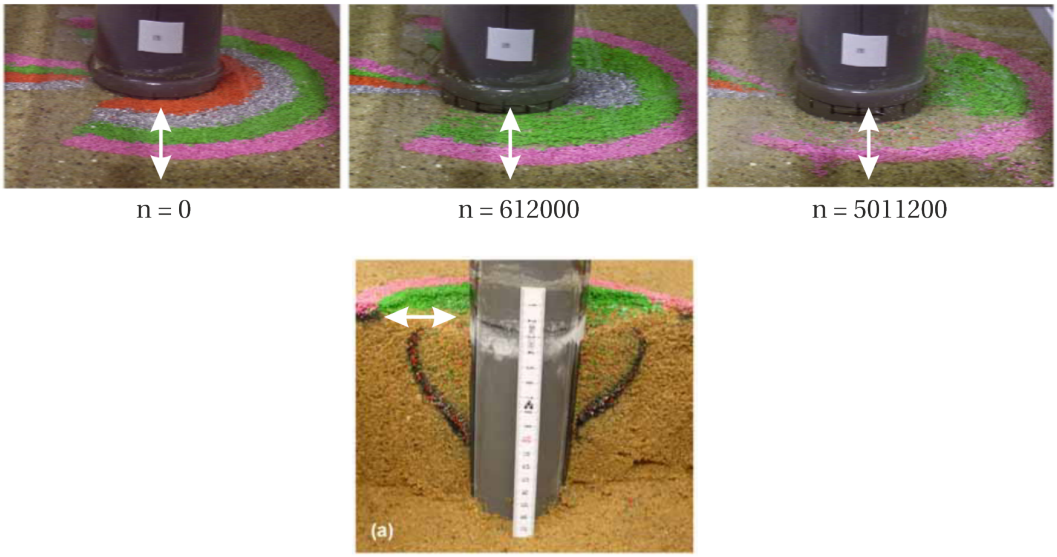

Figure 1.17: Particle migration at soil surface and evidence of convective region following post-test excavation (arrows indicate cyclic loading direction) (modified from Cuéllar *et al.*, 2012)

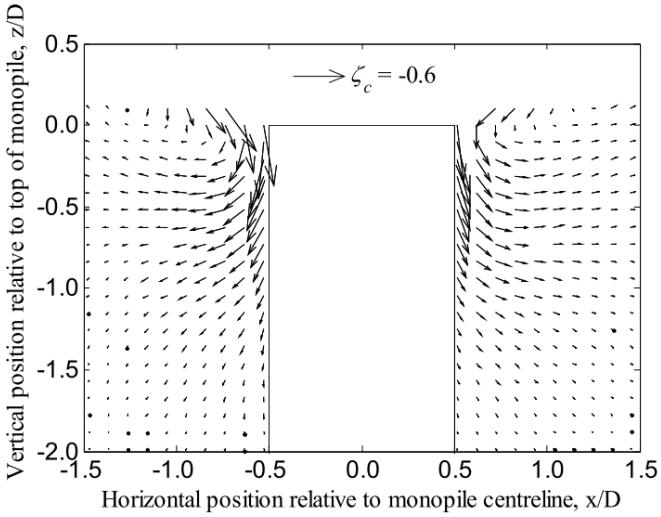

Figure 1.18: Soil velocity vectors showing total displacement (normalised by pile diameter) after 1000 loading cycles obtained through PIV analysis (Nicolai *et al.*, 2017a)

1.3.2 Mechanistic studies

The mechanistic response of monopiles to cyclic lateral loading in sand has been explored variously using Particle Image Velocimetry (PIV) on model-scale centrifuge tests (Nicolai *et al.*, 2017a), using coloured particles to track grain migration around a model pile at 1g (Cuéllar *et al.*, 2012), and through Discrete Element Modelling (DEM) simulations (Cui and Bhattacharya, 2016; Duan *et al.*, 2017).

Figure 1.17 shows how Cuéllar *et al.* (2012) used coloured particles to track sand migration on the soil surface and reveal convective regions within the soil volume, while Figure 1.18 shows the soil velocity vectors after 1000 load cycles determined from an example PIV analysis by Nicolai *et al.* (2017a). The studies are consistent, and suggest the presence of conical convective regions either side of the pile, in-line with the loading direction and extending to $\sim 1.5D$ depth. The convective particle motion is explained by the cyclic variation of stress in-line with loading and the increasing confining stress with depth (Cuéllar *et al.*, 2012). Local subsidence — inferring local densification — was also observed during the $1g$ tests presented by Cuéllar *et al.* (2012). Local densification is also supported by DEM simulations (Cui and Bhattacharya, 2016; Duan *et al.*, 2017) and PIV results (Nicolai *et al.*, 2017a). The asymmetry of both the convective regions and the densification was found to mirror the asymmetry of the applied cyclic loading.

Ratcheting behaviour may, therefore, be understood to be driven by particle rearrangement within convective regions, as well as any asymmetry in local densification. Meanwhile, evolution of the foundation's hysteretic response is understood to be related to local densification. These mechanisms are, however, expected to be coupled.

1.3.3 Proposed cyclic design methods

A number of methods for predicting the response of monopile foundations under cyclic lateral loading have been proposed, a selection of which are summarised in Table 1.4. Most methods represent the monopile as a single-element (macro) or 1D model, consistent with the requirement for fast design calculations, and many methods have focused on predicting only the ratcheting response. In general, validation of these cyclic design methods has been limited.

Informed by small-scale physical modelling, Leblanc *et al.* (2010a) and Klinkvort and Hededal (2013) presented empirical relationships for ratcheting and evolution of secant stiffness as a function of cycle number. The ratcheting relationships have also been shown to approximately predict the response to packets of multi-amplitude loading when coupled with a strain superposition method (Leblanc *et al.*, 2010b; Abadie

Method	Key reference(s)	Behaviour captured	Modelling details
Empirical relationships	Leblanc *et al.* (2010), Klinkvort and Hededal (2013)	Ratcheting, evolution of secant stiffness	Empirical relationships for macro-response, informed by physical modelling
Degradation Stiffness Model	Achmus *et al.* (2009)	Ratcheting	Degradation of backbone modulus within 3D FE model, informed by element testing and 3D FE modelling
High Cycle Accumulation Model	Niemunis *et al.* (2005)	Ratcheting	Accumulation of strain within 3D FE or 1D model, informed by element testing
Cyclic contour diagrams	Andersen (2015), Zhang *et al.* (2016), Bayton *et al.* (2018)	Ratcheting	Methods for interpreting cyclic response from measured element testing or physical modelling data
Hysteretic macro-model	Page *et al.* (2018)	Hysteretic response	Multi-surface kinematic hardening (MSKH) macro-model, informed by 3D FE modelling
HARM	Houlsby *et al.* (2017)	Ratcheting, hysteretic response, evolution of loop shape	Hyperplastic model based on MSKH model with ratcheting element, implemented as macro- or 1D-model, informed by physical modelling

Table 1.4: Selection of proposed design methods for monopiles under cyclic lateral loading

et al., 2015). However, these simple relationships are not adaptable for complex cyclic loading and calibration for full-scale design has not been explored.

Achmus *et al.* (2009) incorporated an empirical expression for degradation of the backbone secant modulus into an elasto-plastic soil model implemented as an FE model. The resulting *Degradation Stiffness Model* (DSM) has been shown to predict ratcheting responses under regular, 1-way cyclic loading reported by Leblanc *et al.* (2010a) with reasonable accuracy (Achmus *et al.*, 2011). This approach has the advantage of being based on element testing results, which may facilitate calibration. However, it is not clear how multi-amplitude loading can be accounted for.

The *High Cycle Accumulation* (HCA) model was developed to capture the general response of coarse sand (Niemunis *et al.*, 2005), and has been applied in 1D models for application to monopile foundations (Wichtmann *et al.*, 2017). The HCA model uses a hypoplastic model (Niemunis and Herle, 1997) or elastic model (Wichtmann

et al., 2017) to capture the continuous response for the first cycles and an empirical model to capture the ratcheting response under many cycles. The model has not been validated against measured monopile responses, but — like the DSM model — has the advantage of being derived from element testing results.

Cyclic contour diagrams, which compile the measured cyclic responses from a number of element tests (Andersen, 2015), have been used for cyclic design of other offshore structures (*e.g.* gravity bases) for many years, principally in soft clays. For application to piles in clay, Zhang *et al.* (2016) obtained degraded cyclic *p-y* curves by scaling the DSS response inferred from Direct Simple Shear (DSS) cyclic contour diagrams. Meanwhile Bayton *et al.* (2018) generated contour diagrams to capture the macro response of a model monopile in dry sand. These approaches do not depend on empirical relationships, but do require extensive element testing or model testing to generate the contour diagrams, which may be prohibitively expensive for design.

A cyclic pile design method has also been proposed as part of the SOLCYP joint industry project, although this project focused on the response of flexible piles with $L/D \approx 16$ (Garnier, 2013). Similarly to the approach of Long and Vanneste (1994), the SOLCYP approach degrades *p-y* curves with empirical expressions in terms of cycle number and cyclic amplitude. Although based on more extensive testing to higher cycle numbers, this approach — like the cyclic degradation method of Long and Vanneste (1994) — is only able to capture pile rotation at peak load.

While the models presented so far have focused on predicting the ratcheting response, the multi-surface kinematic hardening (MSKH) macro model implemented by Page *et al.* (2018) is able to capture the foundation's hysteretic response and can respond to any arbitrary load history, but cannot capture ratcheting. This model has been validated against the hysteretic response observed in field-sale tests as part of the PISA project (Byrne *et al.*, 2017).

Models in the *Hyperplastic Accelerated Ratcheting Model* (HARM) framework (Houlsby *et al.*, 2017) are also based on MSKH models, and therefore also capture a hysteretic response and respond to any arbitrary loading. Importantly, these models are also able to capture ratcheting and evolution of hysteresis loop shape with loading

history, through the inclusion of a ratcheting element and the selection of empirical evolution functions (Houlsby *et al.*, 2017). This combination of features allows these models to capture all three cyclic design aspects detailed in Section 1.2.5, and makes them very attractive for use in design. Models in the HARM framework have been implemented as macro models (Abadie, 2015) and 1D models (Beuckelaers, 2017) and have been shown to predict the ratcheting and hysteretic response under regular, unidirectional cyclic loading at model-scale in sand (Abadie *et al.*, 2019a) and field-scale in sand and clay (Beuckelaers, 2017).

1.4 Thesis structure

1.4.1 Outline

Section 1.2.5 outlined the need for cyclic design methods for monopile foundations to predict the accumulation of permanent rotation under SLS conditions, the effects of cyclic loading on the strength and stiffness of the foundation response, and the hysteretic response. Given the complex cyclic loading to which monopiles are exposed, design methods should perform under irregular, multi-amplitude and multidirectional cyclic loading conditions.

Much insight into the response of monopiles to cyclic lateral loading has been gained through physical modelling studies, the majority of which have focused on understanding the response to regular, unidirectional cyclic loading (Section 1.3.1). In parallel, a number of design methods have been (and continue to be) developed to capture the response to cyclic loading, in particular the permanent rotation under SLS conditions (Section 1.3.3). Models in the HARM framework show particular promise: able to predict both ratcheting and the hysteretic response, as well as respond to any arbitrary loading. Demonstration of the performance of models in the HARM framework under irregular, multi-amplitude and multidirectional cyclic loading is now necessary to build confidence in their application for full-scale design.

This thesis employs laboratory-scale physical modelling to i) provide fundamental insight into the foundation response and ii) facilitate demonstration and inform development of models in the HARM framework. Regular, unidirectional cyclic tests

complement previous experimental studies (Section 1.3.1), explore the impact of cyclic load amplitude and load asymmetry in detail, and facilitate the interpretation of more complex tests. Next, regular multidirectional tests systematically explore the response to cyclic loading with multiple direction components. The response to realistic, irregular, multi-amplitude and multidirectional storm loading is then explored, and parallels are drawn between these novel responses and those observed under regular cyclic loading.

The majority of the testing was performed at $1g$ at Oxford University (OU), with complementary centrifuge testing performed at The University of Western Australia (UWA) to explore the effect of stress-level on the cyclic response. The results from UWA help to establish the relevance of $1g$ physical modelling and inform comparison of monopile responses observed at various stress-levels.

This thesis forms part of a wider coordinated programme of research at Oxford University, the overall aim of which is to understand monopile performance and develop practical design methods for full-scale monopile foundations under cyclic lateral loading. Related research activities include cyclic element testing, theoretical and numerical model development, and large-scale field testing.

1.4.2 Chapter summary

Figure 1.19 presents the structure of this thesis, highlighting the testing performed and the key interactions between Chapters. Each Chapter is briefly summarised below:

Chapter 1 provides context and motivation for exploration of the response of monopiles to complex cyclic lateral loading. Previous work, on which this thesis builds, is also summarised.

Chapter 2 describes the design of novel computer-controlled experimental apparatus which allows application of continuously-varying, multi-amplitude and multidirectional cyclic loading, at constant eccentricity, to a model monopile under load control. Ancillary apparatus for sample preparation and pile installation is also described. This laboratory apparatus is used to carry out the $1g$ tests at OU, presented in Chapters 3, 4 and 5.

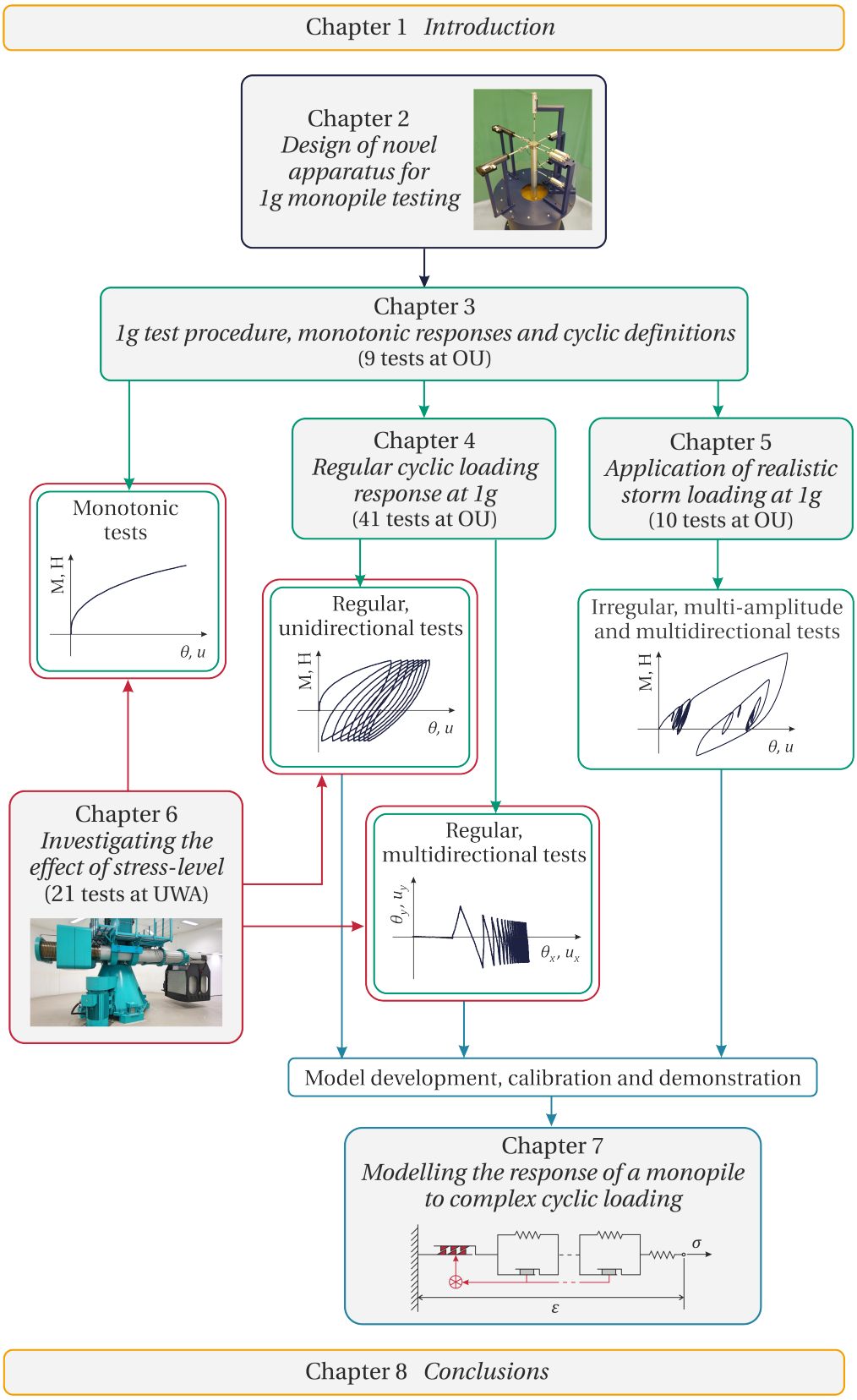

Figure 1.19: Thesis structure

Chapter 3 lays the groundwork for the cyclic results presented in later Chapters. The test procedure for the $1g$ tests at OU is outlined, followed by presentation of the monotonic responses, which underpin the cyclic responses on which this thesis is focused. Normalisation approaches are discussed and consistent definitions for cyclic loading and the cyclic response are presented.

The response of the monopile to regular cyclic loading is explored in detail in **Chapter 4**, with tests in both very loose and dense sand. The impact of cyclic load amplitude, load asymmetry and load directionality is examined, with the cyclic response characterised in terms of ratcheting and evolution of secant stiffness and energy dissipation per cycle. The post-cyclic reloading response is also explored.

Chapter 5 explores the monopile response to realistic multi-amplitude and multidirectional storm loading by application of loading derived from independent model-scale wave basin tests. Parallels are drawn between the responses observed during regular cyclic loading in Chapter 4 and those observed under storm loading.

A key limitation of $1g$ physical modelling is the inability to simulate prototype-scale stress-levels. **Chapter 6** presents the results of a study conducted at UWA to isolate and investigate the effect of stress-level on the response of a monopile in dense sand to cyclic lateral loading. Tests were conducted with an identical set-up at $1g$ and in the centrifuge at $9g$ and $80g$.

Chapter 7 draws on the experimental observations from Chapters 3, 4, 5 and 6 to demonstrate and inform development of numerical models, formulated in the HARM framework (Houlsby *et al.*, 2017), to capture key features of the cyclic response of monopile foundations. Computations are conducted for each of the five datasets presented in this thesis (OU very loose, OU dense, UWA $1g$, UWA $9g$ and UWA $80g$).

Finally, **Chapter 8** summarises the key contributions of this thesis and provides suggestions for future work which have arisen from the research presented herein.

Chapter 2

Design of novel laboratory apparatus for 1g monopile testing

2.1 Introduction

This Chapter describes the design of laboratory apparatus to explore the response of a model monopile to regular and complex cyclic lateral loading at OU at 1g, as reported in Chapters 3, 4 and 5. 1g laboratory testing requires significantly less resource than centrifuge testing or large-scale field testing, and therefore allows a greater number of tests to be performed. More complex systems can also be developed at 1g, without the size and acceleration-level constraints of centrifuge testing or the practical and environmental constraints of field testing.

Many previous studies have used mechanical loading systems to apply cyclic loading to model monopiles (*e.g.* Leblanc *et al.*, 2010a; Nicolai and Ibsen, 2014; Abadie, 2015; Arshad and O'Kelly, 2017). Mechanical systems are reliable, but are generally limited to application of unidirectional loading at a constant amplitude and frequency, at least within individual load packets. A computer-controlled loading system is developed here, in order to apply more complex loading. Computer-controlled loading systems have also been used by *e.g.* Dührkop and Grabe (2008), Rudolph *et al.* (2014b), and Su *et al.* (2014).

This Chapter first describes the design of the model foundation, before describing in detail the loading apparatus and associated software, which is capable of applying continuously varying, multidirectional and multi-amplitude cyclic loading under

External diameter	D	80	mm
Embedded length	L	320	mm
Aspect ratio	η	4	-
Wall thickness	t	5	mm
Loading eccentricity	h	800	mm
Dimensionless loading eccentricity	$\tilde{e}$	2.5	-
Material		Aluminium	
Young's modulus	E	70	GPa
Mass	m	3.53	kg

Table 2.1: Model pile properties

accurate load control. Sample preparation and pile installation apparatus are also presented.

2.2 Model pile

The model pile foundation was first defined, as this controls the size of the tank, loading apparatus and actuator capacity. Table 2.1 summarises the chosen model monopile properties; the diameter $D = 80$ mm scales approximately $1 : 100$ relative to current full-scale monopiles (Sørensen *et al.*, 2017). This size of pile is small enough to enable experiments to be easily managed by one person, but large enough to avoid grain size effects (Klinkvort *et al.*, 2013; Abadie, 2015) with Yellow Leighton Buzzard 14/25 sand (properties in Table 3.1, Section 3.2.1).

The choices of pile length L and loading eccentricity $h = M/H$ were informed by the dimensionless framework derived by Leblanc *et al.* (2010a) for laterally loaded monopiles. The dimensionless load eccentricity $\tilde{e}$ and dimensionless pile aspect ratio η (Equations 2.1 and 2.2, Leblanc *et al.*, 2010a) were chosen to represent full-scale monopiles.

$$\tilde{e} = \frac{h}{L} = \frac{M}{HL} \tag{2.1}$$

$$\eta = \frac{L}{D} \tag{2.2}$$

In the field, $\tilde{e}$ varies continuously with environmental conditions, but the impact of variable loading eccentricity was not explored in this work. A constant eccentricity $\tilde{e} = 2.5$ was therefore chosen, giving $h = 800$ mm. This eccentricity may represent

conditions where thrust loading at the rotor (with eccentricity *e.g.* $4.4L$) is 80% of wave loading (with eccentricity *e.g.* L); this eccentricity may occur during operational conditions, but lower eccentricities are likely during storm loading, when the rotor is parked. A pile aspect ratio $\eta = 4$ was chosen, in-line with aspect ratios for modern full-scale monopiles (Sørensen *et al.*, 2017; Schroeder *et al.*, 2015), giving $L = 320$ mm.

Pile rigidity is also an important consideration for the model monopile. The pile relative stiffness K_R and thresholds derived by Poulos and Hull (1989) are often used to classify pile rigidity:

$$K_R = \frac{E_p I_p}{L^4 E_{SL}} \begin{cases} < 0.0026 & \textit{flexible piles} \\ > 0.208 & \textit{rigid piles} \end{cases} \tag{2.3}$$

Where E_{SL} is the soil's Young's modulus at the pile tip and $E_p I_p$ is the pile bending stiffness. Abadie (2015) demonstrated that most monopiles installed at sand sites pre-2015 have an intermediate rigidity, but future monopiles are expected to behave rigidly. An aluminium model pile with wall thickness $t = 5$ mm was chosen. This pile is classified as fully rigid (Poulos and Hull, 1989) in loose sand, where $E_{SL} < 27$ MPa. In dense sand, where *e.g.* $E_{SL} = 60$ MPa (Geotechdata, 2013) the pile is close-to-rigid ($K_R = 0.093$). Although the pile rigidity is representative, the ratio of pile diameter to wall thickness $D/t = 15.9$, is smaller than for typical full-scale monopiles, where $D/t \approx 100$ (University of Strathclyde, 2015); this is likely to affect installation effects, but not the lateral response directly.

The pile has a normalised mean roughness $R_n = R_a/d_{50} \approx 0.001$ (relative to Yellow Leighton Buzzard 14/25 sand) measured using a hand-held stylus profilometer (Uesugi and Kishida, 1986). The pile is therefore classified as smooth, in contrast to full-scale monopiles which are typically rough. However, surface roughness has been shown to have only a small impact on the monopile's lateral response (Klinkvort, 2012).

2.3 Loading and pile measurement apparatus

2.3.1 Design overview

Figure 2.1 shows the Computer Aided Design (CAD) model of the loading and pile measurement apparatus, and Figure 2.2 shows the apparatus in the laboratory. The

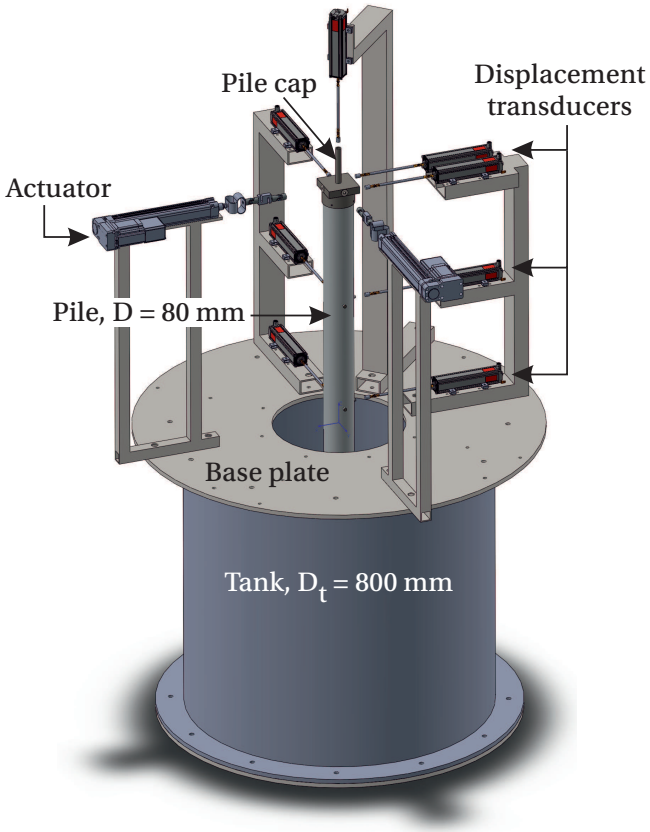

Figure 2.1: CAD model of laboratory apparatus (displacement transducers shown in all possible positions, connections to pile exploded)

apparatus centres on a rigid cylindrical steel tank with upper and lower flanges, which holds the soil sample and doubles as the reaction frame. A steel base plate bolts to the top flange of the tank, on which removable steel brackets are attached to support installation apparatus, actuators and displacement measurement transducers. The modular design ensures that the apparatus is flexible.

Biaxial loading is applied to the pile with two perpendicular computer-controlled actuators, while six displacement measurement transducers track the pile's position in space. A six Degree of Freedom (DoF) pile measurement system is necessary as the pile is not restrained in any direction. A global coordinate system is defined with x- and y-axes aligned with the line of action of the actuators and displacement transducers (see Figure 2.2a). The z-axis is vertical, and the origin is at the sample surface.

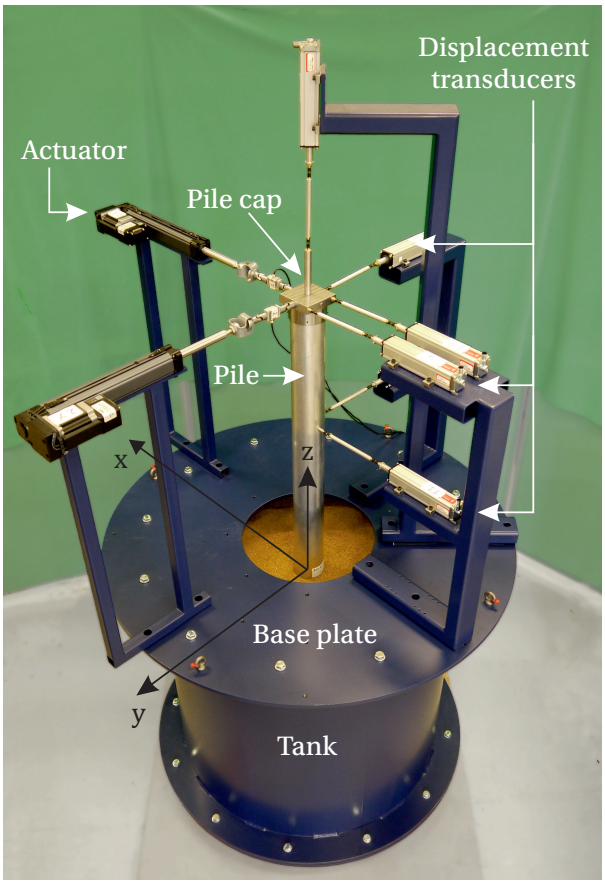

(a)

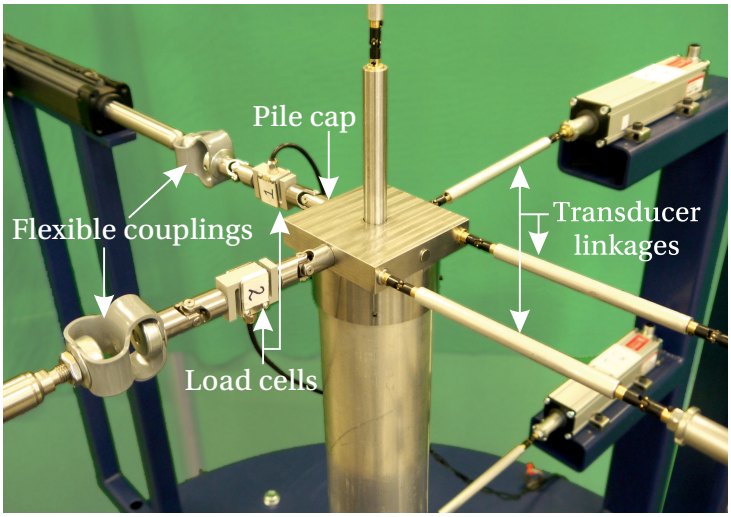

(b)

Figure 2.2: Photographs of laboratory apparatus (electrical and communication connections omitted for clarity)

2.3.2 Tank

The internal tank dimensions were chosen to balance minimising boundary effects and the volume of soil required. Numerical investigations by *e.g.* Achmus *et al.* (2007) state that lateral boundary effects are avoided with a soil volume of diameter $12D$, while previous experimental work has used soil samples with (effective) diameter *e.g.* $7D$ (Leblanc *et al.*, 2010a; Abadie, 2015) and $10D$ (Albiker *et al.*, 2017). Here, a cylindrical tank with diameter $D_t = 10D = 800$ mm was chosen. Little work has investigated the impact of the bottom boundary, however, $2D$ to $3D$ space beneath the pile tip is typical. A tank depth $h_t = 800$ mm ensures sufficient space for piles up to 480 mm long ($L/D = 6$). The design assumes that the soil surface is located 100 mm below the tank top flange, which helps avoid sample disturbance during set-up. The tank was mounted on four soft rubber feet to isolate the system from external vibrations.

2.3.3 Pile cap

A *pile cap* was designed to transfer load to the pile and allow straightforward connection of the upper displacement transducers to the pile. The cap sits on top of the pile, secured by grub screws, and is attached following pile installation. The steel pile cap weighs 1.49 kg and includes a vertical shaft to hold 1 kg $-$ 5 kg ring-shaped masses to apply additional static vertical loading if required.

2.3.4 Actuators and load application

The actuators were sized to achieve $2°$ pile rotation in dense sand. Basic monotonic analyses were performed (following the *p-y* approach described in Section 1.2.4) and the model-scale results of Abadie (2015) and Leblanc *et al.* (2010a) were consulted. Zaber *BAR-E200* linear actuators were chosen, with specification summarised in Table 2.2. High resolution of motion is essential for accurate control at low load amplitudes.

The actuators are supported on brackets at $h = 800$ mm above the sample surface. Figure 2.3 shows the components in-line with each actuator. Fatigue-resistant, HUCO polymer couplings provide a relatively flexible link between each actuator and the pile which masks any changes in the stiffness of the pile-soil system during loading and improves actuator control, while low backlash universal joints allow the pile to

Travel	203	mm
Maximum thrust	540	N
Motor type	Stepper	
Resolution of motion	0.248	μm
Maximum speed	65	mm/s

Table 2.2: Zaber *BAR-E200* linear actuator specification summary

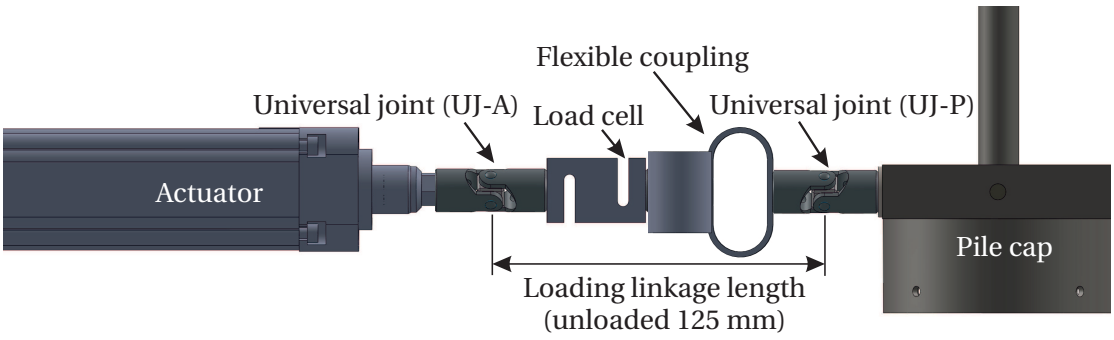

Figure 2.3: Components in-line with actuator (configuration used for testing presented herein)

rotate and settle without applying moment. 200 N capacity S-beam load cells were chosen to measure the in-line load applied to the pile. The load cells and associated data acquisition system (described in Section 2.4.2) have a noise amplitude of around 0.07 N.

2.3.5 Position measurement

Temposonic *ER-type* magnetostrictive displacement transducers were chosen for measurement of the pile position. Compared to standard linear variable differential transformers (LVDTs) these sensors do not require signal processing or regular recalibration. 50 mm travel was chosen to capture the pile's response up to 2° rotation, without compromising on accuracy during low-amplitude cyclic loading. The transducers and associated data acquisition system (described in Section 2.4.2) have a noise amplitude of around 1.5 μm.

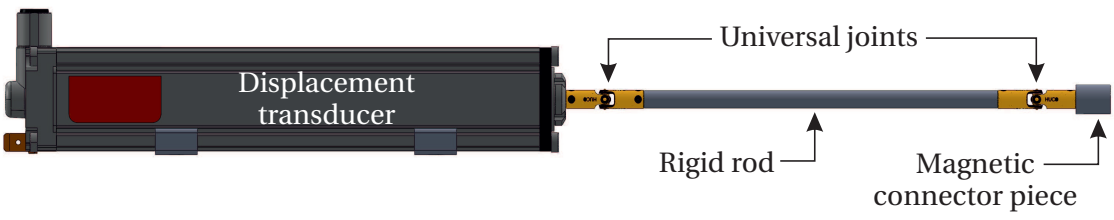

Figure 2.4: Components in-line with displacement transducer

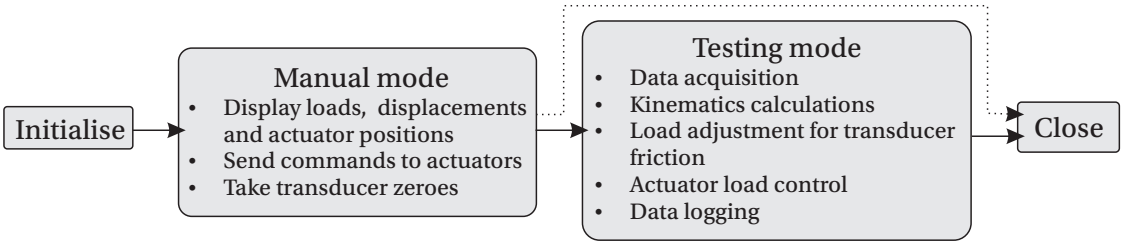

Figure 2.5: Overall structure of *Labview* software

Six transducers are supported on three rigid brackets, appropriately orientated to ensure resolution of the six degrees of freedom. Typically, one transducer is located vertically above the pile; three transducers are located on the bracket aligned with the x-direction, at two levels (800 and 400 mm above the sample surface); and two transducers are located on the bracket aligned with the y-direction, at the same two levels. The transducers attach to the brackets with sliding clamps, which allow the transducer position in-line with the measurement direction to be varied.

Rigid aluminium rods link the transducers to the pile, with low-backlash universal joints at either end to accommodate pile movement, as shown in Figure 2.4. Magnetic connectors provide a simple and secure connection between the rigid rods and either the pile cap (upper transducers) or small bosses on the pile wall (lower transducers).

2.4 Data acquisition, kinematics and control software

2.4.1 Software overview

Software was developed in the National Instruments *Labview* environment to perform the data acquisition, kinematics calculations and control processes necessary to set-up and run tests with the apparatus described in Section 2.3. The software runs on a standard PC and includes a user interface to accept commands and display key data.

The software operates in one of two modes: *Manual* or *Testing*, between *Initialise* and *Close* operations, as indicated in Figure 2.5. The *Manual* mode acquires and displays load and displacement measurements and actuator positions, enables manual commands to be sent to the actuators and records transducer zeroes before testing. This simple mode is primarily used for test set-up, and its operation is not described further.

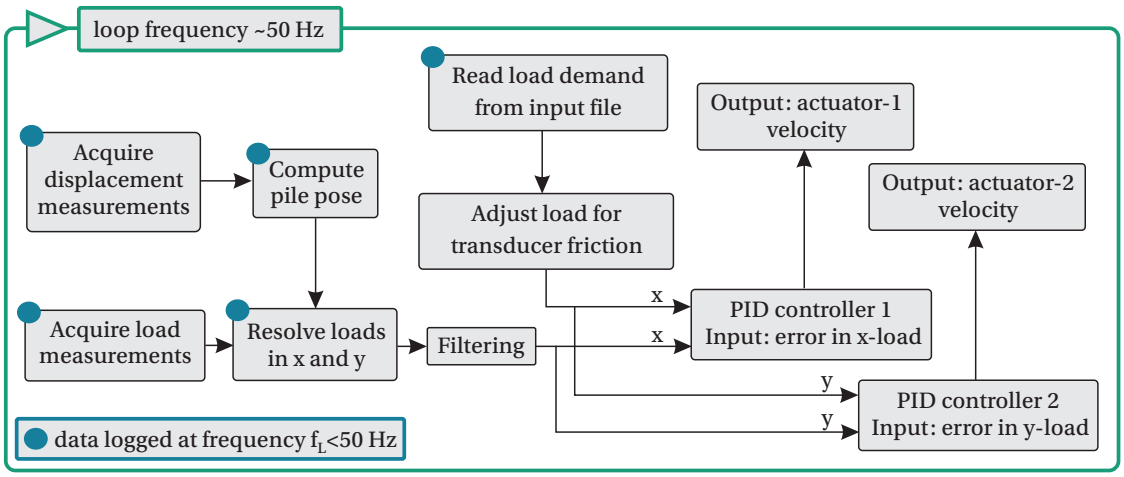

Figure 2.6: Structure of *Testing* mode within *Labview* software

The *Testing* mode is designed for running tests: performing data acquisition, kinematics calculations, load demand adjustments, actuator load control and data logging, as summarised in Figure 2.6. Sections 2.4.2 to 2.4.6 describe the key operations performed within the *Testing* mode, which loops continuously at 50 Hz.

2.4.2 Actuator communication and data acquisition

Communication with the actuators is through a Zaber *X-MCB2* dual-axis controller which connects to the PC via USB. The Binary communication protocol was chosen, as this increases communication speed by around 10 times, compared to default ASCII communication. Fast actuator communication is essential for successful load control.

A *CompactDAQ* system from National Instruments is used for data acquisition and signal conditioning. This modular system consists of a chassis with Ethernet communication and two data acquisition modules. A 16-bit analogue input module (*NI 9205*) acquires data from the displacement transducers, while a 24-bit bridge-specific module (*NI 9237*) provides voltage excitation, signal conditioning and analogue input for the load cells.

2.4.3 Kinematics calculations

Kinematics calculations are necessary to i) calculate the pile's position in space (pose) from the six displacement measurements and ii) calculate the position of the load cells and resolve measured in-line loads to x- and y-components. To calculate the pile pose

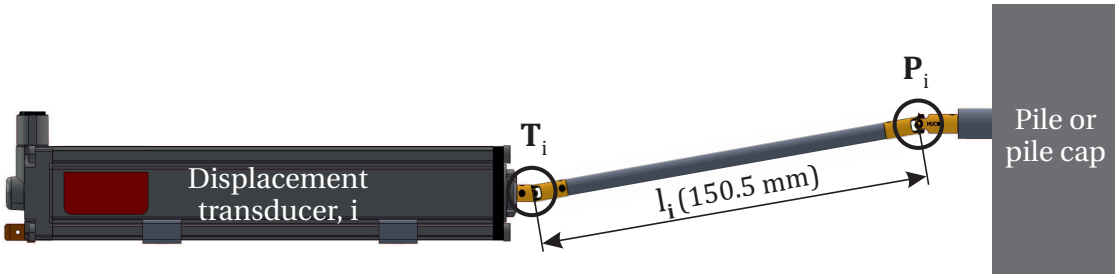

Figure 2.7: Schematic illustrating parameters for forward kinematics calculations ($\mathbf{P}_i, \mathbf{T}_i, l_i$)

from transducer measurements an iterative *forward kinematics* scheme is necessary; the method described by Byrne and Houlsby (2005) and Byrne and Houlsby (2010) for pivoting transducers is adapted here for fixed transducers with pivoting linkages. The load cell positions and resolved loads can then be found directly using more straightforward *inverse kinematics* calculations. The forward and inverse terminology comes from robotics, where forward calculations find the pose of the end piece (here the pile) from joint (here the transducer or load cell) positions, while inverse calculations do the reverse (Kucuk and Bingul, 2006).

The pile's pose is defined by the vector $\mathbf{s} = [u\ v\ w\ \alpha\ \beta\ \gamma]^T$ where u, v, w are pile displacements in the x, y, z directions and α, β, γ are rotations about the x, y, z axes respectively. The global coordinate system is defined in Section 2.3.1, and the pile is treated as a rigid body. For each transducer $i = 1, 2...6$ the coordinates of the associated pivot point on the pile or pile cap $\mathbf{P}_i = [x_i\ y_i\ z_i\ 1]^T$, pivot point on the transducer $\mathbf{T}_i = [x_i\ y_i\ z_i\ 1]^T$ and the linkage vector $\mathbf{L}_i = [x_i\ y_i\ z_i\ 0]^T$, with magnitude $l_i = |\mathbf{L}_i|$, are defined. Figure 2.7 indicates $\mathbf{P}_i, \mathbf{T}_i, l_i$ schematically for transducer i. In this set-up the linkage vector magnitude is fixed, $l_i = 150.5$ mm.

The transformation matrix $\hat{\mathbf{T}}$ translates between global and local coordinate systems, identified with subscripts G and L, respectively. For example:

$$\mathbf{P}_{iG} = \hat{\mathbf{T}}\mathbf{P}_{iL} \tag{2.4}$$

The transformation matrix adopted here follows Byrne and Houlsby (2010):

$$\hat{\mathbf{T}} = \begin{bmatrix} \cos\beta\cos\gamma & \sin\alpha\sin\beta\cos\gamma - \cos\alpha\sin\gamma & \cos\alpha\sin\beta\cos\gamma + \sin\alpha\sin\gamma & x \\ \cos\beta\sin\gamma & \sin\alpha\sin\beta\sin\gamma - \cos\alpha\cos\gamma & \cos\alpha\sin\beta\sin\gamma + \sin\alpha\cos\gamma & y \\ -\sin\beta & \sin\alpha\cos\beta & \cos\alpha\cos\beta & z \\ 0 & 0 & 0 & 1 \end{bmatrix} \tag{2.5}$$

As matrix multiplication is not commutative, the transformation matrix is not uniquely defined, but depends on the order in which transformations are considered to be applied. However, for small displacements the impact of the choice of any transformation matrix is negligible (Byrne and Houlsby, 2010).

The iterative forward calculation requires global transducer pivot coordinates $\mathbf{T}_{iG}$, local pile pivot coordinates $\mathbf{P}_{iL}$ and linkage lengths l_i — which make up a vector of linkage lengths $\mathbf{V} = [l_1, l_2, ..., l_6]^T$ — as inputs. $\mathbf{T}_{iG}$ are determined from the coordinates of the transducer pivot points when fully retracted $\mathbf{T}_{iG}^R$ and the transducer measurements ΔT_i. For a transducer parallel to the x-axis:

$$\mathbf{T}_{iG} = \mathbf{T}_{iG}^R + [\Delta T_i \; 0 \; 0 \; 0]^T \tag{2.6}$$

Both $\mathbf{T}_{iG}^R$ and $\mathbf{P}_{iL}$ were determined with the use of a CNC (Computer Numerical Controlled) coordinate measuring machine. Coordinates of etched points on the base plate and brackets were (CNC) measured relative to the global coordinate system, with nine points measured close to each transducer location. The coordinates of $\mathbf{T}_{iG}^R$ were then determined (with a spreadsheet) from these coordinates and calliper measurements between these points and the transducers, following transducer positioning (which may vary between tests). Local coordinates on the pile and pile cap were (CNC) measured at the magnetic connection points, which are straightforwardly related to the pile pivot points $\mathbf{P}_{iL}$ by the length of the connector pieces. The pile's local coordinate system was defined to be aligned with the global coordinate system for a perfectly vertical pile installation to 320 mm embedment.

The iterative calculation is set up in terms of a change in vector of linkage lengths $\Delta\mathbf{V} = [\Delta l_1, \Delta l_2, ..., \Delta l_6]^T$. As the linkage lengths are fixed in this set-up, a solution is obtained when $\Delta\mathbf{V} \to 0$. It is assumed that the linkage lengths l_i can be linearised with respect to the pile pose following Lazarevic (1997). This is expressed as:

$$\Delta\mathbf{V} = \frac{dl_i}{d\mathbf{s}_j} = \mathbf{R}_{i,j}\Delta\mathbf{s} \tag{2.7}$$

The chain rule can be used to express the matrix components as $\mathbf{R}_{i,j} = \frac{dl_i}{d\mathbf{L}_i} \cdot \frac{d\mathbf{L}_i}{d\mathbf{s}_j}$. Noting that $\mathbf{L_i} = \mathbf{P_{iG}} - \mathbf{T_{iG}} = \hat{\mathbf{T}}\mathbf{P_{iL}} - \mathbf{T_{iG}}$ and $\frac{dl_i}{d\mathbf{L}_i} = \frac{1}{l_i}\mathbf{L}_i$ the matrix components $\mathbf{R}_{i,j}$ become:

$$\mathbf{R}_{i,j} = \frac{\mathbf{L}_i}{l_i} \cdot \frac{d(\hat{\mathbf{T}}\mathbf{P_{iL}} - \mathbf{T_{iG}})}{d\mathbf{s}_j} = \frac{\mathbf{L}_i}{l_i} \cdot \frac{d\hat{\mathbf{T}}}{d\mathbf{s}_j}\mathbf{P}_{iL} \tag{2.8}$$

Having obtained $\mathbf{R}$, the change in pile pose $\Delta\mathbf{s}$ can then be calculated as:

$$\Delta\mathbf{s} = \mathbf{R}^{-1}\Delta\mathbf{V} \tag{2.9}$$

Starting with an initial guess for $\mathbf{s}$, the pose is updated iteratively using the solution from the previous iteration. The scheme converges within a few iterations, although 10 iterations are used in the software, as the kinematics calculations do not limit the loop speed in *Testing* mode (actuator communication speed does).

Calculation of the pile pose allows the position of the universal joints on the pile cap (UJ-P, Figure 2.3) to be determined. The positions of the universal joints attached to the actuators (UJ-A, Figure 2.3) are found independently using encoders in each actuator. With the position of each universal joint known, the load cell angles and resultant loads in the x- and y-direction are found using standard geometry (inverse kinematics), which is not discussed further.

After *e.g.* loading the pile in the y-direction to $1°$ rotation, the resolved load in the x-direction is approximately 83% of that measured in-line by the corresponding load cell, highlighting the need to adjust for load cell angle. This discrepancy is dependent on the length of the loading linkage, which is 125 mm for this set-up, when unloaded (as indicated in Figure 2.3). Both the forward and inverse kinematics calculations are embedded within the *Testing* loop and performed on-line at a rate of 50 Hz.

2.4.4 Adjustment for transducer friction

The displacement transducers (described in Section 2.3.5) have sliding frictional resistance $\bar{F} \approx 0.22$ N. The net force required to overcome the transducer friction is therefore non-negligible when very low amplitude cyclic loading (*e.g.* < 10 N) is applied to the pile. Approximate load adjustment is included in the *Testing* mode, as

indicated in Figure 2.6, to reduce conflation of the frictional response of the transducers with the pile response.

The net friction magnitude is $n\bar{F}$, where n is the number of transducers aligned with the load direction. Typically $n = 3$ in the x-direction and $n = 2$ in the y-direction. Assuming load demand is being accurately tracked, the friction force F_i depends on the rate of change of load demand $\frac{dH_{Di}}{dt}$ in the i-direction as:

$$F_i = \begin{cases} n\bar{F} & \frac{dH_{Di}}{dt} > 0 \\ -n\bar{F} & \frac{dH_{Di}}{dt} < 0 \\ 0 & \frac{dH_{Di}}{dt} = 0 \end{cases} \tag{2.10}$$

To account for transducer friction the load demands H_{Di} are adjusted to $H'_{Di} = H_{Di} + F_i$, while the loads recorded as applied to the pile H_{Ri} are adjusted from the measured loads H_{Mi} as $H_{Ri} = H_{Mi} - F_i$. To smooth abrupt changes in load demand and improve load control performance, a moving average filter is also applied to F_i, which would otherwise be a square wave for constant amplitude cyclic loading. Although this method reduces the effect of transducer friction, it is not perfect, as $\bar{F}$ is not constant and there is always some error in load demand tracking.

2.4.5 Load control

Accurate load control is central to the operation of the *Labview* software in *Testing* mode. Two PID (Proportional Integral Derivative) controllers (inbuilt *Labview* subroutine) perform load control; Figure 2.6 shows how the controllers integrate into the *Testing* structure. The controllers compare the measured x- and y-direction loads H_{Mi} to the (adjusted) load demands H'_{Di}, and output velocities v_i for actuator 1 and 2, respectively. Load demands H'_{Di} are specified in a text file with x- and y-component loads defined at the loop frequency (50 Hz). Actuator 1 and actuator 2 are initially aligned with the x- and y-axes, but as the pile moves the load application axes become misaligned and (*e.g.*) actuator 1 may apply some y-direction load. However, with a fast loop rate and relatively small displacements, this coupling does not generate control issues.

PID controllers determine their output $u(t)$ from the error in the Process Variable (PV) $e(t)$ as (Cannon, 2012):

$$u(t) = K\left(e(t) + \frac{1}{T_i}\int_0^t e(t')dt' + T_d\frac{de}{dt}\right) \tag{2.11}$$

Where the controller variables are gain K, integral time T_i and derivative time T_d. In this case the output is actuator velocity $u(t) = v_i(t)$ and the PV is measured load $H_{Mi}(t)$; the error in the PV is therefore $e(t) = H_{Mi}(t) - H'_{Di}(t)$ for axis i. A second order low-pass Butterworth filter (inbuilt *Labview* subroutine, cut-off frequency 15 Hz) is applied to the PV to remove high frequency components and reduce actuator wear, although this does introduce a small phase lag.

The controllers are tuned manually to achieve a fast response, without overshoot, to a step-change in load applied to the pile-soil system. The flexible couplings (described in Section 2.3.4) introduce a near-constant system compliance which leads to good control performance with a constant gain and no integral and derivative components ($K \approx 5000$, $T_i = \infty$, $T_d = 0$, effectively a simple Proportional controller) in both loose and dense sand, and at variable loading rate. Gain amplification is also included to increase K by factor 1.6 close to zero load ($-1 < H < 1$ N). Small but finite backlash in the universal joints in-line with the actuators introduces additional system compliance close to zero load, and increasing K here improves controller performance.

The control system has been tested under sinusoidal cyclic loading with maximum loading rates up to $2\pi H_{CYC} f = 11$ N/s, where H_{CYC} is the cyclic load amplitude and f is the cyclic frequency. At these loading rates $|e(t)| < 1\ N$, although this instantaneous error is mostly due to the phase lag introduced by filtering.

2.4.6 Data logging

Throughout testing raw measurement data, pile pose, resolved loads and load demand are logged to text files at a frequency f_L suitable for the test, where ($f_L < 50$ Hz).

2.5 Sample preparation apparatus

Apparatus was developed to prepare dense, dry sand samples in the tank described in Section 2.3.2 (very loose samples were prepared manually, and both sample preparation

procedures are described in Section 3.2.2). Vibratory methods and air pluviation (sand raining) methods have been used previously to prepare dense samples. Air pluviation was chosen here as it may simulate a soil fabric similar to that found in natural deposits formed by sedimentation (Rad and Tumay, 1987); is also known to be difficult to achieve repeatable samples with vibratory methods. Air pluviation typically involves pouring sand from a hopper at height h above the sand sample through a flow control mechanism to achieve an effective unit weight γ'. The flow rate Q controls the ability of particles to settle to a close-packed state and γ' reduces with increasing Q. Drop height controls the particle velocity and γ' increases with increasing h, although only to the point at which the sand particles reach terminal velocity (Rad and Tumay, 1987).

Various sand raining devices have been developed. For example, Schnaid (1990) used a large fixed hopper at a high drop height and prepared samples in a single pour, while Peralta (2010) maintained a constant drop height by pouring locally from a flexible hose. Flexible, robotic sand rainers have also been developed by *e.g.* Zhao *et al.* (2006) and Gaudin *et al.* (2018). A simple fixed device was developed here, as shown in Figure 2.8. A hopper, capable of holding around 0.3 m^3 sand, is supported 750 mm above the maximum soil sample height. The resulting minimum drop height h is assumed to be large enough for most particles to reach terminal velocity, following the approach of Schnaid (1990). The hopper is supported on a flanged cylinder, which contains any dust generated by the raining process, but is also likely to introduce boundary effects. Two shutter plates with matching hole patterns are positioned beneath the hopper. The plates are initially misaligned, but moving the lower plate (by impact with a rubber mallet) aligns the holes and allows sand to flow. A diffuser mesh is positioned 150 mm beneath the shutter plates.

The shutter plate and diffuser mesh together control the sand flow rate Q and therefore effective unit weight γ'. 20 mm diameter shutter plate holes on a 80 mm equilateral triangular grid with a 2.54 mm square weldmesh diffuser sieve were found to generate repeatable samples with Yellow Leighton Buzzard 14/25 sand (properties in Table 3.1, Section 3.2.1) with average $\gamma' = 16.2$ kN/m^3 and relative density $D_R = 60\%$. Changing the diffuser mesh to a 1.27 mm square weldmesh and 5 mm diameter circular

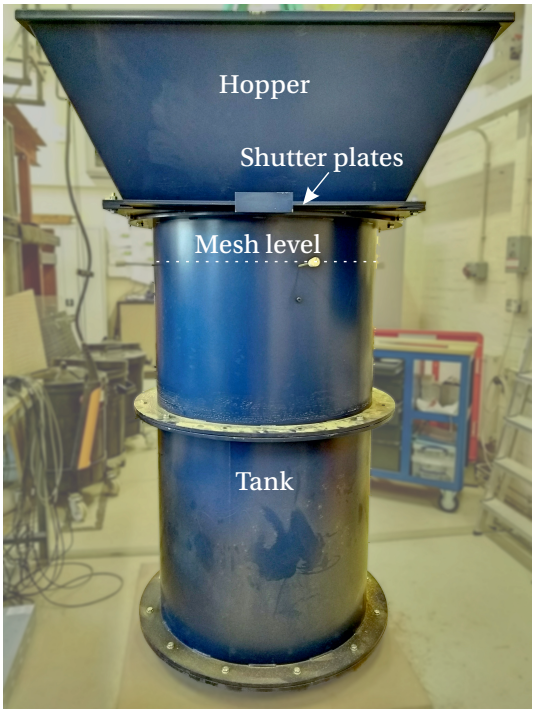

Figure 2.8: Photograph of sand raining apparatus

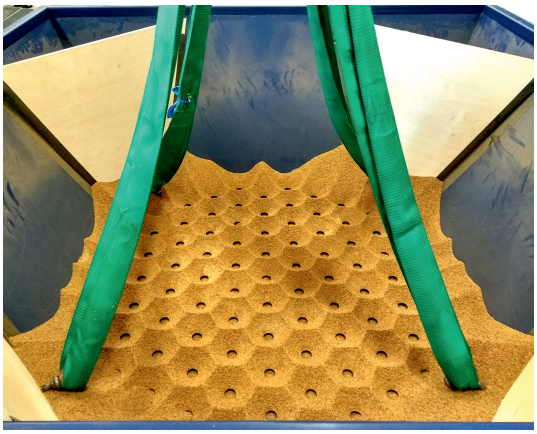

Figure 2.9: Photograph of residual sand in hopper following raining — highlighting shutter grid pattern

perforated plate with 6 mm pitch generated $D_R \approx 70\%$ and $D_R \approx 80\%$, respectively. However, sand accumulated on these meshes during raining, and so preparation of $D_R = 60\%$ samples was preferred. The shutter grid pattern is highlighted by the residual sand in the hopper in Figure 2.9.

2.6 Pile installation apparatus

Apparatus was designed to install the model pile by driving. Figure 2.10 shows the apparatus in the laboratory, with the actuator and transducer brackets omitted for clarity. The pile is installed manually by raising and dropping the hammer mass (1.4 kg or 2.8 kg for very loose and dense sand respectively) onto the pile. The Perspex hammer guide ensures the mass drops squarely onto the pile sleeve from a constant height ($\approx$ 240 mm). The hammer mass and drop height were chosen to ensure pile installation is controlled but not overly slow. Approximately 120 blows and 200 blows were required for installation of the pile in very loose and dense sand respectively. The pile guide holds the pile vertically at the tank centre during installation. It is designed to be easily removed after installation without disturbing the pile.

Figure 2.10: Photograph of pile installation apparatus

2.7 Summary

This Chapter has described the design of novel apparatus to explore the response of a model pile with diameter $D = 80$ mm to cyclic lateral loading under load control. The loading apparatus facilitates the application of complex — multidirectional, multi-amplitude, continuously varying — cyclic loading, which would not have been possible with the mechanical systems used in many previous studies. The accompanying *Labview* software, which performs data acquisition, load control and kinematics calculations, is integral to the performance of this loading apparatus and has been described in detail. Development of ancillary apparatus for sample preparation and pile installation have also been discussed.

Chapter 3

1*g* test procedure, monotonic responses and cyclic definitions

3.1 Introduction

This Chapter describes the sample preparation and test procedures adopted for the tests at OU (presented in this Chapter and Chapters 4 and 5). The monotonic responses, which underpin the cyclic responses on which this thesis focuses, are presented. The effect of loading rate and direction is explored, and normalisation approaches are discussed. Consistent definitions for cyclic loading and the cyclic response are also presented.

3.2 Sand sample

3.2.1 Sand properties

Yellow Leighton Buzzard (YLB) 14/25 sand was used for the tests conducted at OU. This sand has been previously used for physical modelling in the geotechnical group at OU (*e.g.* Villalobos, 2006; Leblanc *et al.*, 2010a; Abadie *et al.*, 2015). In parallel with the work presented in this thesis, White (2020) has conducted extensive laboratory testing to explore the response of this sand at low confining stresses.

Yellow Leighton Buzzard 14/25 sand is a coarse, uniformly graded silica sand. Figure 3.1 presents the measured particle size distribution, which approximately corresponds to the lower bound of *Fraction B*, as defined in BS 1377 : Part 4 (British Standard, 1998). The $0.6 - 1.18$ mm sieve fractions (where the majority of this sand lies) correspond

Specific gravity (Schnaid, 1990)	G_s	2.65	-
Particle size	$d_{10}, d_{30}, d_{50}, d_{60}$	$0.56, 0.69, 0.81, 0.87$	mm
Minimum dry unit weight	γ'_{MIN}	14.43	kN/m^3
Maximum dry unit weight	γ'_{MAX}	17.64	kN/m^3
Maximum void ratio	e_{MAX}	0.80	-
Minimum void ratio	e_{MIN}	0.47	-
Critical friction angle (Schnaid, 1990)	ϕ'_c	34.3	°

Table 3.1: Yellow Leighton Buzzard 14/25 sand properties

to British Standard Sieve Series Mesh No. 14-25, hence common reference to this sand as Yellow Leighton Buzzard 14/25.

Minimum and maximum dry unit weights ($\gamma'_{MIN}, \gamma'_{MAX}$) were obtained following the methods described in BS 1377 : Part 4 (Sections 4.4 and 4.2) (British Standard, 1990), and are reported in Table 3.1. However, methods for obtaining γ'_{MIN} and γ'_{MAX} differ between standards and organisations. Blaker *et al.* (2015) explored method dependency for five different sands (including Yellow Leighton Buzzard 14/25), determining γ'_{MIN} and γ'_{MAX} following four different standards and using in-house methods from three organisations. Vibrating hammer, discrete hammer and mould vibration methods were used to determine γ'_{MAX}, while methods for γ'_{MIN} included placement with funnels, tubes and scoops, and agitation by inversion of a cylinder. Significant variation in both γ'_{MIN} and γ'_{MAX} was observed; for Yellow Leighton Buzzard 14/25, $14.12 \leq \gamma'_{MIN} \leq 15.13$ kN/m^3 and $16.45 \leq \gamma'_{MAX} \leq 17.85$ kN/m^3 (Blaker *et al.*, 2015).

Variation in values of γ'_{MIN} and γ'_{MAX} leads to variation in reported relative density D_R values. Figure 3.2 plots lower and upper bounds for relative density D_R as a function of unit weight γ', using the ranges of γ'_{MIN} and γ'_{MAX} reported by Blaker *et al.* (2015). In this work, D_R is obtained using the measured values of γ'_{MIN} and γ'_{MAX}, but Figure 3.2 highlights how comparisons to other data sets should be made with caution, considering the significant method dependency reported (Blaker *et al.*, 2015).

3.2.2 Sample preparation

The tests at OU were conducted at two densities: very loose and dense. The very loose samples were built up in three layers by repeated manual pouring from a very low

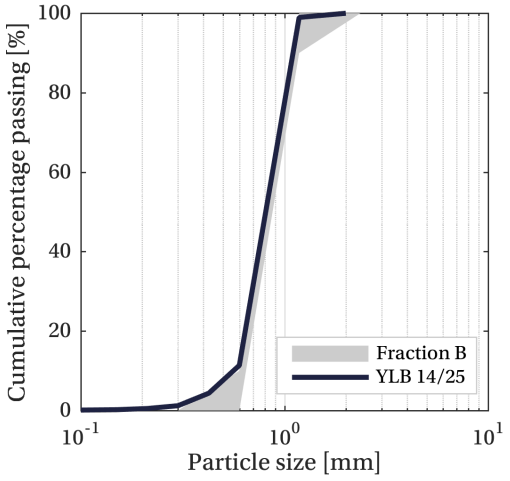

Figure 3.1: YLB 14/25 particle size distribution

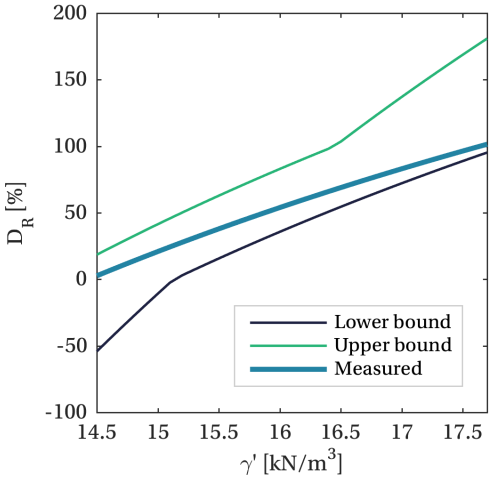

Figure 3.2: Relative density D_R of YLB 14/25 as a function of effective unit weight γ' (lower and upper bounds use values of γ'_{MAX} and γ'_{MIN} from Blaker *et al.* (2015))

drop height (< 70 mm) using a shovel with approximate volume 0.0015 m^3. A constant sample depth was achieved by careful pouring to the required depth, indicated by a guide. The average unit weight across 80 samples (determined from global mass and volume measurements) was $\gamma'_{AV} = 14.46 \pm 0.08$ kN/m^3, corresponding to an average relative density at model-scale of $D_R = 1\%$. These samples were straightforward to prepare and are aligned with the very loose samples used by Leblanc *et al.* (2010a) and Abadie *et al.* (2015), but do not represent field conditions.

The dense samples were prepared using the sand raining device described in Section 2.5. Due to lifting restrictions, the sample was prepared in two stages (rains). A constant sample depth was achieved by vacuuming down to the required level with the vacuum nozzle positioned in a jig. An average unit weight of $\gamma'_{AV} = 16.20 \pm 0.06$ kN/m^3 was achieved across 10 samples (the unit weight was not recorded for all dense samples, given the confidence in the sample preparation technique), corresponding to an average relative density at model-scale of $D_R = 60\%$. These samples are more representative of conditions off the UK coast, where sand deposits have relative densities up to $D_R = 100\%$ (*e.g.* Lunne, 2012).

Pile installation did not cause visible grain crushing, but did cause sample densification close to the pile in both the very loose and dense samples. The reported

densities must therefore be considered as pre-installation values.

All tests were performed in dry sand to simulate fully drained conditions. Drained conditions may be representative for small diameter monopiles in high permeability sands, but they are less representative for silty sands and large diameter monopiles. Li *et al.* (2019) proposed a preliminary criterion for assessment of the drainage conditions around a monopile under cyclic loading, derived from a $2D$ finite element model with isotropic linear elastic soil (only modelling horizontal drainage). The variation of normalised excess pore pressure $P = u/p$ (where u is excess pore pressure and p is the average bearing pressure on the pile) with normalised loading period $T_p = t_p c_v / D^2$ (where t_p is the cyclic loading period and c_v is the coefficient of consolidation) and distance from the pile was explored, and the results are presented in Figure 3.3.

An 8 m diameter monopile in coarse clean sand ($c_v \approx 10$ m^2/s) exposed to wave loading with period $t_p = 10$ s gives $T_p = 1.56$, with the response predicted to be partially drained. This is in agreement with the work of Peralta *et al.* (2017), who used analytical solutions for consolidation around a laterally loaded pile from Osman and Randolph (2012) to show that soil close to the monopile (in the same system) would behave as partially drained. The magnitude of pore pressure accumulation also depends on the load amplitude, as indicated by the pore pressure normalisation chosen by Li *et al.* (2019), and so the effects will be more pronounced under large amplitude storm loading.

Partial drainage and the effect of pore pressure build-up during cyclic loading is an important area of research. However, the response of monopiles to cyclic loading is compound, and there is a need to isolate behaviour to properly understand the response mechanisms. Understanding the drained response facilitates assessment of more complex partially drained behaviour.

3.2.3 Impact of stress-level

The behaviour of sand is inherently stress-level dependent: typically peak friction angle ϕ'_p increases logarithmically with decreasing stress-level (Bolton, 1986), while maximum shear modulus G_{MAX} increases approximately with the square root of stress-level (Hardin, 1965). To understand what soil state the low-stress laboratory sample may represent at full-scale, either stiffness, friction angle or state parameter (Altaee and

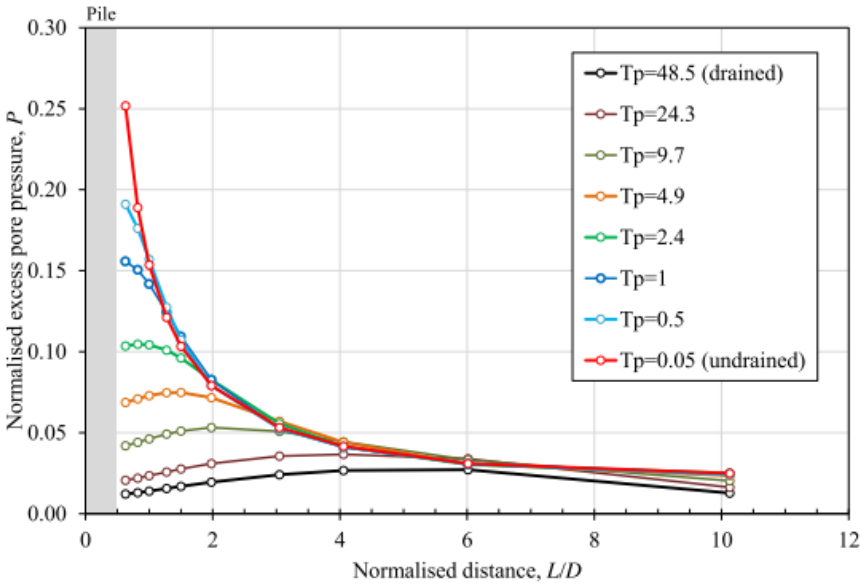

Figure 3.3: Variation of normalised excess pore pressure P at peak cyclic load with normalised distance from pile L/D and normalised loading period T_p (Li *et al.*, 2019)

Fellenius, 1994) may be matched (it is not possible to match all these parameters with laboratory-scale testing). Here, expressions for peak friction angle ϕ'_p at laboratory-scale and full-scale were equated to determine the full-scale relative density simulated in the laboratory, consistent with previous work (*e.g.* Leblanc *et al.*, 2010a; Zhu *et al.*, 2017).

Bolton (1986) collated data on the strength and dilatancy of 17 sands, measured in triaxial and plane strain conditions, and proposed empirical relationships to relate peak friction angle ϕ'_p with stress-level and relative density. The relationships can be combined into the following expression for ϕ'_p:

$$\phi'_p = \phi'_c + \alpha \left(D_R \left(Q - \ln p' \right) - 1 \right) \tag{3.1}$$

Where p' is the mean effective stress and α, Q and R are empirical values ($\alpha = 3$ for triaxial strain and $\alpha = 5$ for plane strain, $Q = 10$ and $R = 1$). Limited data were available at low stress levels and a dilation limit was therefore proposed, equivalent to constraining $\phi'_p - \phi'_c \leq 12°$ in triaxial strain (Bolton, 1986). In a discussion on this work, Tatsuoka (1987) presented additional data at low confining stresses $5 \leq \sigma'_c \leq 50$ kPa which led to a revision of the empirical relations to limit dilation more strongly (Bolton,

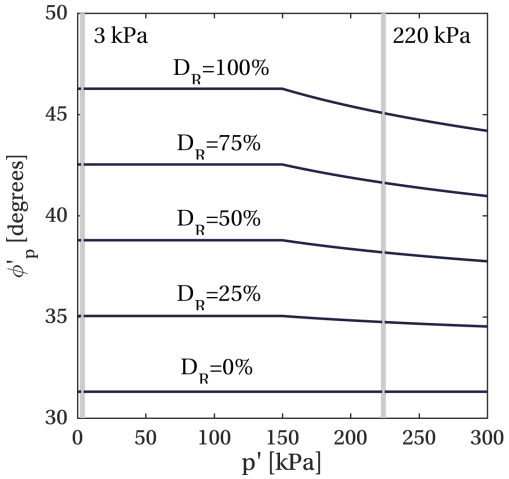

Figure 3.4: Graphical representation of Equation 3.2 (Bolton, 1987), with approximate representative stress-levels at laboratory (3 kPa) and full-scale (220 kPa) indicated

1987):

$$\phi'_p = \begin{cases} \phi'_c + \alpha \left(D_R \left(5 - \ln \left(\frac{p'}{150} \right) \right) - 1 \right) & \text{for } p' > 150 \text{ kPa} \\ \phi'_c + \alpha \left(5 D_R - 1 \right) & \text{for } p' < 150 \text{ kPa} \end{cases} \tag{3.2}$$

Chakraborty and Salgado (2010) also analysed data for Toyoura sand at confining stresses $2 \leq \sigma'_c \leq 197$ kPa and proposed varying empirical factor Q with stress level.

The experimental investigations of White (2020), which explore the behaviour of Yellow Leighton Buzzard 14/25 sand at low confining stresses, show a reduction in dilation at low stress levels and support the use of Equation 3.2. Figure 3.4 presents Equation 3.2 graphically (for triaxial conditions), and indicates approximate representative stress-levels $\sigma_{REF}{}'$ at laboratory and full-scale ($\sigma_{REF}{}' \approx 3$ kPa, $\sigma_{REF}{}' \approx 220$ kPa, respectively). $\sigma_{REF}{}'$ is defined here as the vertical effective stress at 70% pile embedment ($\sigma_{REF}{}' = 0.7 L \gamma'$), and is used as a proxy for mean effective stress. Using Equation 3.2 and matching ϕ'_p at laboratory- and full-scale suggests that the very loose and dense samples represent relative densities of $D_R = 1.1\%$ and $D_R = 65\%$ at full-scale, respectively. Classification of the samples as *very loose* and *dense* is therefore not affected by stress-level.

3.2.4 Cone penetration tests

Cone penetration tests (CPTs) were performed on samples of Yellow Leighton Buzzard 14/25 sand prepared to various densities to calibrate a new laboratory CPT device for

the experimental studies of Mayall (2019), as described in Mayall *et al.* (2019). The CPT has cone diameter 8 mm and angle $60°$, with resistance measured locally at the pile tip. As part of the CPT calibration work, three CPTs were performed on very loose and dense samples prepared as described in Section 3.2.2, in the test tank described in Section 2.3.2. All CPTs were performed at the centre of the sample – the sample's radial homogeneity was therefore not explored. However, monotonic tests in various loading directions (presented in Section 3.4.1) demonstrate invariance to loading direction.

Figure 3.5 shows the measured cone resistance q_c, while Figure 3.6 shows the associated relative density D_R profiles, obtained by application of the relationships presented by Mayall (2019) for Yellow Leighton Buzzard 14/25 sand. Data is presented for one very loose sample and two dense samples.

The CPT device was sized for dense sand, and so there is significant noise in the very loose q_c and associated D_R profiles. Nevertheless, two regions of locally higher resistance/density are observable at around -500 mm and around -260 mm. These regions approximately correspond to the intersections of the three sand layers deposited; similar layer depths were used to ensure repeatability. A region of higher resistance/density can also be observed in the dense sand at around -400 mm, corresponding to the intersection of the two rained layers. In this case, the layer was positioned around $1D$ beneath the pile tip to minimise the impact on the pile response.

The dense samples exhibit an increase in D_R with depth. The significant increase in the first 80 mm embedment is attributable to the change in CPT bearing behaviour (Gui *et al.*, 1998), but the continued increase beyond 80 mm is likely to be an artefact of the sample preparation technique. However, the consistency of the two profiles — obtained from virgin samples — gives confidence in the repeatability of the dense samples, particularly when coupled with the consistency in global unit weight measurements (see Section 3.2.2).

3.3 Set-up and test procedure

The following procedure was adopted for the tests at OU. All tests were conducted under load control using the apparatus described in Chapter 2.

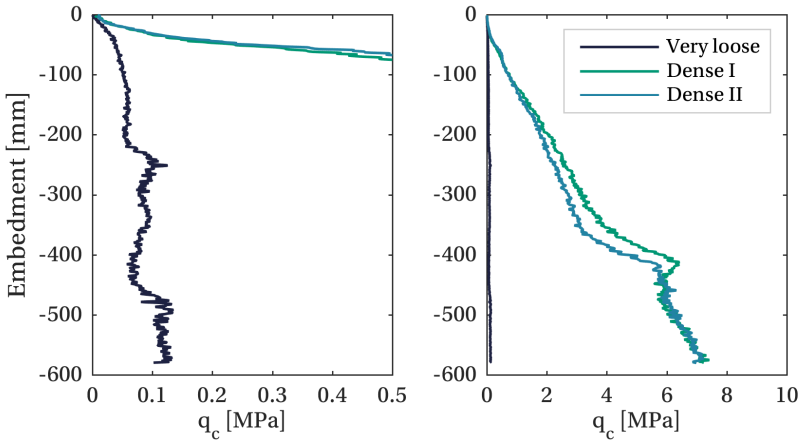

Figure 3.5: CPT resistance q_c for one very loose and two dense samples (data presented on two q_c scales for clarity)

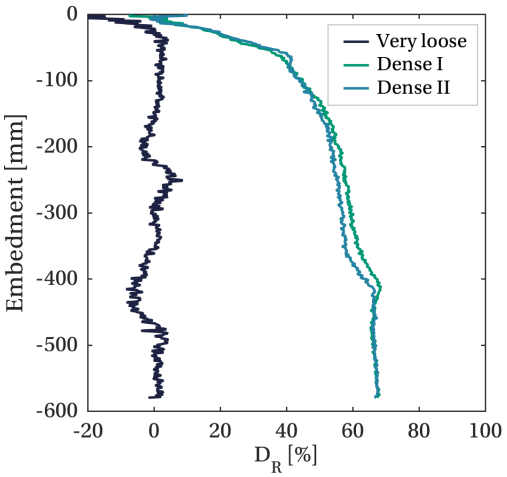

Figure 3.6: Relative density profiles determined from CPT measurements for one very loose and two dense samples (employing relationship between q_c and D_R from Mayall, 2019)

1. **Preparation of sample**. Either very loose or dense samples were prepared following the methods described in Section 3.2.2. Sample preparation was performed with the base plate and brackets unattached.

2. **Location of base plate and brackets**. The base plate — with brackets, displacement transducers and actuators attached — was then located on the tank and secured with bolts, before making the necessary power and data communication connections.

3. **Installation of pile**. The pile installation apparatus described in Section 2.6 was

then attached to the base plate and the pile was installed to the target embedment depth (320 mm) by manual hammering. Following pile installation, the pile hammer and hammer frame were removed to create space for the remaining test set-up.

4. **Location of displacement transducers**. The vertical displacement transducer bracket was positioned above the pile and the displacement transducers were located in positions appropriate for the particular test. The positions of the transducers relative to the brackets were measured and used to determine the coordinates of $\mathbf{T}_{iG}^{R}$ (defined in Section 2.4.3) using a spreadsheet. These values were input to the *Labview* software to allow determination of the pile pose during testing.

5. **Attachment of transducers and load lines**. Next, the pile cap was positioned on the pile and secured with grub screws, four transducers were connected to the pile cap and two were connected to bosses on the pile wall, and the actuators were jogged carefully into an initial position to minimise load applied to the pile upon connection. The loading lines were then connected using grub screws at the join between the flexible coupling and universal joint. The pile pose was recorded throughout this process and care was taken to avoid disturbing the pile.

6. **Running test**. Before running the test, transducer zero readings were taken using the *Manual* mode within the *Labview* software (Section 2.4), the load demand text file was loaded, and an appropriate data logging rate f_L was chosen. When running the test, software operation moved to the *Testing* mode, where load control, kinematics calculations and data logging were performed.

3.4 Monotonic response

Table 3.2 summarises the monotonic tests reported in this thesis. Tests were performed in very loose and dense sand samples, in various loading directions and at various loading rates. The test names indicate sequentially: sand density, test type (Monotonic), loading rate, loading direction and repeat number (where relevant).

Test name	Loading direction	Loading rate [N/s]
Very loose sand samples		
L.M.01.x	x	0.1
L.M.01.y	y	0.1
L.M.01.45	$45°$ to x	0.1
L.M.1.x	x	1.0
L.M.001.x	y	0.01
L.M.Var.x	y	1 & 0.01
Dense sand samples		
D.M.02.x.1	x	0.2
D.M.02.x.2	x	0.2
D.M.02.x.3	x	0.2

Table 3.2: Monotonic test programme

3.4.1 Moment-rotation response

Figure 3.7 presents the monotonic response of the model monopile. As monopile design criteria are typically defined in terms of foundation rotation (*e.g.* 3.10.2.2 DNVGL-ST-0126 (DNV GL, 2016)), the OU responses are presented in this thesis in moment-rotation ($M-\theta$) space. The upper plots in Figure 3.7 present the full monotonic response, while the lower plots focus on the low amplitude region relevant for cyclic loading.

Monotonic tests were conducted in three different directions in very loose sand, following the x- and y-axes of the apparatus, and at $45°$ to the axes (L.M.01.x, L.M.01.y, L.M.01.45). The consistency of these responses demonstrates invariance of the apparatus, software and sand sample to load direction, which is essential for investigation of the pile's multidirectional response. The impact of loading rate was also explored in the very loose samples, with tests at $0.01, 0.1$ and 1.0 N/s, and with rate changing between 0.01 and 1 N/s four times within a test (L.M.1.x, L.M.01.x, L.M.001.x, L.M.Var.x). No discernible rate dependency was observed, as expected in fully drained or dry sand. In general, the monotonic responses demonstrate excellent repeatability at both densities.

Mean monotonic responses are determined from the tests summarised in Table 3.2. These mean monotonic responses or mean *backbone curves* provide a baseline

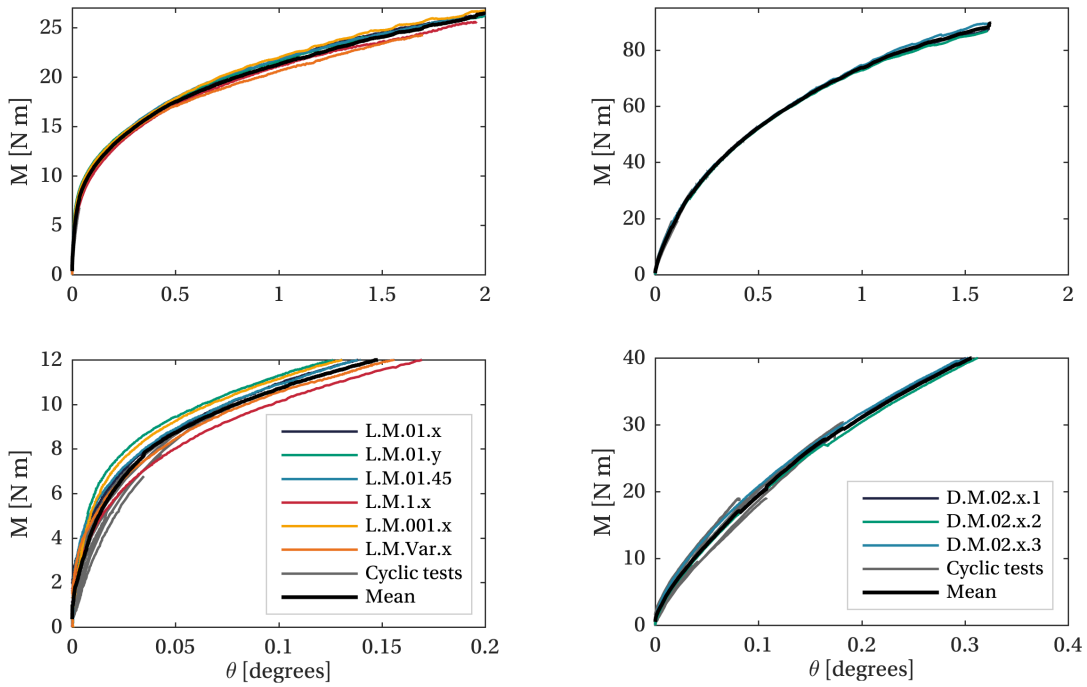

(a) Very loose sand **(b)** Dense sand

Figure 3.7: Monotonic response (lower plots show low amplitude region relevant for cyclic testing, note different scales)

for interpretation of the response to cyclic loading, and are included in various plots in Chapters 4 and 5. The initial monotonic loading responses for the unidirectional cyclic loading tests summarised in Tables 4.1 and 4.2 (Section 4.2) are also presented in Figure 3.7, and exhibit behaviour consistent with the monotonic tests.

3.4.2 Maximum stiffness

The maximum stiffness of the monopile k_{MAX} is an important parameter in monopile design as it controls the foundation's (initial) dynamic response, and is a key input for integrated dynamic analyses. In this work, k_{MAX} is used as a reference value for presentation of stiffness data (*e.g.* Section 4.4.2) and as an input parameter for numerical modelling (Section 7.4.3). The maximum stiffness k_{MAX} is most straightforwardly estimated from the initial portion of the monotonic response, but can also be obtained from the first unloading portion during cyclic tests. The initial

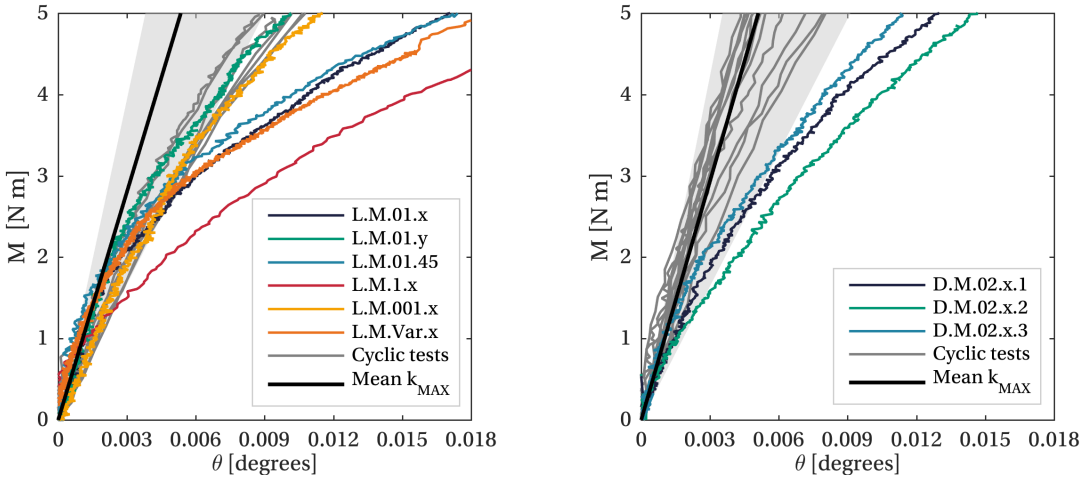

(a) Very loose sand **(b)** Dense sand

Figure 3.8: Initial portion of monotonic tests and first unloading from cyclic tests for estimation of maximum stiffness k_{MAX} (grey shaded region shows range of estimates for k_{MAX})

maximum stiffness is undisturbed, but may be subject to bedding-in effects which would not be expected to affect the first unloading maximum stiffness.

Figure 3.8 presents the initial portion of the $M - \theta$ response for the monotonic tests summarised in Table 3.2 alongside reflected unloading responses for the unidirectional cyclic loading tests summarised in Tables 4.1 and 4.2 (Section 4.2). The monotonic responses are zeroed from the onset of pile movement, while the cyclic tests are zeroed from the point of maximum load on the 0^{th} cycle (see Section 3.5.1). At very low rotations ($\theta < 0.003°$) there is little variation in the initial and unloading responses in very loose sand, but in dense sand the unloading responses are a little stiffer than the initial responses. No purely elastic region is observed at either sand density, *i.e.* the response is non-linear even at very small rotations. Upper, lower and mean estimates for k_{MAX} are obtained by manual fitting to both the initial and unloading data at $\theta < 0.003°$, and are summarised in Table 3.3.

The mean maximum stiffness values (936 N m/° and 979 N m/° for very loose and dense sand respectively) are less than $1/6$ of the equivalent stiffness of the monopile stick-up (modelled as a cantilever beam), confirming that it is appropriate to treat the monopile as rigid.

Sample	Max. stiffness k_{MAX}		Reference rotation θ_R [°]	Reference moment M_R [N m]
	Mean [N m/°]	Range [N m/°]		
Very loose	936	557–1315	2	26
Dense	979	548–1410	2	95

Table 3.3: Reference values for monopile response

3.4.3 Normalisation

To facilitate comparison of experimental data, it is typical to present foundation responses in a normalised form. Normalisations can either be conducted using reference values or using dimensionless groups, which should capture the physics of the system.

Leblanc *et al.* (2010a) and Kelly *et al.* (2006) develop dimensionless frameworks for monopiles and caissons, respectively, which aim to capture the key behaviour of the foundation-soil system and allow translation between scales. Both frameworks incorporate stress-level dependent stiffness, with shear modulus $G \propto p'^{\eta}$. The exponent is chosen as $\eta = 0.5$, which is generally accepted at small strains ($G_{MAX} \propto p'^{0.5}$), but at larger strains $\eta \to 1$ (Oztoprak and Bolton, 2013). Kelly *et al.* (2006) used this framework to successfully compare tests on caissons conducted in the laboratory and field. The results presented in Section 6.4.1 show that the similar framework of Leblanc *et al.* (2010a) is able to account for stress-level effects under monotonic loading at load amplitudes of interest. The dimensionless parameters for vertical load, horizontal load, moment and rotation presented by Leblanc *et al.* (2010a), and the displacement parameter presented by Abadie *et al.* (2015), are summarised in Table 3.4.

The dimensionless framework (Table 3.4) is used to discuss realistic cyclic load amplitudes in Section 4.2, to scale between model and prototype-scale in Sections 5.3.4 and 7.6 and to interpret stress-level effects in Section 6.4.1. However, for standard comparisons of the monopile response, data in this thesis is generally normalised using reference values, rather than the dimensionless framework, as this is deemed to be more intuitive.

Vertical load	$\tilde{V} = \dfrac{V}{L^2 D\gamma'}$
Horizontal load	$\tilde{H} = \dfrac{H}{L^2 D\gamma'}$
Moment	$\tilde{M} = \dfrac{M}{L^3 D\gamma'}$
Displacement	$\tilde{u} = \dfrac{u}{D}\sqrt{\dfrac{p_a}{L\gamma'}}$
Rotation	$\tilde{\theta} = \theta\sqrt{\dfrac{p_a}{L\gamma'}}$

Table 3.4: Key dimensionless parameters (Leblanc *et al.*, 2010a; Abadie *et al.*, 2015)

Monopiles in sand do not typically reach well-defined failure, and instead show continued hardening to large rotations. It is therefore necessary to arbitrarily define a reference rotation (or displacement) value, from which a reference moment (or horizontal load) can be determined. A variety of different reference values have been used by previous researchers in this area. For example, Leblanc *et al.* (2010a) used a dimensionless reference rotation of $4°$, Abadie *et al.* (2015) used a ground level displacement of $0.1D$ at model-scale, Arshad and O'Kelly (2017) used a rotation of $1.5°$ at model-scale, while Bayton *et al.* (2018) defined a reference rotation of $0.25°$ on unloading corresponding to the SLS criteria suggested by DNV GL (2016). A reference rotation of $\theta_R = 2°$ at model-scale was defined for this work, broadly consistent with Abadie *et al.* (2015) and Arshad and O'Kelly (2017). It is emphasised that the reference rotation is arbitrary and is not intended to represent a design rotation.

Table 3.3 presents reference moment M_R values for each sand density, approximately corresponding to $\theta_R = 2°$, while Figure 3.9 presents the normalised mean monotonic responses in very loose and dense sand. Employing this normalisation, the response in dense sand has a lower rate of change of normalised

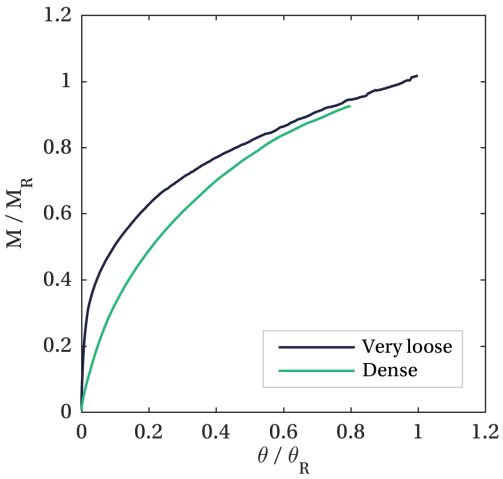

Figure 3.9: Mean monotonic responses in very loose and dense sand normalised by reference values in Table 3.3

tangent stiffness – and therefore appears more linear – than the response in very loose sand.

3.5 Definitions for cyclic loading and the cyclic response

The definitions presented in this Section were developed in collaboration with T. D. Balaam.

Various definitions for cyclic loading and the cyclic response have been used in previous physical modelling studies (see Table 1.2, Section 1.3.1), which hinders the comparison of behaviour between studies. Cyclic definitions used in physical modelling studies also differ from those used in cyclic element testing, which complicates the comparison of behaviour observed at element and macro level; such comparisons might inform numerical model calibration (Balaam, 2020). This Section presents a consistent and rigorous framework, which brings together approaches from previous studies, and proposes new definitions where inconsistencies arise. This framework is adopted in the following Chapters.

The framework is presented generally in terms of stress σ and strain ε to emphasise that the framework may be applied to both physical modelling of pile-soil systems and to cyclic element testing. When considering the macro-response of a monopile σ and ε may correspond to either applied moment M and pile rotation θ or applied load H and

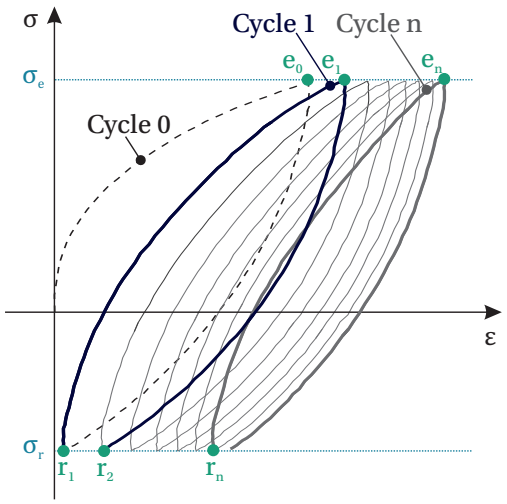

Figure 3.10: Cycle definitions

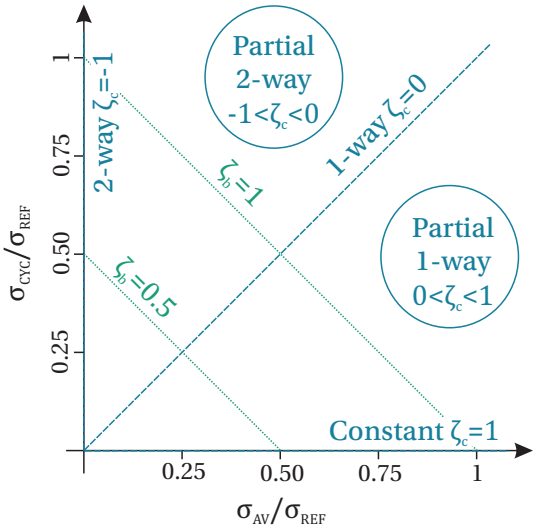

Figure 3.11: Graphical representation of relationship between ζ_b, ζ_c, σ_{AV}, σ_{CYC}

pile displacement u (as discussed in Section 1.2.2). For element testing, σ and ε may correspond to deviator stress q and axial strain ε_a or shear stress τ and shear strain γ.

The cyclic response is characterised in terms of ratcheting, secant stiffness and energy dissipation, following previous studies (*e.g.* Leblanc *et al.*, 2010a; Klinkvort, 2012; Abadie *et al.*, 2019b) and in-line with the cyclic design considerations for monopiles discussed in Section 1.2.5. Focus is primarily placed on definitions for regular, unidirectional cyclic loading, although definitions for multi-amplitude, unidirectional cyclic loading are briefly discussed. Extension of this framework for multidirectional loading is discussed in later Chapters, as required.

3.5.1 Cycle definition

A loading cycle is defined as a load-unload loop from the reversal stress σ_r to the extreme stress σ_e and back to the reversal stress σ_r (points $r_n \rightarrow e_n \rightarrow r_{n+1}$ in Figure 3.10). This definition is consistent with typical definitions used in physical modelling studies (*e.g.* Klinkvort, 2012), but in element testing, cycles are typically defined as starting and finishing at the average stress. The physical modelling approach is preferred as it allows straightforward extension to half cycles for multi-amplitude loading.

The stress bounds (σ_e, σ_r) are rigorously defined to account for loading in either

"positive" or "negative" stress directions (as may occur for element tests in extension):

$$\sigma_e = \begin{cases} \sigma_{AV} + \sigma_{CYC} & \text{if } \sigma_{AV} \geq 0 \\ \sigma_{AV} - \sigma_{CYC} & \text{if } \sigma_{AV} < 0 \end{cases} \tag{3.3}$$

$$\sigma_r = \begin{cases} \sigma_{AV} - \sigma_{CYC} & \text{if } \sigma_{AV} \geq 0 \\ \sigma_{AV} + \sigma_{CYC} & \text{if } \sigma_{AV} < 0 \end{cases} \tag{3.4}$$

Note, however, that for applications such as lateral loading of piles, the definition of a "positive" or "negative" stress direction is arbitrary. In this case σ_e and σ_r correspond to the more commonly used values σ_{MAX} and σ_{MIN}, respectively.

Cycle 1 is defined as the second load-unload loop to pass through σ_e. Cycle 0 is defined as all loading that occurs before Cycle 1, as indicated in Figure 3.10. The cyclic response is typically presented for cycles $1 \leq n \leq N$.

3.5.2 Cyclic load characterisation

In physical modelling, cyclic loading is typically characterised by parameters ζ_b (Leblanc *et al.*, 2010a) and ζ_c (Long and Vanneste, 1994; Leblanc *et al.*, 2010a), as presented in Section 1.3.1. These parameters are defined here in terms of σ_e and σ_r:

$$\zeta_b = \frac{\sigma_e}{\sigma_R} \tag{3.5}$$

$$\zeta_c = \frac{\sigma_r}{\sigma_e} \tag{3.6}$$

Load asymmetry is defined by ζ_c, while load amplitude is together defined by ζ_b and ζ_c. Definition of an (arbitrary) reference stress σ_R is also required, for example, as discussed in Section 3.4.3.

In contrast, in element testing (*e.g.* Andersen, 2015), cyclic loading is typically characterised by parameters σ_{CYC} and σ_{AV}:

$$\sigma_{CYC} = \frac{\sigma_e - \sigma_r}{2} \tag{3.7}$$

$$\sigma_{AV} = \frac{\sigma_e + \sigma_r}{2} \tag{3.8}$$

Parameter σ_{CYC} defines the cyclic amplitude while σ_{AV} defines the mean cyclic load or load bias. These parameters may also be normalised by σ_R for consistency with parameters ζ_b and ζ_c.

All four parameters (ζ_b, ζ_c, σ_{AV}, σ_{CYC}) are useful in characterising the cyclic load, but parameters ζ_b and ζ_c are principally used in this thesis, for consistency with previous physical modelling studies. Equations 3.9 and 3.10 express ζ_b and ζ_c in terms of σ_{CYC} and σ_{AV}, while Figure 3.11 presents the relationship between these parameters graphically for $\sigma_{AV} > 0$.

$$\zeta_b = \frac{\sigma_{AV} + \sigma_{CYC}}{\sigma_R} \tag{3.9}$$

$$\zeta_c = 1 - \frac{2\sigma_{CYC}}{\sigma_{AV} + \sigma_{CYC}} \tag{3.10}$$

3.5.3 Ratcheting definition

Ratcheting is the accumulation of permanent strain during cyclic loading, and therefore requires a measure of strain per cycle ε_n. In physical modelling studies, ε_n has typically been defined at the point of extreme load e_n (*e.g.* Leblanc *et al.*, 2010a; Abadie, 2015; Klinkvort and Hededal, 2013; Truong *et al.*, 2019). However, this definition is at odds with ratcheting being a measure of permanent strain, and conflates changes in stiffness with ratcheting behaviour. In element testing, ε_n is typically defined as the mean of strains at points e_n and r_n (*e.g.* Andersen, 2015).

In physical modelling studies, it is typical to report permanent strain as an *accumulated* strain per cycle $\Delta\varepsilon_n$, relative to the equivalent monotonic strain component (at $n = 0$); this helps to decouple ratcheting behaviour from the monotonic response. Although the element testing definition for ε_n is more aligned with our understanding of ratcheting as a permanent strain, and minimises conflation with stiffness change, it does not have a well-defined equivalent monotonic strain, given that r_0 does not necessarily exist.

A new definition for permanent strain per cycle ε_n is therefore proposed, as the mean value of strain at σ_{AV} on loading (at point a_n) and at σ_{AV} on unloading (at point b_n), as indicated in Figure 3.12. This definition is aligned with the element testing definition, but also allows straightforward definition of accumulated strain. Equation 3.11 and Equation 3.12 define ε_n and $\Delta\varepsilon_n$, in terms of points a_n and b_n, respectively.

$$\varepsilon_n = \frac{1}{2}\left(\varepsilon(a_n) + \varepsilon(b_n)\right) \tag{3.11}$$

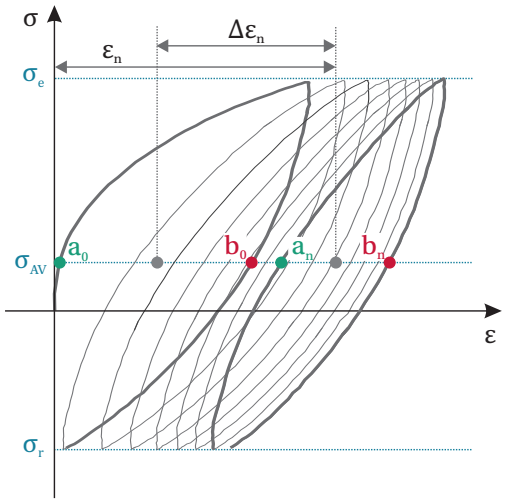

Figure 3.12: Definition of permanent strain per cycle

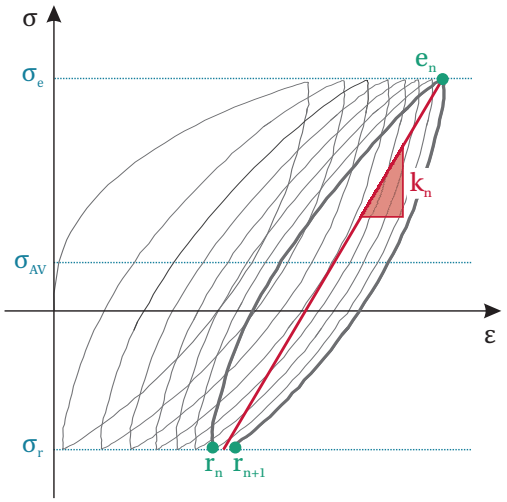

Figure 3.13: Definition of secant stiffness per cycle

$$\Delta\varepsilon_n = \frac{1}{2}\left((\varepsilon(a_n) + \varepsilon(b_n)) - (\varepsilon(a_0) + \varepsilon(b_0))\right) \tag{3.12}$$

3.5.4 Secant stiffness definition

Secant stiffness per cycle k_n has previously been defined in physical modelling studies as a loading stiffness between r_n and e_n (Klinkvort and Hededal, 2013; Abadie, 2015) and as an unloading stiffness between e_n and r_{n+1} (Leblanc *et al.*, 2010a). However, both these definitions conflate stiffness change with ratcheting behaviour.

A new definition for k_n is proposed which minimises conflation of stiffness change with ratcheting. Visually, this stiffness is at the cycle centre, as indicated in Figure 3.13. It is defined by Equation 3.13 in terms of points e_n and r_n, and is the inverse of the average of the loading and unloading flexibilities.

$$k_n = \frac{\sigma(e_n) - \sigma(r_n)}{\varepsilon(e_n) - \frac{1}{2}\left(\varepsilon(r_{n+1}) + \varepsilon(r_n)\right)} \tag{3.13}$$

3.5.5 Energy dissipation definition

Cyclic energy dissipation is generally quantified for a symmetric closed hysteresis loop by a metric proportional to the ratio of hysteretic energy loss E_H to maximum stored elastic energy E_E. The areas representing these energies are shown in Figure 3.14.

Løvholt *et al.* (2020) and Inman (2014) use an energy loss factor η equal to the energy lost per radian divided by the elastic energy (Equation 3.14). However, Kramer (1996),

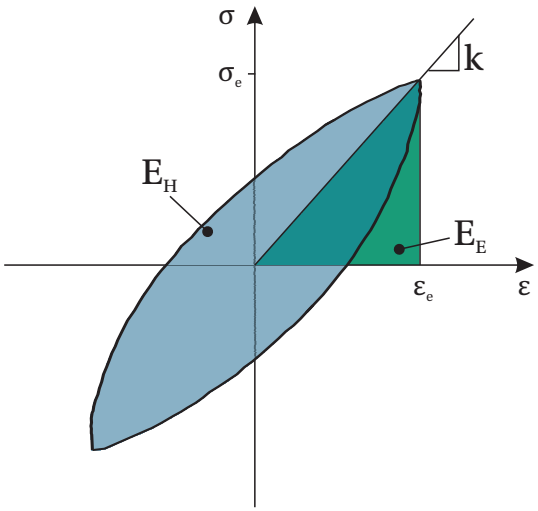

Figure 3.14: Definition of E_H and E_E for a closed hysteresis loop

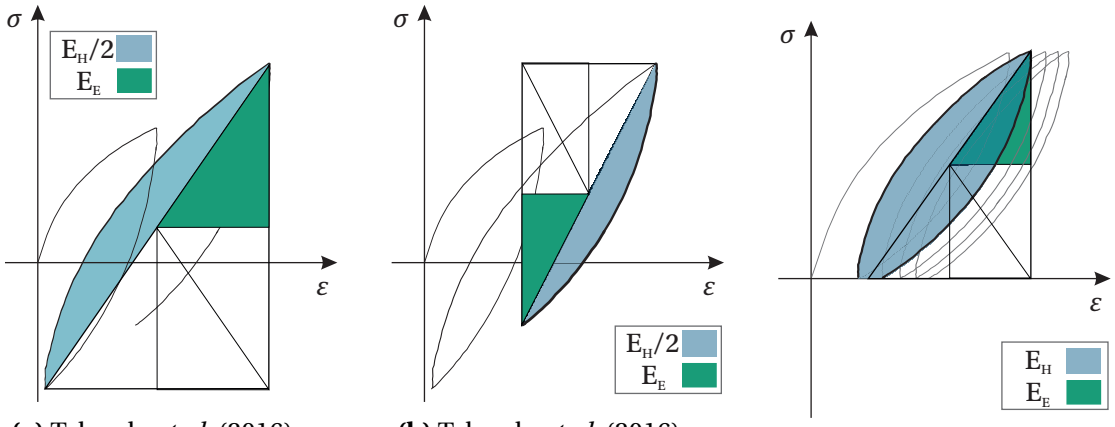

(a) Taborda *et al.* (2016) on loading

(b) Taborda *et al.* (2016) on unloading

(c) Abadie (2015)

Figure 3.15: Definitions of E_H and E_E for open loops proposed by previous studies

Abadie (2015) and Taborda *et al.* (2016) use a factor equal to half this value. Equation 3.14 is preferred as it is consistent with the *quality factor* often used to describe resonant systems (Green, 1955). This energy dissipation measure is referred to as an *energy loss factor* rather than a *damping ratio* to avoid confusion with the structural dynamics term for the ratio of viscous damping to critical damping for a single degree of freedom system (ξ). For a closed loop, η is bounded: $0 \leq \eta \leq 4/\pi$.

$$\eta = \frac{1}{2\pi}\left(\frac{E_H}{E_E}\right) \tag{3.14}$$

E_H and E_E are straightforwardly defined for a symmetric closed loop with Equations 3.15 and 3.16, respectively. However, adaptation is needed for non-closing loops, which

occur when ratcheting occurs or multi-amplitude loading is applied.

$$E_E = \frac{1}{2}\left(\sigma_e \varepsilon_e\right) = \frac{\sigma_e^2}{2k} \tag{3.15}$$

$$E_H = \oint \sigma(\varepsilon)\, d\varepsilon \tag{3.16}$$

Taborda *et al.* (2016) propose a method to calculate energy loss factor (presented as "damping") for non-closing loops caused by multi-amplitude loading, where the energy loss is calculated incrementally from the previous load reversal to the current strain (Figure 3.15a,b); this method is aimed at application to half-cycles. Meanwhile, Abadie (2015) proposes an energy loss factor (also presented as "damping") to account for open loops due to ratcheting behaviour. The energy loss is equal to the area enclosed by the hysteresis loop (closed at the load reversal), while the elastic energy is calculated using a stiffness equivalent to k_n (Figure 3.15c). This method was also used by Beuckelaers (2017). However, this geometric definition of energy loss is only appropriate for 1-way loading.

The hysteretic energy loss E_H can be more generally defined by Equation 3.17. This definition is equivalent to the approach of Abadie (2015) for 1-way loading, but is also applicable to partial 2-way and partial 1-way loading, where the net energy loss will not equate to the loop area.

Equation 3.18 defines the elastic energy E_E, which follows the approach of Abadie (2015) and is consistent with the definition for closed loops (Taborda *et al.*, 2016). The proposed energy loss factor per cycle η_n is then defined by Equation 3.19, following Equation 3.14, where η_n is bounded as $0 \leq \eta_n \leq 4/\pi$ for closed loops. Figure 3.16 visualises the calculation of η_n for an example partial 2-way loading case.

$$E_H = \int_{r_n}^{e_n} \sigma(\varepsilon)\, d\varepsilon + \int_{e_n}^{r_{n+1}} \sigma(\varepsilon)\, d\varepsilon \tag{3.17}$$

$$E_E = \frac{\left(\sigma_e - \sigma_r\right)^2}{8k_n} \tag{3.18}$$

$$\eta_n = \frac{4k_n}{\pi\left(\sigma_e - \sigma_r\right)^2}\left(\int_{r_n}^{e_n} \sigma(\varepsilon)\, d\varepsilon + \int_{e_n}^{r_{n+1}} \sigma(\varepsilon)\, d\varepsilon\right) \tag{3.19}$$

This definition of η_n is equivalent to *Method 0* presented by Løvholt *et al.* (2020). Løvholt *et al.* (2020) also present more complex methods for calculation of η which i)

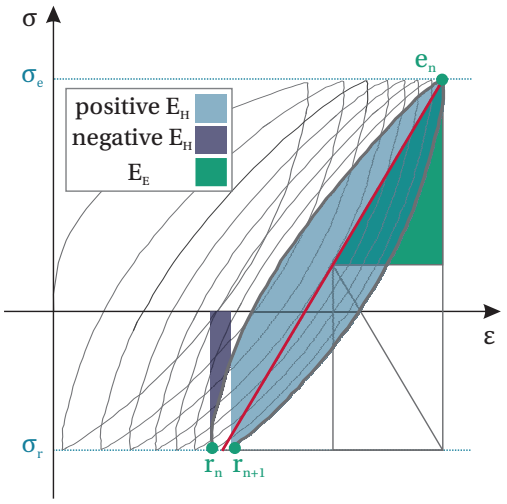

Figure 3.16: Visualisation of general E_H and E_E for partial 2-way loading

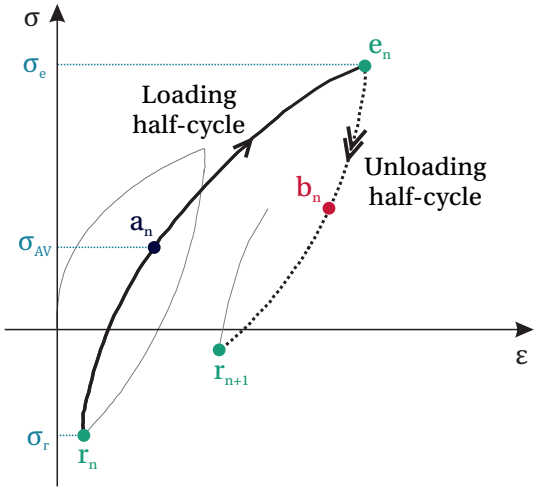

Figure 3.17: Definitions for multi-amplitude cyclic response

attempt to remove the contribution of ratcheting to damping, and ii) relate the energy loss factor to the phase angle between stress and strain in the frequency domain.

3.5.6 Application to multi-amplitude loading

For extension of the cyclic response definitions to multi-amplitude loading, cycles are divided into alternate loading and unloading half-cycles between alternate extreme and reversal points. The extreme points are defined as having greater mean stress across the signal than the reversal points. Extreme and reversal points (e_n, r_n) and extreme, reversal and average stresses $(\sigma_e,\ \sigma_r,\ \sigma_{AV})$ are defined for each loading half-cycle in Figure 3.17.

Strain per cycle can be defined at the half-cycle average stress on either loading (at point a_n, ε_{na}), or unloading (at point b_n, ε_{nb}) as indicated in Figure 3.17. For multi-amplitude loading, evolution of strain is generally presented in terms of strain per cycle (ε_{na} or ε_{nb}) rather than an *accumulated* strain per cycle ($\Delta\varepsilon_n$), as the equivalent monotonic strain component necessary to obtain $\Delta\varepsilon_n$ is poorly defined under multi-amplitude loading.

Stiffness may be calculated for each half-cycle following Abadie (2015) on loading (k_{nl}, Equation 3.20) and Leblanc *et al.* (2010a) on unloading (k_{nu}, Equation 3.21),

although these definitions conflate ratcheting with stiffness change.

$$k_{nl} = \frac{\sigma(e_n) - \sigma(r_n)}{\varepsilon(e_n) - \varepsilon(r_n)} \tag{3.20}$$

$$k_{nu} = \frac{\sigma(e_n) - \sigma(r_{n+1})}{\varepsilon(e_n) - \varepsilon(r_{n+1})} \tag{3.21}$$

The energy loss factor may also be calculated per half-cycle, using the definitions for E_E and E_H proposed by Taborda *et al.* (2016) (see Figure 3.15a,b); however, this approach is not entirely consistent with the approach presented in Section 3.5.5, which includes dissipation due to ratcheting.

3.6 Summary

This Chapter has laid the groundwork for exploration of the cyclic response of monopile foundations in the following Chapters. The sample preparation and test procedures used for testing at OU were described and the monotonic responses at $1g$ in very loose and dense sand were presented. Normalisation approaches were discussed and consistent definitions for cyclic loading and the cyclic response were proposed; these definitions are adopted in the following Chapters.

Chapter 4

Regular cyclic loading response at 1g

4.1 Introduction

This Chapter presents the response of a model monopile to regular, unidirectional and multidirectional cyclic lateral loading in very loose and dense dry sand at 1g. All tests were conducted using the apparatus presented in Chapter 2 following the test procedures outlined in Chapter 3. The tests build in complexity: from unidirectional, symmetric tests with a few cycles to multidirectional tests with continuously varying loading direction and 1000 cycles. The tests provide fundamental insight into the response of a monopile to cyclic lateral loading and inform development of models within the HARM framework (Houlsby *et al.*, 2017), as described in Chapter 7.

4.2 Test programme

Figure 4.1 illustrates the six test types which constitute the regular cyclic loading test programme. These six test types allow exploration of the hysteretic (few cycle) response and high cycle response, under unidirectional and multidirectional loading. The hysteretic responses reveal fundamental behaviour and adherence to Masing rules (Masing, 1926), while the high cycle responses show evolution of pile rotation (ratcheting), secant stiffness and energy dissipation with cycle number. Unidirectional, 1-way tests were conducted to 10000 cycles but many other tests were conducted to 1000 cycles given the diminishing returns associated with performing longer-term tests. The unidirectional tests complement previous test campaigns (*e.g.* Leblanc *et al.*,

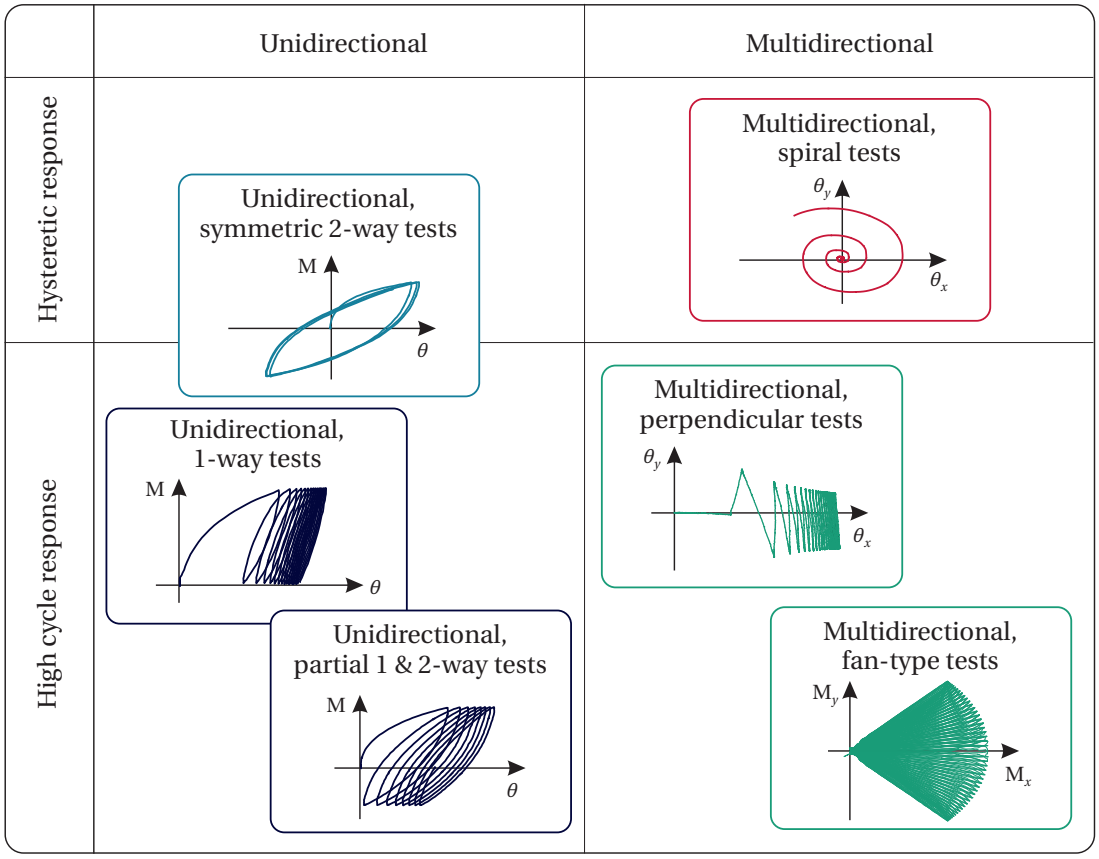

Figure 4.1: Illustration and categorisation of regular cyclic loading test types

2010a; Abadie *et al.*, 2015; Truong *et al.*, 2019) and exhibit behaviour consistent with previous observations, while the multidirectional tests are more novel. Tests of each type are performed in both very loose and dense sand, and the results are presented side-by-side, although the test programmes are not identical. The very loose and dense test programmes are summarised in Tables 4.1 and 4.2 respectively.

The test names indicate sequentially: sand density, load type (2-way (TW), 1-way (OW), partial 2-way (PT), partial 1-way (PO), spiral (SP), T-shape (T), L-shape (L), high mean T-shape (TH), fan-type (F)), and load amplitude or direction. The cyclic loading was applied using sinusoidal waveforms, and post-cyclic reloading to $0.8M_R$ was conducted as part of many tests to explore the impact of cyclic loading on the response under large loads. To ensure accurate load control, tests were conducted at a range of frequencies $0.025 \leq f \leq 0.2$ Hz depending on the cyclic amplitude. As shown in Section 3.4.1, rate effects are not observed.

The cyclic amplitudes (and corresponding ζ_b values) were selected considering a) experimental limitations, and b) representative cyclic loading. The minimum cyclic amplitude was set by the amplitude of transducer friction ($n\bar{F} = 0.44$ or 0.66 N, Section 2.4.4). Given the approximations made in adjusting for the transducer friction, it was not deemed sensible to run tests where the moment caused by transducer friction was greater than around 15% of the cyclic amplitude. This restricted cyclic amplitudes to $M_{CYC} > 3.5$ N m or $\zeta_b > 0.13$ and $\zeta_b > 0.04$ for 1-way cyclic loading in very loose and dense sand, respectively.

Representative SLS cyclic load amplitudes may be estimated following the dimensionless framework of Leblanc *et al.* (2010a) (Table 3.4, Section 3.4.3), by equating $\tilde{\theta}$ at laboratory- and prototype-scale. For a prototype-scale monopile with diameter $D = 8$ m and $L/D = 4$ in dense, saturated sand with $\gamma' = 10$ kN/m^3, the ratio of prototype-scale rotation (θ_P) to laboratory-scale rotation (θ_L) $f_\theta = \theta_P/\theta_L \approx 8.3$. Prototype-scale rotation under SLS conditions of $0.25°$ (DNV GL, 2016) therefore corresponds to approximately $0.03°$ rotation at laboratory-scale in both very loose and dense sand. The associated moments under monotonic loading are 7.3 N m and 8.5 N m in very loose and dense sand respectively. This analysis suggests that cyclic loading with $\zeta_b > 0.28$ in very loose sand and $\zeta_b > 0.085$ in dense sand may not represent SLS conditions, as it would lead, upon initial monotonic loading, to $\theta > 0.25°$ at prototype-scale.

To best represent SLS conditions, tests were conducted at cyclic amplitudes which were as low as possible, while satisfying the restriction due to transducer friction. For the unidirectional, 1-way tests – where the effect of cyclic amplitude was explored – tests were conducted at $\zeta_b = 0.2, 0.3, 0.4$ in very loose sand and $\zeta_b = 0.05, 0.1, 0.2, 0.3$ in dense sand. Other test types were conducted at fewer, but often corresponding, cyclic amplitudes. While many of the tests were conducted at amplitudes which may be greater than those expected under SLS conditions, given the non-linear monotonic response (Figure 3.7, Section 3.4.1) there is no reason to expect a step-change in the behaviour at lower cyclic load amplitudes. Exploration of the response under realistic loading is considered in Chapter 5.

Test name	Loading direction	ζ_b	ζ_c	Cycle Number N	Reload
Unidirectional, symmetric 2-way tests					
L.TW.Var	x	0.2, 0.4, 0.6	-1	3.5	No
L.TW.04	x	0.4	-1	2000	Yes
Unidirectional, 1-way tests					
L.OW.02	x	0.2	0	10000	No
L.OW.03	x	0.3	0	10000	Yes
L.OW.04	x	0.4	0	10000	Yes
Unidirectional, partial 1-way and 2-way tests					
L.PT.260	x	0.2	-0.60	1000	Yes
L.PT.460	x	0.4	-0.60	1000	Yes
L.PO.633	x	0.6	0.33	1000	No
Multidirectional, spiral test					
L.SP.1	Spiral $(x-y)$	$<$0.60	-	5	No
Multidirectional, perpendicular tests					
L.T.02	x y	0.2 0.2	1 -1	1000	No
L.L.04	x y	0.2 0.4	1 0	1000	No
L.TH.04	x y	0.4 0.2	1 -1	1000	No
Multidirectional, fan-type tests					
L.F.15	$\pm$15° fan	0.4	0	1000	Yes
L.F.30	$\pm$30° fan	0.4	0	1000	Yes
L.F.45	$\pm$45° fan	0.4	0	1000	Yes
L.F.60	$\pm$60° fan	0.4	0	1000	Yes
L.F.90	$\pm$90° fan	0.4	0	1000	Yes
L.F.120	$\pm$120° fan	0.4	0	1000	Yes
L.F.150	$\pm$150° fan	0.4	0	1000	Yes

Table 4.1: Regular cyclic test programme in very loose sand

Test name	Loading direction	ζ_b	ζ_c	Cycle Number N	Reload
Unidirectional, symmetric 2-way tests					
D.TW.Var	x	0.08, 0.16, 0.24, 0.32, 0.40	-1	5.5	No
D.TW.008	x	0.08	-1	1000	Yes
D.TW.016	x	0.16	-1	1000	Yes
D.TW.032	x	0.32	-1	1000	Yes
D.TW.04.W0	x	0.4	-1	1000	No
D.TW.04.W2	x	0.4	-1	1000	No
D.TW.04.W5	x	0.4	-1	1000	No
Unidirectional, 1-way tests					
D.OW.005	x	0.05	0	10000	Yes
D.OW.01	x	0.1	0	10000	Yes
D.OW.02	x	0.2	0	10000	Yes
D.OW.03	x	0.3	0	10000	Yes
Unidirectional, partial 1-way and 2-way tests					
D.PT.160	x	0.1	-0.60	1000	Yes
D.PT.260	x	0.2	-0.60	1000	Yes
D.PT.245	x	0.2	-0.45	1000	Yes
D.PT.275	x	0.2	-0.75	1000	Yes
D.PO.333	x	0.3	0.33	1000	No
Multidirectional spiral test					
D.SP.1	Spiral $(x-y)$	$<$0.45	-	4	No
Multidirectional, perpendicular tests					
D.T.01	x y	0.1 0.1	1 -1	1000	No
D.L.02	x y	0.1 0.2	1 0	1000	No
D.TH.02	x y	0.2 0.1	1 -1	1000	No
Multidirectional, fan-type tests					
D.F.30	$\pm$30° fan	0.2	0	1000	Yes
D.F.90	$\pm$90° fan	0.2	0	1000	Yes

Table 4.2: Regular cyclic test programme in dense sand

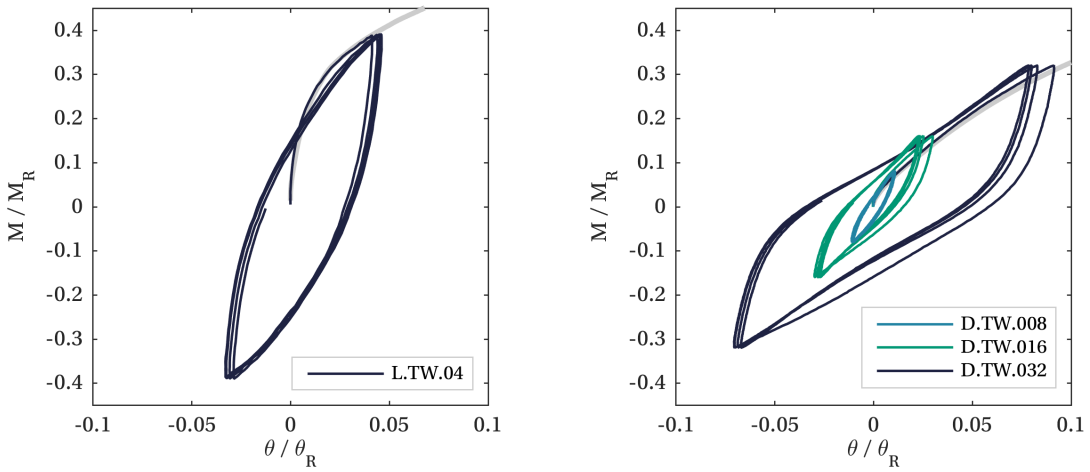

(a) Very loose sand **(b)** Dense sand

Figure 4.2: Response to first four cycles of unidirectional 2-way cyclic loading (mean monotonic response shown in grey)

Test	Mean η_n value
L.TW.04	0.56
D.TW.008	0.36
D.TW.016	0.38
D.TW.032	0.42

Table 4.3: Mean energy loss factors η_n for first four cycles

4.3 Unidirectional hysteretic response

Figure 4.2 presents the response of the model monopile to constant amplitude, 2-way (TW) cyclic loading. These symmetric tests minimise ratcheting and allow focus to be placed on the underlying hysteretic response. Only the first four loading cycles are presented in Figure 4.2; evolution of secant stiffness and energy dissipation under many cycles of 2-way loading is discussed in Section 4.4.

The shape of the hysteretic response is related to the foundation's energy dissipation, which is quantified by the energy loss factor η_n (defined in Section 3.5.5). Table 4.3 summarises the mean η_n values for the data presented in Figure 4.2. The mean energy loss factor η_n increases with cyclic amplitude M_{CYC} (or ζ_b) and is greater for the test in very loose sand, which exhibits a more convex response and no gapping-type behaviour.

In Figure 4.2b, the inflexion in the response around zero load for the dense sand

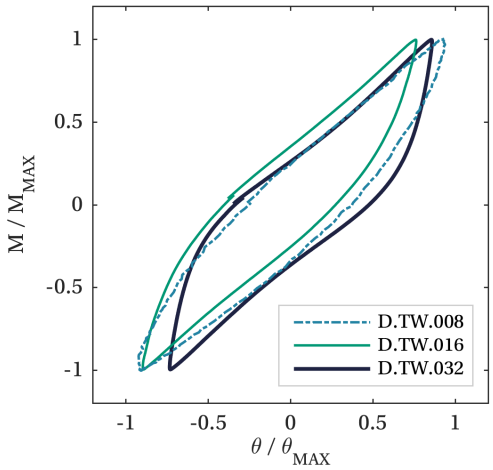

Figure 4.3: Hysteretic response at $n = 4$ in dense sand normalised by maximum moment and rotation to highlight variation in shape of hysteretic response

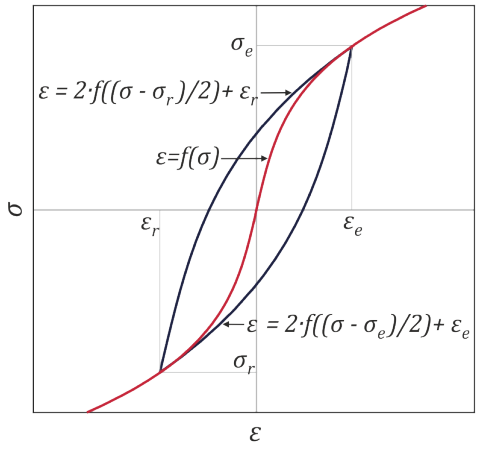

Figure 4.4: Illustration of Masing rules for single hysteresis loop following Puzrin and Shiran (2000)

tests, observed most clearly for test D.TW.032, is indicative of gapping-type behaviour: the tangent stiffness reduces as the pile traverses a gap or region of low-stress. Figure 4.3 highlights the increase in gapping-type behaviour with cyclic amplitude M_{CYC} (or ζ_b), by presenting the hysteretic response at $n = 4$ normalised by maximum moment and rotation values (M_{MAX}, θ_{MAX}) for each test (note that θ_{MAX} occurs at $n = 1$). As no physical gap was observed during these tests, it cannot be determined whether either a very small gap or a region of low stress was the cause of the gapping-type response. Gapping-type behaviour is not generally expected in dry sand, however, electrostatic forces, ambient moisture or particle interlocking may provide enough effective cohesion to generate a gap or low-stress region under cyclic loading.

Gapping-type behaviour is not observed in the very loose sand responses, perhaps due to a reduced tendency for particle interlocking or reduced electrostatic forces given the different sample preparation method. In the tests at UWA, gapping-type behaviour is also observed under symmetric 2-way loading in dense sand at $1g$ and $9g$ (reported in Section 6.5.1). In field tests as part of the PISA project, gapping-type responses were recorded in both sand and clay, and gapping was also observed on site (Beuckelaers, 2017).

The hysteretic responses also allow exploration of adherence of the system to *Masing rules* (Masing, 1926). The Masing rules allow definition of the cyclic response given definition of an initial loading (backbone) curve $\varepsilon = f(\sigma)$, as shown in Figure 4.4, and describe behaviour which complies with kinematic hardening models (Pyke, 1979). Masing (1926) proposed the following rules, which were initially concerned with modelling the behaviour of brass:

- The shape of the unloading or reloading curves is the same as that of the backbone curve, with the scale enlarged by a factor of 2.
- The initial tangent modulus on each loading reversal is the same as the initial tangent modulus on the backbone curve.

Pyke (1979) later extended the Masing rules for application to irregular cyclic loading:

- The unloading and reloading curves should follow the backbone curve if the previous maximum stress is exceeded.
- If the current loading or unloading curve intersects the curve described by a previous loading or unloading curve, the stress-strain response follows that of the previous curve.

The *extended Masing rules* have been found to capture the key behaviour of many materials and systems, including: soil behaviour in cyclic element tests (*e.g.* Puzrin and Shiran, 2000), the lateral response of laboratory-scale caissons in dense sand at $1g$ (Byrne, 2000; Villalobos, 2006), and the first few cycles of the lateral response of a laboratory-scale monopile in very loose sand at $1g$ (Abadie, 2015). The extended Masing rules also provided a basis for modelling the response of large-scale monopile tests in sand and clay, as part of the PISA project (Beuckelaers, 2017).

Figure 4.5 presents the response of the monopile to 2-way loading with ζ_b increasing on each successive cycle. These tests are similar to those conducted by Byrne (2000) and Abadie (2015), and explore adherence to the extended Masing rules. The upper plots show the experimental response and the lower plots show the response predicted by the extended Masing rules. In very loose sand, the response is

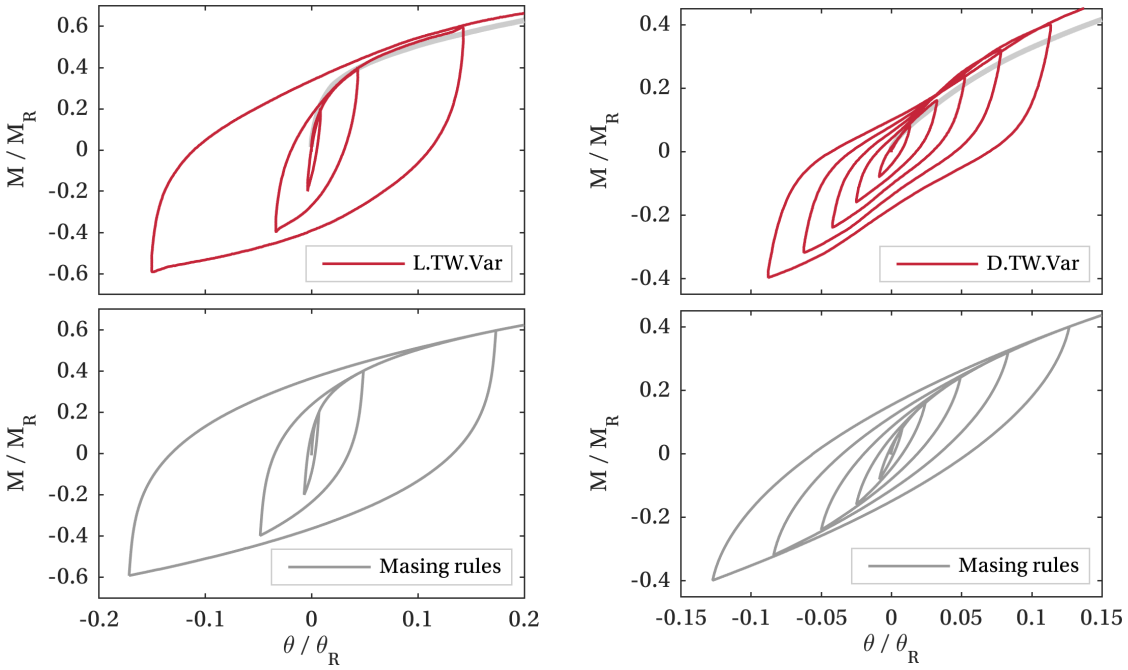

(a) Very loose sand **(b)** Dense sand

Figure 4.5: Response to 2-way cyclic loading with increasing amplitude alongside prediction of the response following extended Masing rules (mean monotonic response shown in grey in upper plots)

captured by the extended Masing rules with good accuracy. In dense sand, the response broadly adheres to the extended Masing rules but exhibits some hardening, and the aforementioned gapping-type behaviour, which are not captured by Masing rules. The greater number of cycles in dense sand may contribute to the increased hardening (or increase in secant stiffness) observed.

4.4 Unidirectional high cycle response

This Section explores the response of the monopile to at least 1000 regular, unidirectional loading cycles. The response is characterised by accumulation of pile rotation (ratcheting) and evolution of stiffness and energy dissipation.

4.4.1 Ratcheting

Although the monopile response approximately adheres to the extended Masing rules under symmetric 2-way loading, accumulation of rotation (ratcheting) occurs under biased loading. Figure 4.6 shows an example of the response to four cycles of 1-way

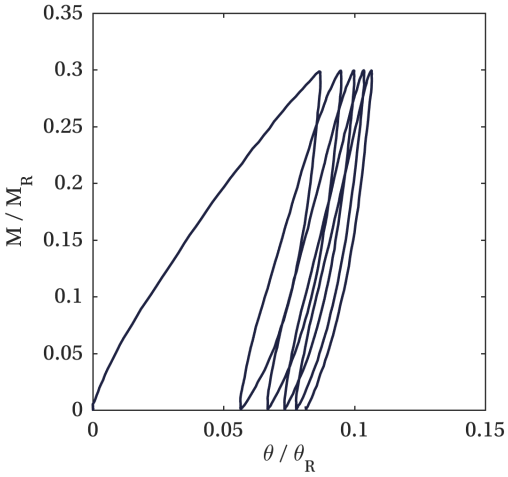

Figure 4.6: Example response to first four cycles of 1-way loading in dense sand to highlight ratcheting (test D.OW.03)

loading in dense sand. Rotation accumulates in the direction of the load bias, as evidenced by the non-closing hysteresis loops.

Figure 4.7 presents the accumulated rotation per cycle $\Delta\theta_n$ (defined in Section 3.5.3) for the 1-way (OW), partial 1-way (PO) and partial 2-way (PT) tests summarised in Tables 4.1 and 4.2 (the ratcheting response under 2-way loading is not of interest). The magnitude and rate of ratcheting increases with cyclic amplitude M_{CYC} (or ζ_b, given constant ζ_c), while ζ_c impacts the shape of evolution of ratcheting. Ratcheting continually slows with cycle number but does not stop accumulating, at least for the cycle numbers tested here. Similar behaviour is observed at both densities, although the response of test D.PT.275 is anomalous, with no data plotted at $n = 1$. For this test, the combination of a slower initial ratcheting rate due to the loading asymmetry and the development of a concave (gapping-type) hysteretic response between $n = 1$ and $n = 2$ (like seen in *e.g.* Figure 4.2b) led to a negative value of $\Delta\theta_n$ at $n = 1$.

To assess the impact of ζ_b and ζ_c on the ratcheting response, a power-law is fitted to the evolution of accumulated rotation $\Delta\theta_n$ with cycle number n:

$$\frac{\Delta\theta_n}{\theta_R} = An^{\alpha} \tag{4.1}$$

The coefficient A controls the initial magnitude of $\Delta\theta_n$ while the exponent α controls the evolution of $\Delta\theta_n$ with n. Power-laws capture the reduction in ratcheting rate with

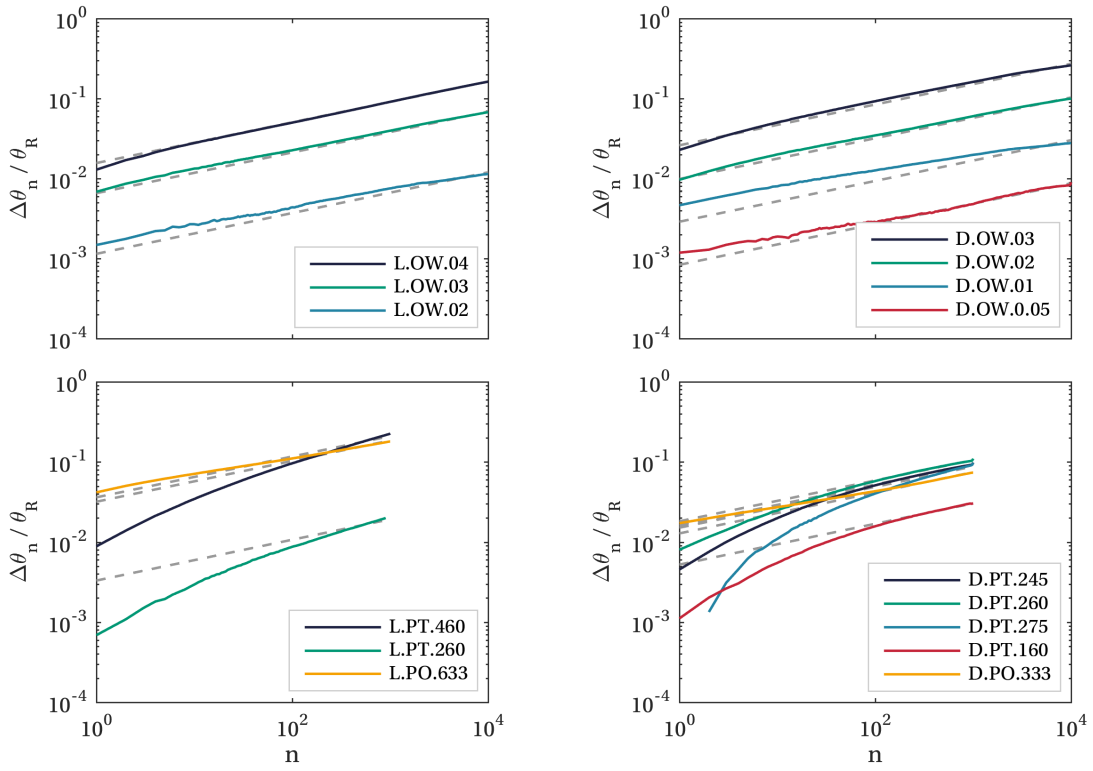

(a) Very loose sand **(b)** Dense sand

Figure 4.7: Unidirectional ratcheting response with power-law fit (Equation 4.1) using common exponent $\alpha_c = 0.25$ shown dashed

cycle number and have been used by various authors to approximate the ratcheting response of a pile (*e.g.* Leblanc *et al.*, 2010a; Klinkvort and Hededal, 2013; Abadie *et al.*, 2019b; Truong *et al.*, 2019). Leblanc *et al.* (2010a) assumed a constant exponent α and made A a function of load characteristics and relative density as $A = T_b(\zeta_b, D_R)T_c(\zeta_c)$, while Truong *et al.* (2019) made A equal to the measured ratcheting accumulated on the first cycle $\Delta\theta_1$ and let α vary with D_R and ζ_c.

First, the empirical approach of Leblanc *et al.* (2010a) is followed. The dashed lines in Figure 4.7 show the result of fitting Equation 4.1 to the data in Figure 4.7 with a common (fitted) exponent α_c. With $\alpha_c = 0.25$, a very good fit is obtained to the 1-way and partial 1-way data, and a reasonable fit is obtained to the partial 2-way data for $n > 100$. The reported exponent α depends on the chosen strain variable. For example, with accumulated rotation at cycle extreme as the strain variable instead, $\alpha_c = 0.30$, aligned with the results of Leblanc *et al.* (2010a) and Abadie (2015); with total rotation

at cycle extreme as the strain variable, $\alpha_c = 0.17$.

Figure 4.8 presents the variation of T_b with ζ_b and D_R obtained from power-law fits to the 1-way data with common exponent α_c. T_b increases with D_R and varies with ζ_b as a power-law (shown dashed) with exponent $m_\sigma = 3.1$ for very loose sand and $m_\sigma = 2.3$ for dense sand. This behaviour is similar to that reported by Leblanc *et al.* (2010a) and Abadie (2015), although Abadie (2015) found T_b to vary with ζ_b as a power-law with exponent $m_\sigma = 4$.

Figure 4.9 plots the variation of T_c with ζ_c obtained from power-law fits with common exponent α_c. Figure 4.9 also presents data from other studies (Leblanc *et al.*, 2010a; Nicolai and Ibsen, 2014; Albiker *et al.*, 2017), where tests were conducted to a range of cycle numbers $1000 \leq N \leq 100000$. Despite some scatter, there is a clear trend across the datasets for greatest T_c values under partial 2-way loading at $\zeta_c \approx -0.6$, with T_c reducing as $\zeta_c \to -1$ and $\zeta_c \to 1$. The impact of ζ_c is significant, with $1.3 \leq T_c \leq 4$ at $\zeta_c \approx -0.6$, and with the highest T_c values occurring in looser sand samples. Like for α, the choice of strain variable impacts the T_c values, and the choice of accumulated or total strain is particularly significant (Albiker *et al.*, 2017). All studies presented in Figure 4.9 use an accumulated rotation value ($\Delta\theta$) as the strain variable, and are therefore approximately comparable.

Alternatively, the effect of ζ_c on the ratcheting response can be explored by letting α vary with ζ_c and D_R, following the approach of Truong *et al.* (2019). Equation 4.1 is fitted independently to each test shown in Figure 4.7, which leads to better fits, particularly for the partial 2-way and 2-way tests. The α values obtained are plotted in Figure 4.10 against ζ_c, and with distinction between sand densities. There is a trend for decreasing α with increasing ζ_c for $-0.75 \leq \zeta_c \leq 0$, but for $0 \leq \zeta_c \leq 0.33$ there is no clear variation in α. The impact of sand density is not strong, although there is a weak tendency for greater α values in the looser sample. The impact of density is therefore less pronounced than that observed by Truong *et al.* (2019), although the impact of ζ_c is broadly consistent with Truong *et al.* (2019).

Both empirical approaches demonstrate the importance of load asymmetry (ζ_c) in controlling ratcheting: the approach of Leblanc *et al.* (2010a) allows the impact of ζ_c

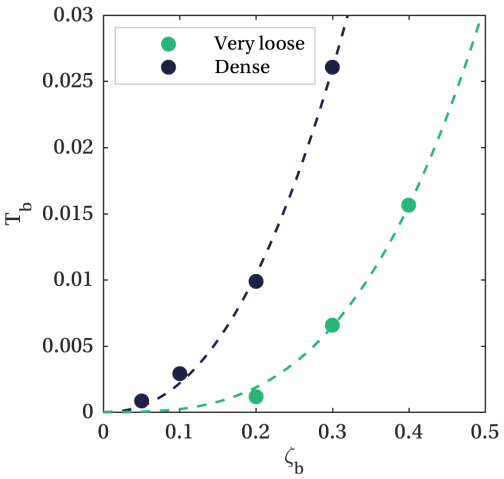

Figure 4.8: Variation of T_b with ζ_b and density following the empirical approach of Leblanc *et al.* (2010a) (power-law fit shown dashed)

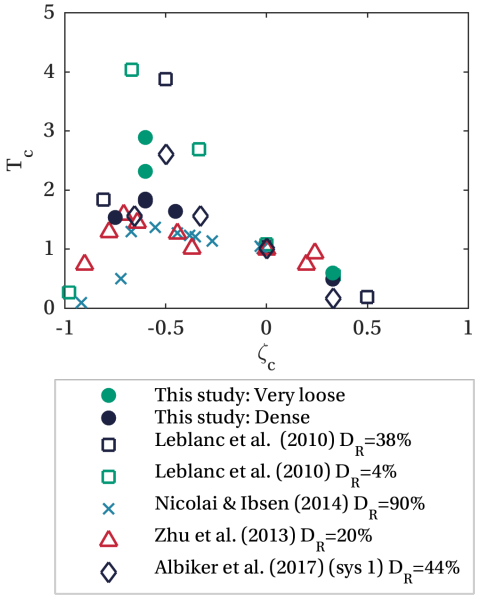

Figure 4.9: Variation of T_c with ζ_c following the empirical approach of Leblanc *et al.* (2010a) including comparison to other studies

on the initial magnitude of ratcheting to be assessed (Figure 4.9), while the separate approach of Truong *et al.* (2019) assesses the impact of ζ_c on ratcheting evolution (Figure 4.10). The empirical approach of Leblanc *et al.* (2010a) also provides insight into the impact of ζ_b, and indicates that the initial magnitude of ratcheting increases as a power-law (exponent $2.3 - 3.1$) with ζ_b (Figure 4.8).

Qualitatively, the impact of ζ_c on ratcheting may be understood as a competition between (a) an increasing cyclic amplitude M_{CYC} with increasingly negative ζ_c, which increases pile movement and therefore the potential for soil particle rearrangement and (b) a decreasing mean load M_{AV} with increasingly negative ζ_c. Greater particle rearrangement is likely to lead to greater ratcheting, which is understood to occur through a combination of densification and convective mechanisms (Cuéllar *et al.*, 2012; Nicolai, 2017, Section 1.3.2), while a reduction in mean load will reduce ratcheting behaviour as the mechanism becomes more symmetric. There is no such competition when considering the impact of ζ_b on ratcheting, as both the cyclic amplitude M_{CYC} and mean load M_{AV} increase with increasing ζ_b. This interpretation supports the

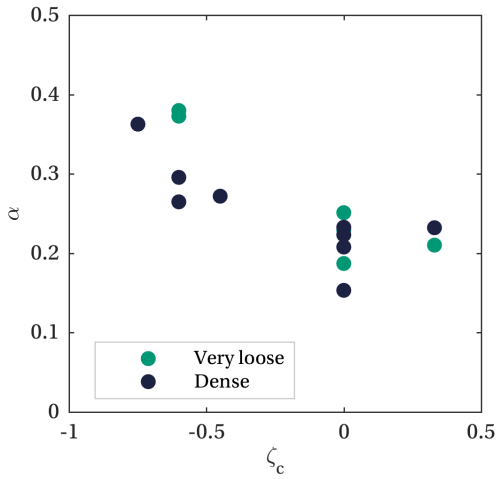

Figure 4.10: Variation of α with ζ_c following the empirical approach of Truong *et al.* (2019)

use of parameters M_{CYC} and M_{AV} to describe cyclic loading, as is commonplace in element testing (*e.g.* Andersen, 2015).

4.4.2 Secant stiffness

During cyclic loading in dry sand, an increase in secant stiffness k_n (defined in Section 3.5.4) tends to be observed. Figure 4.11 highlights how k_n changes between cycle $n = 1$ and $n = 10$ for example 1-way cyclic loading in dense sand. Figure 4.12 presents the evolution of secant stiffness k_n with cycle number n under 2-way (TW), 1-way (OW), partial 1-way (PO) and partial 2-way (PT) loading. An increase in k_n is observed during all tests, with a mean ratio of secant stiffness at $n = 1000$ ($k_{n=1000}$) to initial stiffness $k_{n=1}$ ($k_{n=1000}/k_{n=1}$) of approximately 3. However, the shape of evolution varies significantly with the loading asymmetry (ζ_c). The stiffness response of test D.OW.005 appears to be anomalous, with stiffness plateauing for $100 \leq n \leq 1000$ and increasing again for $n \geq 1000$.

Leblanc *et al.* (2010a) and Klinkvort and Hededal (2013) both proposed logarithmic relationships to capture the evolution of secant stiffness k_n with cycle number n under cyclic loading in dry sand. The expressions used by Leblanc *et al.* (2010a) and Klinkvort and Hededal (2013) differ slightly, but have the same general form, which is expressed here as:

$$\frac{k_n}{k_{MAX}} = \frac{k_{n=1}}{k_{MAX}} + B_L \ln(n) \tag{4.2}$$

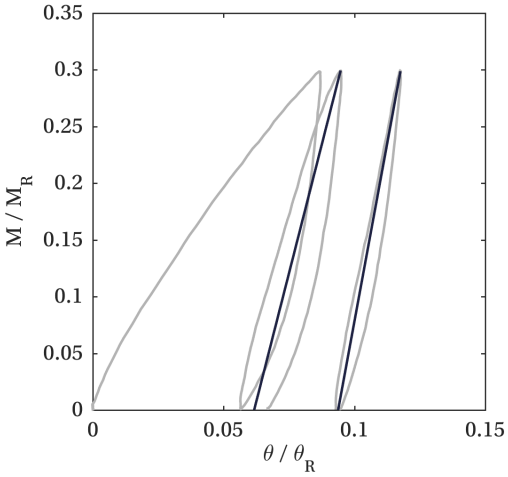

Figure 4.11: Example response to 1-way loading in dense sand highlighting secant stiffness at cycles $n = 1$ and $n = 10$ (test D.OW.03)

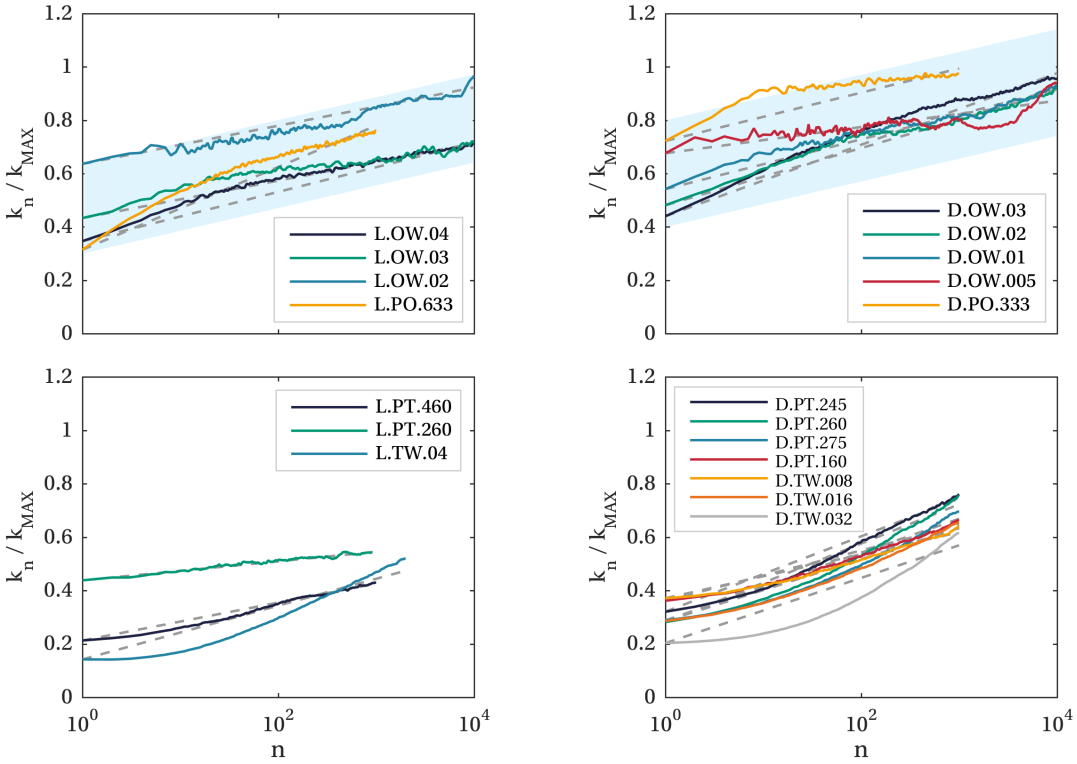

(a) Very loose sand **(b)** Dense sand

Figure 4.12: Secant stiffness evolution under unidirectional cyclic loading with individual logarithmic fits (Equation 4.2) shown dashed and range of fits to 1-way and partial 1-way data with common coefficient B_{Lc} indicated by blue shaded region

Coefficient B_L controls the rate of change of k_n. Leblanc *et al.* (2010a) found B_L to be independent of D_R and loading type (ζ_b, ζ_c) within the tested range, while Klinkvort and Hededal (2013) let B_L vary with ζ_b and ζ_c. Both authors let the initial stiffness $k_{n=1}$ vary with the loading characteristics with an expression of the form $k_{n=1}/k_{MAX} = K_b(\zeta_b)K_c(\zeta_c)$, with $K_c = 1$ at $\zeta_c = 0$.

Figures 4.13 and 4.14 plot the variation of K_b and K_c with ζ_b and ζ_c respectively, obtained from the initial stiffness values $k_{n=1}$. Despite some scatter, there is a clear trend for increasing K_b with reducing ζ_b and increasing K_c with increasing ζ_c. The variation of $k_{n=1}$, and therefore K_b and K_c, can also be approximated analytically by application of the extended Masing rules (Section 4.3). Given a function for the backbone curve $\varepsilon = f(\sigma)$, $k_{n=1}$ may be approximated as:

$$k_{n=1} = K_b(\zeta_b)K_c(\zeta_c)k_{MAX} \approx \frac{M_R\zeta_b(1-\zeta_c)}{2f\left(\frac{M_R}{2}\zeta_b(1-\zeta_c)\right)} \tag{4.3}$$

This analytical approximation is presented in terms of K_b and K_c in Figures 4.13 and 4.14 for very loose sand, where the backbone curve is approximated with a Ramburg-Osgood (Ramberg and Osgood, 1943) or power-law expression with exponent 3.4 (see Section 7.4.3). The approximate analytical expression does not account for the stiffness reduction due to ratcheting in the first cycle, but nevertheless captures the variation of K_b and K_c for very loose sand with good accuracy.

Leblanc *et al.* (2010a) and Abadie (2015) both used a constant coefficient B_L to approximate the evolution of stiffness under various cyclic loading conditions. A constant coefficient ($B_{Lc} = 0.037$) is able to approximately fit the evolution of k_n for the 1-way and partial 1-way tests presented here, as indicated by the blue shaded areas in Figure 4.12, but cannot adequately capture the response to partial 2-way and particularly 2-way cyclic loading. Following the approach of Klinkvort and Hededal (2013) Equation 4.2 is fitted to each test independently to obtain the fits shown dashed in Figure 4.12. However, even with independent fitting, the logarithmic expression is unable to adequately capture the shape of evolution of k_n under partial 2-way and 2-way loading. A power-law of the form:

$$\frac{k_n}{k_{MAX}} = Bn^{\beta} \tag{4.4}$$

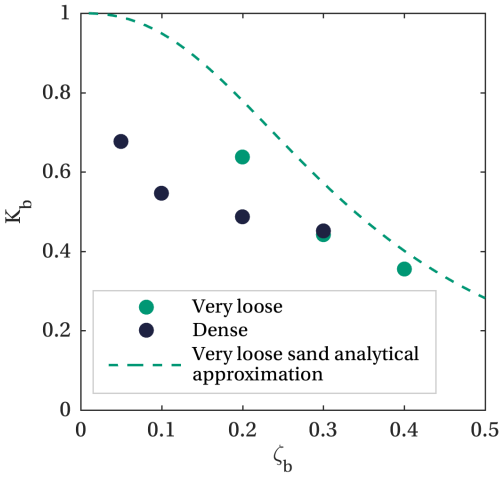

Figure 4.13: Variation of K_b with ζ_b for 1-way data following empirical approach of Klinkvort and Hededal (2013) and Leblanc *et al.* (2010a)

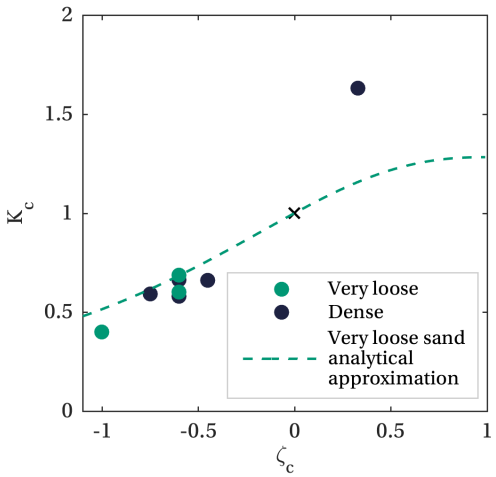

Figure 4.14: Variation of K_c with ζ_c following empirical approach of Klinkvort and Hededal (2013) and Leblanc *et al.* (2010a)

is able to capture a faster rate of change of stiffness at higher cycles and provides a better fit to the 2-way and partial 2-way data, at least for $n > 10$, as shown in Figure 4.15.

Secant stiffness change is understood to be caused by local densification (discussed in Section 1.3.2), which relies on particle rearrangement. It is conceivable that 2-way and partial 2-way loading (which passes through zero load, $\zeta_c < 0$) leads to greater particle rearrangement, and therefore a greater rate of stiffening, than 1-way and partial 1-way loading ($\zeta_c \geq 0$). Greater particle movement is certainly likely to accompany the gapping-type behaviour which was observed under larger amplitude 2-way loading in dense sand (Section 4.3).

4.4.3 Energy dissipation

Figure 4.16 highlights how the hysteretic response of the monopile changes under 1-way cyclic loading in dense sand, with the loop area (representing the hysteretic energy loss E_H, defined in Section 3.5.5) shaded at cycle $n = 1$ and $n = 10$. Figure 4.17 presents the evolution of hysteretic energy loss E_H with cycle number n under 1-way (OW), partial 1-way (PO), 2-way (TW) and partial 2-way (PT) cyclic loading. Hysteretic energy loss E_H generally reduces with cycle number n in-line with the increase in secant stiffness k_n with n; indeed, Abadie (2015) showed that E_H can be approximated

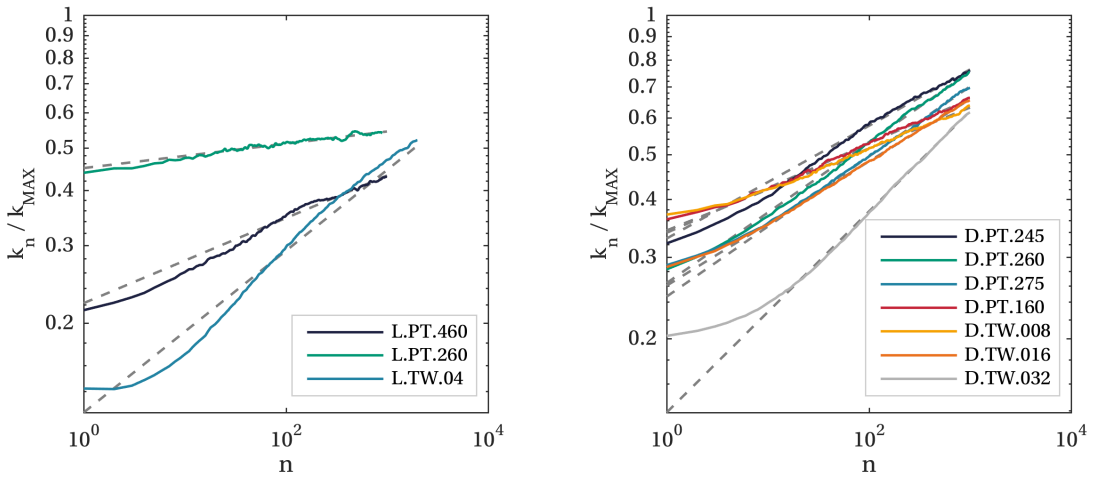

(a) Very loose sand **(b)** Dense sand

Figure 4.15: Secant stiffness evolution under partial 2-way and 2-way loading with individual power-law fits (Equation 4.4) shown dashed

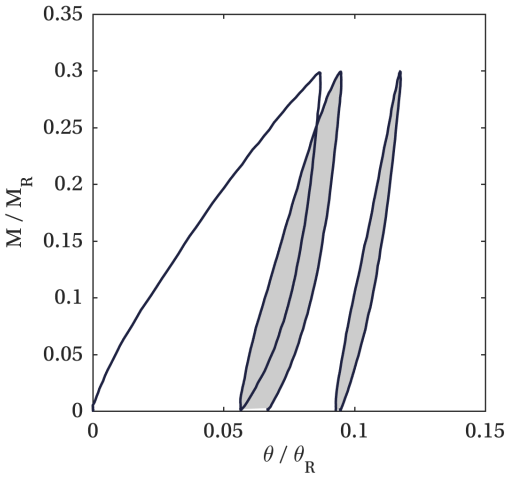

Figure 4.16: Example response to 1-way loading in dense sand highlighting energy dissipation with shaded areas equal to hysteretic energy loss E_H at cycles $n = 1$ and $n = 10$ (test D.OW.03)

as a linear function of $1/k_n$. E_H will also decrease with reducing ratcheting rate, which is, in general, aligned with increasing secant stiffness.

The evolution of hysteretic energy loss E_H with n at high cycle numbers is greater under 2-way and partial 2-way loading than under 1-way and partial 1-way loading, consistent with secant stiffness observations. However, for many of the 1-way tests E_H plateaus at high cycle number, which is not consistent with the observed increase in secant stiffness and decrease in ratcheting rate with cycle number. This behaviour is understood to be caused by the contribution from transducer friction, which is

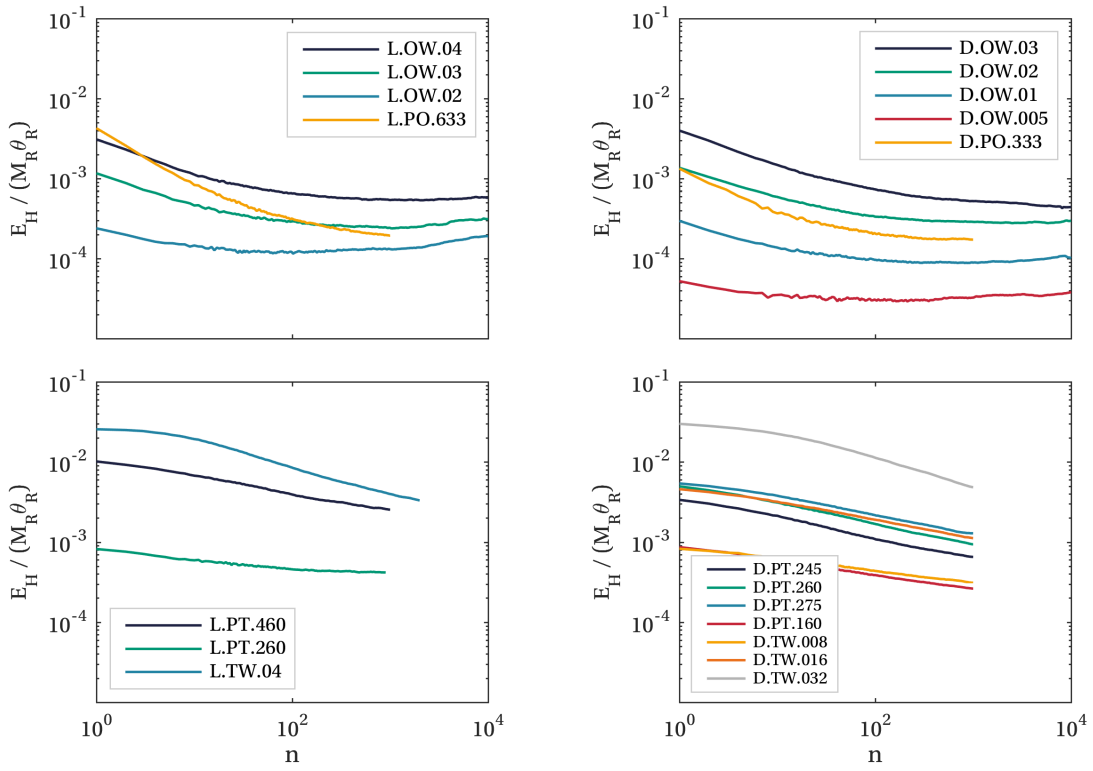

(a) Very loose sand **(b)** Dense sand

Figure 4.17: Evolution of hysteretic energy loss E_H with cycle number n under unidirectional cyclic loading

reduced but not eradicated by the control system (Section 2.4.4). Figure 4.18 presents an example hysteresis loop for test D.OW.01 at $n = 1000$, to highlight the square response at load reversals — and systematic increase in recorded hysteretic energy loss E_H — caused by the transducer friction.

Energy dissipation is quantified by the energy loss factor per cycle η_n (defined in Section 3.5.5) which is proportional to the hysteretic energy loss per cycle E_H normalised by the elastic energy per cycle E_E, which varies with secant stiffness k_n. Figure 4.19 presents the evolution of energy loss factor η_n with cycle number n. Under 2-way and partial 2-way loading, and for 1-way and partial 1-way loading for $n \leq 100$, η_n tends to reduce with cycle number as E_H does. However, where E_H plateaus due to transducer friction contributions, η_n increases: as the secant stiffness k_n increases and therefore E_E decreases. In general, Figure 4.19 shows the significant impact cyclic loading can have on energy dissipation. For example, during tests L.OW.04 and

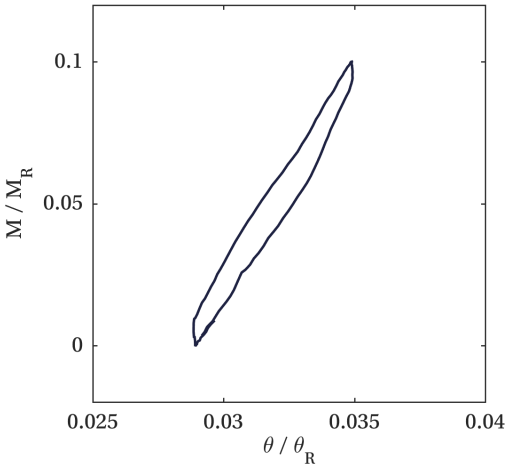

Figure 4.18: Hysteresis loop for test D.OW.01 at $n = 1000$ to highlight the impact of transducer friction on the hysteresis loop shape (squared response at load reversals)

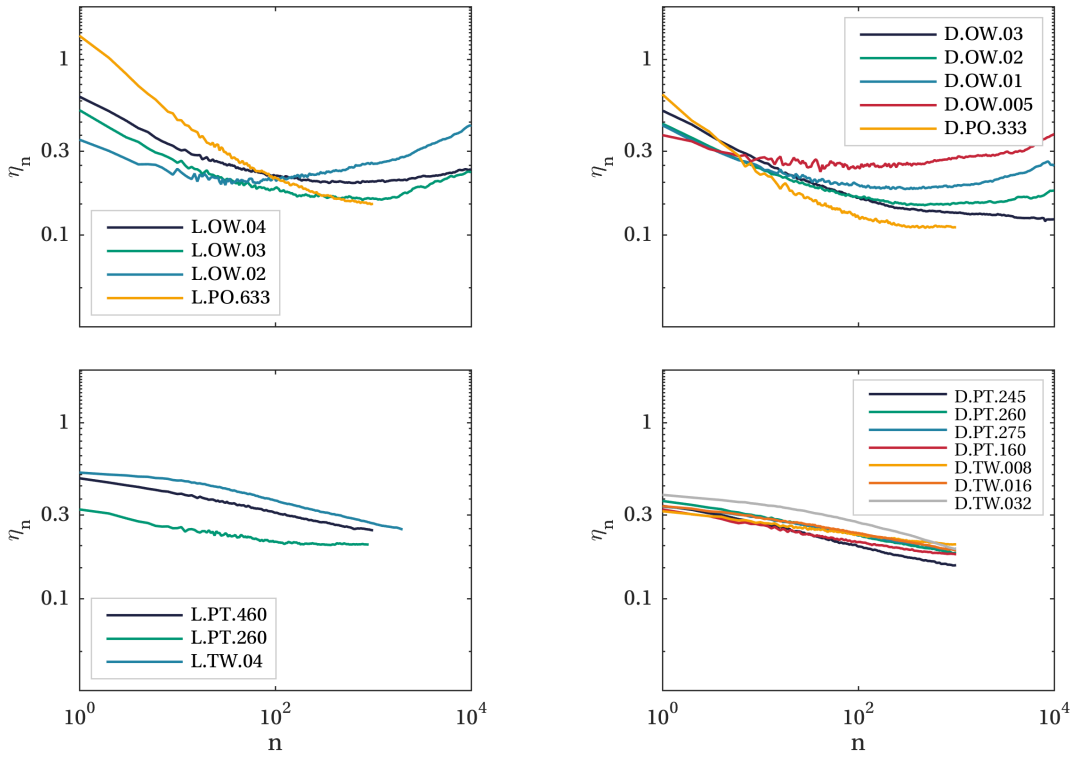

(a) Very loose sand **(b)** Dense sand

Figure 4.19: Evolution of energy loss factor η_n with cycle number n under unidirectional cyclic loading

D.OW.03 η_n reduces by a factor of 3 over 1000 cycles.

Abadie (2015) explored the evolution of energy loss factor (referred to as "damping", but proportional to η_n here for 1-way loading) with cycle number n and fitted a power-law with constant exponent to its evolution under 1-way and partial 1-way loading. A power-law would also approximately capture the evolution of η_n reported here under 2-way and partial 2-way loading, but it would not be appropriate to fit a power-law to the 1-way data distorted by contributions from transducer friction. Empirical expressions for the evolution of η_n with n are not considered further here, in part due to the distortion of the 1-way data by transducer friction, and in part because η_n is considered to be a secondary parameter that is largely dependent on secant stiffness and ratcheting magnitude, the evolution of which have been explored in previous Sections.

4.4.4 Uplift

Significant vertical uplift was observed during test D.TW.04.W0, which was conducted in dense sand with large amplitude ($\zeta_b = 0.4$) 2-way loading. Similar uplift behaviour was observed by Niemann *et al.* (2018), however, minimal vertical pile movement ($|z| < 1$ mm) was observed for the other tests presented here, in very loose sand or at smaller cyclic amplitudes. Observation of uplift prompted the performance of tests D.TW.04.W2 and D.TW.04.W5 with the same loading, but with additional 1.7 kg and 4.8 kg vertical mass applied, respectively. Figure 4.20a shows the vertical displacement of the monopile during these three tests. More than 25mm vertical uplift is observed at $n = 1000$ without additional vertical load applied, but as expected, increasing the vertical load suppresses the uplift, and with 4.8 kg additional mass 1.6mm downward settlement is observed. Figure 4.20b shows the impact of uplift on the secant stiffness k_n. For $n \leq 100$, k_n is comparable across the three tests but k_n reduces rapidly for test D.TW.04.W0 as the cycles progress and the pile moves upwards — reducing pile embedment and increasing the loading eccentricity. Two potential mechanisms which may have driven the uplift behaviour are discussed below and shown schematically in Figure 4.21:

Climbing mechanism As the pile rotates, the horizontal stresses on the pile's passive side will be greater than on the active side. This could cause the pile's rotation

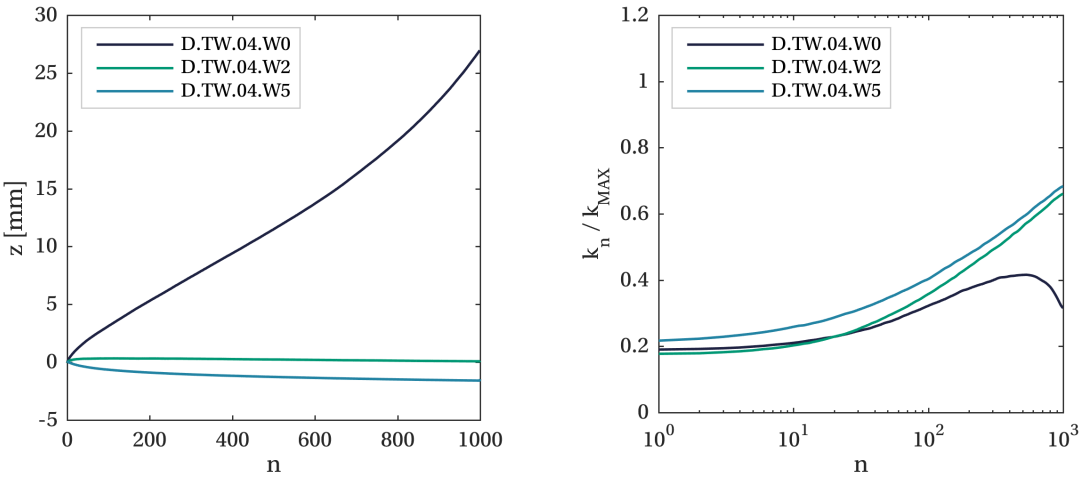

(a) Vertical displacement **(b)** Secant stiffness

Figure 4.20: Response to 2-way cyclic loading at $\zeta_b = 0.4$ in dense sand with additional vertical masses (Wn)

point to move laterally away from the pile centreline, allowing an upwards *climbing* motion to develop during cycling. A similar mechanism was suggested by Villalobos (2006) for uplift observed in tests on laboratory-scale caissons. Unfortunately, noise levels in the measured pile pose were too large to determine and track the pile's instantaneous rotation point with confidence.

Sand migration Migration of sand particles beneath the pile tip could also force the pile upwards. A low-stress region is likely to be generated beneath the pile base on the active side as the pile rotates. Particles may migrate to this low-stress region, incrementally increasing the soil volume beneath the pile and forcing it upwards. Cuéllar *et al.* (2012) and Nicolai *et al.* (2017a) both observe sand particles moving downwards at the pile face, but neither focus on particle migration at the pile base.

The vertical load applied during test D.TW.04.W0 (and all other tests at OU except D.TW.04.W2 and D.TW.04.W5) was equal to the weight of the pile and pile cap: 49.2 N (5.02 kg). However, the weight of these components was largely incidental to other design considerations. It is therefore worth considering what vertical load may be representative for a monopile in the field. Assuming a prototype-scale RNA weight of 4.7 MN (Wind Turbine Models, 2015), a tower weight of 5.6 MN (6 m mean diameter, 40

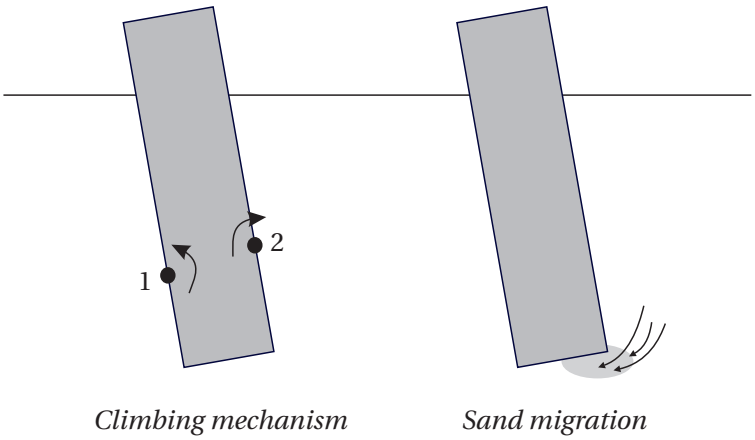

Figure 4.21: Potential uplift mechanisms

mm mean wall thickness, 95 m height, steel) and a buoyant monopile weight of 8.3 MN (8 m diameter, 80 mm mean wall thickness, 60 m total length, steel), the prototype-scale vertical load is estimated as $V_P = 18.6$ MN. Employing the dimensionless framework of Leblanc *et al.* (2010a) (Table 3.4, Section 3.4.3) then gives a representative laboratory-scale vertical load of $V_L = 27.9$ N. The typical vertical load applied in the laboratory is around 80% larger than V_L; applying additional vertical loading (as done for tests D.TW.04.W2 and D.TW.04.W5) is therefore expected to reduce the representativeness of the vertical loading further.

Although uplift was observed in the laboratory with greater vertical loading than expected for equivalent full-scale monopiles, no known uplift has been reported in the field. The rotations generated under loading to $\zeta_b = 0.4$ in the laboratory are significantly larger than the equivalent rotations expected for full-scale monopiles (as discussed in Section 4.2). Given that the suggested uplift mechanisms will become more pronounced at greater pile rotations, this may explain the presence of the observed behaviour in the laboratory. Villalobos (2006) also suggested that the higher stress-level in the field may increase wall friction and reduce uplift, relative to laboratory tests at low stress-level.

4.5 Multidirectional hysteretic response

Figure 4.22 presents the load path and monopile response under multidirectional spiral loading centred on zero load (L.SP.1, D.SP.1). Under spiral loading, the load magnitude

$|M| = \sqrt{M_x^2 + M_y^2}$ increases at a constant rate while the resultant loading direction moves around $360°$ per cycle. In very loose sand 5 cycles were applied up to $\zeta_b = 0.60$, while in dense sand 4 cycles were applied up to $\zeta_b = 0.45$. These tests are not intended to represent loading experienced by a monopile, but instead present a challenge for multidirectional numerical modelling.

Qualitatively, the response is very similar at both sand densities, with the rotation responses also tracing spiral shapes, as expected. The response in the dense sample is slightly elongated in the x-direction, indicating the presence of some sample inhomogeneity. The moment-rotation responses in the x- and y-directions resemble those under unidirectional 2-way loading with increasing load amplitude, which broadly adhere to the extended Masing rules (Figure 4.5). However, the interaction between load components here generates a smooth response at the load reversals in both the x- and y-directions.

4.6 Multidirectional high cycle response

This Section explores the response of the monopile to regular, multidirectional loading cycles. Novel perpendicular loading tests provide fundamental insight into the monopile response, while fan-type tests allow systematic investigation of the impact of the spread of cyclic loading direction. The tests were chosen to elucidate multidirectional behaviour rather than represent realistic loading, although the fan-type loading may represent a simplified storm with varying direction and the perpendicular tests may represent misaligned (approximately constant) wind and (cyclic) wave loading.

4.6.1 Perpendicular cyclic loading

Figure 4.23 describes the *T-shape* and *L-shape* perpendicular loading applied, relative to corresponding unidirectional loading. T-shape tests have mean load perpendicular to the cyclic loading direction, while L-shape tests have equal mean load applied both perpendicular to and aligned with the cyclic loading direction. Load is first increased in the x-direction before cyclic loading is applied in the y-direction.

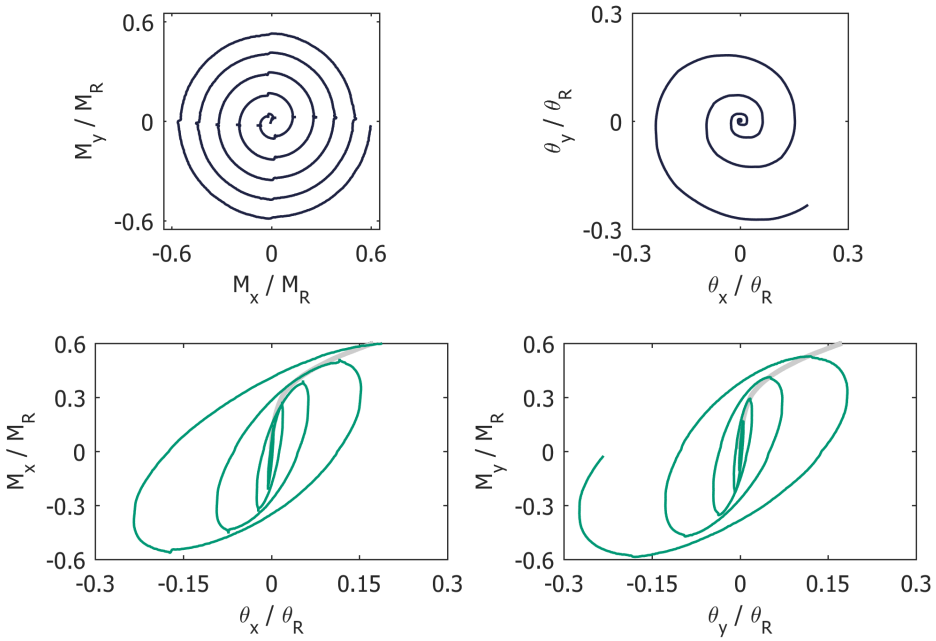

(a) Very loose sand

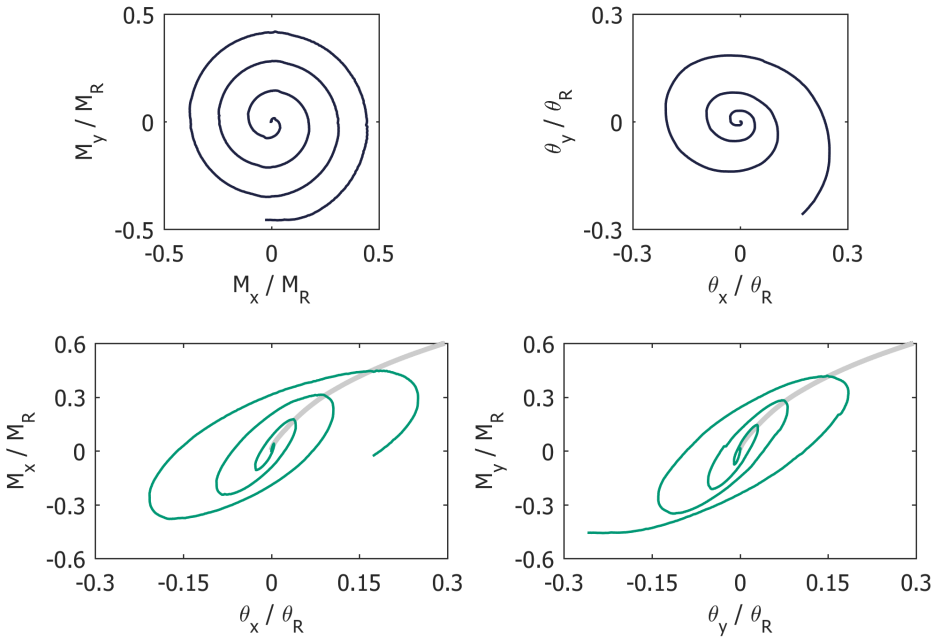

(b) Dense sand

Figure 4.22: Multidirectional spiral loading and response (backbone curve shown in grey)

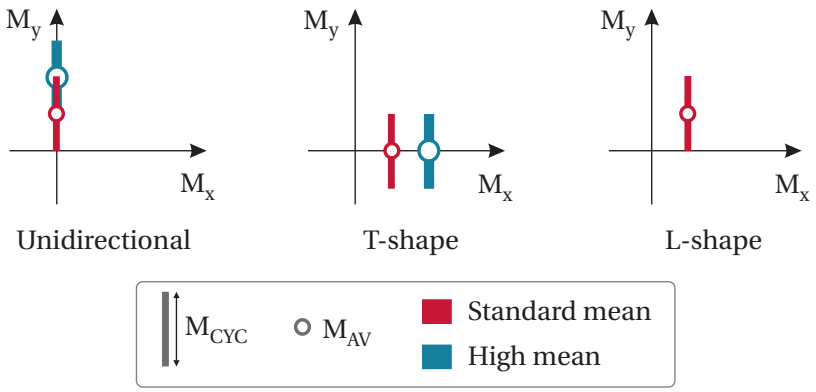

Figure 4.23: Description of perpendicular cyclic loading

Sand density	Description	M_{AV}/M_R	M_{CYC}/M_R	Unidirectional test	T-shape test	L-shape test
Very loose	Standard mean (SM)	0.2	0.4	L.OW.04	L.T.02	L.L.04
Very loose	High mean (HM)	0.4	0.4	L.PO.633	L.TH.04	-
Dense	Standard mean (SM)	0.1	0.2	D.OW.02	D.T.01	D.L.02
Dense	High mean (HM)	0.2	0.2	D.PO.333	D.TH.02	-

Table 4.4: Summary of unidirectional and perpendicular tests designed for comparison

Exploration of the impact of ζ_b and ζ_c on the unidirectional ratcheting response and consideration of the mechanisms driving ratcheting in Section 4.4.1 suggest that the cyclic amplitude M_{CYC} and mean amplitude M_{AV} play an important role in controlling the cyclic response. To explore this further, tests at the same M_{CYC} and M_{AV} are compared here. The impact of mean load M_{AV} is also explored with unidirectional and T-shape tests conducted at two different M_{AV} values at each density: high mean (HM) and standard mean (SM). Table 4.4 summarises the sets of relevant tests. The responses to unidirectional loading (L.OW.04, L.PO.633, D.OW.02, D.PO.333) are presented throughout this Section for comparison, but were previously presented in Section 4.4.

Figure 4.24 presents the continuous rotation responses for the unidirectional and perpendicular tests summarised in Table 4.4. The pile rotates broadly in the direction of M_{AV} regardless of the cyclic loading direction: the unidirectional tests move in the

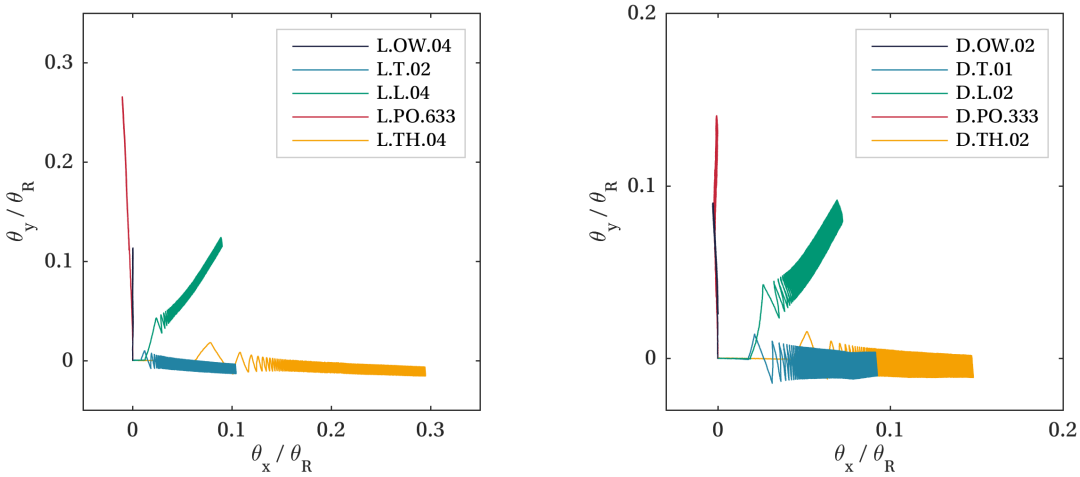

(a) Very loose sand **(b)** Dense sand

Figure 4.24: Total rotation response under unidirectional and perpendicular cyclic loading (note different scales; response to first 1000 cycles shown)

y-direction, the T-shape tests move in the x-direction and the L-shape tests move at approximately $45°$ to the axes. The impact of load bias is also clear in Figure 4.24, with the HM tests accumulating significantly more rotation than the SM tests.

Ratcheting

Figure 4.25 presents the ratcheting response of the monopile in the x-direction for the T-shape tests and in both the x- and y-directions for the L-shape tests. The corresponding unidirectional responses are also plotted. The ratcheting magnitude and evolution for the L-shape and T-shape tests is similar to that for the corresponding unidirectional tests, suggesting that — to a first approximation — ratcheting is independent of the cyclic loading direction for a given M_{CYC} and M_{AV}. More subtle variation in the ratcheting response is explored in Figures 4.26 and 4.27.

Following the approach of Truong *et al.* (2019), power-laws (Equation 4.1) are fitted to the evolution of $\Delta\theta_n$ for each individual test, as shown dashed in Figure 4.25. The power-law expression captures the ratcheting response accurately under L-shape loading in both directions and for T-shape loading for $n > 10$. The shape of ratcheting evolution under T-shape loading is similar to that under partial 2-way loading (Figure 4.7); these loadings both pass through zero load ($\zeta_c < 0$).

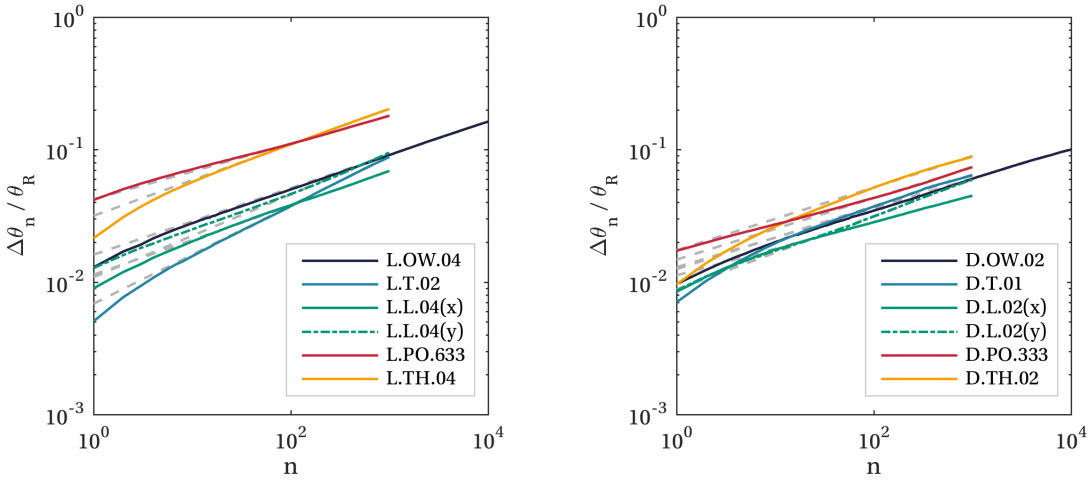

(a) Very loose sand **(b)** Dense sand

Figure 4.25: Ratcheting response under perpendicular cyclic loading with individual power-law fits (Equation 4.1) shown dashed

The variation of power-law exponent α with load type is presented in Figure 4.26, with α normalised by the power-law exponent for the corresponding unidirectional test α_{UD}. The exponents obtained in very loose sand ($1.04 \leq \alpha/\alpha_{UD} \leq 1.47$) are a little higher than those in dense sand ($0.90 \leq \alpha/\alpha_{UD} \leq 1.24$). It is also significant that the exponents under L-shape loading in the x-direction are smaller than the exponents in the y-direction. Figure 4.27 provides complementary information on the impact of load type on ratcheting, with accumulated rotation $\Delta\theta_n$ normalised by accumulated rotation for the corresponding unidirectional test $\Delta\theta_{n,UD}$. The smaller accumulated rotation observed in the x-direction (perpendicular to cycling) under L-shape loading, coupled with the observation of smaller α values in this direction, is indicative of non-linear dependency of ratcheting on load magnitude (although the mean loads are the same in the x- and y-directions, the peak load in the y-direction is twice that in the x-direction). This observation is in-line with the observed power-law variation of ratcheting magnitude coefficient T_b with cyclic amplitude for unidirectional, 1-way loading ζ_b (Figure 4.8).

Figure 4.24 highlighted the significant impact of M_{AV} on the rotation response. To further assess the impact of M_{AV}, a ratio of accumulated rotation for the HM tests $\Delta\theta_{n,HM}$ to that for the SM tests $\Delta\theta_{n,SM}$ is plotted in Figure 4.28. Given that $M_{AV,HM} =$

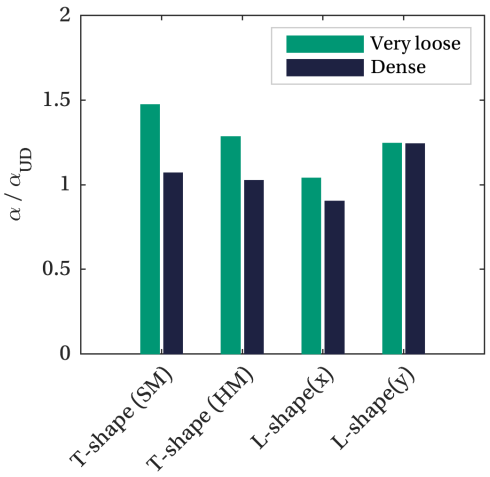

Figure 4.26: Variation of power-law exponent α with perpendicular load type

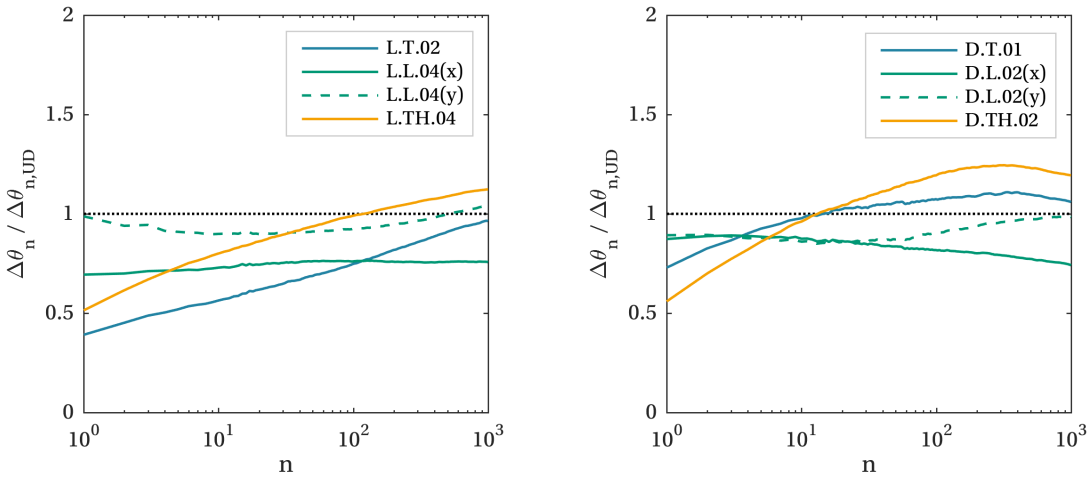

(a) Very loose sand **(b)** Dense sand

Figure 4.27: Accumulated rotation under perpendicular cyclic loading normalised by accumulated rotation for corresponding unidirectional tests

$2M_{AV,SM}$, values of $\Delta\theta_{n,HM}/2\Delta\theta_{n,SM}$ may be expected to equal unity if ratcheting is proportional to M_{AV}. Figure 4.28 shows how ratcheting may be proportional to M_{AV} in very loose sand at high cycle numbers, but in dense sand the impact of M_{AV} is less significant. The variation with density might be explained by the difference in linearity of the backbone curves: the ratio of rotation generated under monotonic loading up to M_{AV} under HM loading to that under SM loading ($\theta_{AV,HM}/\theta_{AV,SM}$) is around 6 in very loose sand but only around 3 in dense sand. As previously discussed, greater rotations lead to a greater likelihood of particle rearrangement and therefore

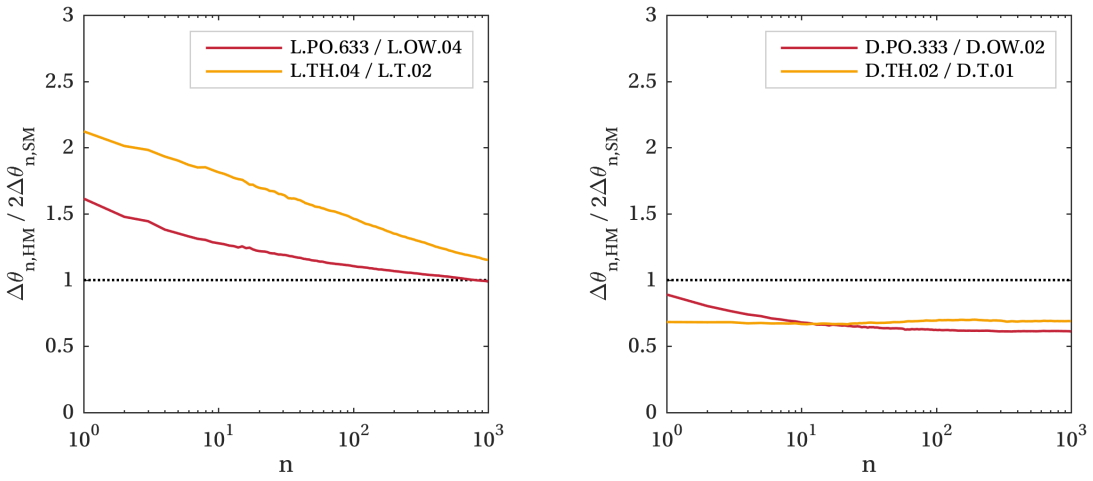

(a) Very loose sand **(b)** Dense sand

Figure 4.28: Accumulated rotation for high mean (HM) tests normalised by accumulated rotation for standard mean (SM) tests

ratcheting. To provide further insight, these tests could be repeated with a constant ratio of $\theta_{AV,HM}/\theta_{AV,SM}$. It should be noted that the comparisons of unidirectional tests L.OW.04 & L.PO.633 and D.OW.02 & D.PO.333 are included in Figure 4.28 given the focus on the impact of M_{AV} and M_{CYC} in this Section.

Secant stiffness

The evolution of secant stiffness k_n/k_{MAX} with cycle number n under perpendicular loading is plotted in Figure 4.29 (stiffness is only relevant in the cycling direction, y). Stiffness evolves approximately logarithmically (following Equation 4.2) under T-shape and L-shape loading, as shown by the dashed logarithmic fits in Figure 4.29. The addition of mean load M_{AV} perpendicular to the cyclic loading direction appears to have little impact on the stiffness: the L-shape secant stiffness follows the corresponding unidirectional stiffness closely at both densities, while the stiffness for the HM T-shape tests is similar to that for the SM tests. It is interesting that the stiffness under T-shape loading evolves logarithmically, as a power-law better captured the evolution of k_n under 2-way unidirectional loading, which is equivalent to T-shape loading in the y-direction.

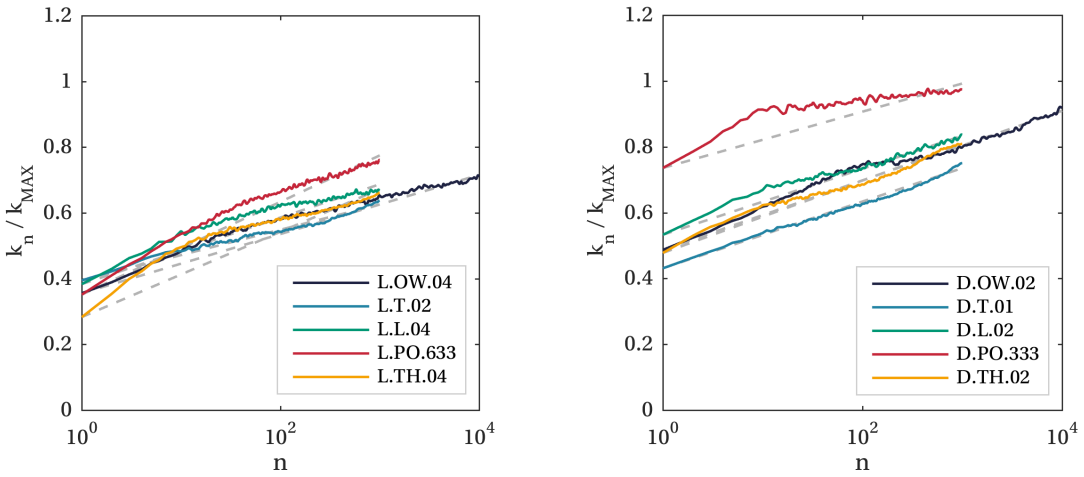

(a) Very loose sand **(b)** Dense sand

Figure 4.29: Secant stiffness evolution under perpendicular cyclic loading with logarithmic fits (Equation 4.2) shown dashed

Energy dissipation

The evolution of energy loss factor η_n with cycle number n is shown for the perpendicular tests in Figure 4.30 (η_n is only relevant in the cycling direction, y). The values of η_n for $n > 20$ are remarkably similar for the L-shape and T-shape tests at both mean load M_{AV} amplitudes, consistent with the similarity of secant stiffness k_n values. For $n > 20$, η_n for the perpendicular tests is greater than for the equivalent unidirectional tests, despite similar values for ratcheting and secant stiffness. For example, $\eta_{n=1000}$ for the perpendicular tests is at least 1.6 times larger than $\eta_{n=1000}$ for the corresponding unidirectional tests. Figure 4.31 shows the hysteretic response at $n = 1000$ for an example unidirectional test and an equivalent L-shape test; the loop area, equivalent to hysteretic energy loss E_H, is evidently larger for the L-shape test. The increase in E_H and therefore η_n under perpendicular cyclic loading may be explained by the additional soil volume disturbed, which would increase dissipation.

Overview

The broad similarity in the cyclic response under unidirectional, T-shape and L-shape loading at a given M_{CYC} and M_{AV} demonstrates the insensitivity of the response to the direction of cyclic loading (relative to mean load direction), whilst also highlighting the

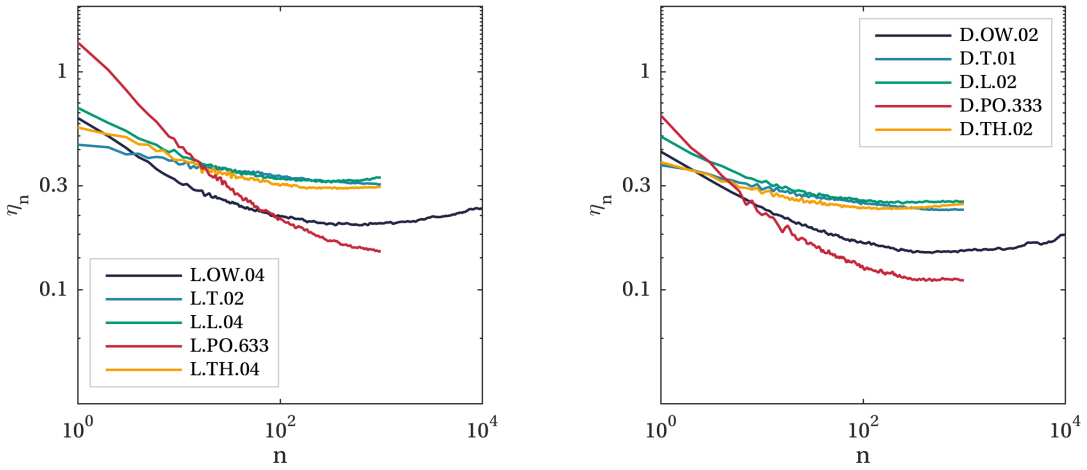

(a) Very loose sand **(b)** Dense sand

Figure 4.30: Evolution of energy loss factor under perpendicular cyclic loading

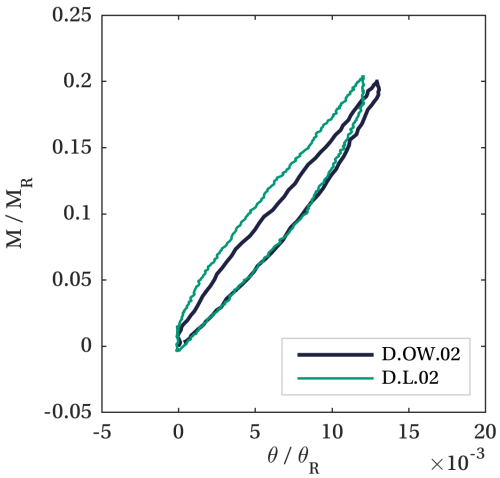

Figure 4.31: Example hysteretic response in dense sand under unidirectional and L-shape loading at $n = 1000$ to highlight difference in hysteretic loop shape

importance of M_{CYC} and M_{AV} in controlling the cyclic response. Although characterisation of cyclic loading in terms of ζ_b and ζ_c is useful, using these parameters alone does not reveal the full picture. For example, using ζ_b and ζ_c does not reveal the similarities in loading between a T-shape test ($\zeta_{c,y} = -1$) and a corresponding unidirectional test ($\zeta_c = 0$). Comparison of SM and HM tests reveals that M_{AV} affects the magnitude of ratcheting, but does not significantly affect stiffness or energy dissipation.

4.6.2 Fan-type cyclic loading

Figure 4.32 describes the fan-type loading applied in $M_x - M_y$ space, which allows exploration of the impact of the spread of cyclic loading direction. The loading traces the sector of a circle with radius $\zeta_b M_R$ and half internal spread angle Φ. 1-way cyclic loading is applied within this sector at a frequency f, while the loading direction changes sinusoidally at a frequency $f/100$, so that 1000 cycles corresponds to 10 complete sweeps of the sector. Loading starts and finishes in the x-direction. Equations 4.5 and 4.6 define $M_x(t)$ and $M_y(t)$ for a maximum load $\zeta_b M_R$ and cyclic loading frequency f. This loading closely follows the multidirectional loading applied by Dührkop and Grabe (2008), Rudolph *et al.* (2014b), and in other related work.

$$M_x(t) = \frac{\zeta_b M_R}{2}\left(1 + \sin\left(2\pi f t\right)\right)\cos\left(\Phi \sin\left(\frac{2\pi f t}{100}\right)\right) \tag{4.5}$$

$$M_y(t) = \frac{\zeta_b M_R}{2}\left(1 + \sin\left(2\pi f t\right)\right)\sin\left(\Phi \sin\left(\frac{2\pi f t}{100}\right)\right) \tag{4.6}$$

Seven fan-type tests were performed in very loose sand with $15° \leq \Phi \leq 150°$, while two tests were performed in dense sand with $\Phi = 30°$ and $\Phi = 90°$ (as summarised in Tables 4.1 and 4.2). In practice, loading directionality is site-specific and depends on the time-scale considered. For a single storm with a following sea state, a spreading angle of around $25°$ may be typical. However, loading direction will vary more significantly over the structure's lifetime, as shown for an example site offshore the Netherlands in Figure 1.8 (Chapter 1).

All loose tests were conducted at $\zeta_b = 0.4$ and all dense tests at $\zeta_b = 0.2$; the fan-type tests are therefore comparable to unidirectional tests L.OW.04 and D.OW.02 respectively. Figure 4.33 shows the rotation response for an example fan-type test in very loose sand with $\Phi = 60°$. Rotation accumulates in the x-direction, but significant transient rotation also occurs in the y-direction as the loading direction changes over each sweep of the sector.

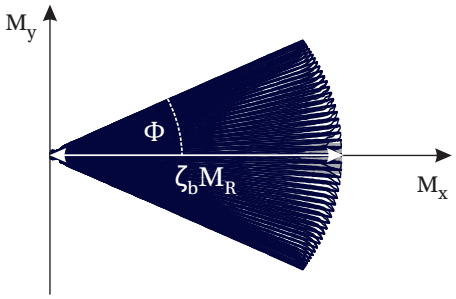

Figure 4.32: Description of fan-type loading

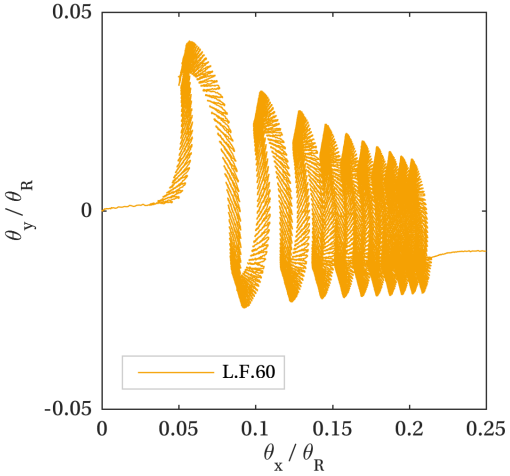

Figure 4.33: Example rotation response under fan-type loading (test L.F.60)

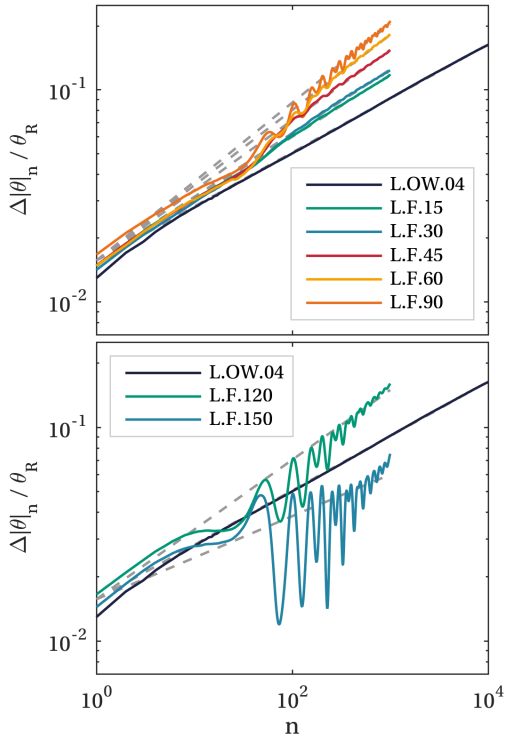

(a) Very loose sand

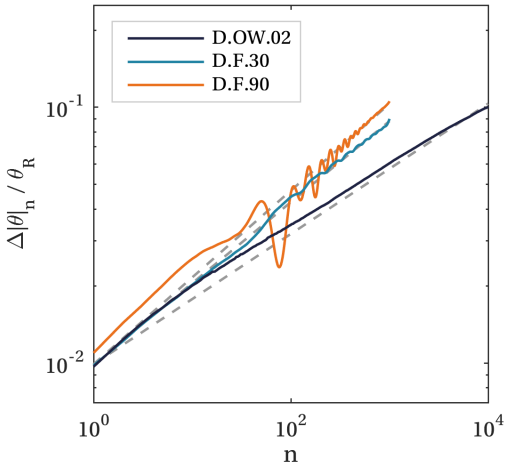

(b) Dense sand

Figure 4.34: Ratcheting response under fan-type cyclic loading with individual power-law fits (Equation 4.1) shown dashed

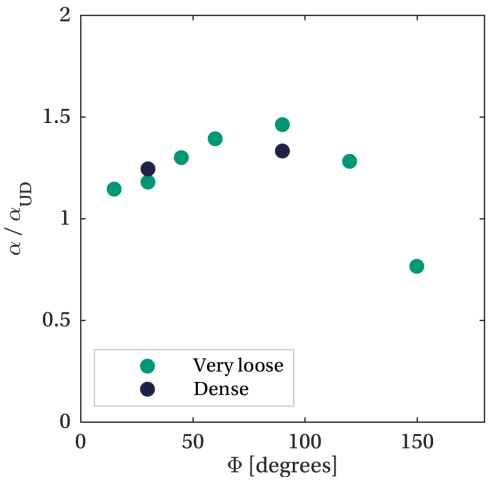

Figure 4.35: Variation of α with spread angle Φ under fan-type loading

Ratcheting

Figure 4.34 presents the accumulated rotation $\Delta|\theta|_n$ response under fan-type loading alongside the response to corresponding unidirectional loading. The modulus notation indicates that the data presented has been obtained from the absolute moment-rotation response ($|M| = \sqrt{M_x^2 + M_y^2}$, $|\theta| = \sqrt{\theta_x^2 + \theta_y^2}$), which is appropriate given that the absolute load $|M|$ has constant amplitude throughout the tests. The secant stiffness $|k|_n$ and the energy loss factor $|\eta|_n$ are also determined from the absolute response.

As the loading direction changes, the rate of evolution of ratcheting varies — seen as ripples in Figure 4.34. The magnitude of these ripples increases with increasing spread angle Φ, and for $\Phi \geq 90°$ significant negative ratcheting is observed transiently where the load in the x-direction goes negative ($\sigma_{AV,x} < 0$). The spread angle also impacts the overall ratcheting evolution, and is assessed by fitting power-law expressions (Equation 4.1) to each fan-type test, as shown dashed in Figure 4.34. The coefficients A are set equal to the values for the corresponding unidirectional tests as the initial loading cycle is unidirectional. The variation of exponent α is plotted in Figure 4.35 normalised by the corresponding unidirectional exponent α_{UD}. For $0° \leq \Phi \leq 90°$, α increases with spread angle Φ and in very loose sand at $\Phi = 90°$, $\alpha/\alpha_{UD} = 1.46$. However, α decreases at larger Φ values (observed in very loose sand only).

Study	Test conditions	Cycle No. N	Strain metric ε	Worst angle Φ^*	Multidirectional factor $\varepsilon_{N,F}/\varepsilon_{N,UD}$
Dührkop and Grabe (2008)	$1g$, medium-dense sand	50000	Pile head displacement	45°	13
	$1g$, dense sand	50000		45°	$2-3$
Rudolph *et al.* (2014a)	$1g$, medium-dense sand	10000	Displacement at lowest LVDT	90°	1.2
	$1g$, dense sand	10000		120°	1.4
	$200g$, medium-dense sand	3000		30°	1.7
	$200g$, dense sand	3000		90°	1.5
This study	$1g$, very loose sand	1000	Accumulated pile rotation	90°	2.3
	$1g$, dense sand	1000		90°	1.8

Table 4.5: Comparison of worst-case spread angles and multidirectional factors for ratcheting response under fan-type loading (this study and similar studies)

The impact of spread angle Φ on ratcheting can also be assessed with the ratio of strain at cycle N under fan-type loading $\varepsilon_{N,F}$ to that under corresponding unidirectional loading $\varepsilon_{N,UD}$. This multidirectional factor is summarised for this study and similar studies by Dührkop and Grabe (2008) and Rudolph *et al.* (2014a) in Table 4.5. Whilst an increase in strain under fan-type loading relative to unidirectional loading is observed in all cases, there is significant variation in both the spread angle which causes the greatest ratcheting (Φ^*) and the multidirectional factor ($\varepsilon_{N,F}/\varepsilon_{N,UD}$). Ratcheting behaviour is likely to vary with the specific load regime (*e.g.* rate of change of load direction), as reported by Rudolph *et al.* (2014b). Application of a blanket multidirectional factor on ratcheting is therefore not recommended, but these results together highlight the need to account for changing cyclic loading direction to ensure that ratcheting is not underestimated.

In a similar way to the impact of ζ_c on ratcheting under unidirectional cyclic loading, the impact of spread angle Φ on ratcheting may be understood as a competition between (a) increasing pile and therefore soil movement with increasing Φ, and (b) decreasing mean load in the dominant loading direction with increasing Φ.

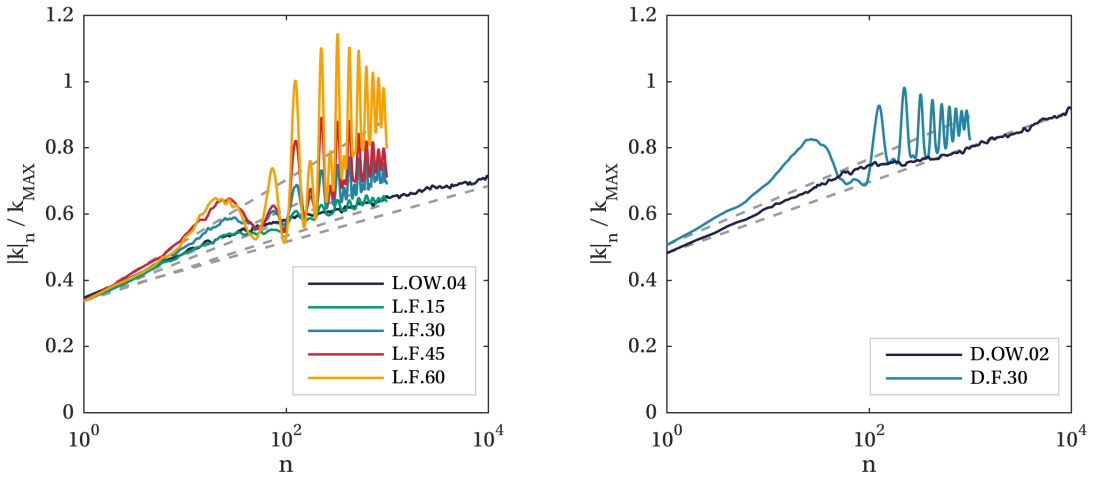

(a) Very loose sand **(b)** Dense sand

Figure 4.36: Secant stiffness evolution under fan-type cyclic loading with logarithmic fits (Equation 4.2) shown dashed

Secant stiffness

The evolution of secant stiffness of the absolute response $|k|_n$ is plotted in Figure 4.36 for the fan-type and corresponding unidirectional cyclic tests. Secant stiffness varies with the loading direction, causing ripples similar to those observed in the ratcheting response. These ripples become very large for $\Phi \geq 90°$, as $|k|_n$ passes through theoretically infinite stiffness and becomes negative when the direction of ratcheting accumulation reverses. The responses for $\Phi \geq 90°$ therefore cannot be presented on the axes used in Figure 4.36.

Logarithmic fits (Equation 4.2) approximately capture the overall evolution of secant stiffness for $\Phi < 90°$, as shown in Figure 4.36. The impact of spread angle Φ is assessed by plotting the variation of coefficient B_L (which controls the rate of change of stiffness, see Equation 4.2), normalised by the unidirectional coefficient $B_{L,UD}$, against Φ in Figure 4.37. There is a clear trend for increasing B_L, and therefore rate of stiffening, with spread angle Φ. This trend may be expected: as Φ increases, the volume of soil likely to densify under cyclic loading also increases.

Energy dissipation

The energy dissipation under fan-type loading is presented in Figure 4.38, with the energy loss factor of the absolute response $|\eta|_n$ plotted against cycle number n. Data

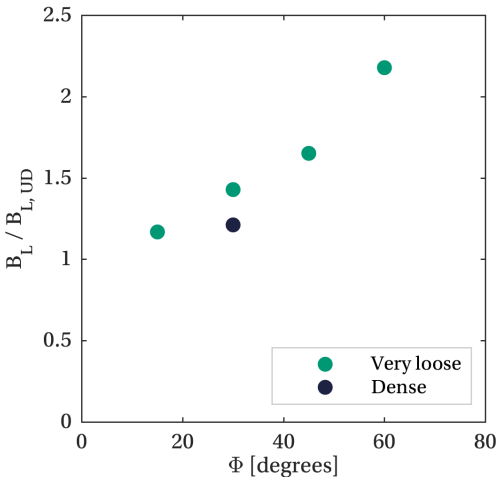

Figure 4.37: Variation of B_L with spread angle Φ under fan-type loading

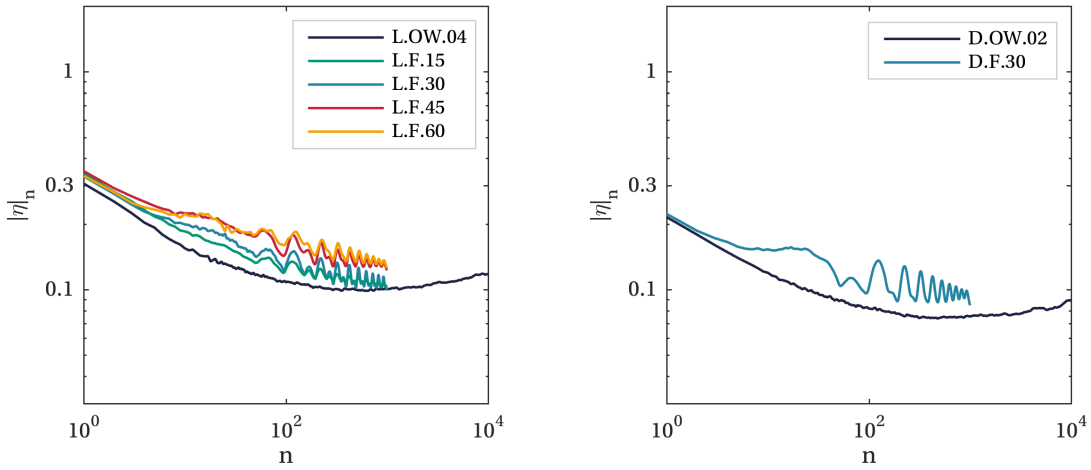

(a) Very loose sand **(b)** Dense sand

Figure 4.38: Evolution of energy loss factor under fan-type cyclic loading

for $\Phi \geq 90°$ is not presented, given that $|\eta|_n \to 0$ for these tests when the direction of ratcheting accumulation reverses. Again, ripples in the $|\eta|_n$ response are observed as the loading direction changes. The overall energy dissipation follows a similar trend to that for the corresponding unidirectional tests, although $|\eta|_n$ is consistently larger at given cycle number n for tests with larger spread angles. This trend is explained by the increase in soil volume disturbed as spread angle Φ increases, which is likely to increase dissipation. A similar observation on energy dissipation was made for perpendicular loading.

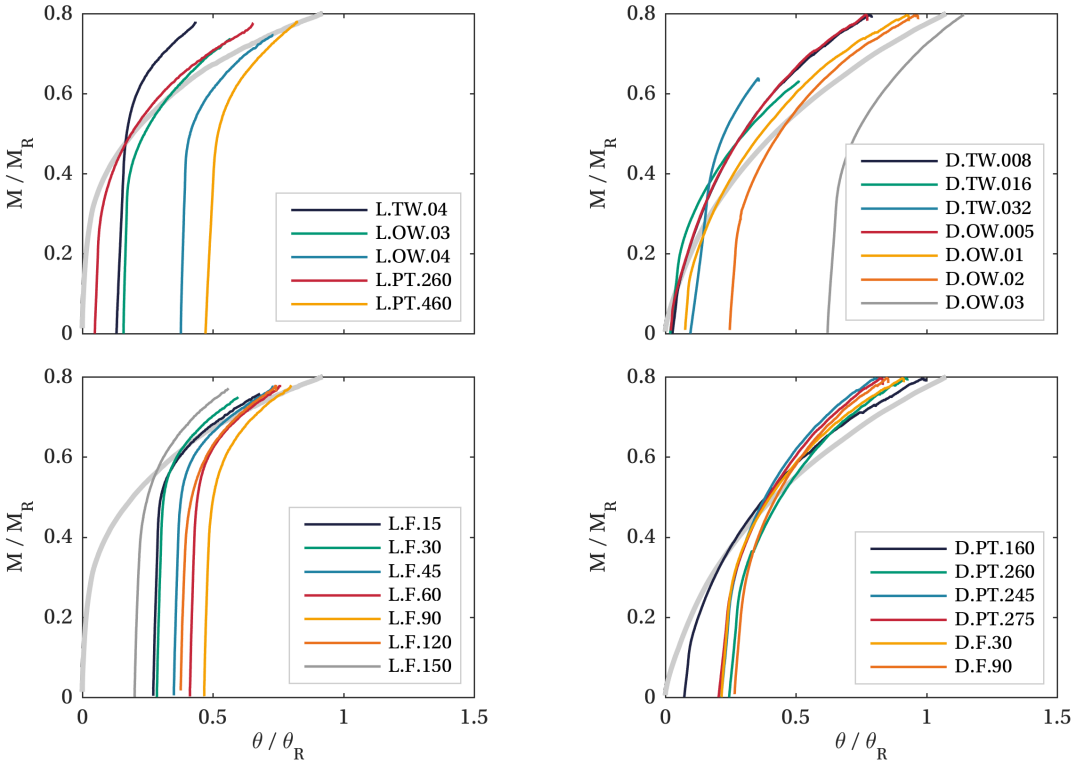

(a) Very loose sand **(b)** Dense sand

Figure 4.39: Post-cyclic reloading responses (mean monotonic response shown in grey)

4.7 Post-cyclic reloading response

Post-cyclic reloading was performed as part of many of the cyclic tests, as identified in Tables 4.1 and 4.2. The post-cyclic response is analogous to the response which might be expected during the ULS event, and can also inform interpretation of irregular multi-amplitude loading. Figure 4.39 presents the reloading responses with the cyclic responses omitted for clarity. In many cases the reloading responses exceed the mean monotonic response (backbone curve), indicating an increase in capacity. In other cases the reloading responses approach the backbone curve. The greatest exceedance of the backbone curve occurs for large amplitude 2-way tests (L.TW.04, D.TW.032), where significant secant stiffening but relatively little ratcheting occurred. The reloading responses are also plotted in Figure 4.40 for $M/M_R < 0.5$, with the rotation zeroed from the onset of reloading (at $\theta = \theta_{r0}$). This plot highlights the increase in stiffness relative to the backbone curve, particularly for $M/M_R < \zeta_b$, which is consistent with

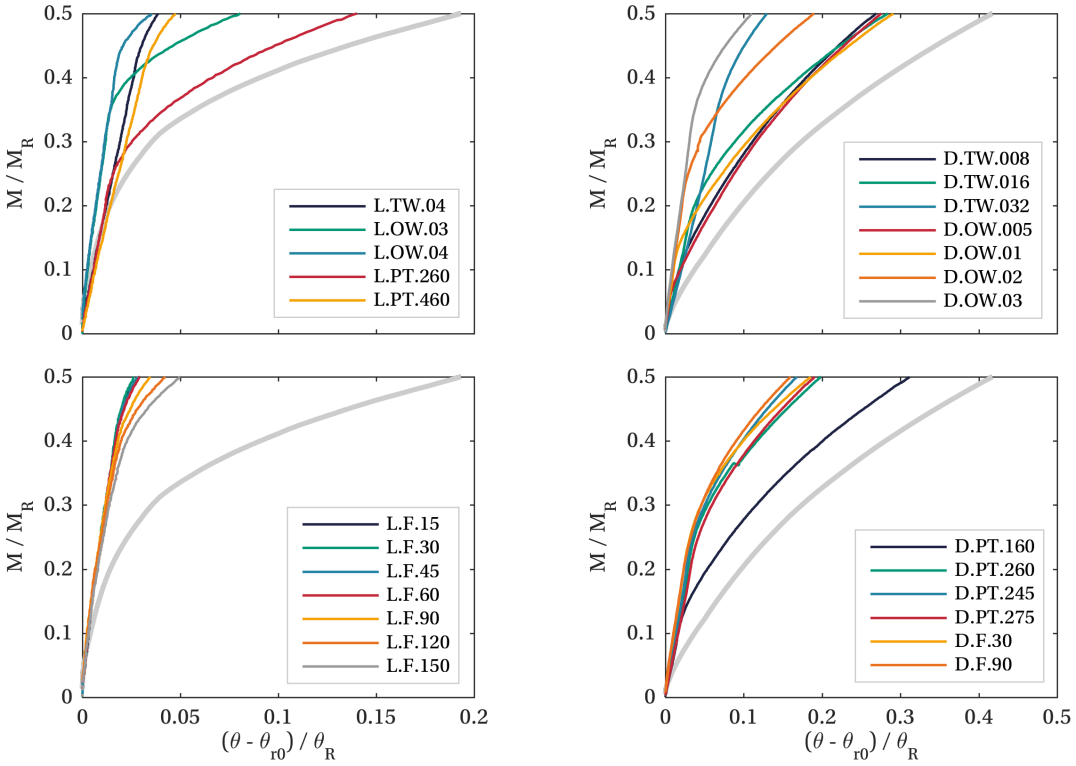

(a) Very loose sand **(b)** Dense sand

Figure 4.40: Post-cyclic reloading responses with rotation zeroed from the onset of reloading at θ_{r0} (mean monotonic response shown in grey)

the observed increase in secant stiffness under cyclic loading.

As discussed throughout this Chapter, ratcheting and secant stiffening often occur in parallel under cyclic loading in dry sand. Ratcheting moves the reloading responses beneath the backbone curve and increases pile rotation on reloading, while the densification driving secant stiffening also increases stiffness beyond the region strained under cyclic loading, leading to a decrease in pile rotation on reloading. These processes are therefore in competition, as discussed by Abadie *et al.* (2019b). Under some conditions, the balance of ratcheting and stiffening processes may lead to no significant change in the response at large loads, as observed by Abadie *et al.* (2019b) and for many of the 1-way tests presented here. Where stiffening processes dominate, such as for the large amplitude 2-way tests presented here, an increase in post-cyclic monotonic capacity can be observed. Truong *et al.* (2019) and Nicolai *et al.* (2017b) also report an increase in post-cyclic monotonic capacity, and Nicolai *et al.* (2017b) are

further able to quantify the increase in capacity in terms of cycle number, ζ_c and ζ_b, given that their reloading tests reach clear yield.

The conventional cyclic degradation approaches apply reduction factors to *p-y* curves to reduce the pile's lateral capacity (Section 1.2.5), consistent with the idea that cyclic loading is an intrinsically damaging process. Whilst this may be true for clays, the current experimental evidence does not support a decrease in post-cyclic capacity in (fully drained) sands, and under some conditions an increase in capacity is observed which may be exploited to optimise monopile design.

4.8 Summary

This Chapter has explored the response of a model monopile foundation to regular, unidirectional and multidirectional cyclic lateral loading in dry sand at $1g$. The following points summarise the key observations, which are, in general, applicable to both very loose and dense sand.

Unidirectional hysteretic response (Section 4.3)

- The hysteretic response under 2-way loading broadly adheres to the extended Masing rules for the first few ($n < 4$) loading cycles.
- Behaviour indicative of gapping is observed under high amplitude 2-way loading in dense sand.

Unidirectional high cycle response (Section 4.4)

- Accumulation of pile rotation (ratcheting) occurs under biased cyclic loading and tends to evolve as a power-law with cycle number.
- The magnitude of ratcheting increases as a power-law with cyclic amplitude (characterised by ζ_b for constant ζ_c).
- The ratcheting shape, rate and therefore magnitude is impacted by load asymmetry. Ratcheting increases under partial 2-way loading where loading passes through zero load ($\zeta_c < 0$).

- Secant stiffness increases under cyclic loading. A logarithmic relationship captures the evolution of stiffness under 1-way and partial 1-way loading, but a power-law captures the behaviour better under 2-way and partial 2-way loading, where loading passes through zero load ($\zeta_c < 0$).
- Energy dissipation varies significantly with cyclic loading as the secant stiffness and ratcheting rate change.
- Uplift is possible under large amplitude cyclic loading, even with larger than representative vertical loading.

Multidirectional hysteretic response (Section 4.5)

- The hysteretic response under multidirectional spiral loading in either the x- or y-direction resembles that under equivalent unidirectional loading (which adheres to the extended Masing rules) although some interaction between loading components is observed.

Multidirectional high cycle response (Section 4.6)

- The response to unidirectional, T-shape and L-shape cyclic loading at a given cyclic amplitude M_{CYC} and mean load M_{AV} is similar, demonstrating insensitivity of the response to the cyclic loading direction (relative to the mean load direction) and highlighting the importance of parameters M_{AV} and M_{CYC} in controlling the cyclic response.
- Ratcheting occurs in the direction of the mean load, regardless of the cyclic loading direction.
- The spread of loading directions has a significant impact on the evolution of ratcheting and stiffening under fan-type loading. For the most damaging spread angle, accumulated pile rotation at $n = 1000$ is 2.3 and 1.8 times larger than the rotation under corresponding unidirectional loading, in very loose and dense sand respectively.
- Energy dissipation under perpendicular loading and fan-type loading is greater than under corresponding unidirectional loading.

Post-cyclic reloading response (Section 4.7)

- The reloading response is understood to be controlled by the ratcheting and stiffening processes which occur under cyclic loading in dry sand and have opposing effects on the reloading response.
- The inferred post-cyclic capacity is equal to or greater than the monotonic capacity for all applied load cases, at odds with the cyclic degradation approach (see Section 1.2.5).
- The reloading response tends to the backbone curve following 1-way cyclic loading.

In summary, the monopile response adheres to the extended Masing rules for the first few cycles, but evolution of secant stiffness and associated energy dissipation are observed under many cycles. Ratcheting also occurs under many cycles of biased loading. The behaviour observed under unidirectional loading is generally consistent with observations from previous studies (*e.g.* Abadie *et al.*, 2019b; Truong *et al.*, 2019), while multidirectional tests provide new insights. Fan-type tests highlight the significant impact of the spread of loading direction on both ratcheting and stiffening behaviour, while perpendicular tests reveal the insensitivity of the cyclic response to cyclic load direction (relative to the mean load direction) and confirm that ratcheting occurs in the direction of the mean load.

The energy dissipation evolution and reloading responses are mostly explicable in terms of ratcheting and stiffening behaviour, and are therefore considered to be secondary, but no less important, phenomena. The observation that the post-cyclic capacity is equal to or greater than the monotonic capacity has important implications for ULS design, and contrasts with the conventional cyclic degradation approach.

Throughout, the observed behaviour was interpreted in terms of the densification and convective mechanisms understood to be driving stiffening and ratcheting at the macro scale, as discussed in Section 1.3.2. In general, increased ratcheting (magnitude and evolution) and stiffening (rate) coincided with an increased potential for soil particle rearrangement, which is necessary for both densification and convective mechanisms. Increased soil particle rearrangement is likely with increased cyclic load

amplitude, increased loading multidirectionality, and where loading passes through zero load.

As well as providing fundamental insight into the response of a monopile to cyclic lateral loading, the observations in this Chapter i) provide a basis for interpretation of the response of the monopile to realistic multi-amplitude, multidirectional storm loading in Chapter 5, and ii) inform development and calibration of models in the HARM framework in Chapter 7.

Chapter 5

Application of realistic storm loading at 1*g*

5.1 Introduction

Regular cyclic loading tests, such as those presented in Chapter 4, allow systematic investigation of the cyclic response of monopile foundations. But in reality, monopiles supporting OWTs are exposed to continuously varying cyclic loading. This Chapter explores the response to more realistic, multi-amplitude and multidirectional, storm loading. The results provide novel insight into the response of monopiles and allow parallels to be drawn with the regular cyclic loading response. The results also provide valuable data for validation of numerical models, such as presented in Chapter 7.

The tests were conducted in dry sand at 1g using the apparatus described in Chapter 2, with the test procedures outlined in Chapter 3. The applied loads were derived from wave basin tests performed as part of the DeRisk project (Bredmose *et al.*, 2016). The processing steps required for appropriate application of these loads to the geotechnical model monopile are discussed in detail. Understanding the characteristics of realistic storm loading is also an important aspect of this work.

5.2 DeRisk wave tank tests (Bredmose *et al.*, 2016)

The DeRisk project aimed to reduce the risk associated with predicting ULS wave loads on OWT structures (Bredmose *et al.*, 2016). The multi-centre project was funded by Innovation Fund Denmark and conducted over the period 2015 to 2019. As part of the

Figure 5.1: High speed photograph from DeRisk wave basin testing showing model monopile and wave (Bredmose *et al.*, 2016)

project, wave loading tests were performed on model monopiles in a shallow water basin at the Danish Hydraulic Institute (DHI), as shown in Figure 5.1.

An approximately rigid cylinder with diameter 140 mm was used to represent a 7 m diameter prototype monopile structure in the water column ($1:50$ scale). The cylinder was instrumented with (amongst other instruments) four load cells for resolution of the applied horizontal and moment load in two orthogonal directions (x, y). Various sea states were generated, representing medium to severe storms in the North Sea. The sea states chosen for deriving loading for the geotechnical model monopile were in a prototype water depth of 33m, with peak spectral period 15s and significant wave height 9.5 m, approximately corresponding to a 100-year return period. Loads were derived from both a unidirectional (UD) and multidirectional (MD) sea state. The waves in the unidirectional sea state were all aligned with the x-direction. Meanwhile, the waves in the multidirectional sea state varied in direction (around x) with spreading angle $\Phi = 22°$, where Φ is the standard deviation of a wrapped normal spreading distribution (*e.g.* Adcock and Taylor, 2009). This spreading angle may be typical for a following sea state, where one weather system is present.

Deriving loading from measured wave data introduces non-Gaussian skewness in loads that is representative of loading in the field. Wave skewness affects the mean and peak wave loads, both of which play an important role in determining the monopile

response. This compares to the use of simplified wave models which underestimate wave skewness (*e.g.* Wang, 2018), and linear wave models which predict symmetric waves with zero mean load.

5.3 Wave load processing and test programme

The wave loads were provided by the DeRisk team at prototype-scale with moment M and horizontal load H components in the x-direction for the UD sea state and in the x- and y-directions for the MD sea state. Storms of up to 70 hours in length (at prototype scale) were generated in the wave basin, but only the first 6 hours of data were used here. A number of processing steps were necessary before application of the wave loads to the geotechnical model:

1. Application of a transfer function (TF) to approximate the dynamic response of an OWT structure.
2. Addition of constant wind loading in the x-direction to better model combined environmental loading.
3. Projection of loads to a constant loading eccentricity to allow application with the apparatus described in Chapter 2.
4. Scaling of the prototype loads for application to the laboratory-scale geotechnical model.

Figure 5.2 shows the effect of processing steps 1-3 on the first 6 hours of prototype wave loads for the MD sea state.

5.3.1 Application of transfer function

Offshore wind turbine structures on monopile foundations typically have first natural frequencies close to the frequency content of waves (Bachynski *et al.*, 2017), whereas the natural frequency of the approximately rigid cylinder used in the wave basin experiments was much higher ($f_0 \approx 5.7$ Hz). Dynamic amplification of loads will therefore be significant for the real structure but negligible for the rigid cylinder. To account for dynamic amplification of loads, the OWT structure was approximated as a single degree of freedom system with a natural frequency f_0 and damping ratio ξ. The

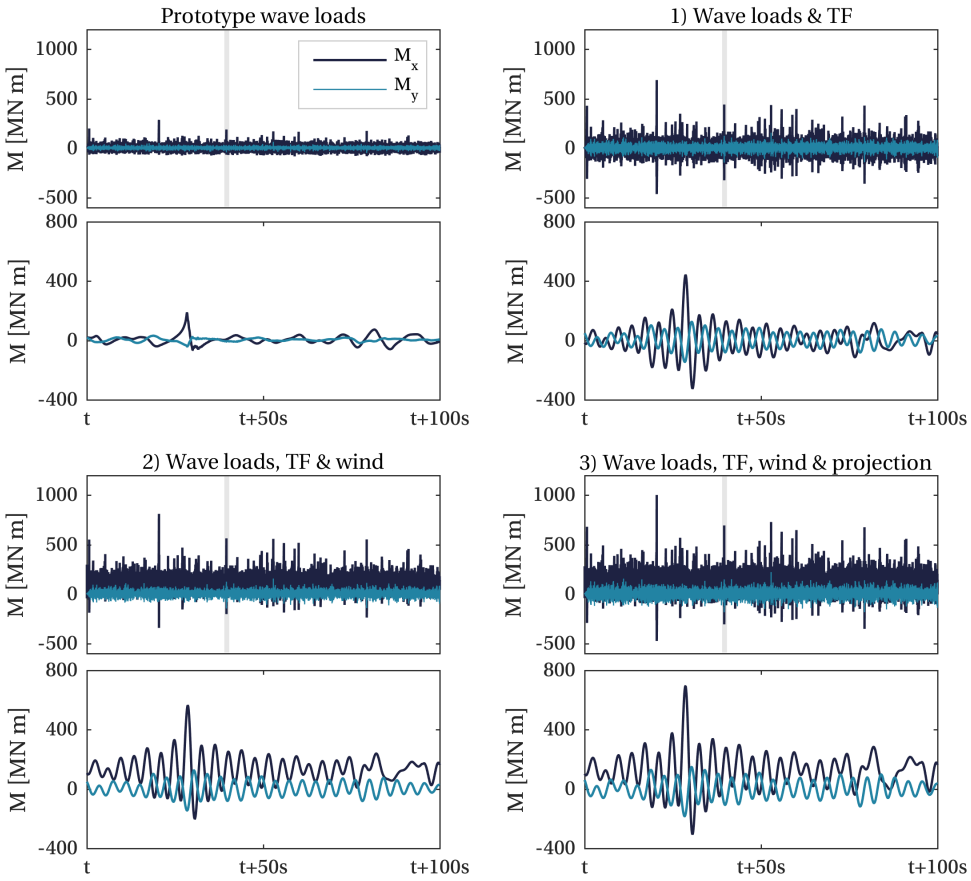

Figure 5.2: Impact of wave processing steps 1) to 3) on prototype-scale loads for the MD sea state (upper plots show first six hours of the sea state, lower plots highlight arbitrary $100\ s$ of loading indicated by grey shaded region in upper plots)

ratio of transmitted force F_T to excitation force F_E can then be found with the transfer function (TF):

$$\frac{F_T}{F_E} = \frac{1}{\sqrt{\left(1-\left(\frac{f}{f_0}\right)^2\right)^2 + \left(2\xi\frac{f}{f_0}\right)^2}} \tag{5.1}$$

Dynamic amplification of loads will also occur at higher frequency modes (*e.g.* second tower bending mode and blade bending modes) but this simple transfer function captures the key dynamic behaviour of the OWT structure, and has been used by *e.g.* Arany *et al.* (2017).

The first natural frequency of the prototype structure was estimated as $f_0 = 0.26$ Hz, between the 1P and 3P blade passing excitation frequencies for a Vestas V164-8.0MW turbine (University of Strathclyde, 2015). Given that the sea states used represent extreme storm conditions, the turbine is assumed to be parked. In parked conditions,

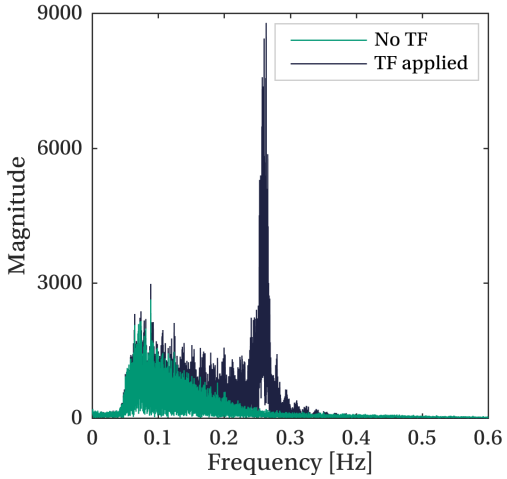

Figure 5.3: Impact of TF on frequency content of MD moment loads in the x-direction

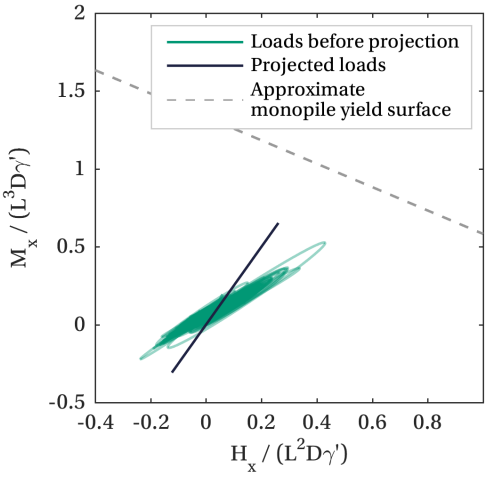

Figure 5.4: Illustration of projection of MD loads in x-direction to constant loading eccentricity

where aerodynamic damping is negligible, the total damping is estimated as $\xi = 0.65\%$, in-line with Kementzetzidis *et al.* (2019) for dense sand.

The transfer function was approximated as an arbitrary magnitude filter and applied to loads in both directions in the frequency domain. Figure 5.3 demonstrates the impact of the transfer function on the frequency content of the MD moment loads in the x-direction, showing clearly the amplification of the signal around the natural frequency of the structure. Figure 5.2(1) shows the impact of the transfer function on the MD moment loads in the time domain. The close proximity of the structure's natural frequency f_0 to the frequency content of the waves, coupled with the low damping ratio ξ, leads to significant dynamic amplification of wave loads. The peak moment amplitudes approximately double and the number of cycles increases by around 50% (for both the UD and MD cases). The impact of this transfer function is consistent with the experimental observations of Bachynski *et al.* (2017), who used an appropriately flexible monopile to explore dynamic amplification of wave loads.

5.3.2 Addition of wind loading

Wind loading may be added to the prototype wave loads to better represent combined environmental loading. A wind load of 1.4 MN acting at a height 85.5 m above the mudline was estimated by assuming appropriate prototype OWT dimensions (water

depth 33 m, tower height 105 m, mean tower diameter 6 m), with the turbine parked and blades feathered, and employing a 50-year design wind speed of 50 m/s, consistent with the extreme storm conditions represented by the waves. The relatively low-frequency fluctuations in wind amplitude were neglected, with the wind load approximated as a constant load. Wind loading was aligned with the dominant wave loading direction (x).

Figure 5.2(2) shows how the addition of wind loading adds a constant load bias in the x-direction and increases the overall mean load $\bar{M}$ and peak moment load M_p. Throughout, the monopile response is explored with and without wind loading.

5.3.3 Projection of loads to constant eccentricity

The measured wave loads have a variable eccentricity ($\tilde{e} = M/HL$). However, for loads to be applied using the loading system described in Chapter 2, the loads must be projected to a constant eccentricity. Loads were projected to a *load line* in $M-H$ space, with a gradient representative of that applied by the laboratory apparatus ($\tilde{e} = 2.50$), in a direction parallel to an approximate monopile yield surface. The x- and y-direction loads were projected independently.

By assuming a distributed lateral load per unit pile length of $DK\gamma' z$, assuming $K = 3K_p$ (Broms, 1964) and linearising the yield surface in the region of interest (where M/H is positive), an approximate yield surface can be defined by:

$$\frac{M}{L^3 D\gamma'} + 0.75\frac{H}{L^2 D\gamma'} = 0.29K_p \tag{5.2}$$

Figure 5.4 illustrates the process of projecting the x-direction loads for the MD sea state (assuming example prototype parameters $D = 7$ m, $L = 28$ m, $\gamma' = 10$ kN/m^3, $\phi' = 40°$) while Figure 5.2(3) shows the impact on the moment loads for the MD case. The eccentricity of the measured wave loads is smaller than the eccentricity applied by the laboratory apparatus, thus the amplitude of moment loads increases upon projection.

5.3.4 Scaling wave loads

Lastly, the prototype-scale wave loads were scaled down to model-scale using the dimensionless framework of Leblanc *et al.* (2010a) (Table 3.4, Section 3.4.3), by equating expressions for $\tilde{H}$ and $\tilde{M}$ at laboratory- and prototype-scale. Parameters L, D

and γ' therefore required specification at prototype-scale. Although the wave basin model represented a prototype monopile with diameter 7 m in the water column, from a geotechnical design perspective the monopile size would vary with sand density. Therefore, a prototype pile diameter of 6.9 m was chosen for tests in dense sand and a prototype pile diameter of 9.7 m was chosen for tests in very loose sand; the aspect ratio $\eta = 4$ at both densities.

The dimensionless framework accounts for the effect of stress-level on stiffness, but does not account for the variation of friction angle with stress-level and density. Peak friction angle ϕ'_p is therefore matched between prototype- and laboratory-scale using the empirical relations presented by Bolton (1987) (discussed in Section 3.2.3) to determine D_R and hence γ' at prototype-scale for each density. Table 5.1 summarises the prototype parameters used to scale the wave loads at each density and the resulting ratio of prototype-scale moment to laboratory-scale moment ($f_M = M_P/M_L$). The sand is assumed to be saturated at prototype-scale.

Density	Pile diameter D [m]	Pile length L [m]	Unit weight γ' [kN/m^3]	f_M
Very loose	9.7	38.8	4.7	69.7×10^6
Dense	6.9	27.6	6.5	22.2×10^6

Table 5.1: Prototype-scale parameters used for scaling wave loads

5.3.5 Test programme

Table 5.2 summarises the realistic storm loading tests performed. The loading is summarised in terms of the peak moment M_p and overall mean moment $\bar{M}$ across the test, in the x- and y-directions. The test names indicate sequentially: sand density, source sea state, addition of wind loading, and loading direction details where necessary. To obtain the cycle number N, extreme and reversal points were defined where the peak prominence of M exceeds $M_R/100$; cycles were then defined between these points following Section 3.5.6.

The loading frequency was reduced relative to prototype-scale to ensure accurate load control, and a greater reduction was necessary for the tests in dense sand, where the load amplitudes were greater. To avoid tests running for an excessively long time

Test name	Source sea state and details	Wind	Cycle No. N	Loads $[/M_R]$			
				$M_{p,x}$	$\bar{M}_x$	$M_{p,y}$	$\bar{M}_y$
Very loose sand samples							
L.UD.0	UD	No	5400	0.40	0.004	0	0
L.UD.W	UD	Yes	5400	0.46	0.070	0	0
L.MD.0	MD	No	5400	0.49	0.002	0.12	0.002
L.MD.W.x	MD, applied twice in x-direction.	Yes	10400	0.55	0.065	0.12	0.002
L.MD.W.45	MD, applied in x-direction then at $45°$ to x *(italic loads)*	Yes	10400	0.55 *0.39*	0.065 *0.046*	0.12 *0.38*	0.002 *0.049*
L.MD.0.I	MD, only x-direction component applied	No	5400	0.49	0.002	0	0
L.MD.W.I	MD, only x-direction component applied	Yes	5400	0.55	0.065	0	0
Dense sand samples							
D.MD.0	MD	No	2000	0.42	0.002	0.1	0.002
D.MD.W	MD	Yes	2000	0.48	0.058	0.1	0.002
D.MD.W.I	MD, only x-direction component applied	Yes	2000	0.48	0.058	0	0

Table 5.2: Realistic storm loading test programme at $1g$

(> 18 hr), the first 6 prototype hours of sea state data were used for the very loose tests and the first 3.4 prototype hours of data were used for the dense tests. Changing the loading frequency was not expected to impact the results, given that significant rate effects were not observed in the monotonic tests (Section 3.4.1).

Tests were conducted with (.W) and without (.0) wind loading to explore the effect of the increase in load bias (see variations in $\bar{M}$ and M_p) caused by the wind load. Tests identified with .I were derived from MD sea states, but applied loading in only the x-direction; comparison of these tests with the equivalent multidirectional tests therefore allows exploration of multidirectionality effects. Moment loading for example tests L.MD.0 and L.MD.0.I is shown in Figure 5.5. Tests L.MD.W.x and L.MD.W.45 involve application of the MD sea state aligned with the x-direction, followed by application of the same loading either aligned with (.x) or at $45°$ to (.45) the x-direction. These tests allow exploration of the impact of consecutive storms and the impact of changing storm direction.

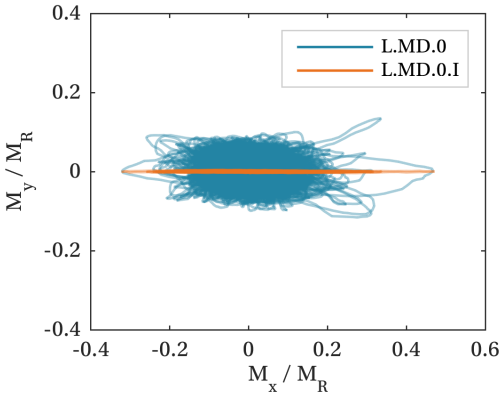

Figure 5.5: Applied loading for multidirectional test L.MD.0 compared with loading for corresponding unidirectional test L.MD.0.I

Figure 5.6 presents the distribution of applied M_{CYC}/M_R and M_{AV}/M_R (and equivalently ζ_b and ζ_c, as shown in Figure 3.11, Section 3.5.1) in the x-direction for key tests presented in Table 5.2. The distributions are presented in terms of the sum of number of half-cycles ($\sum n_{0.5}$) in a given bin (size $0.01M/M_R$), on a logarithmic scale. The figure shows how the addition of wind loading shifts the distribution on the M_{AV}/M_R axis, increasing $\bar{M}$ and leading to more 1-way and partial 1-way loading. The largest half-cycles tend to be partial 2-way. Across the tests, the vast majority of loading occurs at $\zeta_b < 0.25$ and much of the loading occurs at $\zeta_b < 0.15$, despite these tests representing extreme storm conditions. Presentation of realistic multi-amplitude loading in this way can help inform the design of focused physical modelling programmes.

5.4 Storm loading response

5.4.1 General observations

The response of the monopile to multi-amplitude storm loading is presented in moment-rotation space in the left and mid plots in Figures 5.7, 5.8 and 5.9. The continuous responses show the shape of the hysteretic loops and may be compared to the backbone curve (shown in grey in the plots). In general, the hysteretic responses are consistent with those observed for regular cyclic loading (in Section 4.3), with some

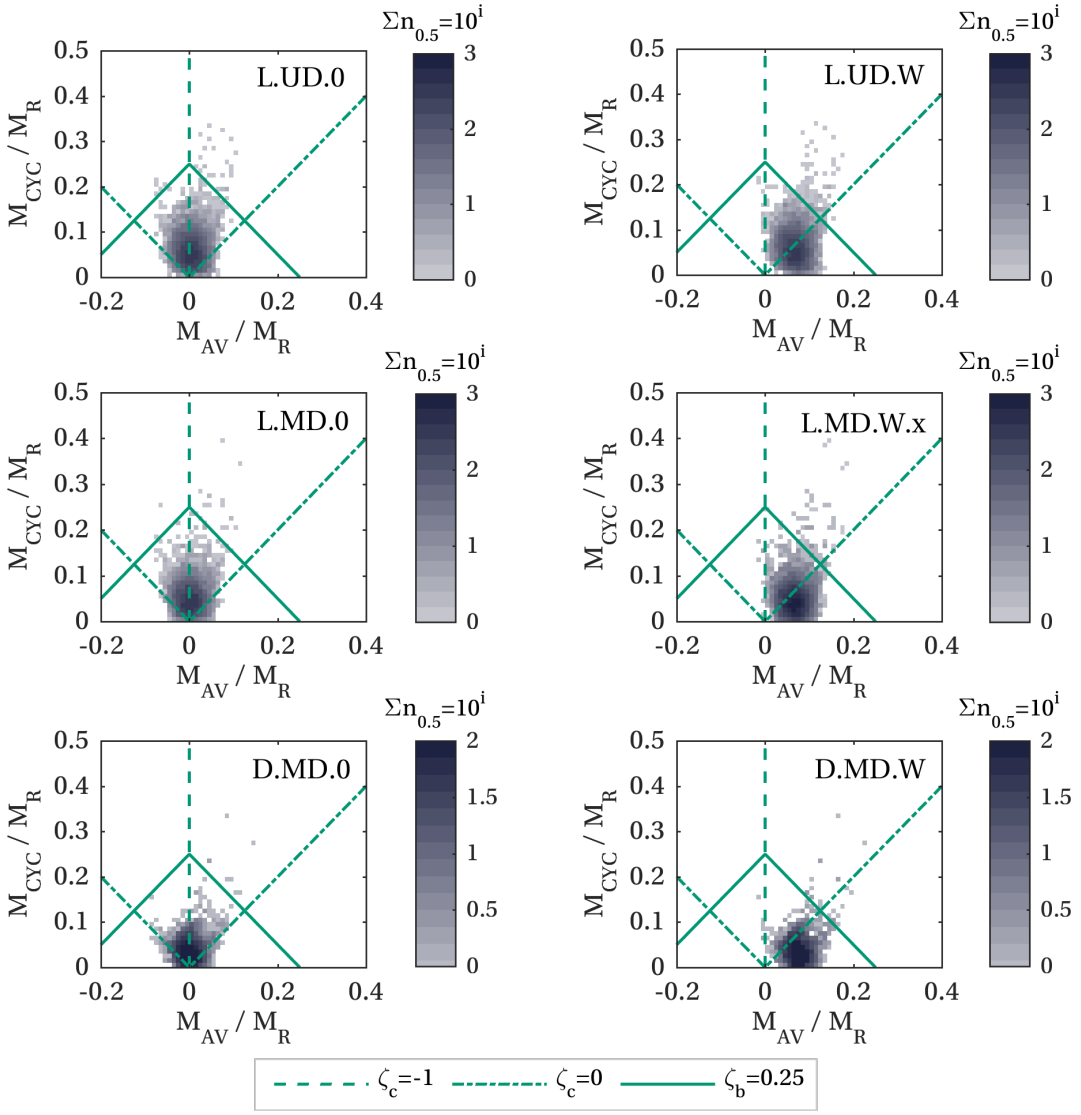

Figure 5.6: Distribution of applied M_{CYC}/M_R and M_{AV}/M_R in the x-direction for multi-amplitude storm loading tests (generated with software from T. D. Balaam)

gapping-type behaviour (inflexion in the moment-rotation responses around zero load) observed under large amplitude loading in dense sand (Figures 5.7c and 5.8c). Upon applying loads greater than those previously applied, the responses approximately follow the backbone curve. This behaviour is consistent with one of the two Masing rules extensions proposed by Pyke (1979) and with many of the reloading responses observed following regular 1-way cycling, as shown in Section 4.7.

The evolution of pile rotation with cycle number is presented in the right-most plots in Figures 5.7, 5.8 and 5.9. As described in Section 3.5.6, pile rotation per cycle may be defined for multi-amplitude loading on either the loading or unloading

half-cycles, at the half-cycle average load. The rotation per cycle on loading (θ_{na}) is used here, although the observed behaviour is not affected by the choice of either parameter. The rotation on loading θ_{na} responses are dominated by rotation accumulated during the large load events, in agreement with observations from Leblanc *et al.* (2010b) and Abadie *et al.* (2019b) under regular multi-amplitude cyclic loading. However, rotation also accumulates between the large load events. This behaviour is consistent with the ratcheting observations in Chapter 4: ratcheting occurs under biased cyclic loading at all explored amplitudes, but its magnitude and evolution is rather dependent on the loading characteristics.

Accumulated rotation ($\Delta\theta_n$) is not presented here, as the rotation during Cycle 0 depends on the (variable) amplitude of Cycle 0. It should also be noted that pile rotation is plotted on linear scales in this Chapter, in contrast to the logarithmic scales used in Chapters 4 and 6. The evolution of secant stiffness and energy loss factor are not presented for these tests, as any changes in these parameters with cyclic loading are conflated with the more significant impact of cyclic load amplitude on them, which varies from cycle to cycle. However, the application of consecutive storms does provide some insight into the evolution of secant stiffness and energy dissipation.

5.4.2 Impact of wind loading

Figure 5.7 specifically explores the impact of additional wind loading on the x-direction response. Wind load increases $\bar{M}$ and M_p but leaves M_{CYC} unchanged. As M_p increases, the peak rotations increase to an even greater degree, given the non-linearity of the backbone curve. The ratcheting rate between large load events also increases, given the increase in $\bar{M}$, and consistent with observations under regular cyclic loading. For the tests presented, pile rotation on loading at cycle N (θ_{Na}) increases by between 2.5 and 3.5 times with the addition of wind loading.

5.4.3 Impact of storm multidirectionality

Figure 5.8 highlights the impact of storm multidirectionality by presenting the response to multidirectional tests derived from MD sea states with spreading angle $22°$ alongside the response to corresponding unidirectional tests (indicated by .I). Slightly greater pile

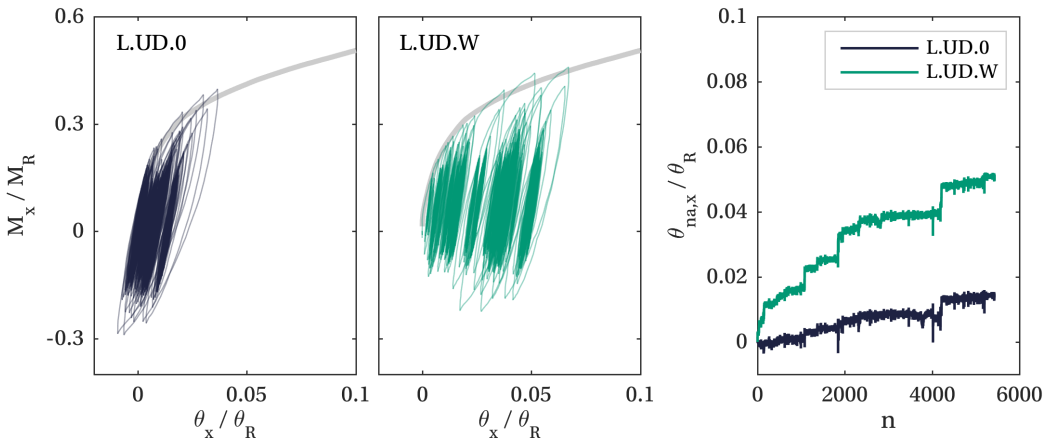

(a) UD sea state, very loose sand

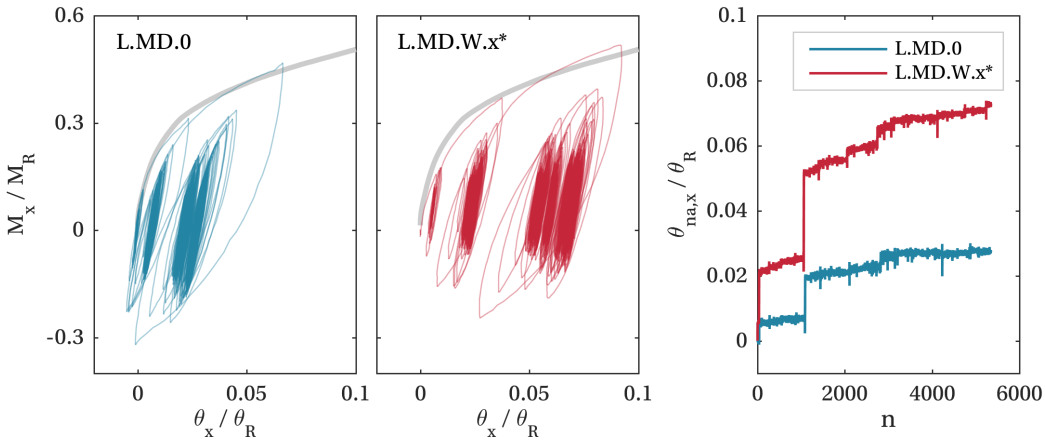

(b) MD sea state, very loose sand

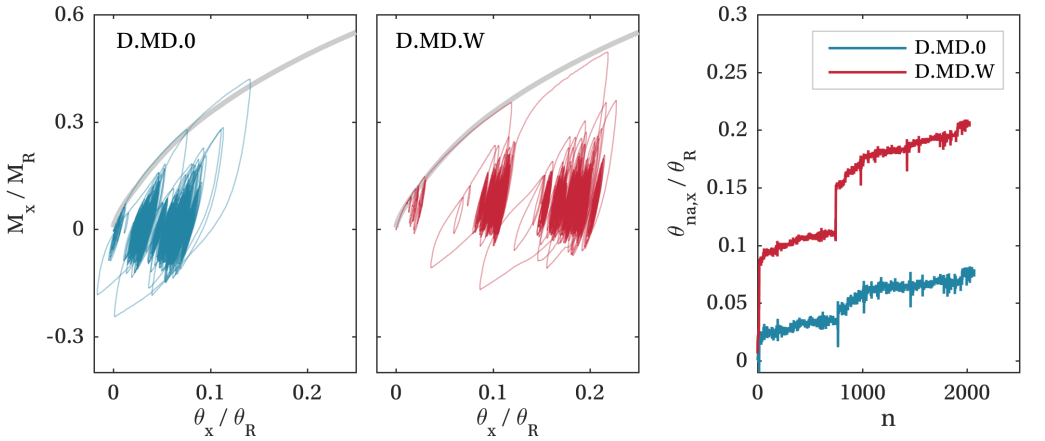

(c) MD sea state, dense sand

Figure 5.7: Impact of additional wind loading on the x-direction response (mean monotonic response shown in grey)
* First half of test L.MD.W.x presented

rotations are observed in the x-direction under multidirectional loading, compared to under corresponding unidirectional loading. However, the difference in pile rotation is small, particularly in the dense sand, and could be attributed to experimental variability. Minimal pile rotation is observed in the y-direction.

The observations made here are consistent with the results from regular fan-type loading tests (Section 4.6.2). The fan-type results suggest that for half internal spread angles $< 30°$ (where the vast majority of this multidirectional loading occurs) a small increase in ratcheting rate may be observed, with the ratio of multidirectional ratcheting exponent to unidirectional ratcheting exponent expected to be $1 < \alpha/\alpha_{UD} < 1.24$ (see Figure 4.34, Section 4.6.2).

5.4.4 Application of consecutive storms

Figure 5.9 presents the response to tests L.MD.W.x and L.MD.W.45, where two consecutive storms were applied. The second storm was either aligned (.x) or misaligned at $45°$ (.45) to the first. The small difference in response for $n < 5200$, where identical loading was applied, is attributed to experimental variability.

The black loops in the moment-rotation plot for test L.MD.W.x highlight the response during application of the same large amplitude cycle in each of the two storms ($n = 2050, 7250$). This cycle occurs after the peak cyclic load M_p and therefore allows the change in secant stiffness and energy loss factor to be explored without conflation with Masing behaviour. The loading secant stiffness k_{nl} increases by a factor of 1.23 (from $k_{nl}/k_{MAX} = 0.26$ to $k_{nl}/k_{MAX} = 0.31$), while the energy loss factor on loading η_{nl} decreases very slightly (from $\eta_{nl} = 0.52$ to $\eta_{nl} = 0.51$) over 5200 multi-amplitude cycles. The factor of increase in stiffness is less pronounced than across the same number of regular cycles (Section 4.4.2), which may be explained by the low average cyclic amplitude for these tests (mean $M_{CYC}/M_R = 0.046$) compared to the regular cyclic tests ($M_{CYC}/M_R \geq 0.2$ in very loose sand for 1-way loading). The minimal change in energy loss factor is consistent with observations under 1-way regular cyclic loading beyond $n = 100$.

The pile begins to rotate in the y-direction when the storm is applied at $45°$ to the axes during the second half of test L.MD.W.45. The y-direction hysteretic response

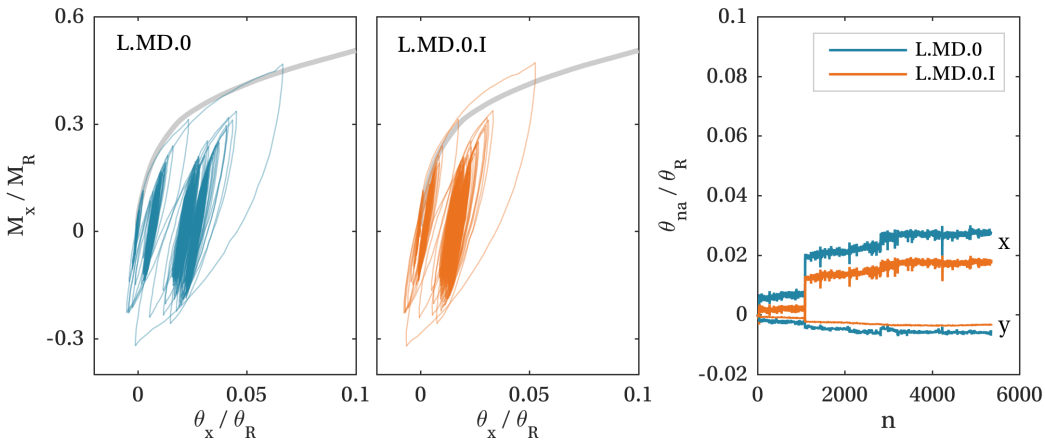

(a) Without wind load, very loose sand

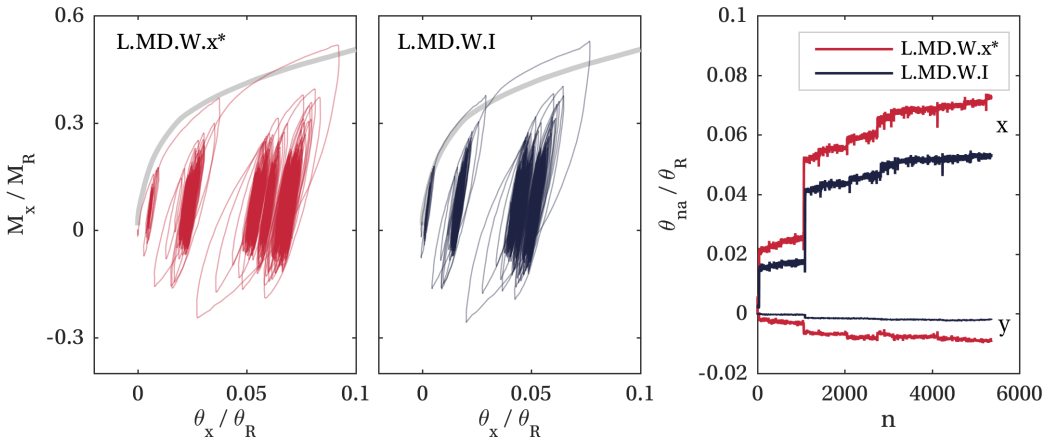

(b) With wind load, very loose sand

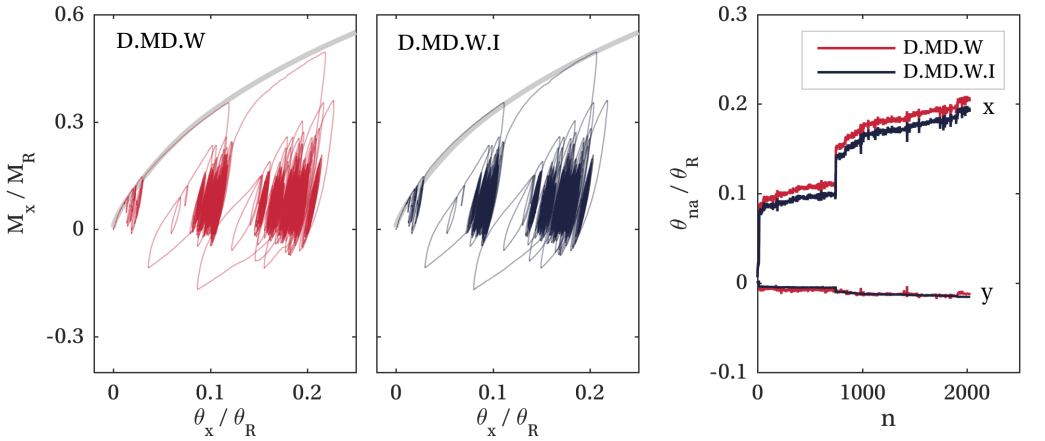

(c) With wind load, dense sand

Figure 5.8: Impact of multidirectionality on the response (mean monotonic response shown in grey)
* First half of test L.MD.W.x presented

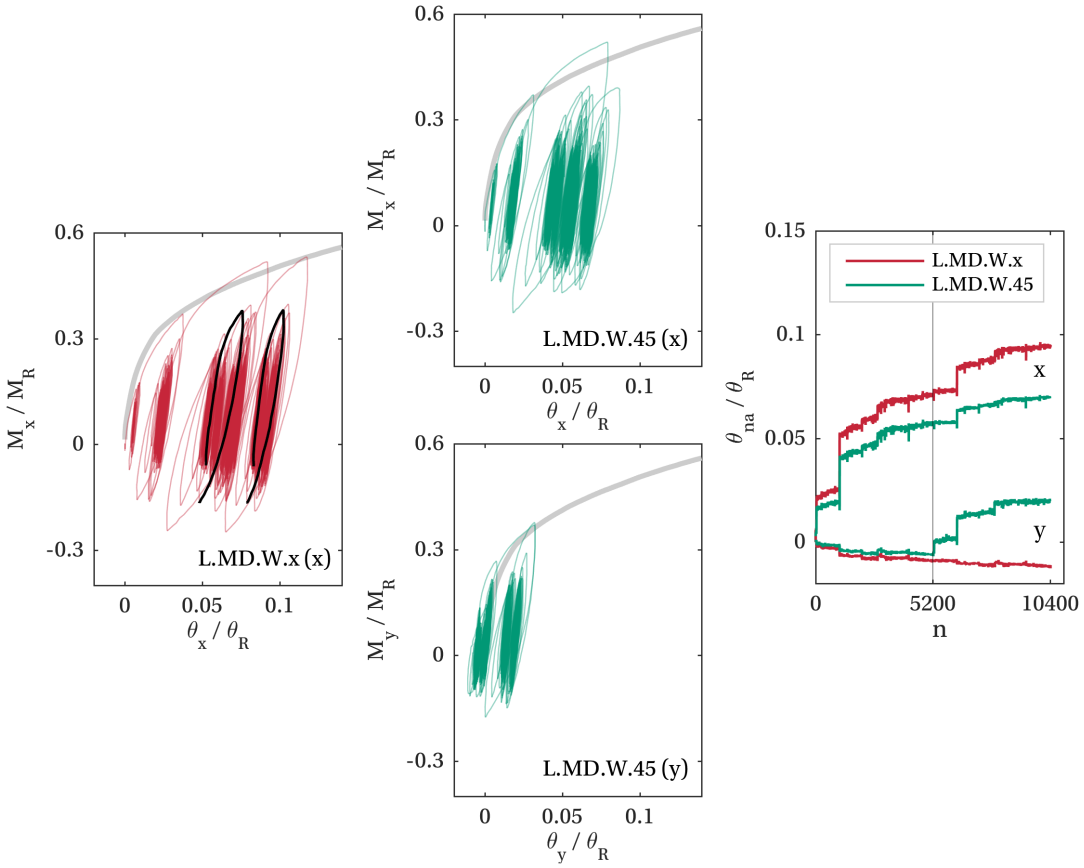

Figure 5.9: Response to consecutive MD storms in very loose sand aligned and misaligned at $45°$ to each other (mean monotonic response shown in grey)

follows the backbone curve on reloading, similarly to in the x-direction. The rotation accumulated in the y-direction exceeds that accumulated in the x-direction during the second half of the test, despite the loading in the x- and y-directions being very similar. The smaller rotation accumulated in the x-direction in the second half of test L.MD.W.45 may be explained by greater densification caused by previous cycling in this direction. Densification is expected to vary spatially with the loading direction, as also indicated by the ripples in the secant stiffness response under fan-type loading (Section 4.6.2).

The magnitude of pile rotation accumulated during the second storm is approximately 30% of the rotation accumulated during the first storm, in both the aligned and misaligned case.

5.5 Summary

The experimental results presented in this Chapter reveal the response of monopile foundations to realistic multi-amplitude and multidirectional storm loading in dry sand. The preliminary load processing also highlighted the importance of the structural dynamic response in determining the cyclic load amplitude and number of load cycles experienced by monopile foundations. The list below summarises the key experimental observations, which are valid for both very loose and dense sand unless stated otherwise:

- Upon applying loads greater than those previously applied, the response approximately follows the backbone curve.
- Pile rotation is dominated by large load events, although ratcheting is also observed during application of smaller-amplitude cyclic loading between the large load events.
- The addition of wind loading, and the associated increase in load bias, significantly increases the magnitude of pile rotation.
- Typical storm multidirectionality (spreading angle $22°$) does not have a significant impact on pile rotation in the dominant loading direction.
- Storm misalignment has no significant impact on the magnitude of pile rotation, for a misalignment angle of $45°$.
- There is evidence of an increase in equivalent secant stiffness under multi-amplitude loading (in very loose sand).

In general, the response to multi-amplitude and multidirectional storm loading is consistent with many of the observations for regular cyclic loading in Chapter 4: ratcheting occurs under biased loading and increases with load bias and load amplitude, and secant stiffness increases under general cyclic loading. The effects of multidirectionality are small or negligible for the realistic spreading angle and storm misalignment angle explored here. Importantly, the tendency for the backbone curve to be followed when applying loads greater than those previously applied suggests that

the maximum rotation during a short storm may be approximated by the monotonic response. As well as providing novel insight into the response of monopiles to realistic cyclic loading, these results constitute a valuable set of validation data for use in model development.

Chapter 6

Investigating the effect of stress-level

6.1 Introduction

As it is not practical to test monopiles at full-scale, given their large size (*e.g.* $D = 8$ m, Sørensen *et al.*, 2017), the response may be explored through physical modelling at reduced-scale. Various physical modelling approaches exist:

1. Laboratory-scale testing at $1g$, as employed in Chapters 3, 4 and 5, and in many previous similar studies (see Section 1.3.1);

2. Laboratory-scale testing at elevated stress-level using a centrifuge, as conducted by *e.g.* Klinkvort and Hededal (2013);

3. Medium- to large-scale testing in natural deposits in field conditions, as performed as part of the PISA project (Byrne *et al.*, 2015) and by *e.g.* Cox *et al.* (1974) for the development of conventional *p-y* curves.

Laboratory-scale testing at $1g$ allows the development of complex systems and requires less resource than the other two physical modelling approaches, facilitating more extensive and longer-term testing. However, full-scale stress-levels cannot be simulated with $1g$ laboratory testing, and it is difficult to simulate natural soil deposits. Centrifuge testing involves subjecting a geotechnical model to accelerations n times Earth's gravity (ng) to simulate effective unit weights and therefore stress-levels n times larger than would be experienced on the laboratory floor. With the geotechnical model spun in a centrifuge at angular velocity ω, the acceleration experienced at effective radius R_e is

$ng = R_e\omega^2$. Centrifuge testing allows full-scale stress-levels to be simulated, but the high acceleration levels and space restrictions can constrain the model geometry and complexity, compared to $1g$ testing (Byrne, 2014). Medium- and large-scale field testing allows exploration of the response in natural deposits, and approximates the ratio of foundation to soil grain size better than in $1g$ or centrifuge laboratory-scale testing. However, field testing is costly and logistically challenging.

In practice, a combination of these modelling approaches might be used to most efficiently explore the response of monopile foundations, but stress-level varies significantly between them, with only centrifuge testing able to simulate full-scale stresses. Understanding the impact of stress-level on the response of monopile foundations is therefore an important step to i) inform comparison of observations at $1g$, in the centrifuge and at medium to large-scale in the field, and ii) establish the relevance of physical modelling at low stress-levels.

The fundamental behaviour of sand depends on the stress-level. For example, dilatancy and peak friction angle ϕ'_p increase approximately logarithmically with reducing stress-level (at least at relatively high stress-levels (Bolton, 1987)), while the maximum shear modulus G_{MAX} increases as a power function of stress-level, with the exponent typically 0.5 (Hardin, 1965; Oztoprak and Bolton, 2013). This fundamental stress-level dependent behaviour is reflected in the global foundation response, as observed by *e.g.* Ovesen (1975) for footings, Kelly *et al.* (2006) for caissons, and Klinkvort (2012) for monotonically laterally loaded monopiles.

Very few studies have explored the impact of stress-level on the response of monopiles to cyclic lateral loading. Rudolph *et al.* (2014b) and Rudolph and Grabe (2013) report a decrease in accumulated displacement for centrifuge tests compared to $1g$ tests, while Nicolai *et al.* (2017b) compare post-cyclic behaviour between $1g$ and centrifuge tests. However, the set-up and sand type varied between $1g$ and centrifuge tests in these studies, and so stress-level effects were not completely isolated.

To specifically explore issues relating to stress-level, this Chapter presents a series of monotonic, unidirectional cyclic and multidirectional cyclic tests, performed at three different stress-levels using the 5 m radius beam centrifuge at UWA (Figure 6.1). By

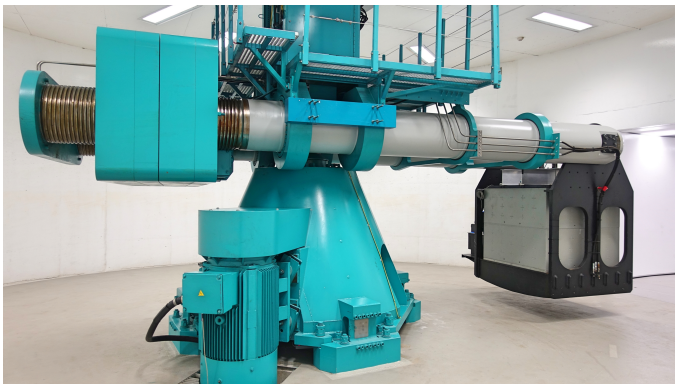

Figure 6.1: 5 m radius beam centrifuge at UWA

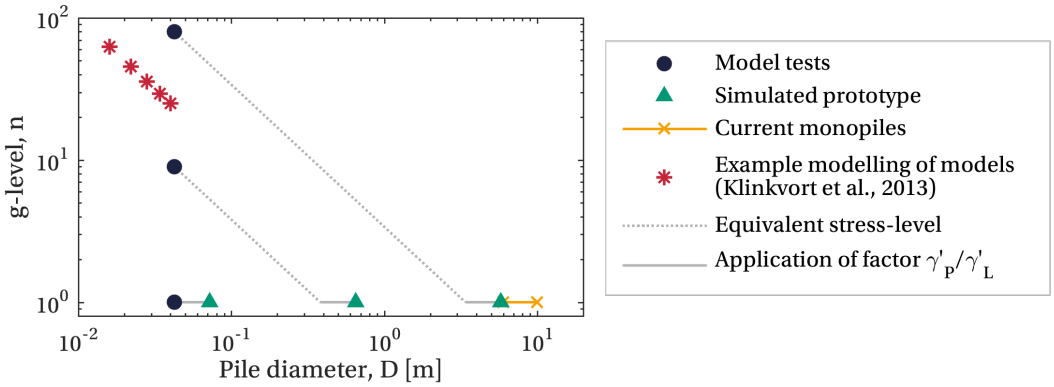

Figure 6.2: Location of model tests at ng, simulated prototypes at $1g$ and current full-scale monopiles

varying the centrifuge velocity ω, and therefore g-level, stress-level can be controlled; and with an identical set-up at each g-level, stress-level effects can be isolated.

g-levels of $1g$, $9g$ and $80g$ were chosen, corresponding to normalised reference stress-levels (defined as the vertical effective stress at 70% pile embedment, $\sigma'_{REF}/p_a = 0.7L\gamma'/p_a$) of 0.02, 0.18 and 1.60 for a 42 mm diameter pile with $L/D = 4$, in dense, dry sand ($\gamma'_L = 17$ kN/m^3). These tests simulate monopiles with diameters between 71 mm and 5.7 m in dense, saturated sand ($\gamma'_P = 10$ kN/m^3), as shown in Figure 6.2. Although real monopiles are typically even larger, this range of stress levels is deemed sufficiently large to observe relevant stress-level effects. The logarithmic variation of g-level was chosen to be in-line with the expected logarithmic variation of dilatancy and friction angle with stress-level.

So-called *modelling of models* test campaigns are more common than investigations

External diameter	D	42	mm
Target embedded length	L	170	mm
Aspect ratio	η	4	-
Wall thickness	t	3.2	mm
Loading eccentricity	h	424	mm
Dimensionless loading eccentricity	$\tilde{e}$	2.5	-
Material		Mild steel	
Young's modulus	E	200	GPa
Mass	m	1.69	kg

Table 6.1: Model pile properties

into stress-level effects (*e.g.* Ovesen, 1975; Dewoolkar *et al.*, 1999; Klinkvort *et al.*, 2013), and typically involve tests at different g-levels and model sizes which all simulate the same stress-level and prototype. Modelling of models tests lie along diagonal lines in Figure 6.2, as illustrated with the example tests of Klinkvort *et al.* (2013). Modelling of models campaigns can help identify scale effects specific to centrifuge testing (*e.g.* grain-size effects) and provide verification of centrifuge modelling techniques, but do not provide independent information on stress-level effects.

6.2 Experimental set-up

6.2.1 Model pile, loading and instrumentation

Tests were performed on sandblasted mild steel piles with properties summarised in Table 6.1. The L/D ratio, h/L ratio and smooth surface ($R_n = R_a/d_{50} \approx 0.016$, measured using a stylus profilometer) are consistent with the pile used for $1g$ testing at OU. The pile has a closed-end (appropriate given the wished in place installation method) and is assumed to behave rigidly.

Figure 6.3 shows the loading and instrumentation apparatus, which is modified from that designed by Herduin (2019) for multidirectional loading of anchors for wave energy devices. Actuators sit perpendicular to platform A and apply load to the pile via cables which travel around pulleys on platform C and attach to 1 kN capacity inline load cells at the base of the pile stick-up. Pile displacements are measured with six string potentiometers. Three are positioned on platform B (253 mm above the load application point) and three are positioned on platform C (30 mm above the load application point).

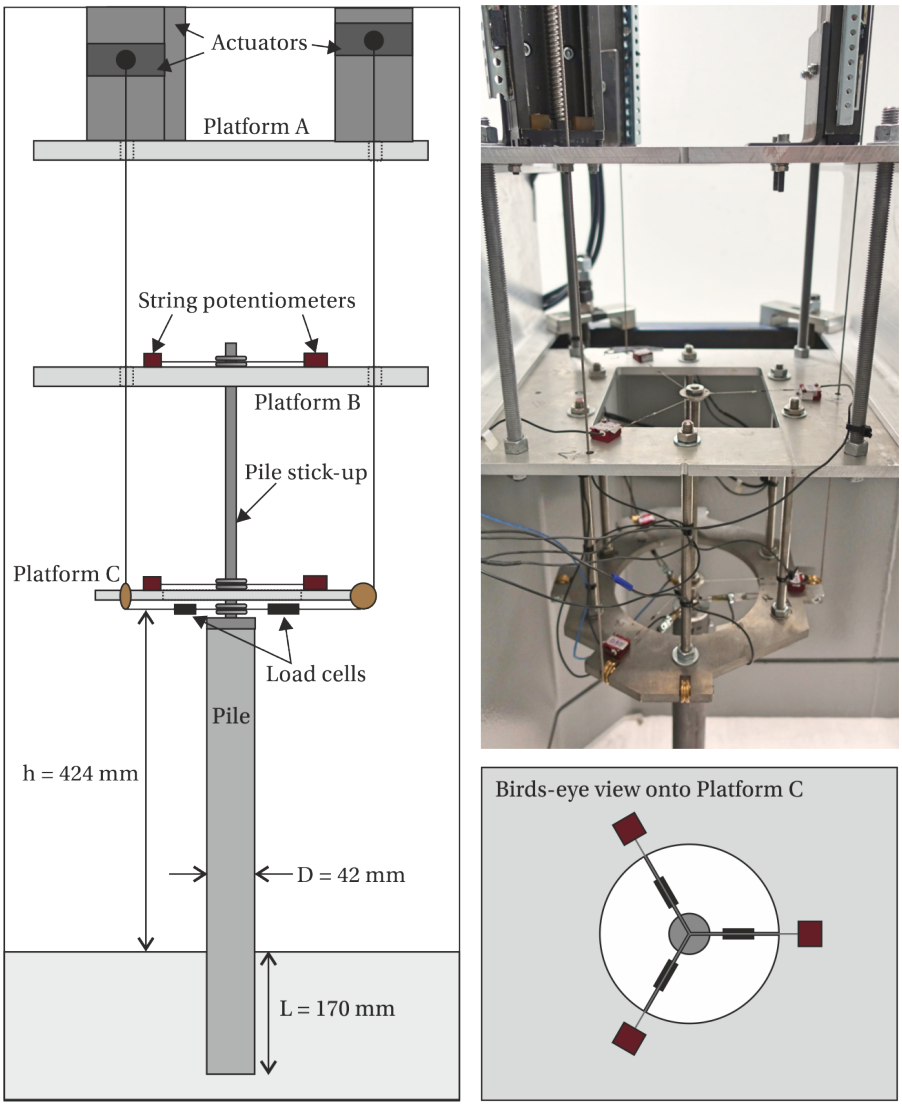

Figure 6.3: Schematic and photograph of loading and instrumentation apparatus

Each triplet of string potentiometers is arranged in a $120°$ star to minimise the net load applied to the pile by these sensors, as each applies a tensile load of around 1 N.

The pile stick-up allows straightforward connection of the string potentiometers and load lines to the pile. The stick-up comprises an insert, which is fixed inside the pile head with two bolts and two grub screws, and a threaded rod to which the potentiometers and load lines are attached.

The set-up shown in Figure 6.3 is for multidirectional loading, with three actuators and associated load lines positioned $120°$ apart. For unidirectional loading two actuators are used, positioned $180°$ apart, to simplify the set-up.

Specific gravity	G_s	2.67	-
Particle size	d_{10}, d_{50}, d_{60}	$0.12, 0.18, 0.19$	mm
Minimum effective unit weight	γ'_{MIN}	14.69	kN/m^3
Maximum effective unit weight	γ'_{MAX}	17.40	kN/m^3
Maximum void ratio	e_{MAX}	0.78	-
Minimum void ratio	e_{MIN}	0.51	-
Critical friction angle	ϕ'_c	31.9	°

Table 6.2: UWA SF sand properties (Chow *et al.*, 2018)

6.2.2 Sample preparation

UWA superfine (SF) silica sand was used for these tests, with properties summarised in Table 6.2. Soil samples were prepared by air pluviation using an automatic sand raining device into a square strongbox with base 996×996 mm and height 500 mm. Three dense samples were prepared to an average unit weight $\gamma'_{AV} = 17.00 \pm 0.20$ kN/m^3 ($D_{R,AV} = 87.4 \pm 5\%$). The samples were prepared dry to simulate a fully-drained response. Figures 6.4 and 6.5 show the sand raining procedure and prepared sample. To avoid the introduction of complex stress-fields and local density changes through in-flight (or $1g$) installation, the piles were *wished-in-place* during the sand raining process. Sand was first rained to the depth of the pile tip, before hanging the piles in position and raining further sand around them. The sand surface was then vacuumed to achieve an average installed pile embedment $L_{AV} = 167 \pm 3$ mm ($L/D \approx 4$). Nine piles were installed per strongbox, with a minimum centre-to-centre spacing of $7.4D$.

Cone penetration tests (CPTs) were performed using a 7 mm diameter $60°$ cone to characterise each soil sample. For sample S1, used for $1g$ testing, two CPTs were performed at each stage: a) pre-testing and b) post-testing. For samples S2 and S3, used for testing at $9g$ and $80g$ respectively, one CPT was performed at each stage: a) at $1g$ pre-spinning, b) at ng pre-testing, c) at ng post-testing, and d) at $1g$ post-spinning. Figure 6.6 presents the CPT cone resistance q_c profiles measured at each g-level. At $1g$, the S1 CPTs and the pre-spinning S2 and S3 CPTs show good consistency, in-line with the small variation in global unit weight measured across the samples. The consistency of the pre- and post-testing S2 and S3 CPTs also gives confidence in

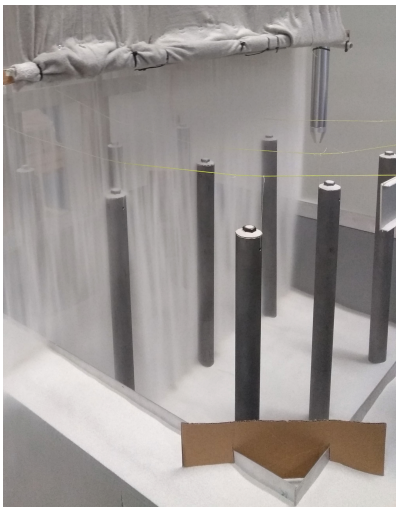

Figure 6.4: Sample preparation with sand raining device

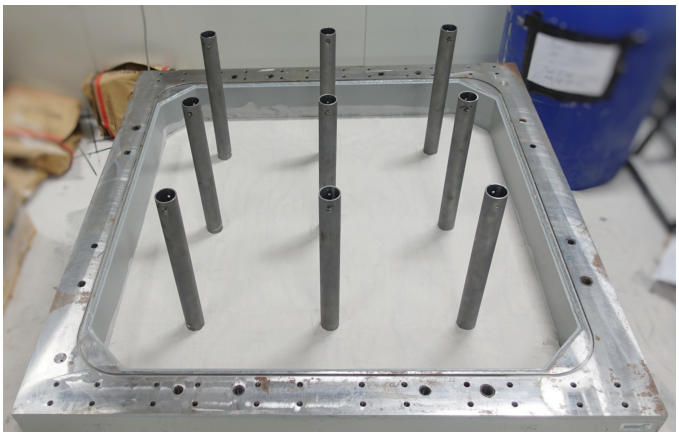

Figure 6.5: Prepared sample with nine piles wished in place

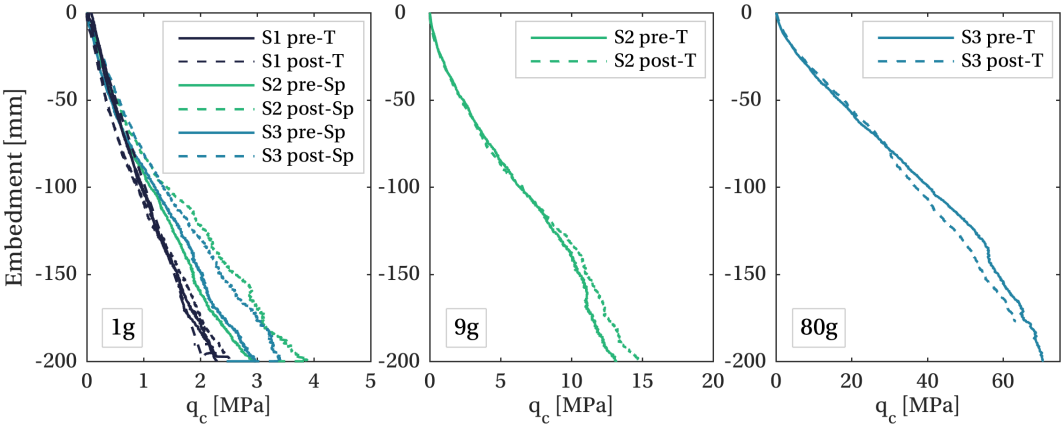

Figure 6.6: CPT profiles in SF sand ($D_{R,AV} = 87.4\%$, note different q_c scales, T=testing, Sp=spinning)

the homogeneity of the sample and insensitivity to repeated centrifuge spin cycles (the centrifuge was spun down after each test).

The $1g$ post-spinning S2 and S3 CPTs show increased CPT resistance, although bulk mass and volume measurements imply a minimal increase in density post-spinning (a 0.45% and 0.57% increase in γ' following $9g$ and $80g$ testing respectively). This result is therefore attributable to overconsolidation effects, also observed by *e.g.* Gui *et al.* (1998) and Roy *et al.* (2019). However, no monopile tests were performed on these overconsolidated samples.

6.2.3 Test procedure

$9g$ and $80g$ tests were performed in the 5 m radius, $240g$-tonne capacity beam centrifuge at UWA (Gaudin *et al.*, 2018), while the $1g$ tests were conducted with the same set-up on the laboratory floor. For the centrifuge tests the effective radius R_e, at which the nominal g-level is achieved, was chosen to be at $1/3$ pile embedment ($R_e \approx 4.66$ m). Given the size of the centrifuge relative to the model, the variation of acceleration in the radial direction and associated stress error is negligible (Schofield, 1980).

Monotonic tests were performed under displacement control with a single load line, whereas cyclic tests were performed under load control with sinusoidal waveforms, using either two or three load lines. Actuator control and data-acquisition was performed using UWA's in-house software (PACS and DigiDac).

To ensure accurate load control with the (flexible) load lines, the lines were kept in tension during cyclic testing, with one or two load lines holding constant load. Appropriate choice of load demands for each line allows application of cyclic loading, including symmetric 2-way and multidirectional cyclic loading. Before application of cyclic loading, loads in the lines were increased simultaneously to an appropriate pre-tension. Data was not re-zeroed following this procedure, as negligible net load was applied to the pile and negligible pile movement was recorded.

To ensure accurate load control, a cyclic frequency of $0.15 - 0.20$ Hz was used for the $9g$ and $80g$ tests. To achieve accurate load control at $1g$, where the load cells were significantly over-sized, the cyclic frequency was reduced (to $0.01 - 0.05$ Hz). The pile response is not expected to be rate dependent, given the tests were performed in dry sand (see also Section 3.4).

6.2.4 Resolution of pile displacement and applied loads

Time limitations did not allow development of software to perform kinematics calculations (resolution of pile pose and load line angles) on-line, as described for the OU apparatus in Section 2.4. Instead, the pile displacement and applied loads were resolved during post-processing. The actual applied loads therefore differ slightly from

the nominal load demands under multidirectional loading, where the load line angles change as the pile moves. This is discussed further in Section 6.6.

To resolve pile position, vertical displacements were neglected and the planar position of the pile at the level of each triplet of string potentiometers was calculated. Under unidirectional loading, pile displacement was obtained directly from the string potentiometer aligned with the loading direction and net loads were obtained directly from the load measurements aligned with loading. Under multidirectional loading, measurements from all three potentiometers were used to calculate pile displacement, and to account for measurement redundancy the error between actual and measured length was assumed to be equal for all three string potentiometers. The net loads were then resolved, accounting for the instantaneous pile position and load line angle.

6.3 Test programme

Tables 6.3 and 6.4 summarise the tests completed as part of this investigation into stress-level effects. The test programme was informed by testing conducted at $1g$ at OU. Monotonic tests provide a baseline for interpretation of cyclic tests; unidirectional, symmetric 2-way cyclic tests explore the hysteretic response; unidirectional 1-way cyclic tests explore ratcheting, stiffening and evolution of dissipation at various load amplitudes; and multidirectional, perpendicular cyclic tests explore the impact of cyclic loading direction, following the T- and L-shaped loading described in Section 4.6.1. The cyclic tests were conducted at values of ζ_b comparable to those used at OU, with the minimum cyclic amplitude dictated by the accuracy of the control system at $1g$.

The results presented in Chapter 4 show how key cyclic behaviour is observable within 1000 cycles. As such, tests were conducted to 1000 cycles here, except where load application issues occurred. The post-cyclic response was also explored with reloading to $0.8H_R$ following many unidirectional cyclic tests. Figure 6.7 shows the sequence of testing within each sample; the loading directions are also indicated.

Results are presented in terms of both g-level n and normalised reference stress-level σ'_{REF}/p_a. Table 6.5 expedites translation between these two measures of stress-level, and presents the (prototype) monopile diameter D_P simulated at each g-level.

Test name	g-level	ζ_b	ζ_c	No. of cycles N	Reload
Monotonic tests					
1G.M.1	$1g$	-	-	-	-
9G.M.1	$9g$	-	-	-	-
9G.M.2	$9g$	-	-	-	-
80G.M.1	$80g$	-	-	-	-
Symmetric 2-way cyclic tests					
1G.TW.04	$1g$	0.4	-1	500	No
9G.TW.04	$9g$	0.4	-1	1000	Yes
80G.TW.04	$80g$	0.4	-1	1000	Partial
1-way cyclic tests					
1G.OW.02	$1g$	0.2	0	1000	Yes
1G.OW.03	$1g$	0.3	0	770	Yes
1G.OW.04	$1g$	0.4	0	1000	Yes
9G.OW.02	$9g$	0.2	0	1000	Yes
9G.OW.03	$9g$	0.3	0	1000	Yes
9G.OW.04	$9g$	0.4	0	1000	Yes
80G.OW.02	$80g$	0.2	0	1000	Yes
80G.OW.04	$80g$	0.4	0	1000	Yes

Table 6.3: Unidirectional test programme investigating stress-level effects

Test name	g-level	Loading direction	ζ_b		ζ_c		No. of cycles N
			Nominal	Applied	Nominal	Applied	
1G.T.02	$1g$	x y	0.35 0.2	0.37–0.39 0.19–0.22	1 -1	0.80–1.05 -(1.20–0.80)	250
1G.L.04	$1g$	x y	0.35 0.4	0.36–0.39 0.37–0.38	1 0	0.98–1.08 -(0.07–0.00)	153
9G.T.02	$9g$	x y	0.2 0.2	0.20–0.23 0.19–0.20	1 -1	0.95–0.99 -(1.03–0.99)	1000
9G.L.04	$9g$	x y	0.2 0.4	0.21–0.24 0.38–0.39	1 0	0.93–0.97 -(0.06–0.00)	1000
80G.T.02	$80g$	x y	0.2 0.2	0.20–0.22 0.20–0.20	1 -1	0.95–1.00 -(1.00–0.95)	1000
80G.L.04	$80g$	x y	0.2 0.4	0.20–0.22 0.39–0.39	1 0	0.95–1.00 -(0.02–0.00)	1000

Table 6.4: Multidirectional test programme investigating stress-level effects

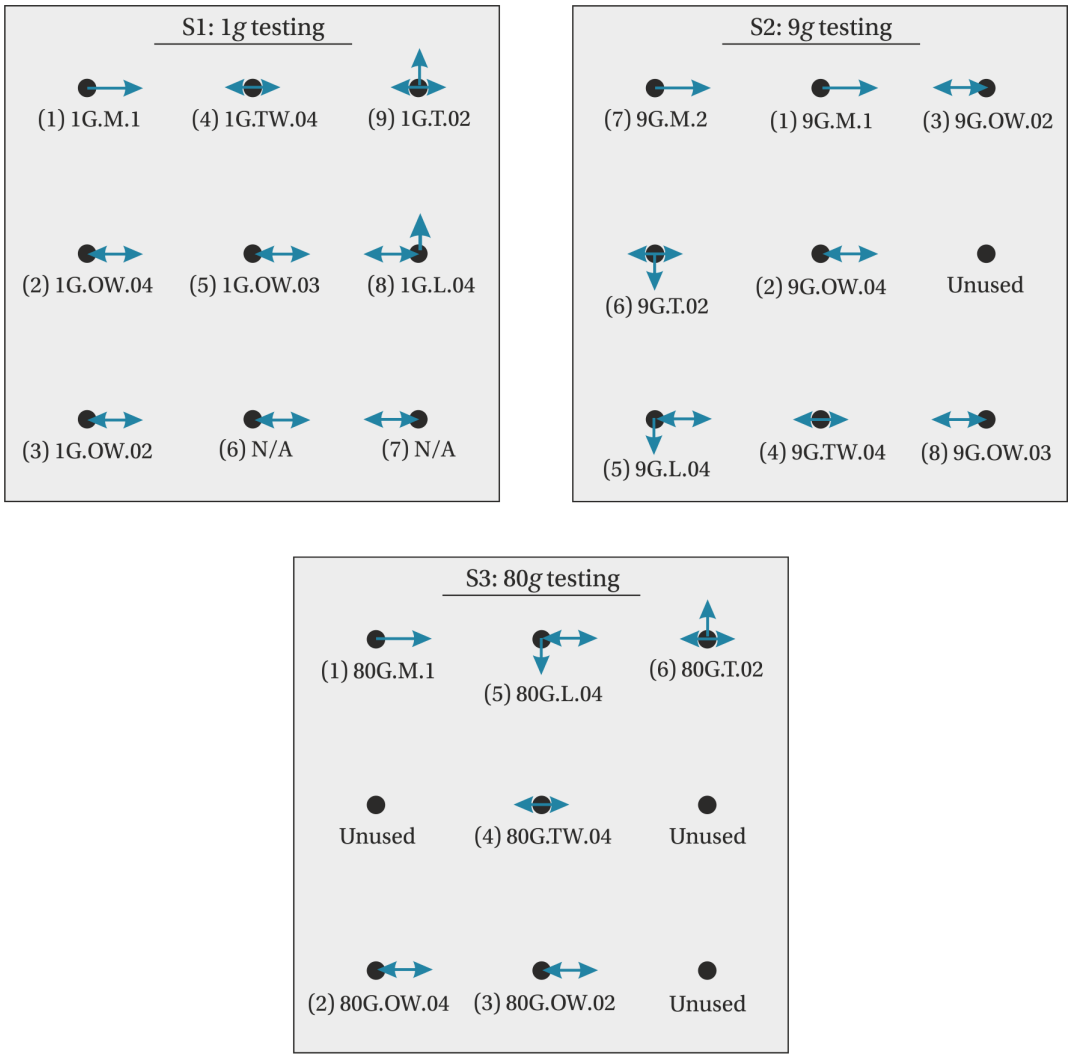

Figure 6.7: Sequence of testing within each sample, with arrows indicating loading direction

g-level, n	1	9	80
σ'_{REF}/p_a	0.02	0.18	1.60
D_P [m]	0.071	0.64	5.7

Table 6.5: Corresponding g-levels, normalised stress levels and simulated prototype monopile diameters

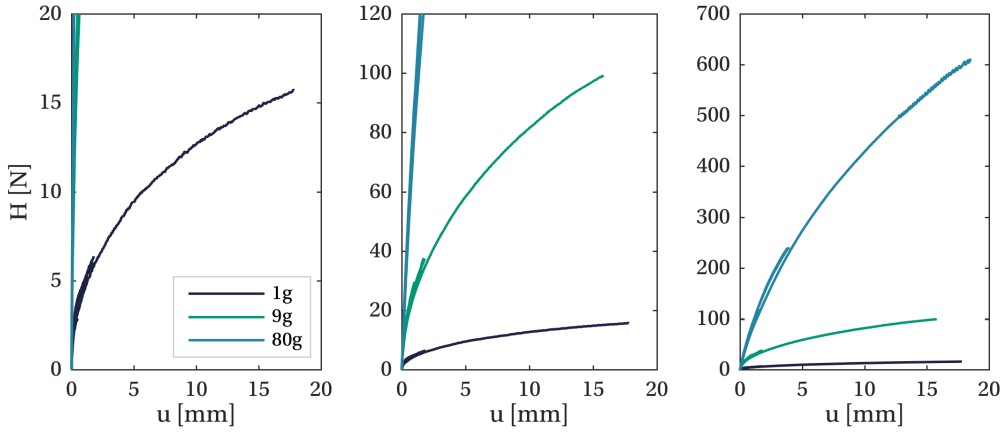

Figure 6.8: Monotonic responses (data presented on three different H-axes for clarity)

6.4 Monotonic response

Figure 6.8 presents the response for the monotonic tests alongside the responses for the initial loading portion of the unidirectional cyclic tests. At $9g$, where two monotonic tests were performed, the average monotonic response is presented. Figure 6.8 highlights the significant variation in load amplitude with stress-level, as well as consistency of behaviour at each stress-level.

Data is presented in terms of applied horizontal load H and pile displacement at the load application point u (both at model-scale). The imperfectly rigid connection between the pile and pile stick-up introduced error into the resolved pile rotation and prevents presentation of the response in terms of applied moment M and pile rotation θ, as used in previous Chapters. However, conclusions on stress-level effects are not expected to be affected by the choice of either work-conjugate pair.

6.4.1 Normalisation approaches

Casting the monotonic response in a dimensionless form facilitates comparison between tests and helps provide insight into stress-level effects. Three different normalisation approaches are considered: i) Klinkvort *et al.* (2013), ii) Klinkvort (2012), and iii) Leblanc *et al.* (2010a), as summarised in Table 6.6. The approach of Leblanc *et al.* (2010a) was also presented in Table 3.4, Section 3.4.3.

	i) Klinkvort *et al.* (2013)	ii) Klinkvort (2012)	iii) Leblanc *et al.* (2010a)
Load normalisation	$\frac{H}{D^3\gamma'}$	$\frac{H}{K_p D^3\gamma'}$	$\frac{H}{L^2 D\gamma'}$
Displacement normalisation	$\frac{u}{D}$	$\frac{u}{D}$	$\frac{u}{D}\left(\frac{p_a}{L\gamma'}\right)^{\eta-1}$ $(\eta = 0.5)$

Table 6.6: Comparison of normalisation approaches

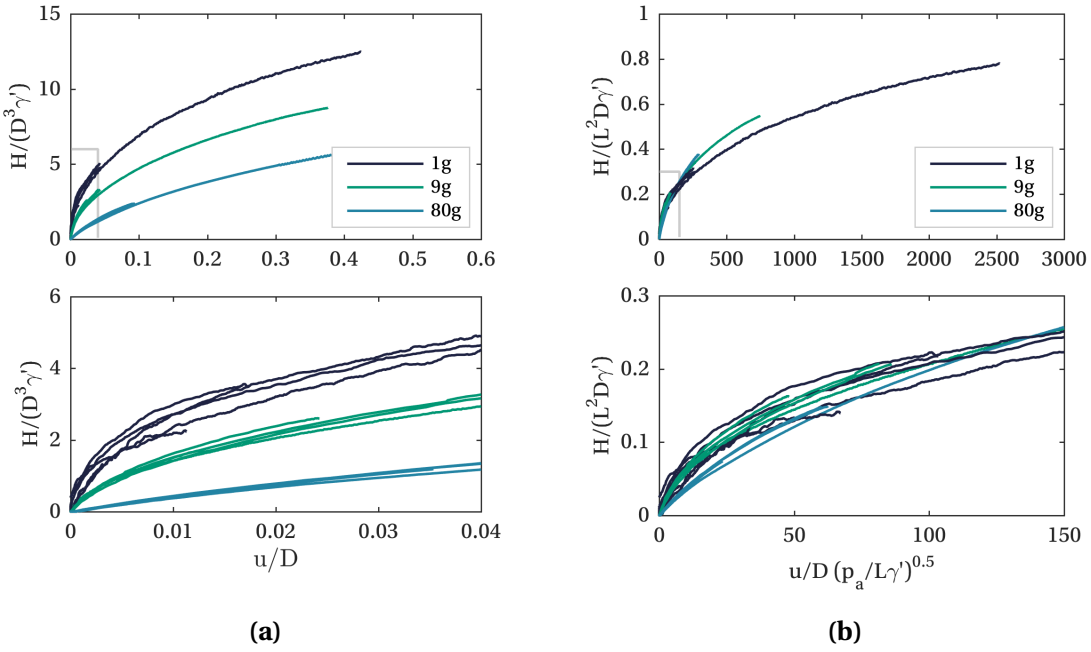

Figure 6.9: Normalisation of monotonic responses; (a) following (i) Klinkvort *et al.* (2013), (b) following (iii) Leblanc *et al.* (2010a) (lower plots show low amplitude region highlighted by grey box in upper plots)

Figure 6.9a shows the result of applying normalisation (i), which accounts for variation of γ', to the monotonic responses. This normalisation does not collapse the responses to one curve, but rather highlights stress-level effects: the decrease in normalised initial stiffness and inferred normalised capacity with increasing stress-level are indicative of stress-dependent stiffness and dilatant behaviour.

While exploring stress-level effects Klinkvort (2012) proposed a normalisation method (ii) which introduces Rankine's passive earth pressure coefficient K_p to account for stress-dependent dilatancy. Klinkvort (2012) used this normalisation to successfully collapse the response of a model monopile at stress-levels from around

70 kPa to around 350 kPa, with ϕ'_p values obtained from complementary triaxial testing.

Complementary triaxial tests are not available for this study, and moreover, obtaining definitive ϕ'_p values at stress-levels corresponding to the $1g$ tests is likely to be very challenging. There are a few approaches for estimating ϕ'_p at low stress-levels (as discussed in Section 3.2.3), although recent work by White (2020) supports the use of relationships proposed by Bolton (1987). If the framework of Bolton (1987) is employed to estimate ϕ'_p for normalisation (ii), then K_p changes negligibly and the plot resembles that in Figure 6.9a.

In contrast to the approach of Klinkvort (2012), Leblanc *et al.* (2010a) incorporate stress-dependent stiffness into normalisation (iii), but do not consider dilatancy (see Section 3.4.3). Figure 6.9b shows the result of normalising with approach (iii). The normalisation does a good job of collapsing the results to a single curve, particularly at small displacements, where the cyclic tests are conducted.

The normalisation proposed by Klinkvort *et al.* (2013) indicates the presence of stress-level dependent stiffness and dilatant behaviour. However, it is not possible to decouple these phenomena and draw stronger conclusions, particularly without measured ϕ'_p values at the stress-levels of interest. However, the normalisation approach of Leblanc *et al.* (2010a), which does not account for stress-dependent dilatancy, collapses the monotonic responses well, building confidence in the use of this normalisation framework for translation between scales.

6.4.2 Maximum stiffness

The monopile's maximum stiffness k_{MAX} is expected to vary with stress-level in the same way as the soil's maximum shear modulus G_{MAX} does; indeed, this assumption is incorporated into the normalisation approach presented by Leblanc *et al.* (2010a).

As discussed in Section 3.4.2, k_{MAX} can be obtained from the initial loading or first unloading response. There is more variability in the initial loading response for these tests than for the $1g$ tests at OU, probably due to more significant bedding-in effects given the wished-in-place installation method. Therefore, only the stiffness on first unloading are used to estimate the maximum stiffness of the monopile k_{MAX}.

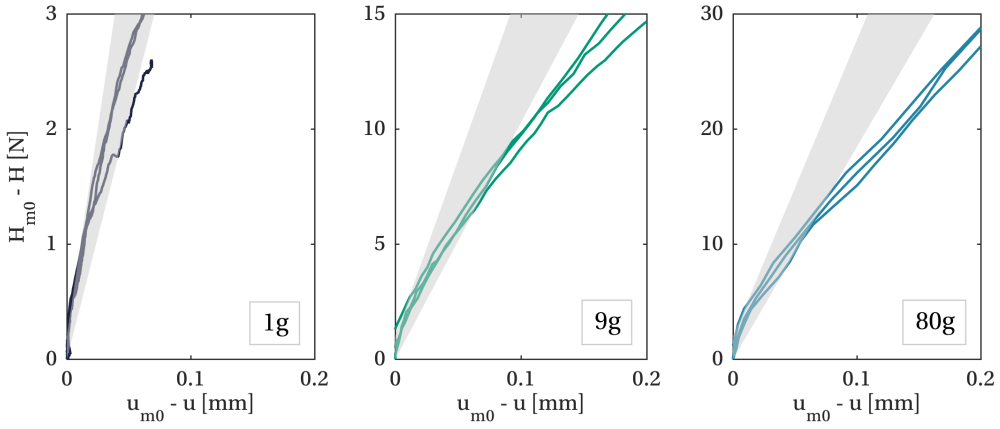

Figure 6.10: Initial portion of first unloading responses showing upper and lower estimates for maximum stiffness k_{MAX} with grey shaded region (note different $H_{m0} - H$ scales)

Figure 6.10 presents the first unloading portion for all relevant tests, with the response re-zeroed from the point of maximum load on the 0^{th} cycle (subscript $m0$). Upper and lower estimates of k_{MAX} are obtained by manual fitting to the initial loading portion ($u_{m0} - u < 0.05$ mm), and the maximum stiffness bounds are indicated by the grey shaded regions in Figure 6.10.

Figure 6.11 presents the variation of k_{MAX} with stress-level, with the range and mean values of k_{MAX} indicated. An exponential function fits the data well, as shown by the dashed line in Figure 6.11. However, the exponent obtained from least-squares fitting is $\eta = 0.31$, somewhat lower than $\eta = 0.5$ implicit in the Leblanc *et al.* (2010a) normalisation and also obtained for UWA SF sand from triaxial testing (Chow *et al.*, 2018). This discrepancy may be explained by experimental variability, the impact of stiffening during the initial loading portion, or three-dimensional effects when considering the monopile system. Interestingly, however, using $\eta = 0.31$ in place of $\eta = 0.5$ in the normalisation approach of Leblanc *et al.* (2010a) generates a poorer result.

6.5 Unidirectional cyclic response

6.5.1 Load-displacement response

Figure 6.12 presents the load-displacement ($H-u$) responses for the unidirectional tests summarised in Table 6.3, alongside the corresponding monotonic responses (nG.M). The full response is shown for the 1-way tests, while only the first five cycles of the 2-way

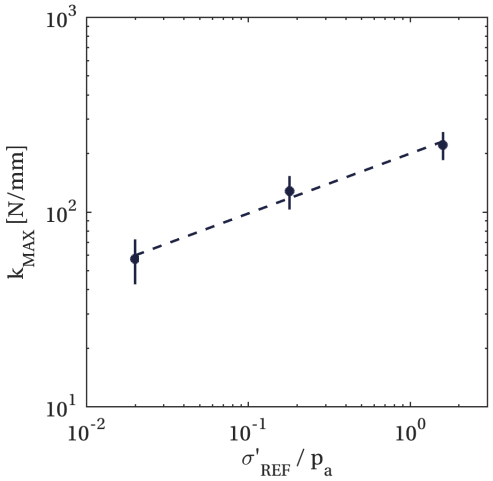

Figure 6.11: Variation of maximum stiffness k_{MAX} with stress-level

	Reference displacement u_R [mm]	Reference horizontal load H_R [N]	Mean max. stiffness k_{MAX} [N/mm]
$1g$	17.8	15.7	57.3
$9g$	17.8	99.5	127.8
$80g$	17.8	597	220.8

Table 6.7: Reference values for monopile response

tests are shown, to highlight the shape of the hysteretic response. The results show good repeatability at each stress-level and qualitatively similar behaviour across the three stress-levels. The responses are normalised by load and displacement reference values (H_R, u_R) as summarised in Table 6.7, where u_R was chosen to approximately correspond to $\theta_R = 2°$ (as used in previous Chapters). This normalisation approach allows data at all three stress-levels to be presented on comparable axes, but is not directly intended to elucidate stress-level effects.

Figure 6.12 shows how the backbone linearity (or dominance of elastic behaviour) increases with stress-level. This variation in linearity is linked to stress-dependent stiffness and dilatant behaviour, as previously discussed, but also depends on the load amplitude. To better match the linearity of the cyclic responses across the stress-levels, the reference pile displacement u_R – which determines H_R and therefore the cyclic amplitudes through ζ_b – may be adjusted with stress-level, perhaps employing the dimensionless framework of Leblanc *et al.* (2010a) (Table 3.4, Section 3.4.3). However,

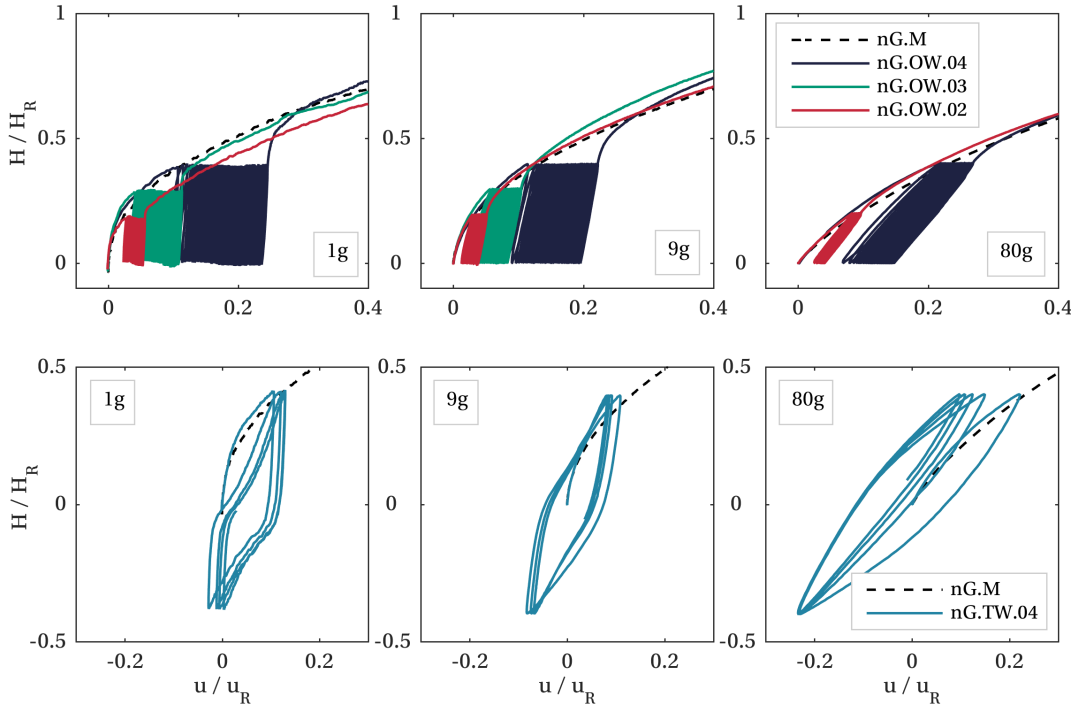

Figure 6.12: Unidirectional load-displacement response (note different scales on lower row)

the variation in backbone linearity is a stress-level effect, and it is not clear whether it is appropriate to minimise or eliminate this effect by modifying u_R.

Figure 6.12 also reveals gapping-type behaviour in the 2-way tests at $1g$ and $9g$, consistent with the observations in dense sand at $1g$ in Section 4.3. The inflexion in the load-displacement response around zero load is indicative of gapping, as the pile's tangent stiffness reduces while traversing a gap or region of low-stress. These tests show gapping-type behaviour increasing with reducing stress-level, which may be explained by a reduction in the tendency for sand particles to move into a gap as stress-level reduces. For gapping to occur at all, some *cohesion* is required, which may be caused by particle interlocking, ambient moisture or electrostatic effects, as discussed in Section 4.3. The wished-in-place installation method will lead to lower horizontal stresses adjacent to the pile, increasing the likelihood of gap formation.

6.5.2 Ratcheting response

Figure 6.13 presents the evolution of normalised accumulated displacement $\Delta u_n/u_R$ with cycle number n for the 1-way unidirectional cyclic tests. A power-law (Equation 6.1) is fitted to each test and shown dashed. Various studies have shown ratcheting to evolve as a power-law with cycle number n (Leblanc *et al.*, 2010a; Klinkvort, 2012; Abadie *et al.*, 2019b; Albiker *et al.*, 2017; Truong *et al.*, 2019), and it was also found to provide a good fit to the $1g$ results in Section 4.4.1.

$$\frac{\Delta u_n}{u_R} = An^{\alpha} \tag{6.1}$$

No dependence of the power-law coefficient A on stress-level is observed, although Figure 6.14 shows how A varies with ζ_b as a power-law with exponent $m_\sigma = 3.4$ (fit shown dashed in Figure 6.14), consistent with the observed variation of equivalent parameter T_b in Figure 4.8, Section 4.4.1, and with the results of Abadie (2015). Conversely, no dependence of α on ζ_b is observed (in-line with previous studies), but there is a trend for decreasing α with increasing stress-level, as shown in Figure 6.15. To facilitate prediction of behaviour at other stress-levels, the ratcheting exponent α is presented in Figure 6.15 against normalised reference stress-level σ'_{REF}/p_a, rather than g-level.

To quantify the variation of α with stress-level, a logarithmic trend line is fitted to the data by least squares regression, and shown dashed in Figure 6.15. The line is defined by Equation 6.2.

$$\alpha = 0.127 - 0.022 \ln\left(\frac{\sigma'_{REF}}{p_a}\right) \tag{6.2}$$

This trend line can be used to inform comparison of behaviour at different stress-levels. For example, it suggests that the ratcheting exponent for an equivalent full size monopile in dense, saturated (fully drained) sand ($D = 8$ m, $\gamma' = 10$ kN/m^3, $\sigma'_{REF}/p_a = 2.2$) may be as low as $\alpha = 0.11$, or approximately half of the value in the $1g$ model tests. This very important observation highlights how ratcheting may be less pronounced at full-scale than observed in $1g$ laboratory-scale physical modelling.

The value of α varies with the chosen strain variable (as discussed in Section 4.4.1) and it is therefore difficult to compare α values from independent test campaigns to

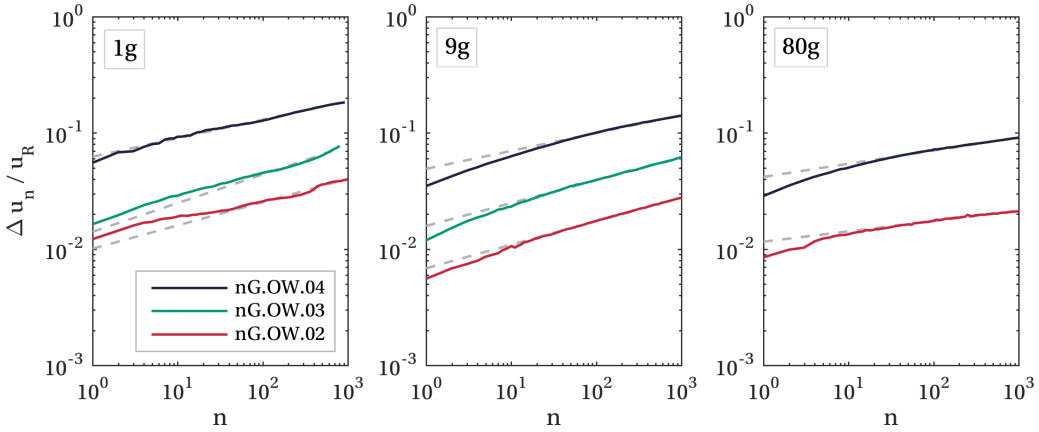

Figure 6.13: Accumulation of displacement Δu_n with unidirectional cyclic loading

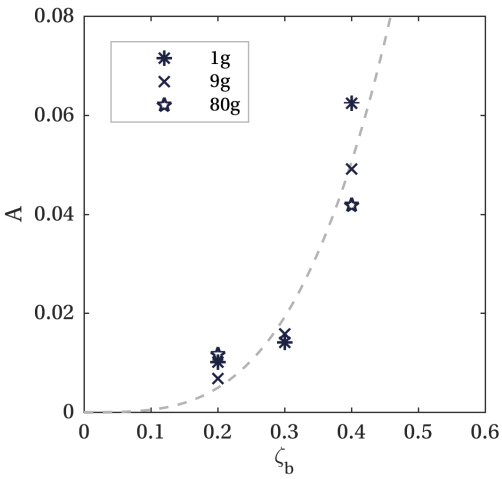

Figure 6.14: Variation of ratcheting power-law coefficient A with ζ_b

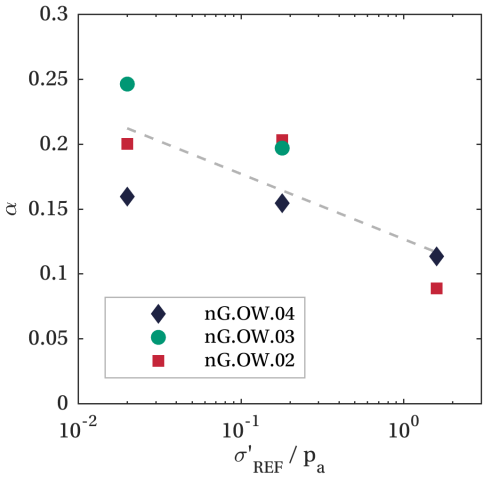

Figure 6.15: Variation of ratcheting power-law exponent α with stress-level for unidirectional cyclic loading

build confidence in this conclusion on stress-dependency. However, the results presented here are consistent with the increase in normalised pile displacement for $1g$ tests compared to centrifuge tests reported by Rudolph *et al.* (2014b) and Rudolph *et al.* (2014a).

6.5.3 Secant stiffness response

Figure 6.16 presents evolution of the secant stiffness of the monopile k_n with cycle number n for all unidirectional cyclic tests. Stiffness is normalised by the mean maximum stiffness, k_{MAX} (defined in Section 6.4.2). An increase in secant stiffness is

observed for all tests, with k_n/k_{MAX} plateauing at high cycle number in all tests except nG.TW.04.

Evolution of secant stiffness with cycle number has previously been described by logarithmic functions (Klinkvort and Hededal, 2013; Leblanc *et al.*, 2010a; Abadie, 2015). For the OU tests in Section 4.4.2 logarithmic fits were found to be appropriate for 1-way and partial 1-way loading, but power-laws fitted the response to 2-way and partial 2-way loading better. Here, a power-law function (Equation 6.3) is preferred and fitted to all data for consistency of interpretation with ratcheting. However, neither a power-law nor a logarithmic function captures the response particularly well for $n < 10$. Power-law fits are shown dashed in Figure 6.16.

$$\frac{k_n}{k_{MAX}} = Bn^{\beta} \tag{6.3}$$

The normalised secant stiffness for the first cycle ($k_{n=1}/k_{MAX}$) is plotted in Figure 6.17. There is no strong dependence of first cycle secant stiffness values on stress-level, however, the spread of stiffness values decreases with increasing stress-level, consistent with the increasing linearity of the responses. At each g-level, the first cycle stiffness values generally decrease with cyclic amplitude H_{CYC}, as expected, given the non-linear load-displacement response. Plotting the power-law coefficient (or y-axis intercept) B instead would have produced a very similar plot.

The impact of stress-level on the evolution of stiffness is assessed by plotting the power-law exponent β against stress-level in Figure 6.18. The exponents for tests 1G.TW.04 ($\beta = 0.304$) and 9G.TW.04 ($\beta = 0.110$) are not presented on this plot, being considerably greater than the other exponents. These high values of β are thought to be linked to the gapping-type behaviour observed for these tests. If a gap is opening, the possibility of grain migration, and therefore densification close to the pile, will be increased.

A logarithmic trend line is fitted to the variation of β with stress-level, neglecting the 2-way tests, and shown dashed in Figure 6.18. The trend line is described by Equation 6.4 and can be used to inform comparison of monopile behaviour at different stress-levels. For example, it suggests that for an equivalent full size monopile the

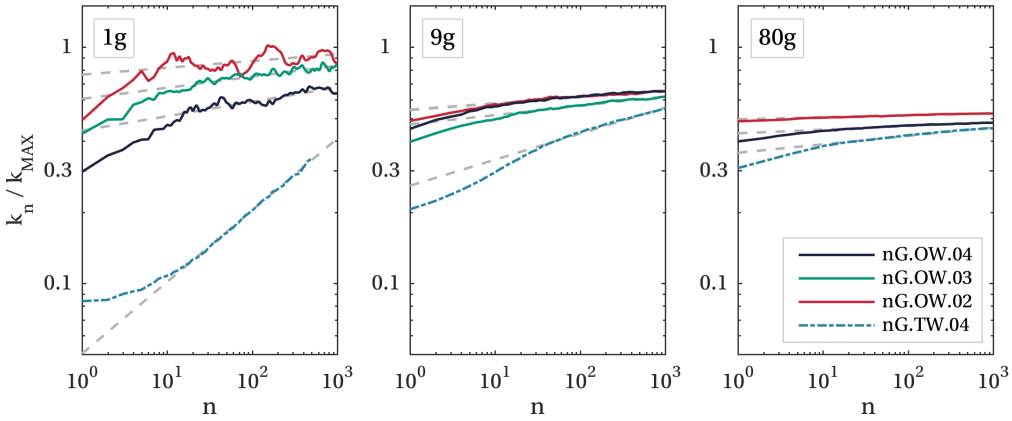

Figure 6.16: Change in secant stiffness k_n with unidirectional cyclic loading

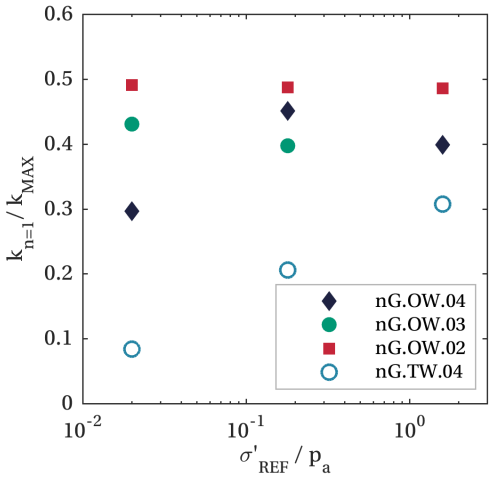

Figure 6.17: Variation of normalised stiffness for the first cycle $k_{n=1}/k_{MAX}$ with stress-level for unidirectional cyclic loading

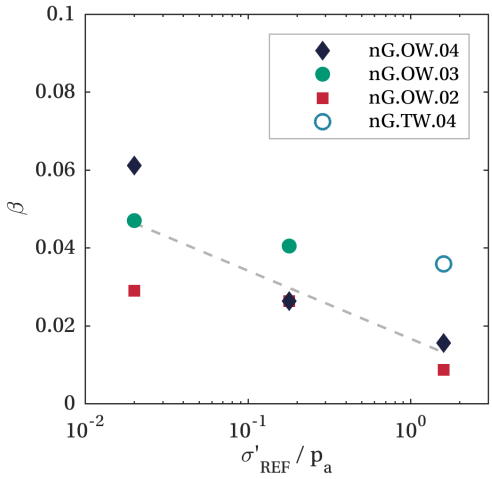

Figure 6.18: Variation of stiffness power-law exponent β with stress-level for unidirectional cyclic loading

1-way stiffness exponent may be as low as $\beta = 0.011$, or 25% of the stiffness exponent value in the $1g$ model tests.

$$\beta = 0.017 - 0.0076 \ln\left(\frac{\sigma'_{REF}}{p_a}\right) \tag{6.4}$$

6.5.4 Energy dissipation response

Figure 6.19 shows the evolution of unidirectional energy loss factor η_n with cycle number n. Although an empirical fit was not made to the OU $1g$ data in Section 4.4.2, a power-law fit (Equation 6.5) is used here to quantify the impact of stress-level on η_n.

The power-law provides a reasonable fit to all data, at least for $n > 10$, with the resulting fits shown dashed in Figure 6.19.

$$\eta_n = Cn^{\gamma} \tag{6.5}$$

As for ratcheting and stiffness evolution, the variation of the energy loss factor power-law exponent γ with stress-level is plotted in Figure 6.21. However, no dependence of γ on stress-level is observed. Instead, the energy loss factor for the first cycle $\eta_{n=1}$ is found to decrease with increasing stress-level, as shown in Figure 6.20. A similar result would be obtained if the power-law coefficient (or y-axis intercept) C had been plotted instead. The anomalously low value of initial energy loss factor for test nG.TW.04 is probably linked to the significant gapping-type behaviour observed, which reduces the hysteretic energy loss E_H, compared to no gapping.

A logarithmic function is fitted to the variation of first cycle energy loss factor $\eta_{n=1}$ with stress-level. The trend line, shown dashed in Figure 6.20, is defined by Equation 6.6.

$$\eta_{n=1} = 0.228 - 0.134 \ln\left(\frac{\sigma'_{REF}}{p_a}\right) \tag{6.6}$$

This trend line suggests that an equivalent full size monopile may have an energy loss factor for the first cycle of around $\eta_{n=1} = 0.12$, which is 16% of the value for the model tests at $1g$.

6.5.5 Reloading response

Post-cyclic reloading was performed after 1000 loading cycles for the majority of the unidirectional cyclic tests. The upper row of Figure 6.22 shows the reloading responses with the cyclic responses omitted, while the lower row shows the reloading responses re-zeroed from the onset of reloading (at $u = u_{r0}$). Qualitatively similar behaviour is observed at all stress-levels.

The reloading responses following 1-way cyclic loading tend to re-join or exceed the backbone curve at all stress-levels, while a significant increase in capacity is observed under 2-way loading at $9g$, where little ratcheting or drift occurred. These observations are consistent with those made in Section 4.7 and support the interpretation of the reloading response as a competition between ratcheting and stiffening processes.

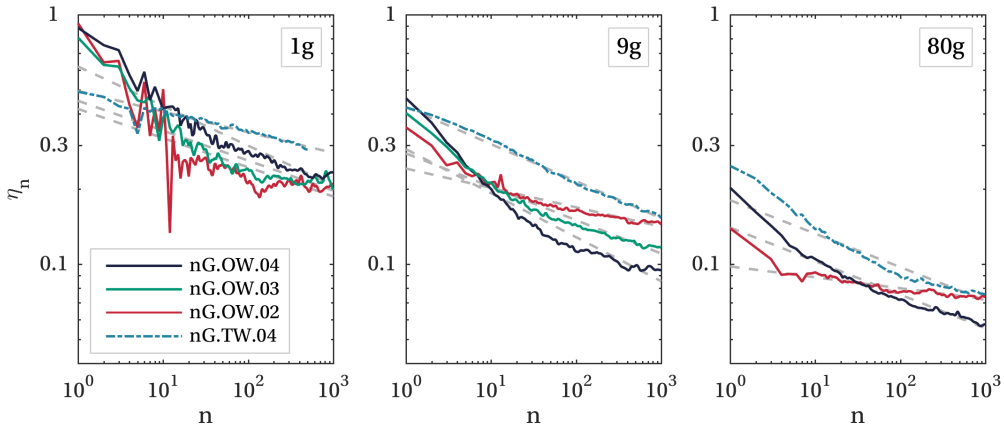

Figure 6.19: Change in energy loss factor η_n with unidirectional cyclic loading

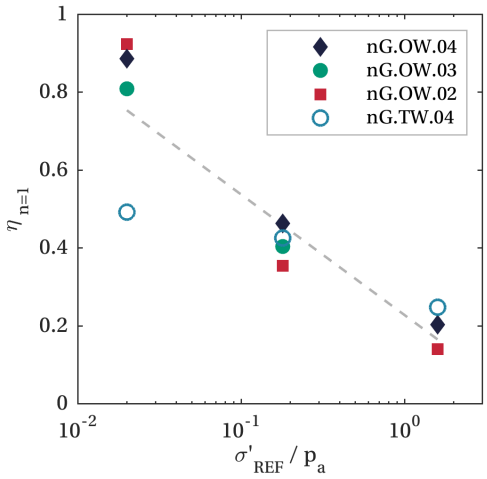

Figure 6.20: Variation of energy loss factor for the first cycle $\eta_{n=1}$ with stress-level for unidirectional cyclic loading

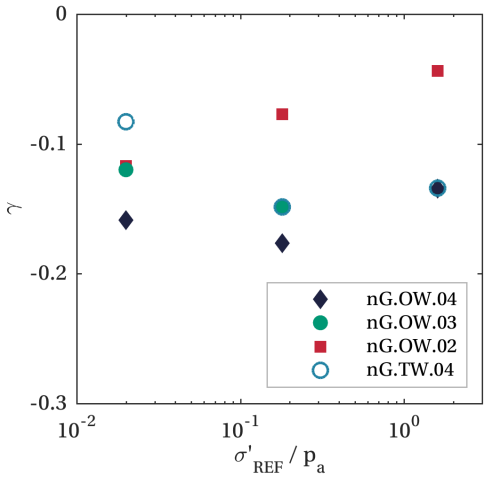

Figure 6.21: Variation of energy loss factor power-law exponent γ with stress-level for unidirectional cyclic loading

Re-zeroing the reloading responses highlights the significant increase in stiffness relative to the monotonic response for $H/H_R < \zeta_b$, consistent with the observed increase in secant stiffness with cycling.

6.5.6 Discussion

Qualitatively, the unidirectional cyclic responses are similar across the three stress-levels investigated, with similar reloading responses and with power-law expressions approximately capturing the evolution of ratcheting, stiffness and energy loss factor. But, quantitatively, the results reveal some important stress-level effects.

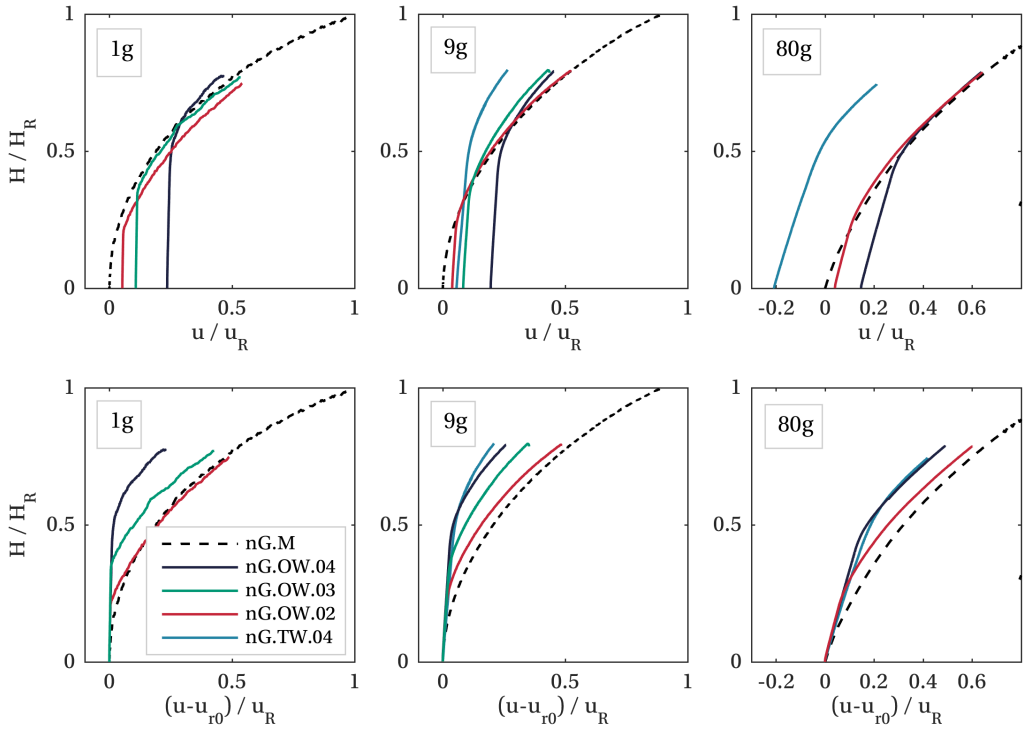

Figure 6.22: Reloading response following unidirectional cyclic loading (cyclic response omitted and response re-zeroed from u_{r0} on lower row, note different scale at 80g)

The decrease of first cycle energy loss factor $\eta_{n=1}$ with stress-level (Figure 6.20) can be directly linked to the linearity of the load-displacement response. The response linearity increases with stress-level, and is linked to stress-dependent stiffness and dilatant behaviour, but also depends on the load amplitude. However, the logarithmic decrease in ratcheting and stiffness exponent with stress-level (Figure 6.15 and Figure 6.18) appears to be independent of load amplitude and therefore linearity of the load-displacement response.

The various studies from Cuéllar *et al.* (2012), Nicolai (2017) and Cui and Bhattacharya (2016) revealed the presence of both convection and densification mechanisms under cyclic loading in dry sand (see Section 1.3.2). The increase in secant stiffness is probably driven by a local densification mechanism, while the ratcheting behaviour is probably caused by both a convection mechanism and any asymmetry in local densification. Given that both mechanisms require particle rearrangement, it is explicable that the associated ratcheting and stiffening behaviour

will be affected by increasing stress-level, where (as highlighted by Cui and Bhattacharya (2016)) there is increasing constraint on particle rearrangement.

6.6 Multidirectional cyclic response

Table 6.4 characterises the multidirectional tests in terms of *nominal* and *applied* ζ_b and ζ_c load values in the x- and y-directions. The nominal values were those demanded of the control system during testing, and do not account for pile movement. The actual applied values were computed post-testing, accounting for the instantaneous pile position and load line angle. Pile movement has a non-negligible effect on the applied loads: the peak cyclic loads vary by up to 10% and the load biases vary by up to 20% from the nominal values. However, the phenomenological observations made in this Section are not expected to be affected by these load variations.

The multidirectional T- and L-shaped tests at $9g$ and $80g$ correspond to unidirectional tests nG.OW.04 – having the same cyclic load amplitude H_{CYC} and average load amplitude H_{AV}. However, the multidirectional $1g$ tests have a load bias in the x-direction 75% larger than 1G.OW.04 and so comparisons at $1g$ are made with caution.

6.6.1 Displacement and ratcheting response

Figure 6.23 presents the displacement responses for the multidirectional tests nG.T.02 and nG.L.04, alongside the corresponding unidirectional tests nG.OW.04. The displacements at cycles 1, 10, 100, (1000) are marked. Figure 6.23 shows how the monopile moves broadly in the direction of the load bias at all stress-levels, although there is some deviation in tests 9G.T.02 and 80G.T.02. The deviation may be caused by systematic error in experimental set-up or boundary effects (test 9G.T.02 deviates towards the strongbox wall while test 80G.T.02 deviates towards the strongbox corner, see Figure 6.7). Figure 6.23 also highlights the increase in amplitude of displacement across each cycle with increasing stress-level, consistent with a decrease in secant stiffness k_n normalised by H_R/u_R ($k_n u_R/H_R$) with increasing stress-level.

Figure 6.24 presents the accumulated rotation responses for the multidirectional tests alongside the corresponding unidirectional tests. For the T-shaped tests significant

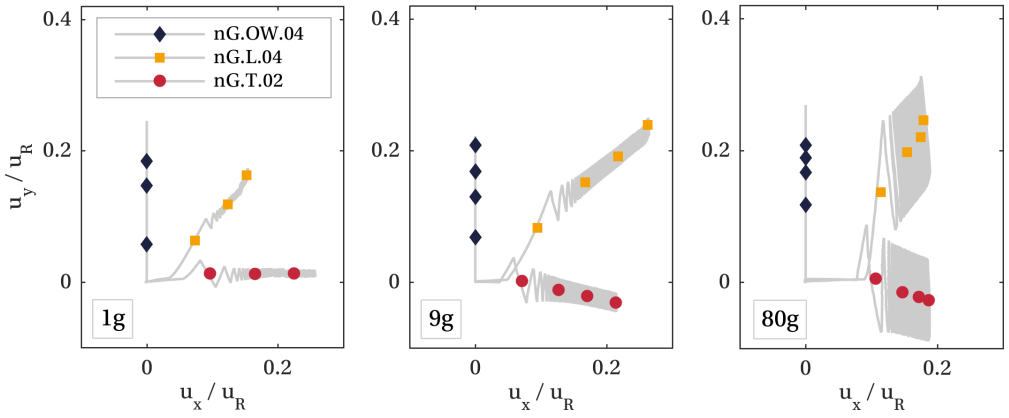

Figure 6.23: Displacement response for multidirectional tests (markers indicate location of cycle 1, 10, 100, (1000))

ratcheting only occurs, and is only reported, in the x-direction. For the L-shaped tests ratcheting is reported in both the x- and y-directions. A power-law (Equation 6.1) is fitted to the evolution of $\Delta u_n/u_R$ with cycle number n and shown dashed in Figure 6.24. The power-law generally captures the evolution of ratcheting well, but tends to over-predict ratcheting for $n < 10$ for the T-shaped tests. The response of test 80G.L.04(x), particularly for $n > 100$, may be anomalous.

Figure 6.25 presents the variation of ratcheting power-law coefficient A with test type and stress-level. No clear dependence of A on either test type or stress-level is observed. The ratcheting power-law exponent α does vary with stress-level, and is plotted in Figure 6.26, accompanied by the dashed trend line obtained for the unidirectional tests (Equation 6.2). This trend line also fits the multidirectional data well. In general, there is no clear dependency of ratcheting behaviour on test type (at least for $n > 10$).

6.6.2 Secant stiffness response

Figure 6.27 presents the evolution of secant stiffness k_n for the multidirectional tests and corresponding unidirectional cyclic tests. For multidirectional loading, evolution of secant stiffness is only relevant in the direction of cycling. For $n > 10$, the response is described well with a power-law (Equation 6.3), which is fitted and shown dashed in Figure 6.27.

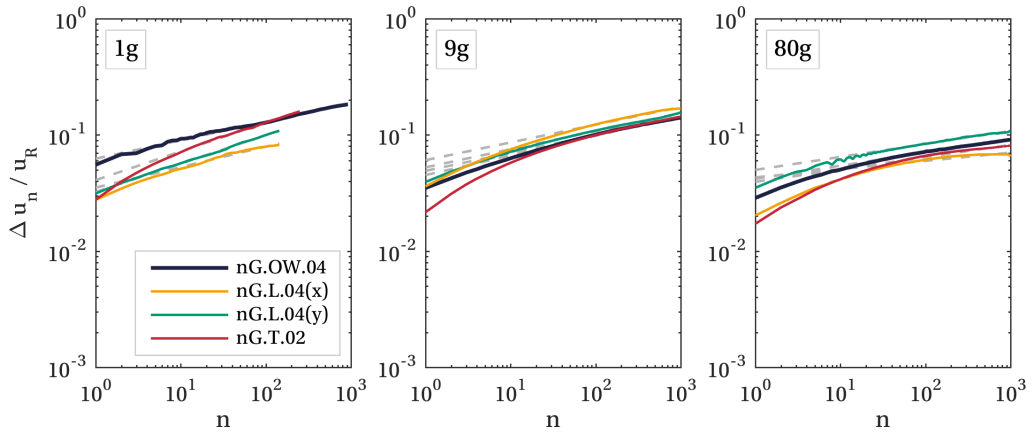

Figure 6.24: Accumulation of displacement Δu_n with multidirectional cyclic loading

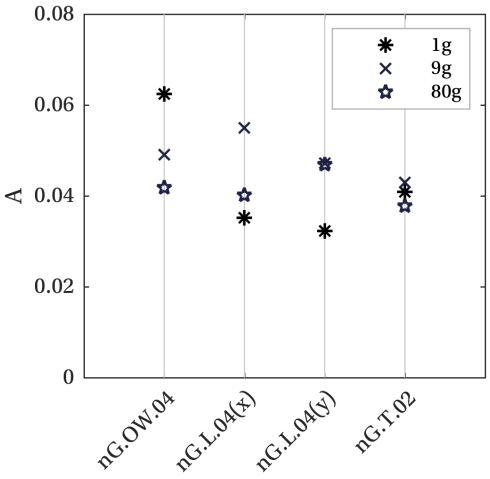

Figure 6.25: Variation of ratcheting power-law coefficient A with multidirectional test type

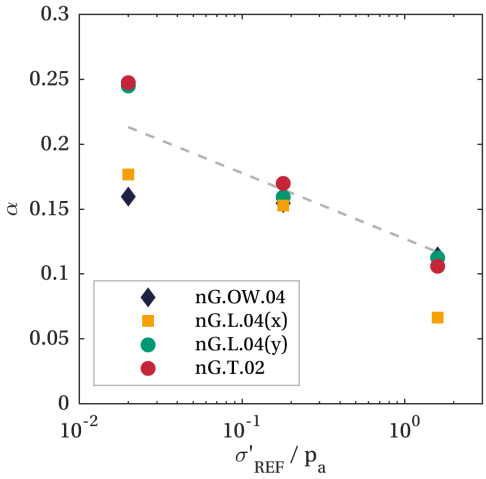

Figure 6.26: Variation of ratcheting power-law exponent α with stress-level for multidirectional cyclic loading

The variation of normalised secant stiffness for the first cycle ($k_{n=1}/k_{MAX}$) is shown in Figure 6.28. As for the unidirectional tests, there is no clear dependence on stress-level; there is also no dependence on test type. The variation in power-law stiffness exponent β is plotted in Figure 6.29, with the trend line obtained for unidirectional loading (Equation 6.4) shown dashed. The values of β for the multidirectional tests at $1g$ depart from the trend line, though there is inconsistency in applied mean load. The multidirectional tests at $9g$ and $80g$ are aligned with the unidirectional trend.

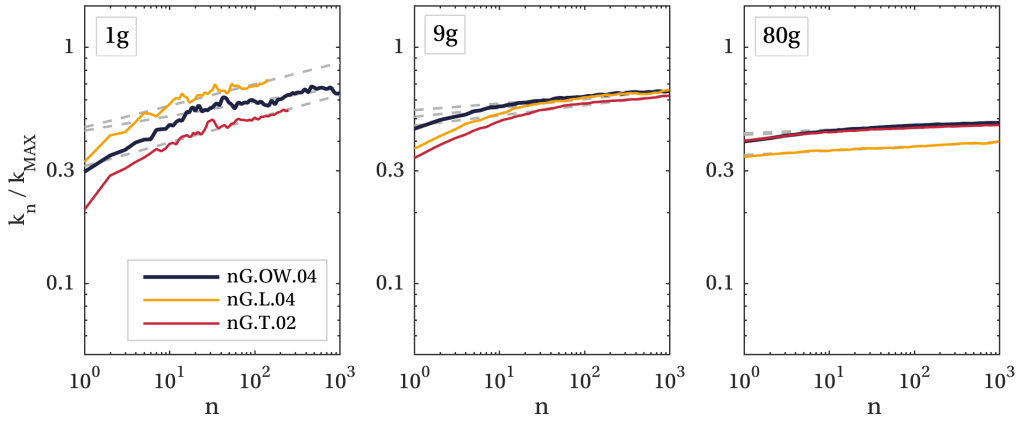

Figure 6.27: Change in secant stiffness k_n with multidirectional cyclic loading

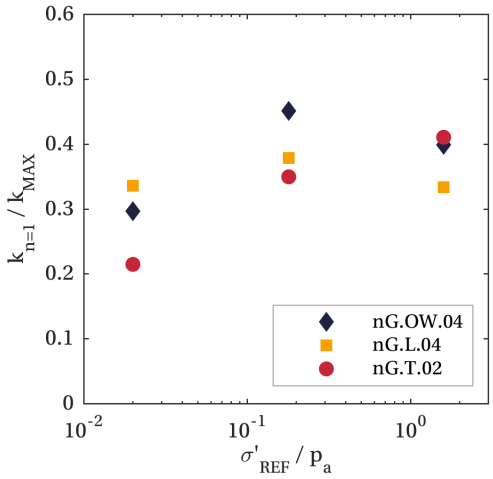

Figure 6.28: Variation of normalised stiffness for the first cycle $k_{n=1}/k_{MAX}$ with stress-level for multidirectional cyclic loading

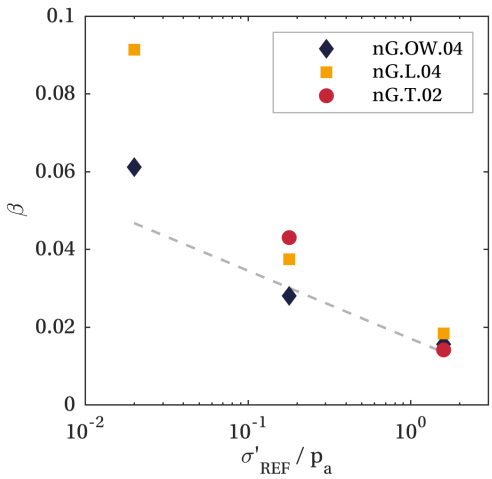

Figure 6.29: Variation of stiffness power-law exponent β with stress-level for multidirectional cyclic loading

6.6.3 Energy dissipation response

The evolution of energy loss factor η_n with cycle number n is shown in Figure 6.30, with a power-law (Equation 6.5) fitted and shown dashed. The multidirectional behaviour is consistent with that observed for the unidirectional tests: there is no clear dependence of the energy loss factor power-law exponent γ on stress-level (Figure 6.32), but the energy loss factor for the first cycle $\eta_{n=1}$ decreases logarithmically with stress-level, as shown in Figure 6.31. The trend line obtained for unidirectional loading (Equation 6.6) also fits this data well, as shown by the dashed line in Figure 6.31. Values of

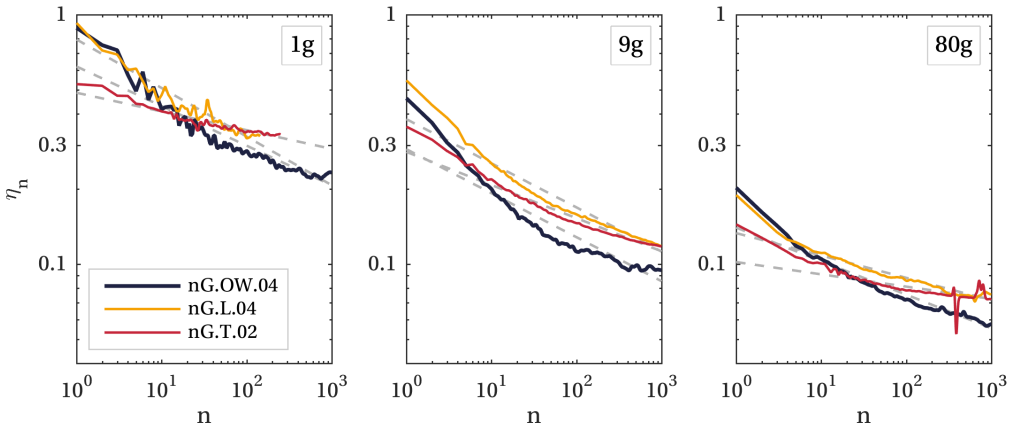

Figure 6.30: Change in energy loss factor η_n with multidirectional cyclic loading

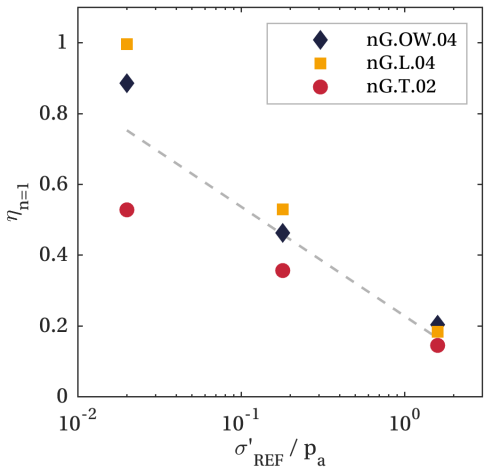

Figure 6.31: Variation of energy loss factor for the first cycle $\eta_{n=1}$ with stress-level for multidirectional cyclic loading

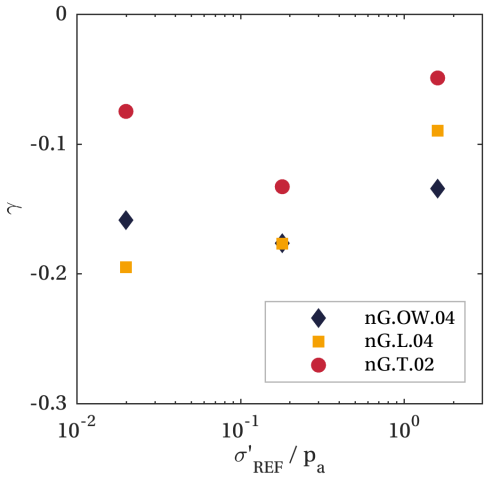

Figure 6.32: Variation of energy loss factor power-law exponent γ with stress-level for multidirectional cyclic loading

$\eta_{n=1}$ and γ are similar for unidirectional and L-shaped tests, but there is a tendency for the T-shaped tests tend to have lower $\eta_{n=1}$ values and higher γ values. This is probably associated with the variation in response linearity over the cyclic loading region with test type, at a given stress-level.

6.6.4 Discussion

In general there is little variation in the magnitude and evolution of ratcheting, stiffness and energy loss factor with multidirectional test type, at all stress-levels. This implies that, for a given mean load H_{AV} and cyclic load amplitude H_{CYC}, the direction of cyclic loading (relative to the mean load) has an insignificant impact on the cyclic response.

Ratcheting also occurs in the direction of the mean load at all stress-levels, regardless of the cyclic loading direction. These observations are in line with those reported for $1g$ testing at OU in Chapter 4, and have important implications for modelling the multidirectional response. Ratcheting in the direction of the applied load is a key feature of models in the HARM framework (Houlsby *et al.*, 2017), and may be included as a feature of other ratcheting models.

In general, the stress-level effects observed in the unidirectional tests are also observed in the multidirectional tests. The trend lines obtained from the unidirectional results for variation of ratcheting exponent, stiffness exponent and first cycle energy loss factor with stress-level are also, in general, appropriate for the multidirectional results.

6.7 Summary

This Chapter has explored the effect of stress-level on the response of monopile foundations to lateral loading. Monotonic, unidirectional cyclic and multidirectional cyclic loading tests were performed on a model monopile in dry, dense sand at three different g-levels. With the same experimental set-up at each g-level, stress-level effects were isolated. The following key observations were made:

- The monotonic responses exhibit stress-level effects which can be explained by stress-dependent stiffness and dilatancy, although decoupling these phenomena is difficult.
- The monotonic results support the use of the normalisation approach proposed by Leblanc *et al.* (2010a), although the observed variation of maximum foundation stiffness with stress-level is not entirely consistent with this approach.
- Gapping-type behaviour reduces with increasing stress-level.
- Qualitatively, the cyclic response is similar across the three stress-levels, with power-law functions providing a reasonable fit to evolution of ratcheting, secant stiffness and energy loss factor with cycle number.

- The ratcheting and stiffness exponents, which control the rate of change of these parameters with cycle number, both decrease logarithmically with increasing stress-level. The trends suggest that, for an equivalent full size monopile ($D = 8$ m), the ratcheting exponent may be half the value at $1g$ and the stiffening exponent may be one quarter the value at $1g$.
- The reduction in ratcheting and stiffening rate with stress-level is explained by the increase in confinement with stress-level, which inhibits particle rearrangement understood to cause ratcheting and stiffness change.
- The energy loss factor for the first cycle reduces with increasing stress-level. This behaviour depends on the linearity of the backbone curve, which is linked to stress-dependent stiffness and dilatant behaviour, but also varies with load amplitude.
- The post-cyclic reloading response shows no clear stress-level dependency.
- The multidirectional tests exhibit stress-level effects consistent with the unidirectional tests, while the multidirectional observations are consistent with those made for OU $1g$ tests in Chapter 4.

Together, these results provide new insight into the impact of stress-level on the response of monopile foundations, and help inform comparison of monopile behaviour at different stress-levels. The observed impact of stress-level on the rate of change of ratcheting and stiffening with cycle number is particularly important, as it suggests the impact of cyclic loading will be less pronounced at full-scale than observed in small-scale $1g$ physical modelling.

The qualitative similarities in response at $1g$, $9g$ and $80g$ demonstrate the insight that can be gained from $1g$ testing, while the observed stress-level effects highlight the need to simulate full-scale stress-levels to thoroughly understand foundation behaviour. This supports the suggestion that an efficient physical modelling campaign might use a combination of modelling approaches. As conducted in Chapters 3, 4 and 5, laboratory-scale $1g$ testing may be used to explore a wide range of behaviour, establish trends

and inform initial development of models for design. Focused centrifuge testing can then assess the applicability of $1g$ observations at higher (ideally full-scale) stress-levels, and inform scaling relationships. Large-scale field testing may be used for validation of design methods in natural deposits.

The results in this Chapter cannot be quantitatively compared to the OU results (reported in Chapters 3 and 4), given the difference in installation method, sand type, stress and strain parameters. However, the behaviour is qualitatively similar: with ratcheting, stiffening and changes in dissipation with repeated cyclic loading, a tendency for the reloading response to approach or exceed the backbone curve, and invariance of the magnitude and evolution of the cyclic response to cyclic load direction.

Chapter 7

Modelling the response of a monopile to complex cyclic loading

7.1 Introduction

This Chapter draws on the experimental observations from previous Chapters to demonstrate and inform development of macro models for monopile foundations under cyclic lateral loading in the *Hyperplastic Accelerated Ratcheting Model* (HARM) framework. The hyperplastic modelling framework and the underlying multi-surface kinematic hardening models are first presented, before the introduction of unidirectional and bi-directional models which are able to capture the high-cycle response, including ratcheting and stiffness evolution.

New evolution functions, which describe how ratcheting and stiffness evolve with cyclic loading, are proposed. Focus is placed on functions which do not significantly distort Masing behaviour, are able to capture the post-cyclic reloading response, and depend on parameters which have a clear impact on the response. The models are calibrated to five datasets (OU very loose and OU dense datasets presented in Chapters 3, 4 and 5, and UWA $1g$, UWA $9g$ and UWA $80g$ datasets presented in Chapter 6) and computations are compared to a representative selection of experimental results. The computations in this Chapter explore the ability of models in the HARM framework to capture the response to unidirectional and multidirectional regular cyclic loading, as well as the response to realistic multi-amplitude storm loading. Predictions are also made at prototype-scale.

7.2 Key behaviours observed experimentally

	Key behaviour	Key evidence
1	The monopile exhibits a non-linear monotonic response.	Section 3.4.1 A, B
2	The extended Masing rules are approximately adhered to during the first few loading cycles.	Section 4.3 A
3	Ratcheting occurs i) under biased cyclic loading and ii) in the direction of the mean load.	i) Section 4.4.1 ii) Section 4.6.1 i) A, B
4	Ratcheting evolves as a power-law with cycle number.	Section 4.4.1 A, B
5	The magnitude of ratcheting increases as a power-law with cyclic amplitude (for constant ζ_c).	Section 4.4.1 A, B
6	Load asymmetry (ζ_c) affects the shape, rate and therefore magnitude of ratcheting.	Section 4.4.1
7	Secant stiffening occurs under cyclic loading and evolves logarithmically or as a power-law, depending on the load asymmetry.	Section 4.4.2 A
8	The cyclic response is broadly independent of the cyclic loading direction, relative to the mean load direction.	Section 4.6.1
9	Multidirectional fan-type loading can lead to greater ratcheting and stiffening than unidirectional loading.	Section 4.6.2
10	The inferred capacity on post-cyclic reloading is equal to or greater than the monotonic capacity.	Section 4.7

Table 7.1: Key behaviours observed experimentally in this work and by Abadie (2015) (A) and Beuckelaers (2017) (B) and sought to be captured in modelling

The combined experimental observations from Chapters 3, 4, 5 and 6 are used to determine the key behaviours which are sought to be captured in modelling, as outlined in Table 7.1. Evolution of energy loss factor is not directly sought to be captured, since it is understood to depend largely on the evolution of stiffness and ratcheting. No attempt is made to capture the gapping-type behaviour observed under high-amplitude 2-way loading in dense dry sand at low stress-levels, given that it occurs only at large rotations and low stress-levels, which are not representative of field conditions.

Table 7.1 indicates which behaviours were also observed by Abadie (2015) (A), as these directly informed the development of the HARM framework presented by Houlsby *et al.* (2017). Behaviours observed by Beuckelaers (2017) (B) at field-scale, in both sand and clay, are also indicated.

7.3 Modelling basis

7.3.1 Hyperplasticity

Models in the HARM framework are formulated in the hyperplasticity framework which is comprehensively described by Houlsby and Puzrin (2006). The hyperplasticity framework allows compact, systematic development of constitutive models which are guaranteed to obey the Laws of Thermodynamics. The method is rooted in the work of Ziegler (1977), and was first presented (for rate-independent materials) by Houlsby (1981). The framework is applicable to both rate-independent and rate-dependent materials or systems, and uses internal variables (α, often plastic strains) to describe the loading history. In general, models are presented in terms of conjugate stress σ and strain ε variables. The variables σ, ε, α and related variables may be scalars, vectors or tensors depending on the model dimensionality.

Models in the hyperplasticity framework are fully specified in terms of two potential functions: one describing stored energy and one describing dissipation. This contrasts with the conventional plasticity approach, where specification of an elastic constitutive relationship, yield criterion, plastic potential and hardening law is required. Stored energy may be defined in terms of the Helmholtz free energy $f(\varepsilon, \alpha)$ or the Gibbs free energy $g(\sigma, \alpha)$. For rate-independent materials, dissipation may be defined in terms of the dissipation function $d(\varepsilon, \alpha, \dot{\alpha})$ or with a yield surface $y(\varepsilon, \alpha, \chi)$; similar functions are defined for rate-dependent materials. The functions f and g are related through a Legendre transform and functions d and y are related through a degenerate Legendre transform.

The constitutive and incremental behaviour of a model is derived from the potentials with standardised procedures. With a model described by Helmholtz free energy f and dissipation d functions the behaviour is derived from:

$$\sigma = \frac{\partial f}{\partial \varepsilon} \qquad \bar{\chi} = -\frac{\partial f}{\partial \alpha} \qquad \chi = \frac{\partial d}{\partial \dot{\alpha}} \qquad \bar{\chi} = \chi \tag{7.1}$$

Where $\bar{\chi}$ is the generalised stress and χ is the dissipative generalised stress, conjugate to the internal variable α. The condition $\bar{\chi} = \chi$ is an expression of Ziegler's orthogonality principle (Ziegler, 1977), which is central to the hyperplasticity

framework. This principle assumes that energy is dissipated at the maximal rate, and allows derivation of the constitutive response without any additional assumptions.

Where additional kinematic constraints are applied $c(\dot{\alpha}) = 0$, the dissipation function is augmented with a Lagrangian multiplier Λ:

$$d^* = d(\varepsilon, \alpha, \dot{\alpha}) + \Lambda c(\dot{\alpha}) \tag{7.2}$$

With the generalised stress given by:

$$\chi = \frac{\partial d^*}{\partial \dot{\alpha}} = \frac{\partial d}{\partial \dot{\alpha}} + \Lambda \frac{\partial c}{\partial \dot{\alpha}} \tag{7.3}$$

The Lagrangian multiplier is eliminated by the use of the constraint $c(\dot{\alpha}) = 0$.

7.3.2 Multi-surface kinematic hardening models

Models in the HARM framework are based on multi-surface kinematic hardening models, which adhere to the extended Masing rules. These models are commonly referred to as Iwan models following the publication of the general characteristics of these models by Iwan (1967) for application to metals. Conceptually, these models are made up of M elastoplastic elements which each consist of a linear spring of stiffness H_m and a rate-independent cohesive (Coulomb) slider of strength K_m. Figure 7.1 shows how the elastoplastic elements (along with an additional solitary spring) are arranged for unidirectional models in either series or parallel configurations; the interpretation of parameters K_m and H_m differs between the configurations. Bi-directional models are more easily represented as a series of yield surfaces (circular with radius K_m for isotropic models) which define regions of constant stiffness E_m ($E_m = f(H_m)$ which varies between series and parallel models), as shown in Figure 7.2. The models generate multi-linear stress-strain ($\sigma - \varepsilon$) responses, as indicated in Figure 7.2 for loading and unloading in the y-direction, and automatically respond to any arbitrary, continuous loading.

As well as forming the basis of the ratcheting models presented by Houlsby *et al.* (2017), multi-surface kinematic hardening models have been used to capture the cyclic response of soils (Prévost, 1977; Mrŏz *et al.*, 1978) and the macro response of caisson foundations (Nguyen-Sy and Houlsby, 2005; Skau *et al.*, 2018) and monopile foundations (Page *et al.*, 2018). Multi-surface kinematic hardening models are

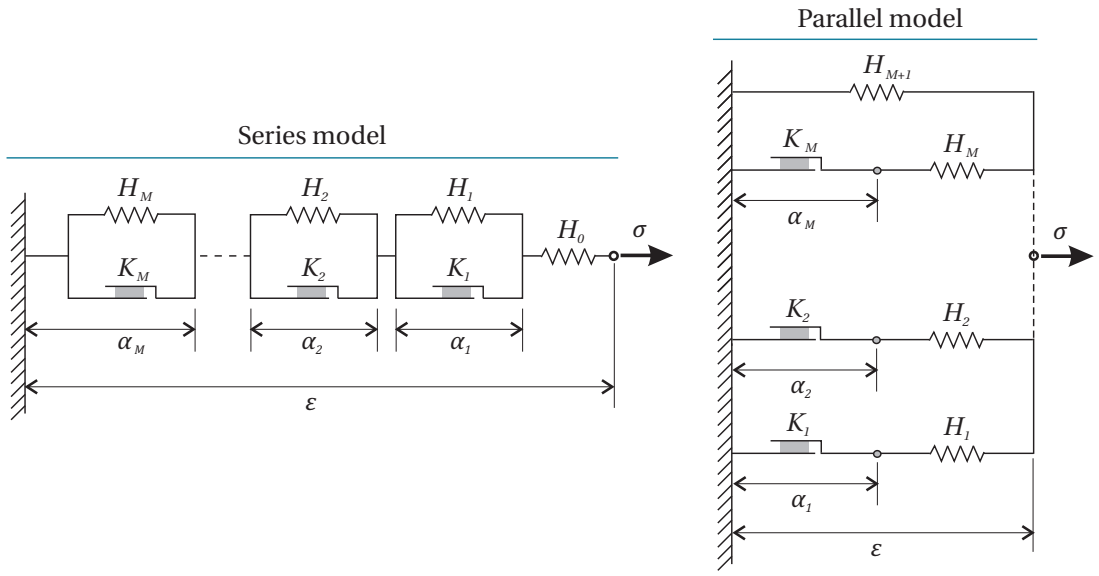

Figure 7.1: Conceptual models of unidirectional multi-surface kinematic hardening models in series and parallel configurations

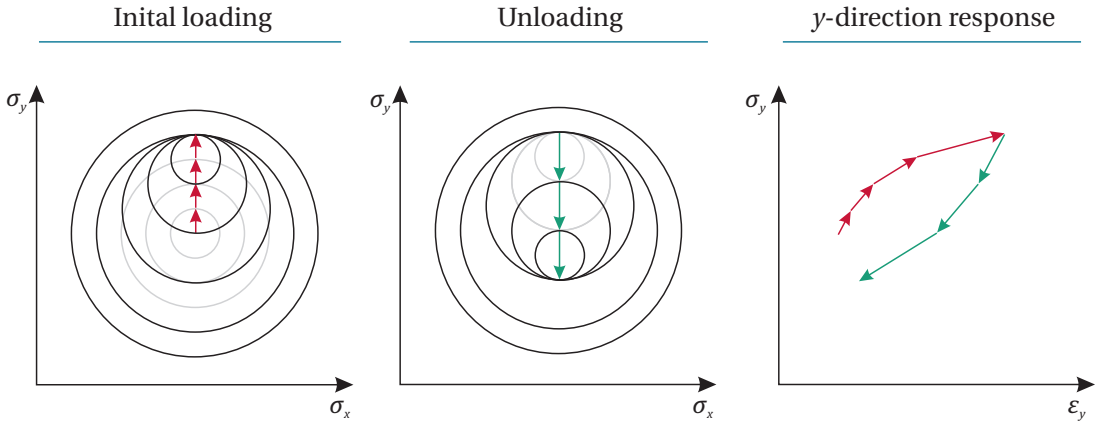

Figure 7.2: Representation of isotropic bi-directional multi-surface kinematic hardening models showing response to loading and unloading in the y-direction

presented here in hyperplasticity theory, but can also be described in conventional plasticity theory.

7.3.3 HARM framework

The *Hyperplastic Accelerated Ratcheting Model* (HARM) framework presented by Houlsby *et al.* (2017) was developed to capture the response of monopile foundations to cyclic lateral loading, but is applicable to other materials or systems which exhibit Masing behaviour augmented by ratcheting. Rate-dependent models of this sort were initially developed by Abadie (2015), and Houlsby *et al.* (2017) expanded the framework

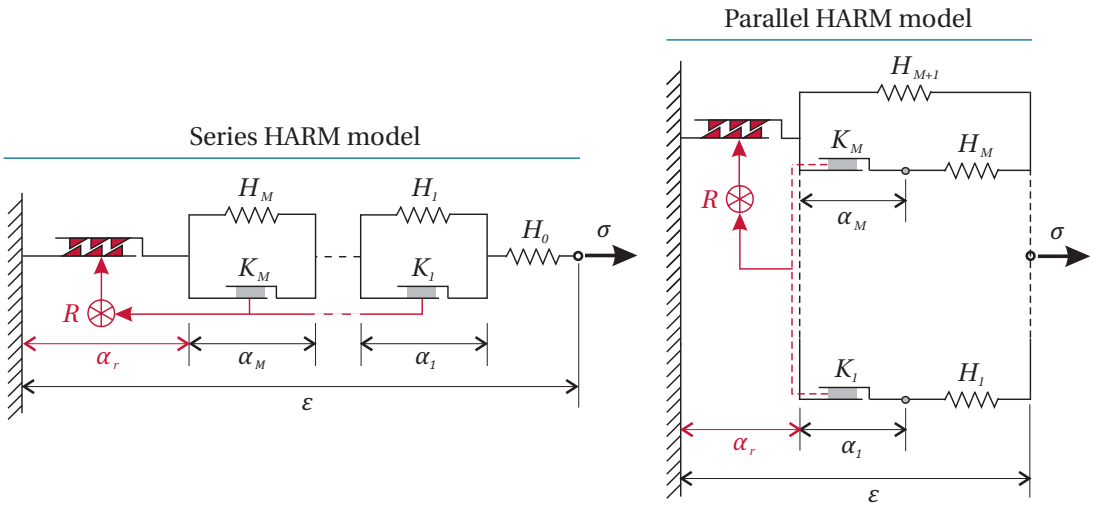

Figure 7.3: Conceptual models of unidirectional HARM models in series and parallel configurations (Houlsby *et al.*, 2017)

to present both rate-dependent and rate-independent models using both series and parallel configurations, with extensions to two-dimensional and tensorial models. These models are able to capture the system's continuous response to any arbitrary loading, but can also be accelerated to capture the total ratcheting response across a packet of regular cyclic loading with explicit calculation of a single cycle (Houlsby *et al.*, 2017).

Models in this framework are based on multi-surface kinematic hardening models but include additional ratcheting elements, as indicated in Figure 7.3. Ratcheting strain α_r accumulates as a proportion R of plastic strain, where R may vary with both loading history and surface m ($R = R_m$ in general). Stiffness evolution can be captured if the strengths K_m are also made functions of the loading history. These models have been shown to capture the response of monopiles to regular, unidirectional cyclic loading at laboratory-scale in loose, dry sand (Abadie *et al.*, 2019a) and at field-scale at both sand and clay sites (Beuckelaers, 2017). Balaam *et al.* (2020) has also demonstrated the ability of these models to capture the cyclic response of clay in cyclic simple shear apparatus to irregular multi-amplitude loading.

7.3.4 Modelling choices

Models in the HARM framework, and kinematic hardening models in general, can be formulated in either series or parallel, may be rate-independent or rate-dependent,

and may be implemented as macro models (Abadie, 2015; Abadie *et al.*, 2019a), 1D Winkler models (Beuckelaers, 2017) or as tensorial models in 3D finite element software (Houlsby *et al.*, 2017).

Series models are employed here as they are more suited to computation of strain given a stress input, and simulations are conducted here with stress input to be consistent with the load-controlled experiments. Series and parallel models can produce identical responses under unidirectional loading, but produce slightly different responses under multidirectional loading (Beuckelaers *et al.*, 2018). Unfortunately, the suitability of either model formulation cannot be determined from the multidirectional data as the differences in model computations are obscured by differences in response due to experimental variability (see Figure 7.7, Section 7.4.4).

Rate-independent models are presented here, given the rate-independence observed experimentally. However, models which capture the rate effects observed in clays and saturated sands have been developed in the HARM framework by Beuckelaers (2017).

Macro models for the global pile response are used here. These single-element models represent the integrated response of the pile-soil system, which may be represented with greater fidelity using a 1D Winkler model or a tensorial model. The conjugate stress σ and strain ε variables therefore represent applied moment M and pile rotation θ (OU datasets) or applied horizontal load H and pile displacement at the load application point u (UWA datasets).

7.4 Capturing the hysteretic response

This Section explores the ability of kinematic hardening models, without ratcheting elements, to capture the hysteretic response of monopile foundations observed in the first few cycles. In particular, the suitability of a bi-directional kinematic hardening model is explored. The hyperplastic model formulations are first presented.

7.4.1 Unidirectional hyperplastic kinematic hardening model

The model is defined in terms of the Helmholtz free energy function f and the dissipation function d:

$$f = \frac{H_0}{2}\left(\varepsilon - \sum_{m=1}^{M} \alpha_m\right)^2 + \sum_{m=1}^{M} \frac{H_m}{2}\alpha_m^2 \tag{7.4}$$

$$d = \sum_{m=1}^{M} K_m |\dot{\alpha}_m| \tag{7.5}$$

The internal variables may be interpreted as the plastic strains α_m, while H_m, K_m and H_0 values are used to calibrate the model, as discussed in Section 7.4.3. The model's constitutive behaviour is derived as:

$$\sigma = \frac{\partial f}{\partial \varepsilon} = H_0\left(\varepsilon - \sum_{m=1}^{M} \alpha_m\right) \tag{7.6}$$

$$\bar{\chi}_m = -\frac{\partial f}{\partial \alpha_m} = H_0\left(\varepsilon - \sum_{m=1}^{M} \alpha_m\right) - H_m\alpha_m = \sigma - H_m\alpha_m \tag{7.7}$$

$$\chi_m = \frac{\partial d}{\partial \dot{\alpha}_m} = K_m \frac{\dot{\alpha}_m}{|\dot{\alpha}_m|} \tag{7.8}$$

$$\chi_m = \bar{\chi}_m \quad \Rightarrow \quad \sigma - H_m\alpha_m = K_m \frac{\dot{\alpha}_m}{|\dot{\alpha}_m|} \tag{7.9}$$

The incremental total strain response can then be derived by differentiation and rearrangement of Equation 7.6:

$$d\varepsilon = \frac{d\sigma}{H_0} + \sum_{m=1}^{M} d\alpha_m \tag{7.10}$$

The yield functions y_m are implicit in Equation 7.9. At yield, when $\dot{\alpha}_m \neq 0$:

$$y_m = |\sigma - H_m\alpha_m| - K_m = |\chi_m| - K_m = 0 \tag{7.11}$$

Finally, the plastic strain increment is found by differentiation of the yield functions y_m with respect to time, where the consistency condition enforces $\dot{y}_m = 0$:

$$d\alpha_m = \frac{d\sigma}{H_m} \tag{7.12}$$

In numerical implementation, the yield conditions are determined using α_m from the previous increment. However, the expression for plastic strain increment is exact.

7.4.2 Bi-directional hyperplastic kinematic hardening model

The unidirectional model presented in Section 7.4.1 is extended here for bi-directional loading. It is a simplified version of the bi-directional ratcheting model presented by Houlsby *et al.* (2017). The model response is independent of loading direction, as expected for piles under lateral loading in a transversely-isotropic soil. The model is developed in terms of x- and y-components of stress $\boldsymbol{\sigma}$ and strain $\boldsymbol{\varepsilon}$:

$$\boldsymbol{\sigma} = \begin{bmatrix} \sigma_x \\ \sigma_y \end{bmatrix} \qquad \boldsymbol{\varepsilon} = \begin{bmatrix} \varepsilon_x \\ \varepsilon_y \end{bmatrix} \tag{7.13}$$

The model is defined in terms of the Helmholtz free energy function f and the dissipation function d:

$$f = \frac{H_0}{2}\left(\left(\varepsilon_x - \sum_{m=1}^{M}\alpha_{mx}\right)^2 + \left(\varepsilon_y - \sum_{m=1}^{M}\alpha_{my}\right)^2\right) + \sum_{m=1}^{M}\frac{H_m}{2}\left(\alpha_{mx}^2 + \alpha_{my}^2\right) \tag{7.14}$$

$$d = \sum_{m=1}^{M} K_m\sqrt{\dot{\alpha}_{mx}^2 + \dot{\alpha}_{my}^2} \tag{7.15}$$

The model's constitutive behaviour is derived as:

$$\sigma_x = \frac{\partial f}{\partial \varepsilon_x} = H_0\left(\varepsilon_x - \sum_{m=1}^{M}\alpha_{mx}\right) \qquad \sigma_y = \frac{\partial f}{\partial \varepsilon_y} = H_0\left(\varepsilon_y - \sum_{m=1}^{M}\alpha_{my}\right) \tag{7.16}$$

$$\begin{aligned} \bar{\chi}_{mx} &= -\frac{\partial f}{\partial \alpha_{mx}} = H_0\left(\varepsilon_x - \sum_{m=1}^{M}\alpha_{mx}\right) - H_m\alpha_{mx} = \sigma_x - H_m\alpha_{mx} \\ \bar{\chi}_{my} &= -\frac{\partial f}{\partial \alpha_{my}} = H_0\left(\varepsilon_y - \sum_{m=1}^{M}\alpha_{my}\right) - H_m\alpha_{my} = \sigma_y - H_m\alpha_{my} \end{aligned} \tag{7.17}$$

$$\chi_{mx} = \frac{\partial d}{\partial \dot{\alpha}_{mx}} = K_m\frac{\dot{\alpha}_{mx}}{\sqrt{\dot{\alpha}_{mx}^2 + \dot{\alpha}_{my}^2}} \qquad \chi_{my} = \frac{\partial d}{\partial \dot{\alpha}_{my}} = K_m\frac{\dot{\alpha}_{my}}{\sqrt{\dot{\alpha}_{mx}^2 + \dot{\alpha}_{my}^2}} \tag{7.18}$$

$$\begin{aligned} \chi_{mx} = \bar{\chi}_{mx} \quad &\Rightarrow \quad \sigma_x - H_m\alpha_{mx} = K_m\frac{\dot{\alpha}_{mx}}{\sqrt{\dot{\alpha}_{mx}^2 + \dot{\alpha}_{my}^2}} \\ \chi_{my} = \bar{\chi}_{my} \quad &\Rightarrow \quad \sigma_y - H_m\alpha_{my} = K_m\frac{\dot{\alpha}_{my}}{\sqrt{\dot{\alpha}_{mx}^2 + \dot{\alpha}_{my}^2}} \end{aligned} \tag{7.19}$$

The incremental total strain response is derived by differentiation and rearrangement of Equation 7.16:

$$d\varepsilon_x = \frac{d\sigma_x}{H_0} + \sum_{m=1}^{M} d\alpha_{mx} \qquad d\varepsilon_y = \frac{d\sigma_y}{H_0} + \sum_{m=1}^{M} d\alpha_{my} \tag{7.20}$$

The yield functions y_m can be obtained by summing the squares of Equation 7.19 in the x- and y-direction. At yield, when $\dot{\alpha}_{mx}^2 + \dot{\alpha}_{my}^2 \neq 0$:

$$y_m = \sqrt{(\sigma_x - H_m\alpha_{mx})^2 + (\sigma_y - H_m\alpha_{my})^2} - K_m = \sqrt{\chi_{mx}^2 + \chi_{my}^2} - K_m = 0 \tag{7.21}$$

The following relationship between generalised stresses and plastic strain rates is also obtained from Equation 7.19:

$$\frac{\chi_{mx}}{\chi_{my}} = \frac{\dot{\alpha}_{mx}}{\dot{\alpha}_{my}} \tag{7.22}$$

Substituting this ratio into the consistency condition ($\dot{y}_m = 0$) yields expressions for the plastic strain increments:

$$d\alpha_{mx} = \lambda\frac{\chi_{mx}}{H_m} \qquad\qquad d\alpha_{my} = \lambda\frac{\chi_{my}}{H_m} \tag{7.23}$$

Where λ is conventionally termed the plastic multiplier, determined as:

$$\lambda = \frac{\chi_{mx}d\sigma_x + \chi_{my}d\sigma_y}{K_m^2} \tag{7.24}$$

In numerical implementation, χ_{mx}, χ_{my} are determined using α_m from the previous increment. The solution for plastic strain increment $d\alpha_{mx}, d\alpha_{my}$ is therefore not exact, however, instabilities are avoided with sufficiently small load increments.

7.4.3 Calibration of kinematic hardening models

The kinematic hardening model parameters K_m and H_m are obtained for a series model from M points on a backbone curve $(\varepsilon_m, \sigma_m)$ using the following relationships:

$$\sigma_m = K_m, \;\; m = 1...M \tag{7.25}$$

$$\varepsilon_m = \sum_{i=0}^{m-1} \frac{K_m - K_i}{H_i}, \;\; m = 1...M, K_0 = 0 \tag{7.26}$$

Any monotonically increasing backbone curve can be captured, satisfying *key behaviour 1* (Table 7.1). The slider strengths are typically arranged in increasing order ($K_{i+1} > K_i$), and the number of surfaces M is chosen to fit a given backbone curve with the required accuracy. Here, $M = 100$ surfaces were typically used, with σ_m evenly distributed from 0 to σ_R.

In practice, the backbone curve is an essential output of a monotonic monopile design, which is a pre-requisite for cyclic design. Various monotonic design approaches may be taken: conducting 3D finite element simulations, applying the numerical or rule-based PISA method (Byrne *et al.*, 2017), or using established *p-y* methods (as presented in *e.g.* DNV GL, 2016). Here, the unidirectional backbone curves obtained experimentally are used for calibration of parameters K_m and H_m, as monotonic design is not the focus of this work.

Although points $(\varepsilon_m, \sigma_m)$, and therefore parameters K_m and H_m, could be obtained directly from the experimental backbone curves, specification of analytical functions for the backbone curves ensures smoothness of the model parameters and facilitates scaling. Three analytical functions are considered:

1. A Ramberg-Osgood (Ramberg and Osgood, 1943) or power-law relationship, as used by Abadie *et al.* (2019a) to capture the response of a model monopile in loose, dry sand:
$$\varepsilon = \frac{\sigma}{E_i} + \left(\varepsilon_R - \frac{\sigma_R}{E_i}\right)\left(\frac{\sigma}{\sigma_R}\right)^{P_p} \tag{7.27}$$

2. An expression presented by Jeanjean *et al.* (2017) for the response of clays, modified to include an elastic component:
$$\varepsilon = \frac{\sigma}{E_i} + \left(\varepsilon_R - \frac{\sigma_R}{E_i}\right)\left(\frac{\operatorname{arctanh}\left(\frac{\sigma}{\sigma_R}\tanh(P_j)\right)}{P_j}\right)^2 \tag{7.28}$$

3. A conic function, as used to represent the soil reactions as part of the PISA project (*e.g.* Burd *et al.*, 2019):
$$\varepsilon = \frac{\sigma}{E_i} + \frac{2\varepsilon_{pu}C}{-B+\sqrt{D}} \tag{7.29}$$
Where $\varepsilon_{pu} = \varepsilon_R - \frac{\sigma_R}{E_i}$; $A = P_c\left(\frac{\sigma_R}{E_i\varepsilon_{pu}}\right)$; $B = -2A\frac{\sigma}{\sigma_R} + (1-P_c)\left(1+\frac{\sigma_R}{E_i\varepsilon_{pu}}\right)^2\left(\frac{\sigma}{\sigma_R}-1\right)$; $C = A\left(\frac{\sigma}{\sigma_R}\right)^2$; $D = \max\left(B^2 - 4AC, 0\right)$.

Figure 7.4 shows the fits obtained to the mean experimental backbone curves, for each of the five datasets, using each of the analytical functions. The fits are presented in three ways, in terms of i) the moment-rotation or load-displacement response, ii) the tangent stiffness K_t response, and iii) the fitting error θ_e or u_e across the response. The

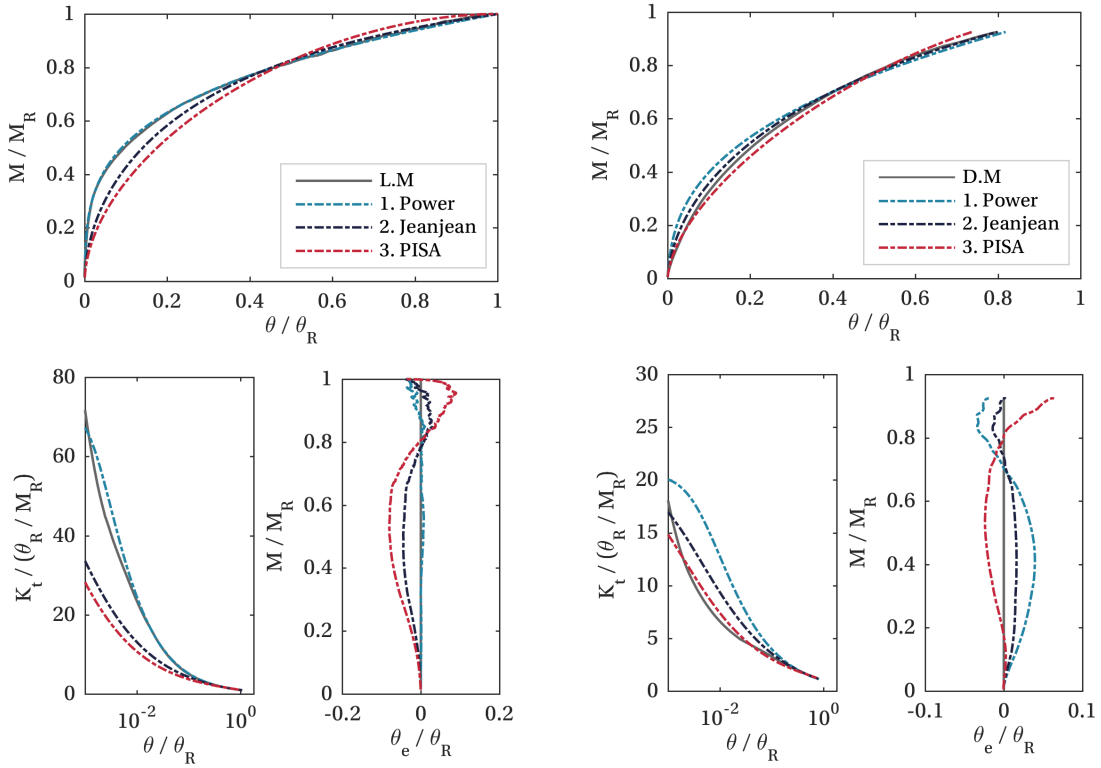

(a) OU very loose

(b) OU dense

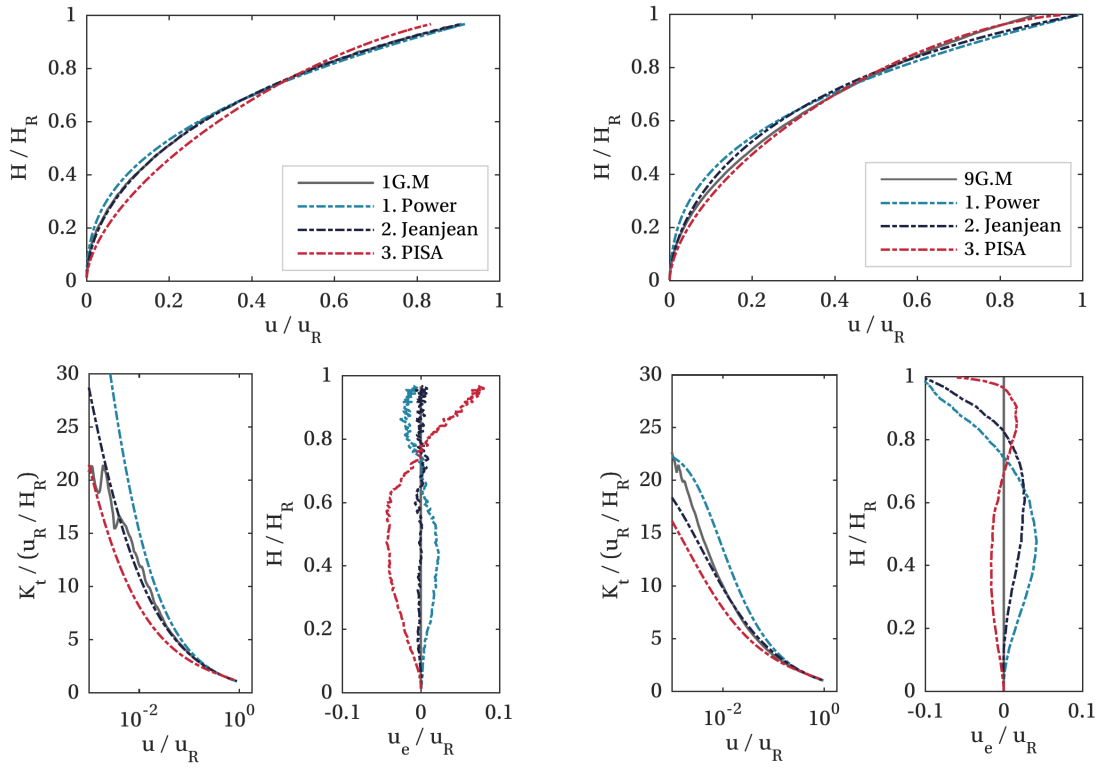

(c) UWA $1g$

(d) UWA $9g$

Figure 7.4: Fitting analytical functions to mean experimental backbone curves

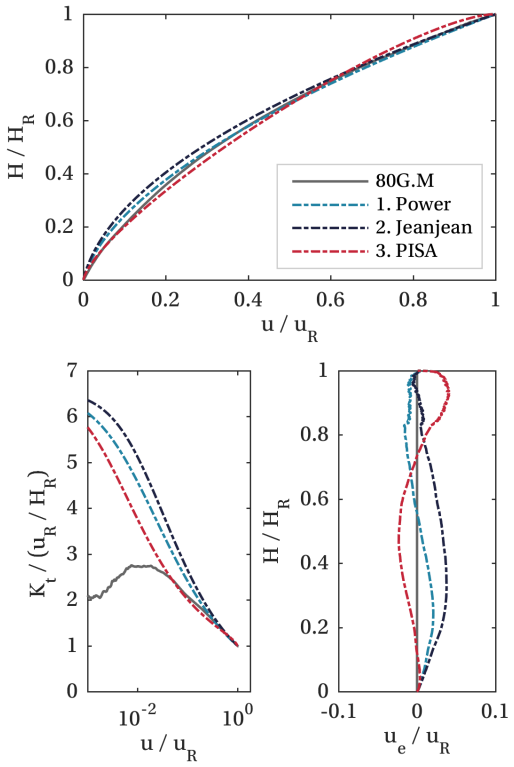

(e) UWA 80g

Figure 7.4: Fitting analytical functions to mean experimental backbone curves

Parameter	OU very loose	OU dense	UWA 1g	UWA 9g	UWA 80g
σ_R	26 N m	95 N m	15.7 N	99.5 N	597 N
ε_R	2°	2°	17.8 mm	17.8 mm	17.8 mm
E_i	936 N m/°	979 N m/°	57.3 N/mm	127.8 N/mm	220.8 N/mm
Analytical function	Power-law	Jeanjean	Jeanjean	Jeanjean	Power-law
Fitting parameter	$P_p = 3.56$	$P_j = 0.865$	$P_j = 0.800$	$P_j = 0.939$	$P_p = 1.82$
R^2	0.997	0.998	0.999	0.991	0.999

Table 7.2: Summary of parameters for analytical functions fitted to mean experimental backbone curves to facilitate calibration of parameters K_m and H_m

initial stiffness E_i values were set equal to the maximum stiffness values $E_i = k_{MAX}$, the reference stress values σ_R were set to either M_R or H_R and the reference strain values ε_R were set to either θ_R or u_R, as defined experimentally in Sections 3.4.3 and 6.5.1. The remaining fitting parameters (P_p, P_j, P_c for Equations 7.27, 7.28, 7.29) were then obtained by regression analyses with θ or u as the dependent variable.

The power-law (Equation 7.27) provides a very good fit to the OU very loose data

and UWA 80g data, while the Jeanjean expression (Equation 7.28) provides the best fit to the OU dense, UWA 1g and UWA 9g data. Table 7.2 summarises the chosen analytical function, fitting parameters and goodness of fit metric (R^2) for each dataset.

7.4.4 Computation of hysteretic response

Figure 7.5 presents computations of the unidirectional hysteretic responses using the unidirectional model described in Section 7.4.1, calibrated to each dataset as described in Section 7.4.3. Increasing amplitude 2-way tests demonstrate the model performance for the OU datasets, while the first four cycles of symmetric 2-way tests are used for the UWA datasets. The kinematic hardening model complies with the extended Masing rules, which the experimental responses approximately follow for the first few cycles (*key behaviour 2*, Table 7.1). The model therefore approximately captures the hysteretic response for all datasets. The model does not capture gapping, which is most marked in the UWA 1g data, and does not capture the increase in secant stiffness observed in the OU dense, UWA 9g and UWA 80g data.

Figure 7.6 shows the performance of the bi-directional model described in Section 7.4.2, calibrated following Section 7.4.3, under multidirectional spiral loading in OU very loose and dense sand. Although spiral loading is not realistic, these data present a robust test of the bi-directional model formulation. The OU very loose data is captured with excellent accuracy, while the OU dense data is captured with reasonable accuracy. The OU dense test was thought to be affected by sample inhomogeneity (discussed in Section 4.5), which may explain the poorer model performance. The results indicate that the bi-directional model formulation proposed by Houlsby *et al.* (2017) is appropriate for capturing the response of a monopile to multidirectional lateral loading.

As discussed in Section 7.3.4, series and parallel kinematic hardening models produce slightly different responses under multidirectional loading (Beuckelaers *et al.*, 2018). To explore this, computations are presented in Figure 7.7 using i) the series model used throughout this Chapter, and ii) an equivalent parallel model (as presented in *e.g.* Houlsby *et al.*, 2017). A range of rotation responses are presented for each model, corresponding to a $\pm 5\%$ variation in the value of σ_R used to define the backbone curve;

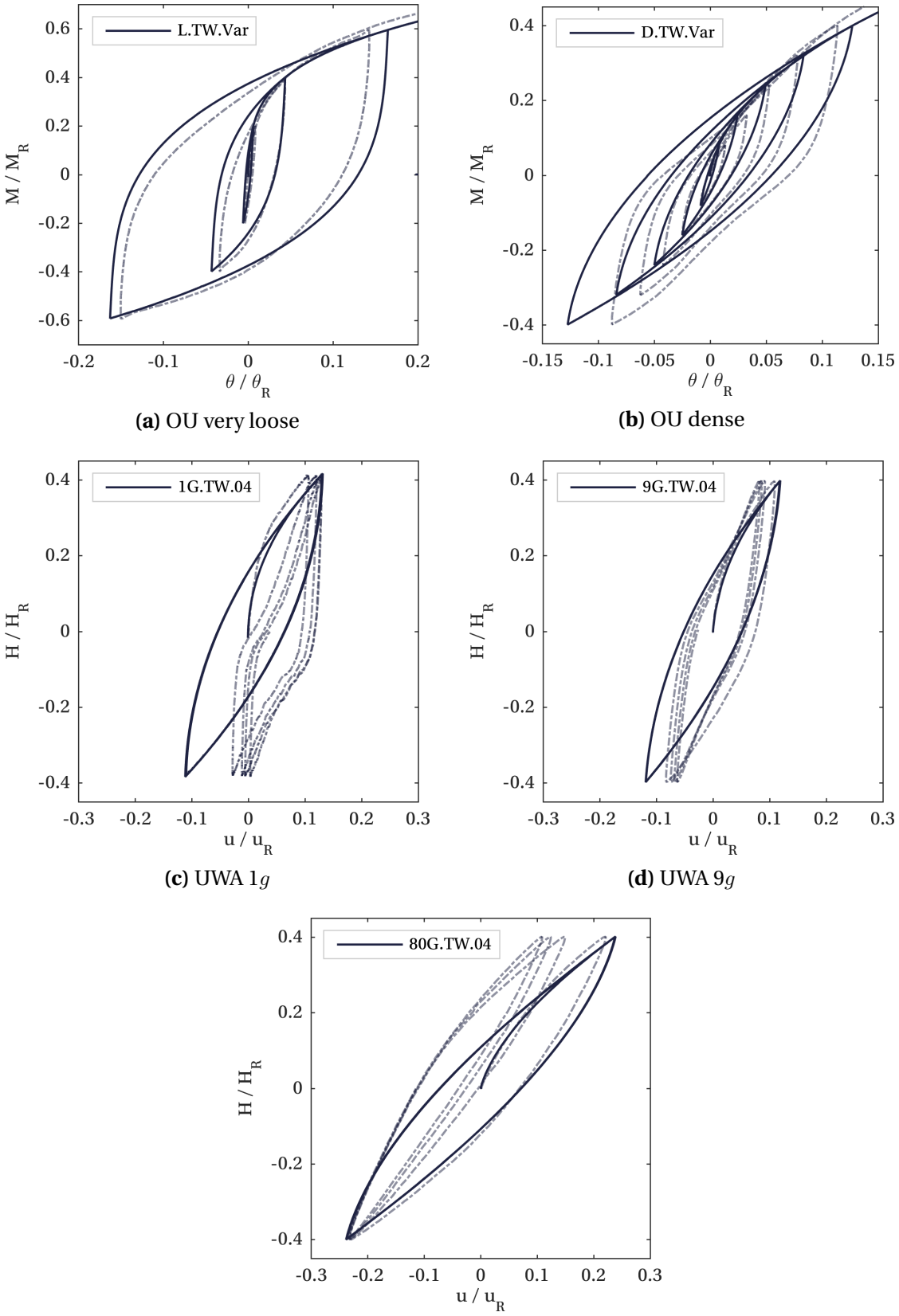

(a) OU very loose

(b) OU dense

(c) UWA $1g$

(d) UWA $9g$

(e) UWA $80g$

Figure 7.5: Computation of unidirectional hysteretic responses using unidirectional kinematic hardening model
(— model computations, ---- experimental data)

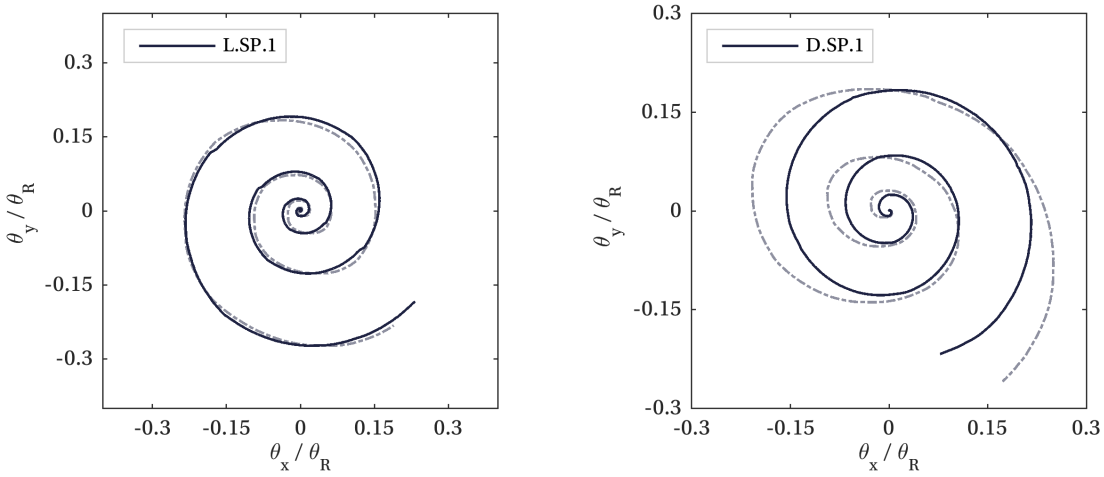

(a) OU very loose **(b)** OU dense

Figure 7.6: Computation of multidirectional hysteretic responses using bi-directional kinematic hardening model
(— model computations, ---- experimental data)

the range of responses therefore account for typical experimental variability. The difference in the computations is sufficiently subtle that, when experimental variability is accounted for, there is significant overlap in the predicted responses. The series model appears to perform better for the OU very loose dataset, but no such distinction can be made for the OU dense dataset; in general it is not possible to establish a preferred model on the basis of these tests. Indeed, additional trial computations suggest that it may not be possible to devise a multidirectional test which is able to establish a preferred model.

7.5 Capturing the high-cycle response

This Section explores the ability of models in the HARM framework to capture the high-cycle response, which includes ratcheting and stiffening. Unidirectional and bi-directional hyperplastic ratcheting models (Houlsby *et al.*, 2017) are first presented, before discussing evolution functions and calibration, and finally computing the responses to regular cyclic loading and multi-amplitude storm loading.

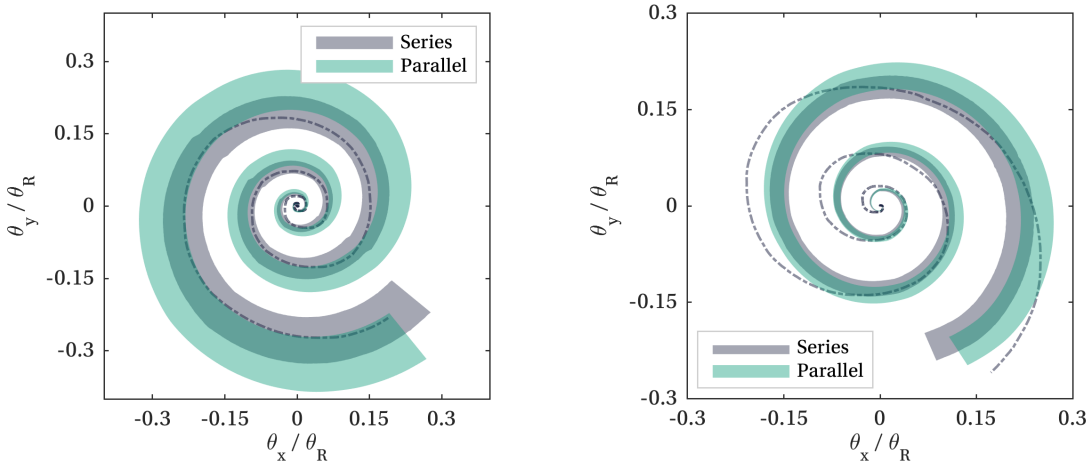

(a) OU very loose **(b)** OU dense

Figure 7.7: Comparison of series and parallel bi-directional kinematic hardening model computations with $\pm 5\%$ variation in σ_R
(- - - - experimental data)

7.5.1 Unidirectional hyperplastic ratcheting model

The unidirectional ratcheting model builds on the unidirectional kinematic hardening model presented in Section 7.4.1, and was presented and demonstrated by Houlsby *et al.* (2017). The Helmholtz free energy function f and dissipation function d both include a contribution from ratcheting strain α_r, which plays the role of an additional internal variable:

$$f = \frac{H_0}{2}\left(\varepsilon - \sum_{m=1}^{M} \alpha_m - \alpha_r\right)^2 + \sum_{m=1}^{M} \frac{H_m}{2}\alpha_m^2 \tag{7.30}$$

$$d = \left(\sum_{m=1}^{M} K_m |\dot{\alpha}_m|\right) + \sigma\dot{\alpha}_r \tag{7.31}$$

Where a constraint defines the ratcheting strain α_r:

$$c = \dot{\alpha}_r - \frac{\sigma}{|\sigma|}\sum_{m=1}^{M} R_m |\dot{\alpha}_m| = 0 \tag{7.32}$$

The model's constitutive behaviour is derived as:

$$\sigma = \frac{\partial f}{\partial \varepsilon} = H_0\left(\varepsilon - \sum_{m=1}^{M} \alpha_m - \alpha_r\right) \tag{7.33}$$

$$\bar{\chi}_m = -\frac{\partial f}{\partial \alpha_m} = H_0\left(\varepsilon - \sum_{m=1}^{M} \alpha_m - \alpha_r\right) - H_m\alpha_m = \sigma - H_m\alpha_m \tag{7.34}$$

$$\bar{\chi}_r = -\frac{\partial f}{\partial \alpha_r} = H_0 \left(\varepsilon - \sum_{m=1}^{M} \alpha_m - \alpha_r \right) = \sigma \tag{7.35}$$

$$\chi_m = \frac{\partial d^*}{\partial \dot{\alpha}_m} = K_m \frac{\dot{\alpha}_m}{|\dot{\alpha}_m|} - \Lambda \frac{\sigma}{|\sigma|} R_m \frac{\dot{\alpha}_m}{|\dot{\alpha}_m|} \tag{7.36}$$

$$\chi_r = \frac{\partial d^*}{\partial \dot{\alpha}_r} = \sigma + \Lambda \tag{7.37}$$

$$\chi_r = \bar{\chi}_r \quad \Rightarrow \quad \Lambda = 0 \tag{7.38}$$

$$\chi_m = \bar{\chi}_m \quad \Rightarrow \quad \sigma - H_m \alpha_m = K_m \frac{\dot{\alpha}_m}{|\dot{\alpha}_m|} \tag{7.39}$$

The incremental total strain response is derived from Equation 7.33:

$$d\varepsilon = \frac{d\sigma}{H_0} + \sum_{m=1}^{M} d\alpha_m + d\alpha_r \tag{7.40}$$

While the constraint (Equation 7.32) defines the increment of ratcheting strain:

$$d\alpha_r = \frac{\sigma}{|\sigma|} \sum_{m=1}^{M} R_m |\dot{\alpha}_m| \tag{7.41}$$

This expression is consistent with *key behaviour 3* (Table 7.1), given that $d\alpha_r$ is aligned with the sign of the incremental load. The yield functions and incremental plastic strain are the same as for the kinematic hardening model, and are implicit in Equation 7.39. At yield, when $\dot{\alpha}_m \neq 0$:

$$y_m = |\sigma - H_m \alpha_m| - K_m = |\chi_m| - K_m = 0 \tag{7.42}$$

$$d\alpha_m = \frac{d\sigma}{H_m} \tag{7.43}$$

7.5.2 Bi-directional hyperplastic ratcheting model

The unidirectional ratcheting model presented in Section 7.5.1 is extended here for bi-directional loading, as proposed by Houlsby *et al.* (2017). This model builds on the bi-directional kinematic hardening model presented in Section 7.4.2, which was shown to capture the multidirectional hysteretic response in Section 7.4.4. The model is developed in terms of x- and y-components of stress σ and strain ε and is defined in terms of the Helmholtz free energy function f, dissipation function d and constraints c_x, c_y:

$$f = \frac{H_0}{2} \left(\left(\varepsilon_x - \sum_{m=1}^{M} \alpha_{mx} - \alpha_{rx} \right)^2 + \left(\varepsilon_y - \sum_{m=1}^{M} \alpha_{my} - \alpha_{ry} \right)^2 \right) + \sum_{m=1}^{M} \frac{H_m}{2} \left(\alpha_{mx}^2 + \alpha_{my}^2 \right) \tag{7.44}$$

$$d = \left(\sum_{m=1}^{M} K_m \sqrt{\dot{\alpha}_{mx}^2 + \dot{\alpha}_{my}^2} \right) + \sigma_x \dot{\alpha}_{rx} + \sigma_y \dot{\alpha}_{ry} \tag{7.45}$$

$$c_x = \dot{\alpha}_{rx} - \frac{\sigma_x}{\sqrt{\sigma_x^2 + \sigma_y^2}} \sum_{m=1}^{M} R_m \sqrt{\dot{\alpha}_{mx}^2 + \dot{\alpha}_{my}^2} = 0 \tag{7.46}$$

$$c_y = \dot{\alpha}_{ry} - \frac{\sigma_y}{\sqrt{\sigma_x^2 + \sigma_y^2}} \sum_{m=1}^{M} R_m \sqrt{\dot{\alpha}_{mx}^2 + \dot{\alpha}_{my}^2} = 0 \tag{7.47}$$

The model's constitutive behaviour is derived here in the x-direction only, for brevity:

$$\sigma_x = \frac{\partial f}{\partial \varepsilon_x} = H_0 \left(\varepsilon_x - \sum_{m=1}^{M} \alpha_{mx} - \alpha_{rx} \right) \tag{7.48}$$

$$\bar{\chi}_{mx} = -\frac{\partial f}{\partial \alpha_{mx}} = H_0 \left(\varepsilon_x - \sum_{m=1}^{M} \alpha_{mx} - \alpha_{rx} \right) - H_m \alpha_{mx} = \sigma_x - H_m \alpha_{mx} \tag{7.49}$$

$$\bar{\chi}_{rx} = -\frac{\partial f}{\partial \alpha_{rx}} = H_0 \left(\varepsilon_x - \sum_{m=1}^{M} \alpha_{mx} - \alpha_{rx} \right) = \sigma_x \tag{7.50}$$

$$\chi_{mx} = \frac{\partial d^*}{\partial \dot{\alpha}_{mx}} = K_m \frac{\dot{\alpha}_{mx}}{\sqrt{\dot{\alpha}_{mx}^2 + \dot{\alpha}_{my}^2}} - \Lambda \frac{\sigma_x}{\sqrt{\sigma_x^2 + \sigma_y^2}} R_m \frac{\dot{\alpha}_{mx}}{\sqrt{\dot{\alpha}_{mx}^2 + \dot{\alpha}_{my}^2}} \tag{7.51}$$

$$\chi_{rx} = \frac{\partial d^*}{\partial \dot{\alpha}_{rx}} = \sigma_x + \Lambda \tag{7.52}$$

$$\chi_{rx} = \bar{\chi}_{rx} \quad \Rightarrow \quad \Lambda = 0 \tag{7.53}$$

$$\chi_{mx} = \bar{\chi}_{mx} \quad \Rightarrow \quad \sigma_x - H_m \alpha_{mx} = K_m \frac{\dot{\alpha}_{mx}}{\sqrt{\dot{\alpha}_{mx}^2 + \dot{\alpha}_{my}^2}} \tag{7.54}$$

The incremental total strain response is derived from Equation 7.48 (the equivalent y-direction expression is also presented):

$$d\varepsilon_x = \frac{d\sigma_x}{H_0} + \sum_{m=1}^{M} d\alpha_{mx} + d\alpha_{rx} \qquad d\varepsilon_y = \frac{d\sigma_y}{H_0} + \sum_{m=1}^{M} d\alpha_{my} + d\alpha_{ry} \tag{7.55}$$

While the constraints (Equation 7.46 and 7.47) define the increments of ratcheting strain:

$$\begin{aligned} d\alpha_{rx} &= \frac{\sigma_x}{\sqrt{\sigma_x^2 + \sigma_y^2}} \sum_{m=1}^{M} R_m \sqrt{d\alpha_{mx}^2 + d\alpha_{my}^2} \\ d\alpha_{ry} &= \frac{\sigma_y}{\sqrt{\sigma_x^2 + \sigma_y^2}} \sum_{m=1}^{M} R_m \sqrt{d\alpha_{mx}^2 + d\alpha_{my}^2} \end{aligned} \tag{7.56}$$

These expressions are consistent with *key behaviour 3* (Table 7.1), with $d\alpha_r$ aligned with the incremental load direction. The yield functions y_m are the same as for the

bi-directional kinematic hardening model, and are implicit in Equation 7.54. At yield, when $\dot{\alpha}_{mx}^2 + \dot{\alpha}_{my}^2 \neq 0$:

$$y_m = \sqrt{(\sigma_x - H_m\alpha_{mx})^2 + (\sigma_y - H_m\alpha_{my})^2} - K_m = \sqrt{\chi_{mx}^2 + \chi_{my}^2} - K_m = 0 \tag{7.57}$$

$$d\alpha_{mx} = \lambda\frac{\chi_{mx}}{H_m} \qquad d\alpha_{my} = \lambda\frac{\chi_{my}}{H_m} \tag{7.58}$$

$$\lambda = \frac{\chi_{mx}d\sigma_x + \chi_{my}d\sigma_y}{K_m^2} \tag{7.59}$$

7.5.3 Calibration of ratcheting models

To capture ratcheting behaviour which decreases in rate with loading history, the ratcheting factor R_m is made a function of a scalar hardening parameter β. Changes in stiffness are also captured by making K_m vary with either the same, or a different, hardening parameter. It is more straightforward to evolve stiffness by evolving the slider strengths K_m than the spring stiffness H_m, as the derivatives of the Helmholtz free energy functions f would change if $H_m = f(\beta)$ (Houlsby *et al.*, 2017). Selection of the evolution functions $R_m = f(\beta)$ and $K_m = f(\beta)$ is discussed in detail in Section 7.5.4, and calibration of these functions is discussed in Section 7.5.5.

The parameters H_m and K_{m0} (the initial values of K_m) are initially calibrated following the approach for kinematic hardening models outlined in Section 7.4.3. However, the inclusion of ratcheting and stiffening causes the initial loading computation to depart from the backbone curve. It is therefore necessary to modify the initial parameters as part of evolution function calibration to ensure the backbone curve is followed on initial loading. Here, backbone correction was achieved by adjusting the H_m values, keeping the K_{m0} values unchanged. A two-parameter function was fitted to the variation of H_m with surface m ($H_m = Dm^E$), and the parameters (D, E) were optimised to minimise the error between the backbone curve and the initial loading computation affected by ratcheting and stiffening.

7.5.4 Evolution functions

This Section describes selection of the hardening parameter β and evolution functions $R_m = f(\beta)$ and $K_m = f(\beta)$, which control the computed ratcheting, stiffening, and related energy dissipation and post-cyclic response.

Hardening parameter β

The hardening parameter β should increase monotonically with loading history, but can take various forms. Houlsby *et al.* (2017) suggest both strain-type values ($\dot{\beta} = |\dot{\alpha}_r|$, $\dot{\beta} = \sum_{m=1}^{M} |\dot{\alpha}_m|$) and work-type values ($\dot{\beta} = \sigma\dot{\alpha}_r$, $\dot{\beta} = \sum_{m=1}^{M} K_m|\dot{\alpha}_m|$). The accumulated ratcheting strain $\dot{\beta} = |\dot{\alpha}_r|$ was used by Abadie (2015), Abadie *et al.* (2019a) and Beuckelaers (2017). However, a work-type hardening parameter is used here as this makes the evolution functions and parameters comparable between series and parallel model formulations. The hardening parameter was also chosen to evolve with plastic strain α_m, rather than ratcheting strain α_r, as this eases calibration of the ratcheting evolution function R_m and allows stiffness evolution to be implemented independently of ratcheting behaviour. Local or surface-specific (β_m) and global (β) hardening parameters are defined here for bi-directional loading:

$$\dot{\beta}_m = \frac{K_m\sqrt{\dot{\alpha}_{mx}^2 + \dot{\alpha}_{my}^2}}{\sigma_R} \tag{7.60}$$

$$\dot{\beta} = \sum_{m=1}^{M} \dot{\beta}_m = \sum_{m=1}^{M} \left(\frac{K_m\sqrt{\dot{\alpha}_{mx}^2 + \dot{\alpha}_{my}^2}}{\sigma_R} \right) \tag{7.61}$$

The hardening parameters are independent of strain direction, allowing the evolution functions to evolve independently of cyclic loading direction to capture *key behaviour 8* (Table 7.1).

Function for R_m

The evolution function for R_m should capture the observed power-law evolution of ratcheting with cycle number n (*key behaviour 4*, Table 7.1). Abadie *et al.* (2015), Abadie *et al.* (2019a) and Beuckelaers (2017) captured the evolution of ratcheting with functions of the form:

$$R_m = R_0 \left(\frac{\beta}{\beta_0} \right)^{-m_r} \cdot f(K_m, \sigma, ...) \tag{7.62}$$

Where β_0 is the initial value of hardening parameter β, and is specified as an arbitrary small value. Although functions of this form are able to capture ratcheting under biased loading, the rate of change of R_m at small β is very large, which can significantly

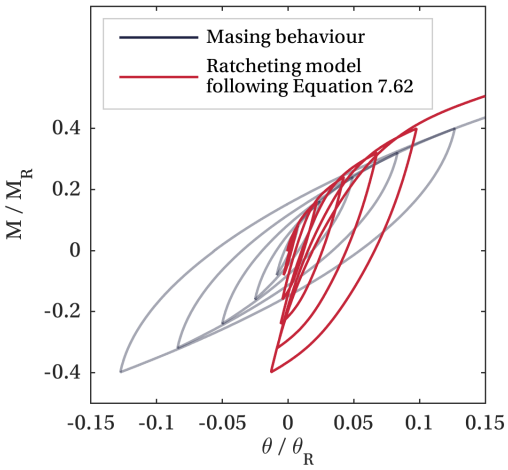

Figure 7.8: Example of distortion of Masing behaviour when using power-law expression for R_m

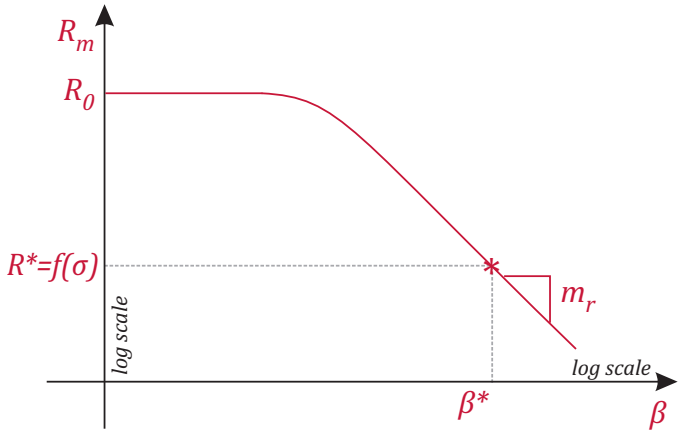

Figure 7.9: Illustration of proposed evolution function for R_m

distort Masing behaviour. Figure 7.8 exemplifies this effect with two computations for test D.TW.04: one using a kinematic hardening model and one using a ratcheting model employing the example evolution functions from Houlsby *et al.* (2017), which follow Equation 7.62.

Instead, a modified power-law function for R_m is proposed, which reduces distortion of Masing behaviour:

$$R_m = R_0 \left(1 + \frac{\beta}{\beta^*}\left(\left(\frac{R_0}{R^*}\right)^{\frac{1}{m_r}} - 1\right)\right)^{-m_r} \tag{7.63}$$

At large values of β this function resembles a power-law, but at small values of β the rate of change of the function is limited. Parameter R_0 is the value of the function at $\beta = 0$, exponent m_r is positive and controls the rate of change of the function

at large β, and the pair of parameters β^* and R^* ($R^* < R_0$) control the magnitude of the function (by pinning it to point $*$). As the parameters β^* and R^* are coupled, one is arbitrary. The function is illustrated in Figure 7.9 and may also be expressed in the following symmetric form:

$$\frac{1}{\beta}\left(\left(\frac{R_0}{R_m}\right)^{\frac{1}{m_r}}-1\right)=\frac{1}{\beta^*}\left(\left(\frac{R_0}{R^*}\right)^{\frac{1}{m_r}}-1\right) \tag{7.64}$$

The function for R_m should also capture the power-law increase in magnitude of ratcheting with cyclic amplitude (*key behaviour 5*, Table 7.1). Here, stress-dependency is captured by making R^* a function of stress σ. For bi-directional loading:

$$R^*=R^*_R\left(\frac{\sqrt{\sigma_x^2+\sigma_y^2}}{\sigma_R}\right)^{m_s} \tag{7.65}$$

Where R^*_R is the value of R^* at $\sqrt{\sigma_x^2+\sigma_y^2}=\sigma_R$ and the exponent m_s is positive. The resulting combined expression for R_m does not vary with surface m and is expressed here as R:

$$R=R_0\left(1+\frac{\beta}{\beta^*}\left(\left(\frac{R_0}{R^*_R\left(\frac{\sqrt{\sigma_x^2+\sigma_y^2}}{\sigma_R}\right)^{m_s}}\right)^{\frac{1}{m_r}}-1\right)\right)^{-m_r} \tag{7.66}$$

Figure 7.10 plots the variation of R with β and $\sqrt{\sigma_x^2+\sigma_y^2}/\sigma_R=|\sigma|/\sigma_R$, using example parameter values. The pinned point (β^*, R^*_R) is indicated $(*)$. The parameter β^* is defined in terms of a global work metric in Equation 7.73.

Function for K_m

To capture the change in secant stiffness k_n under cyclic loading the slider strengths K_m are made a function of the hardening parameter β and expressed in terms of $\kappa = K_m/K_{m0}$. In order to use experimental secant stiffness k_n values to inform the choice of evolution function for K_m (or equivalently κ), the relationship between κ and secant stiffness k_n is first explored.

Figure 7.11 shows how κ scales the computed backbone curves, for the example case of $\kappa = 2$. The increase in secant stiffness (between σ_1 and σ_2, where $\sigma_2 > \sigma_1$) for a given κ may be approximated with the Masing rules, given an analytical expression

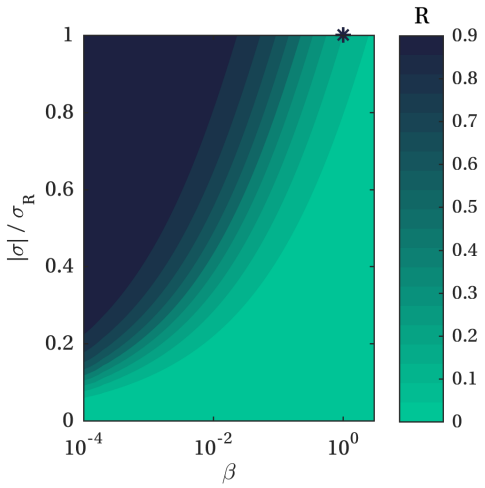

Figure 7.10: Variation of R (Equation 7.66) with β and $|\sigma|/\sigma_R$ ($R_0 = 1, m_r = 0.85, \beta^* = 1, R_R^* = 0.2, m_s = 3$)

for the backbone curve ($\varepsilon = f(\sigma)$). For a backbone curve defined with a power-law (Equation 7.27) secant stiffness approximately varies with κ as:

$$\frac{k_n}{k_0} = \frac{\frac{\sigma_1-\sigma_2}{E_i} + 2\left(\varepsilon_R - \frac{\sigma_R}{E_i}\right)\left(\frac{\sigma_1-\sigma_2}{2\sigma_R}\right)^{P_p}}{\frac{\sigma_1-\sigma_2}{E_i} + 2\kappa^{1-P_p}\left(\varepsilon_R - \frac{\sigma_R}{E_i}\right)\left(\frac{\sigma_1-\sigma_2}{2\sigma_R}\right)^{P_p}} \tag{7.67}$$

Where k_0 is the initial secant stiffness. Meanwhile, for a backbone defined with the Jeanjean expression (Equation 7.28):

$$\frac{k_n}{k_0} = \frac{\frac{\sigma_1-\sigma_2}{E_i} + 2\left(\varepsilon_R - \frac{\sigma_R}{E_i}\right)\left(\arctan\left(\frac{\sigma_1-\sigma_2}{2\sigma_R}\tanh(P_j)\right)/P_j\right)^2}{\frac{\sigma_1-\sigma_2}{E_i} + 2\kappa\left(\varepsilon_R - \frac{\sigma_R}{E_i}\right)\left(\arctan\left(\frac{\sigma_1-\sigma_2}{2\kappa\sigma_R}\tanh(P_j)\right)/P_j\right)^2} \tag{7.68}$$

Figure 7.12 plots k_n/k_0 for the OU dense backbone curve to demonstrate the non-linear dependency of k_n/k_0 on both σ and κ; the dependency is similar for the other backbone curves.

Accounting for this non-linear dependency, approximate experimental values for κ (κ_e) are determined from measured secant stiffness k_n values by employing Equation 7.67 or 7.68 with parameter values from Table 7.2. These values are plotted against cycle number n in Figure 7.13 for exemplar 1-way and 2-way tests from each dataset. Neglecting ratcheting, cycle number n is approximately proportional to β for regular cyclic loading. There is some variation in the shape of evolution of κ_e between 1-way and 2-way loading, consistent with the observed variation of stiffness evolution with

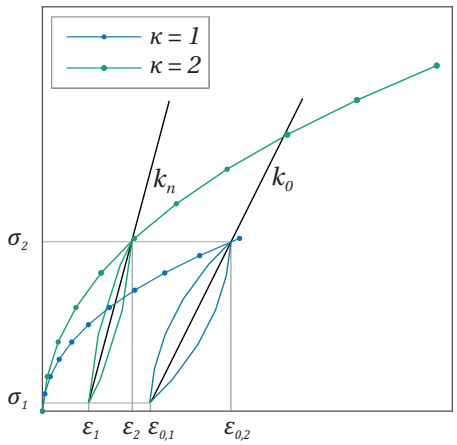

Figure 7.11: Illustration of impact of $\kappa = K_m/K_{m0}$ on secant stiffness k_n

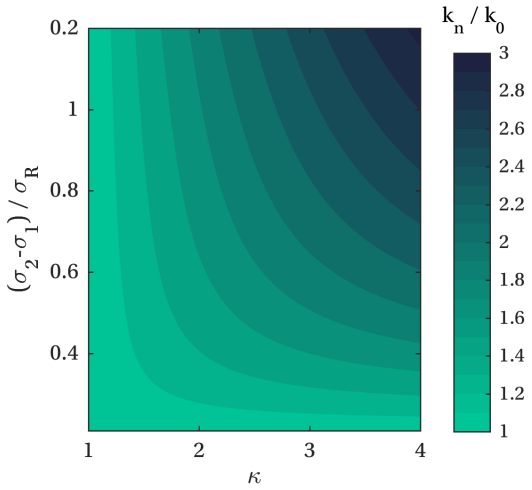

Figure 7.12: Approximate variation of secant stiffness k_n/k_0 with κ and $(\sigma_2 - \sigma_1)/\sigma_R$ for OU dense backbone curve

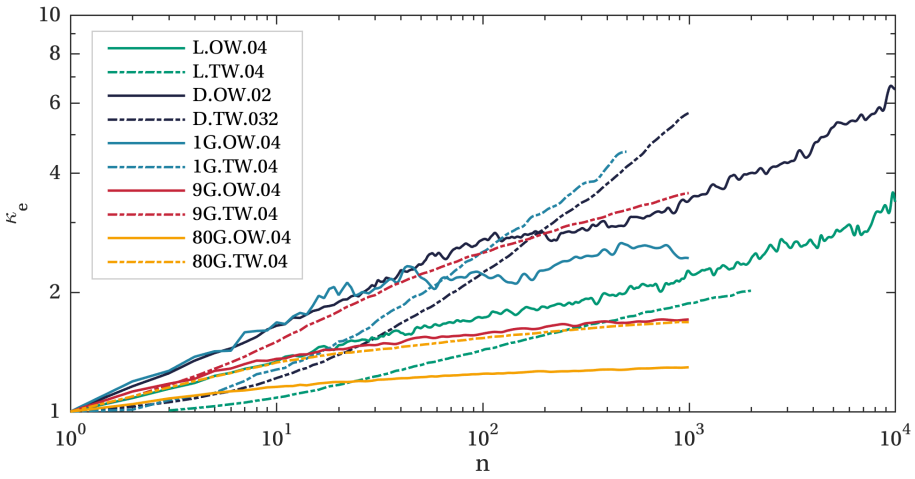

Figure 7.13: Variation of experimental value for κ (κ_e) with cycle number N (approximately proportional to β)

load type. The magnitude of κ_e also varies between datasets. However, overall, the data plots approximately linearly in log-log space and supports the use of a power-law to capture the evolution of κ with β. Power-law functions were also used by Abadie (2015), Houlsby *et al.* (2017) and Abadie *et al.* (2019a).

Modified power-laws with a similar functional form to that used for R are proposed to capture the evolution of stiffness. These functions approximate power-laws at large β and ensure $\kappa = 1$ at $\beta = 0$. Stiffening can be applied globally to all surfaces (as ratcheting is, employing global hardening variable β) or locally at each surface m (employing local

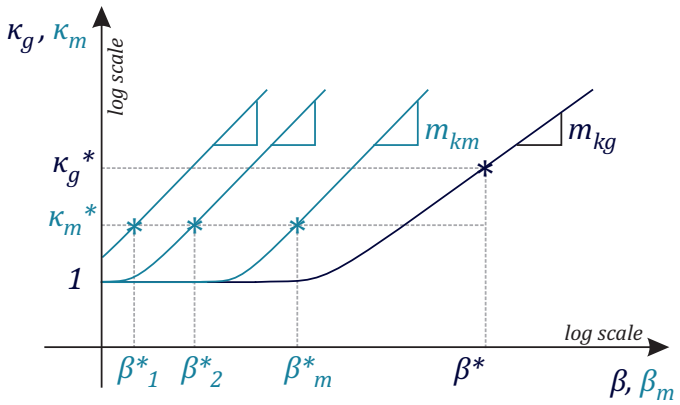

Figure 7.14: Illustration of proposed evolution functions for $\kappa_m = K_m/K_{m0}$ and $\kappa_g = K_m/K_{m0}$

hardening variable β_m). Local stiffness evolution is represented by κ_m (Equation 7.69) and global stiffness evolution by κ_g (Equation 7.70):

$$\kappa_m = \frac{K_m}{K_{m0}} = \left(1 + \frac{\beta_m}{\beta_m^*}\left(\kappa_m^{*(1/m_{km})} - 1\right)\right)^{m_{km}} \tag{7.69}$$

$$\kappa_g = \frac{K_m}{K_{m0}} = \left(1 + \frac{\beta}{\beta^*}\left(\kappa_g^{*(1/m_{kg})} - 1\right)\right)^{m_{kg}} \tag{7.70}$$

These functions are illustrated in Figure 7.14. At $\beta_m = 0$ or $\beta = 0$, the functions are equal to unity, while at large β_m or β the functions evolve as power-laws with exponents m_{km} or m_{kg}. Stiffening behaviour is captured with positive exponents, while softening behaviour can be captured with negative exponents (Balaam, 2020). The function magnitude is controlled by pairs of parameters (β_m^*, κ_m^*) or (β^*, κ_g^*). Although parameters κ_m^* and m_{km} control local stiffness evolution they are assumed not to vary with surface m.

The local stiffening expression (Equation 7.69) is able to capture changes in secant stiffness k_n (*key behaviour 7*, Table 7.1), while the global stiffening expression (Equation 7.70) is also able to capture changes in stiffness beyond the strained region, as observed during post-cyclic reloading (*key behaviour 10*, Table 7.1). Neither equation alters the initial stiffness H_0. Combined local and global stiffening may be captured with the following expression (Balaam, 2020), which partitions local (κ_m) and global (κ_g) stiffening with a factor ρ_κ:

$$\kappa = \frac{K_m}{K_{m0}} = \kappa_m^{\rho_\kappa}\kappa_g^{1-\rho_\kappa} \tag{7.71}$$

To ensure consistency of evolution of κ_m across the surfaces the local reference hardening parameter β^*_m is set as proportional to a surface-specific work quantity. Here, the following expression is used:

$$\beta^*_m = F_{\beta^*} \frac{K_u K_{m0}}{H_m} \tag{7.72}$$

Where $K_u = K_{m0}$ at $m = M$. Alternatively, $\beta^*_m = F_{\beta^*} K^2_{m0}/H_m$ may be used, which leads to very similar results. The global reference hardening parameter β^* may then be set as a corresponding global parameter. Here, the following expression is used:

$$\beta^* = F_{\beta^*} 2A \tag{7.73}$$

Where A is the area beneath the backbone curve $(\varepsilon_m, \sigma_m)$ to K_u.

7.5.5 Evolution function parameters

Table 7.3 summarises the necessary parameters for calibration of the evolution functions for R (Equation 7.66) and K_m (Equations 7.69, 7.70 and 7.71). Four parameters calibrate the evolution of R while five parameters calibrate the evolution of K_m. However, the local and global stiffening parameters are chosen to be equal here ($m_{kg} = m_{km}$, $\kappa^*_g = \kappa^*_m$), for simplicity. Additionally, parameter F_{β^*} controls the value of the reference hardening parameters β^* and β^*_m. With $F_{\beta^*} = 5$ the reference hardening parameters tend to locate where the functions approximate power-laws, which increases parameter independence and therefore eases calibration; larger values of F_{β^*} would also be appropriate.

The evolution function parameters were manually chosen to approximately fit the regular, unidirectional, 1-way cyclic loading data. Focus was placed on capturing the ratcheting and stiffness evolution at high cycle numbers — and in combination — the post-cyclic reloading response. The resulting parameters are summarised in Table 7.4 for each dataset. Calibration methods are not explored in detail here, although the sensitivity of the computations to the parameters is explored. Analytical calibration methods have been presented by Abadie *et al.* (2019a) (for alternative evolution functions), while Balaam (2020) is exploring methods for calibration of HARM models from element testing data.

	R evolution function parameters (Equation 7.66)
R_0	Value of R at $\beta = 0$ and $\|\sigma\| = \sigma_R$.
R_R^*	Value of R at $\beta = \beta^*$ and $\|\sigma\| = \sigma_R$, controls magnitude of R.
m_s	Positive exponent which controls the stress-dependency of the magnitude of R.
m_r	Positive exponent which controls the rate of reduction of R with β at large β.
	K_m evolution function parameters (Equations 7.69, 7.70, 7.71)
κ_g^*	Value of κ_g at $\beta = \beta^*$, controls the magnitude of κ_g.
κ_m^*	Value of κ_m at $\beta_m = \beta_m^*$, controls the magnitude of κ_m. Assumed not to vary with surface m.
m_{kg}	Exponent which controls the rate of change of κ_g with β at large β, positive for stiffening.
m_{km}	Exponent which controls the rate of change of κ_m with β_m at large β_m, positive for stiffening. Assumed not to vary with surface m.
ρ_κ	Factor which partitions local and global stiffness change, $\rho_\kappa = 1$ for solely local stiffness change, $\rho_\kappa = 0$ for solely global stiffness change.
F_{β^*}	Factor which controls the value of β^* and β_m^*.

Table 7.3: Description of parameters for calibration of evolution functions

Parameter	OU very loose	OU dense	UWA $1g$	UWA $9g$	UWA $80g$
R_0	1	1	1	1	1
R_R^*	0.08	0.08	0.09	0.03	0.01
m_s	2.8	2.2	3.2	3.2	3.2
m_r	0.65	0.65	0.8	0.9	1.0
$\kappa_g^* = \kappa_m^*$	2	2	2	2	2
$m_{kg} = m_{km}$	0.1	0.3	0.3	0.1	0.06
ρ_κ	0.7	0.7	0.7	0.7	0.7
F_{β^*}	5	5	5	5	5

Table 7.4: Summary of evolution function parameters manually calibrated to fit the regular, unidirectional, 1-way cyclic loading responses

Figure 7.15 explores the sensitivity of the computations to the parameter values for an example 1-way test in the UWA $9g$ dataset (9G.OW.03). The impact of each parameter on either ratcheting, secant stiffening or reloading is explored in turn, keeping the remaining parameters constant and equal to the values chosen for the UWA $9g$ dataset and presented in Table 7.4. For parameters R_R^*, m_s, m_r and $m_{kg} = m_{km}$, sensitivity is explored across the range of parameter values obtained by manual calibration to each of the five datasets. For parameters $R_0, \kappa_g^* = \kappa_m^*$ and ρ_κ,

where the parameter values do not vary across the manual calibrations, sensitivity is explored across an arbitrary parameter range.

Figure 7.15b, c, d, f shows that the computations are sensitive to parameters R^*_R, m_s, m_r and $m_{kg} = m_{km}$ across the range of values obtained in manual calibration. Parameters R^*_R and m_s affect ratcheting magnitude as expected, but also impact ratcheting rate. Meanwhile, parameter m_r only subtly affects ratcheting rate across the range of values obtained in manual calibration, but also impacts ratcheting magnitude. Parameter $m_{kg} = m_{km}$ affects the rate of stiffness evolution, as expected.

Figure 7.15a shows that the computations are not sensitive to R_0 across $0.1 \leq R_0 \leq 10$, which justifies the choice of a constant value for all computations. $R_0 = 1$ was chosen as ratcheting strain $d\alpha_r$ tends to be small compared to the associated plastic strain $\sum_{m=1}^{M} d\alpha_m$ (this is not, however, a theoretical requirement).

A constant value of parameter $\kappa^*_g = \kappa^*_m$ was found to be suitable across the datasets, however, Figure 7.15e demonstrates that the computations are sensitive to this parameter across the arbitrary range $1.5 \leq \left(\kappa^*_g = \kappa^*_m\right) \leq 5$. A constant value of ρ_κ was also found to be suitable across the datasets. Indeed, including some global stiffening ($0 \leq \rho_\kappa < 1.0$) ensures that $K_i < K_{i+1}$ as K_m evolves and avoids the computation of an elastic hysteretic response (which would occur if $K_i \geq K_{i+1}$ in the loading region). Figure 7.15g demonstrates the impact of ρ_κ on the reloading response over its defined range $0 \leq \rho_\kappa \leq 1$.

Some trends can be observed across the parameters obtained by manual calibration. In particular, parameters R^*_R and $m_{kg} = m_{km}$ decrease with increasing stress-level across the UWA datasets, consistent with the experimental observations in Chapter 6. The parameter m_s is also found to be approximately equal to experimental exponent m_σ, as highlighted in Figure 7.16. The experimental exponent m_σ captures the power-law variation of ratcheting magnitude with cyclic amplitude under 1-way loading (see Figure 4.8, Section 4.4.1; Figure 6.14, Section 6.5.2; Leblanc *et al.* (2010a) and Abadie (2015)). The similarity of these parameters may therefore be expected, as both capture the dependence of ratcheting magnitude on load. It would be appropriate to take $m_s = m_\sigma$ for initial calibration of this model to other datasets.

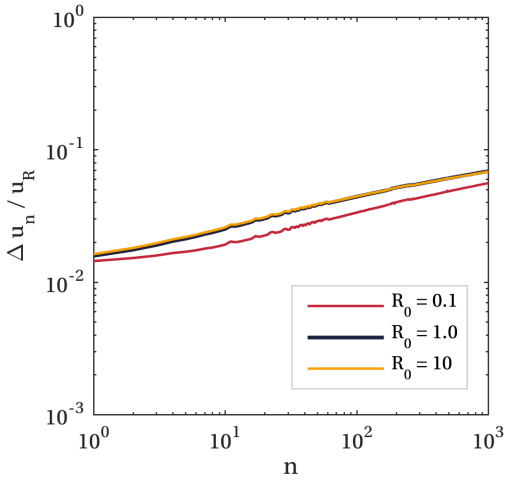

(a) R_0

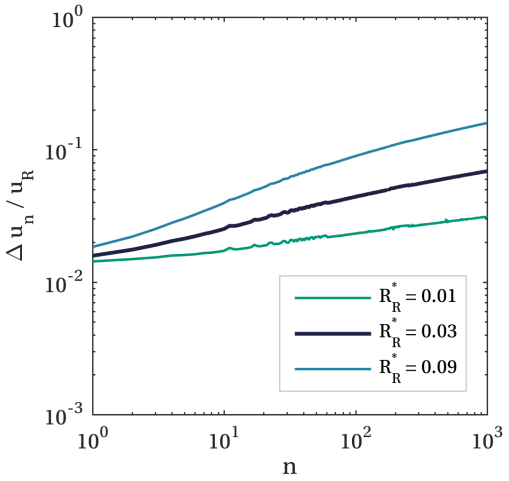

(b) R_R^*

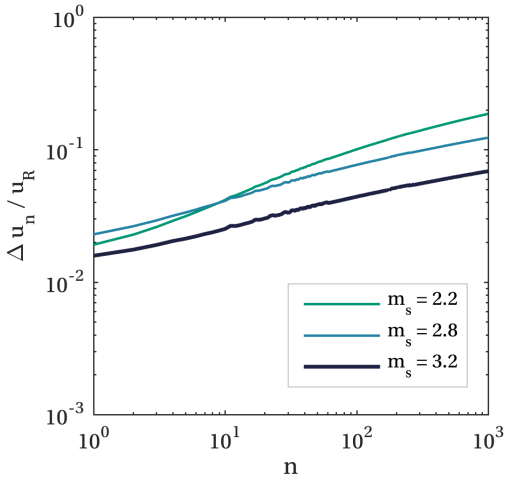

(c) m_s

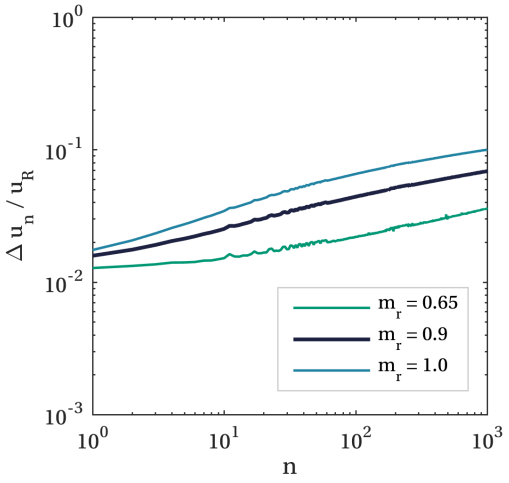

(d) m_r

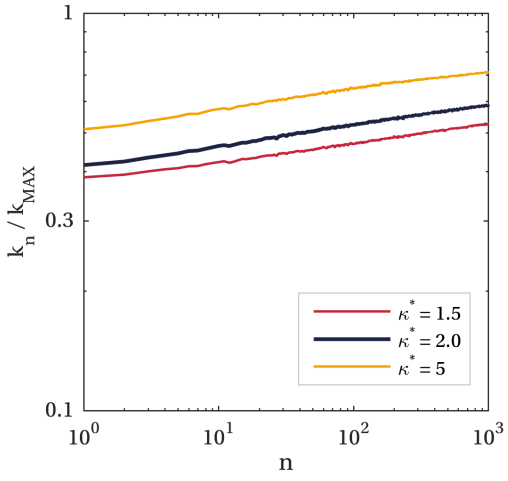

(e) $\kappa_g^* = \kappa_m^*$

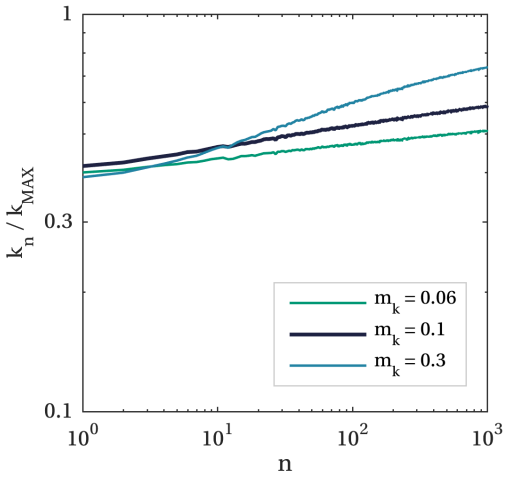

(f) $m_{kg} = m_{km}$

Figure 7.15: Exploration of sensitivity of computations to evolution function parameter values for example test in UWA 9g dataset (9G.OW.03)
(═ parameter values obtained in manual calibrations, ═ arbitrary parameter values)

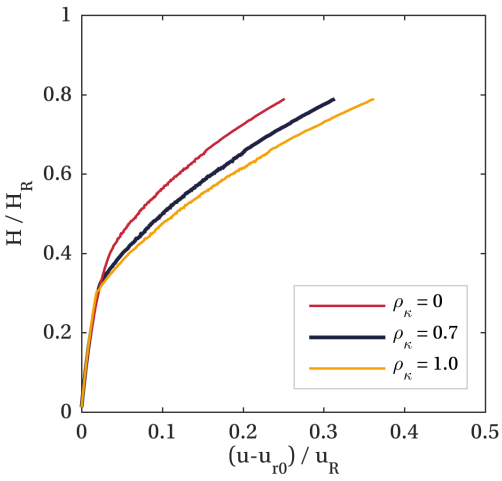

(g) ρ_κ

Figure 7.15: Exploration of sensitivity of computations to evolution function parameter values for example test in UWA 9g dataset (9G.OW.03)
(═ parameter values obtained in manual calibrations, ═ arbitrary parameter values)

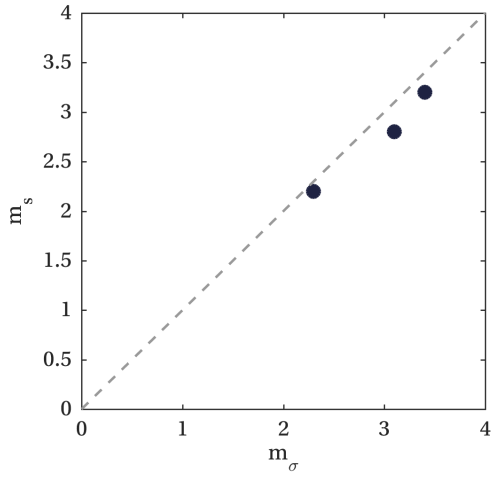

Figure 7.16: Correlation between experimental exponent m_σ and evolution function parameter m_s

7.5.6 Computation of regular cyclic loading response

Figures 7.17 to 7.21 present computations of the regular cyclic response for each of the five datasets, employing either the unidirectional ratcheting model described in Section 7.5.1 or the bi-directional ratcheting model described in Section 7.5.2, with the evolution functions presented in Section 7.5.4. Section 7.4.3 describes calibration of the backbone parameters K_m and H_m, while Table 7.4 summarises the evolution function parameters, which were manually calibrated to unidirectional, 1-way responses. For

the UWA datasets, computations are presented for all tests conducted, as summarised in Tables 6.3 and 6.4, Section 6.3. For the OU datasets, where a greater number of tests were conducted, computations are presented for a representative selection of the tests summarised in Tables 4.1 and 4.2, Section 4.2.

Each Figure (7.17 to 7.21) presents a unidirectional hysteretic response, the evolution of ratcheting, secant stiffness and energy loss factor under various unidirectional and multidirectional cyclic loadings, and post-cyclic reloading responses; a multidirectional hysteretic response is also presented for the OU datasets. The corresponding experimental responses are presented (dashed) alongside the computations, to facilitate direct comparison. Some aspects of the responses are captured very well and others are captured less well, but together, Figures 7.17 to 7.21 demonstrate the ability of the calibrated models to capture the overall patterns of behaviour observed experimentally.

The inclusion of ratcheting and stiffening precludes exact adherence of the model computations to the extended Masing rules. Nevertheless, Masing behaviour is not significantly distorted and the unidirectional hysteretic responses are generally captured with good accuracy; the OU very loose case is an exception, where pile rotation is significantly underestimated upon unloading to $M/M_R = 0.6$. In contrast, the multidirectional hysteretic responses (for the OU datasets) present a challenge for the model. Pile rotation is underestimated at both densities, perhaps due to too rapid an increase in K_m. However, the inability of the models to capture this response is not a key concern, as this loading is not representative of that experienced by monopiles.

The magnitude and evolution of ratcheting under unidirectional, 1-way cyclic loading is captured accurately at various load amplitudes across the five datasets; indeed, these data were used for calibration of the evolution function parameters. Under perpendicular cyclic loading ratcheting is overestimated for the UWA $1g$ dataset but is captured well for the remaining four datasets: ratcheting under L-shape loading is captured accurately in both directions, while ratcheting under T-shape loading tends to be slightly underestimated. Ratcheting under moderate ($\Phi = 30°$) fan-type loading is captured with reasonable accuracy for the OU datasets, although the models cannot

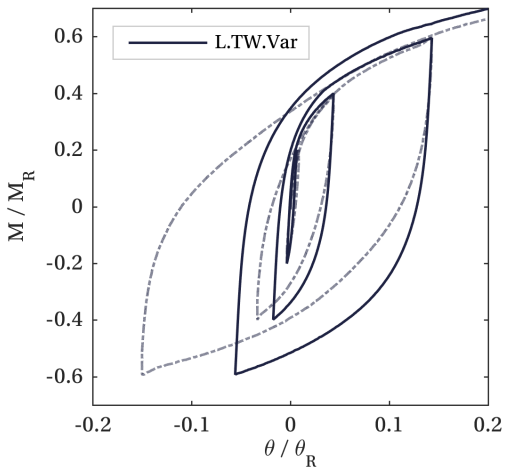

(a) Unidirectional hysteretic response

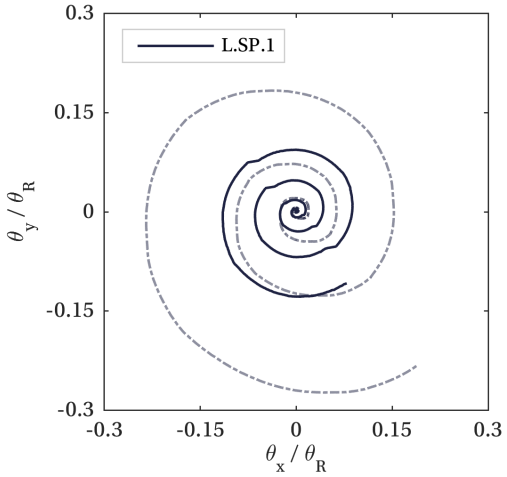

(b) Multidirectional hysteretic response

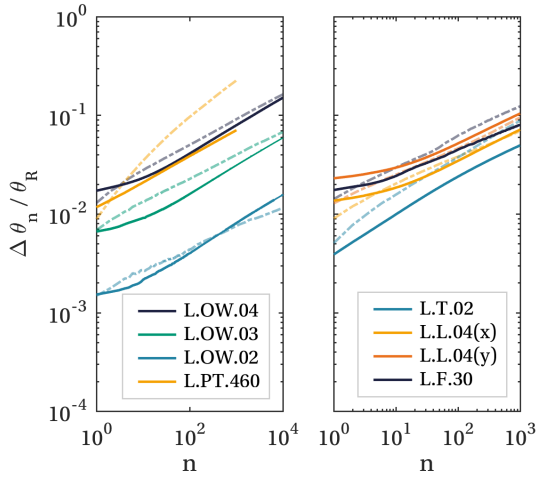

(c) Ratcheting response

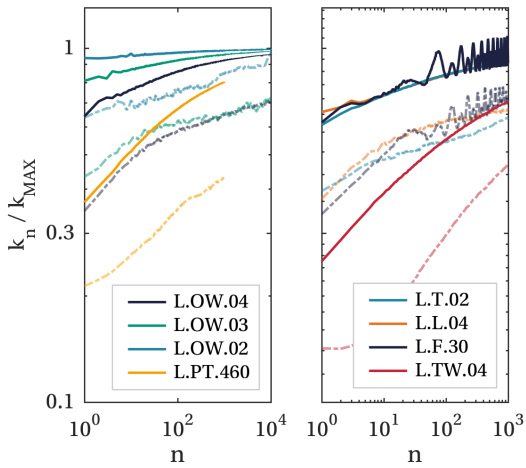

(d) Secant stiffening

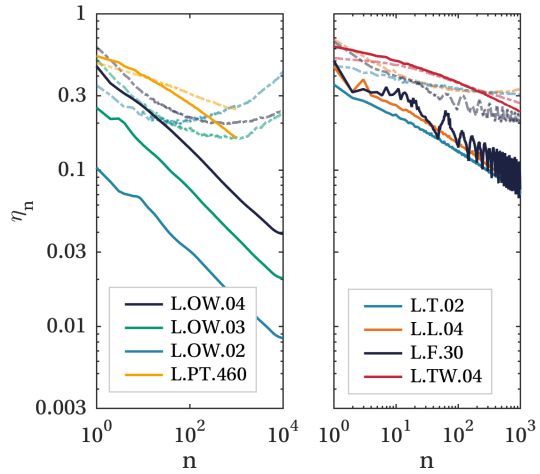

(e) Evolution of energy loss factor

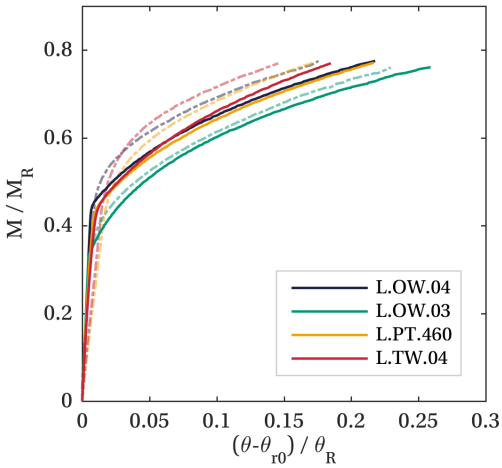

(f) Post-cyclic reloading

Figure 7.17: Computation of regular cyclic responses for OU very loose dataset using ratcheting models
(*E.g.* — model computations, ---- experimental data)

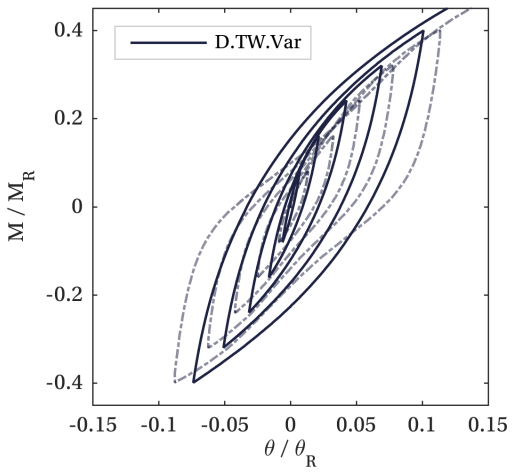

(a) Unidirectional hysteretic response

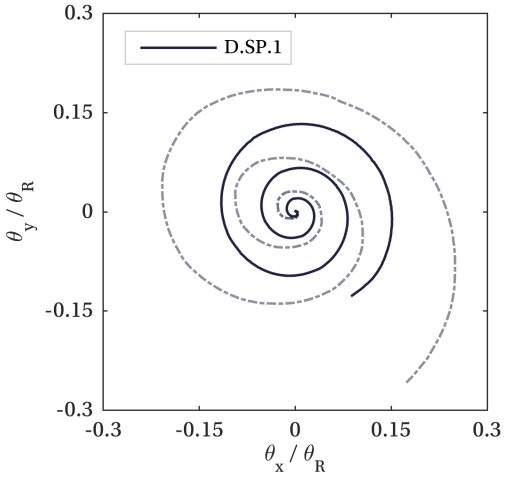

(b) Multidirectional hysteretic response

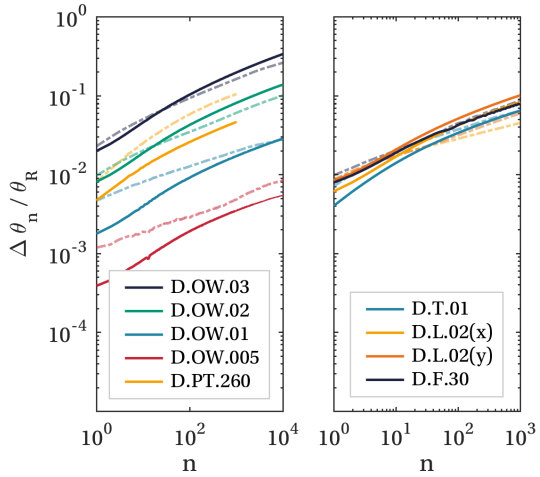

(c) Ratcheting response

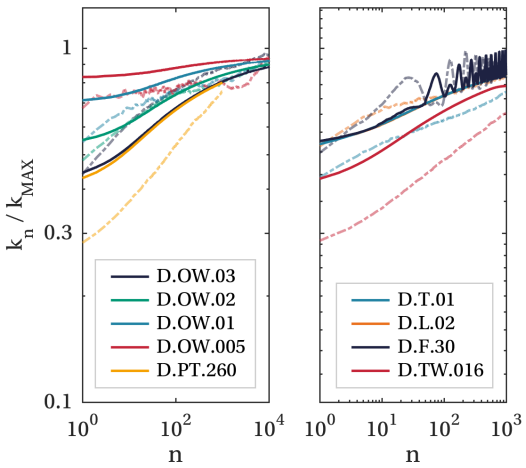

(d) Secant stiffening

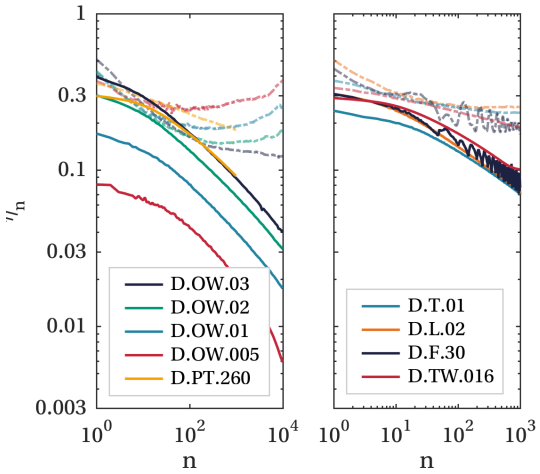

(e) Evolution of energy loss factor

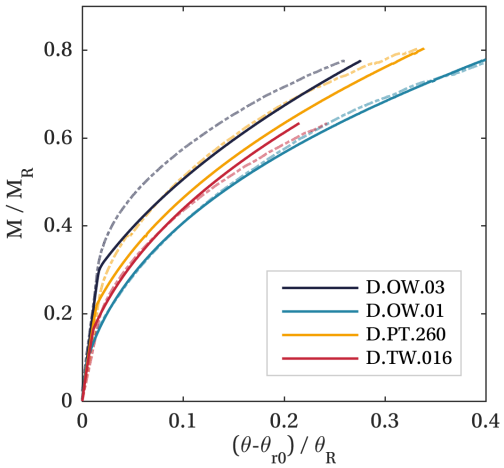

(f) Post-cyclic reloading

Figure 7.18: Computation of regular cyclic responses for OU dense dataset using ratcheting models

(*E.g.* — model computations, ---- experimental data)

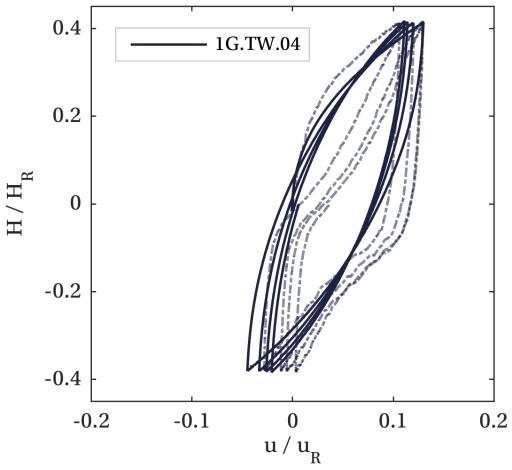

(a) Hysteretic response

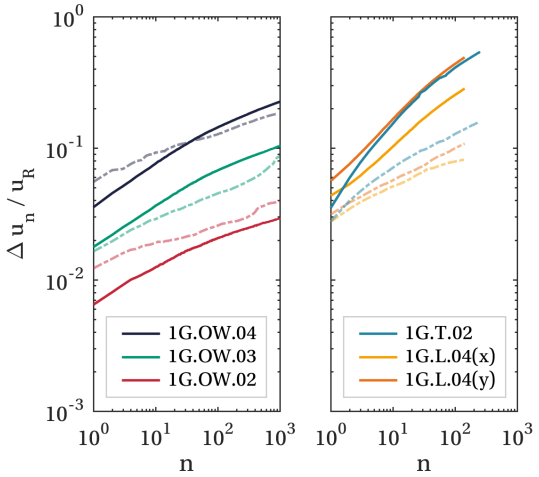

(b) Ratcheting response

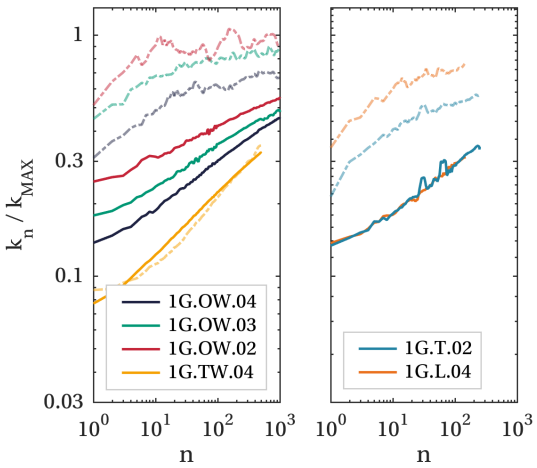

(c) Secant stiffening

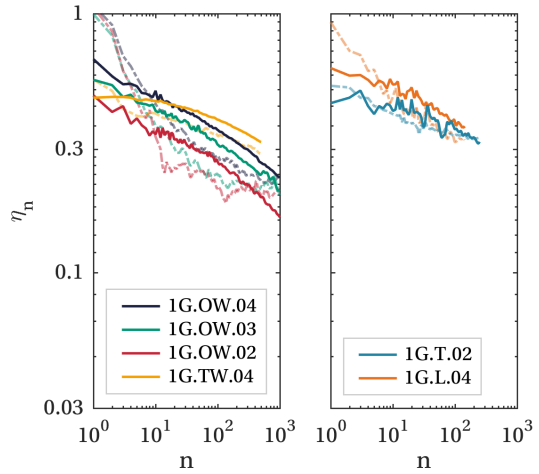

(d) Evolution of energy loss factor

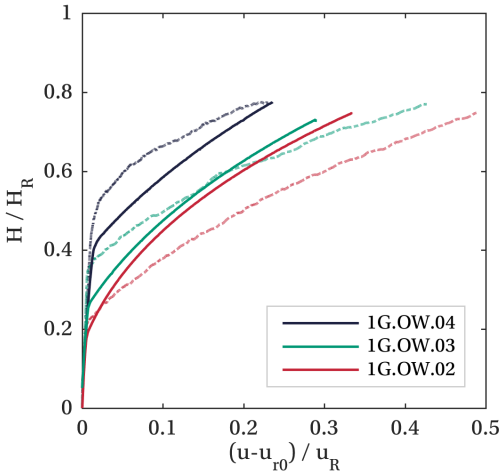

(e) Post-cyclic reloading

Figure 7.19: Computation of regular cyclic responses for UWA 1g dataset using ratcheting models
(*E.g.* — model computations, ---- experimental data)

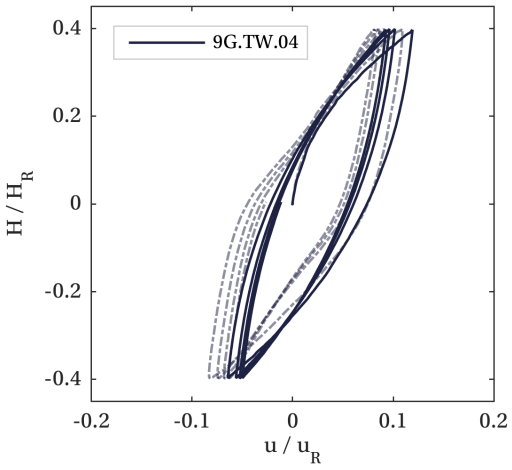

(a) Hysteretic response

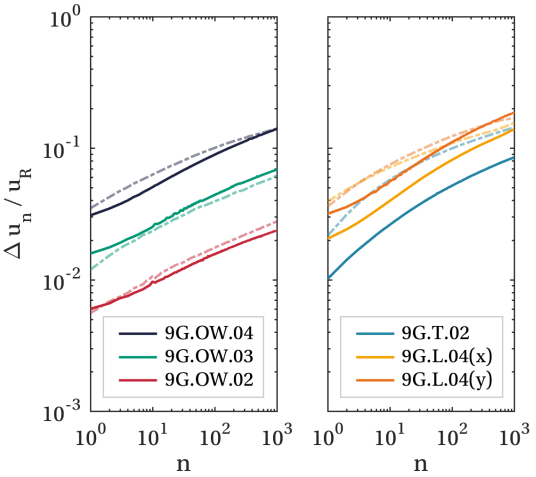

(b) Ratcheting response

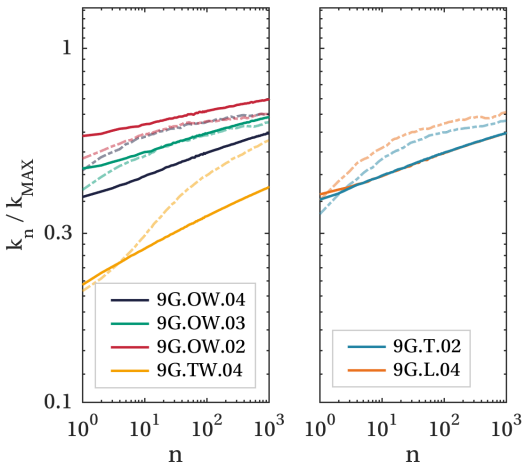

(c) Secant stiffening

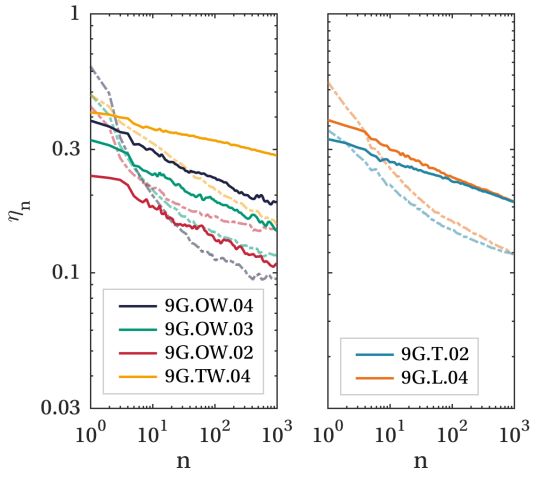

(d) Evolution of energy loss factor

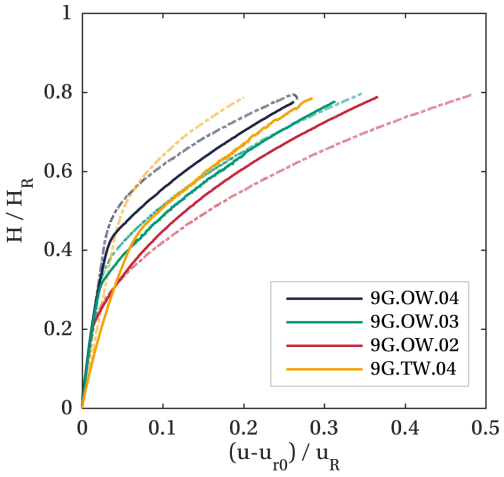

(e) Post-cyclic reloading

Figure 7.20: Computation of regular cyclic responses for UWA 9g dataset using ratcheting models
(*E.g.* — model computations, ---- experimental data)

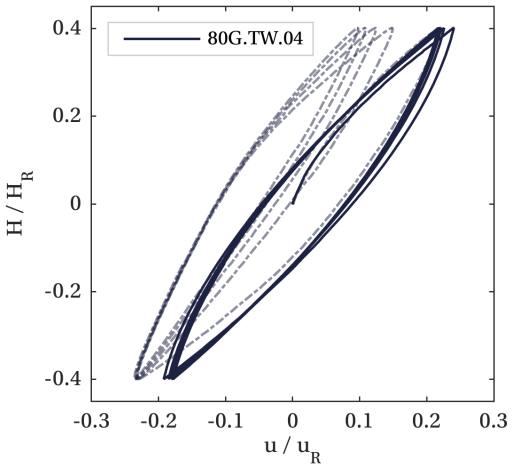

(a) Hysteretic response

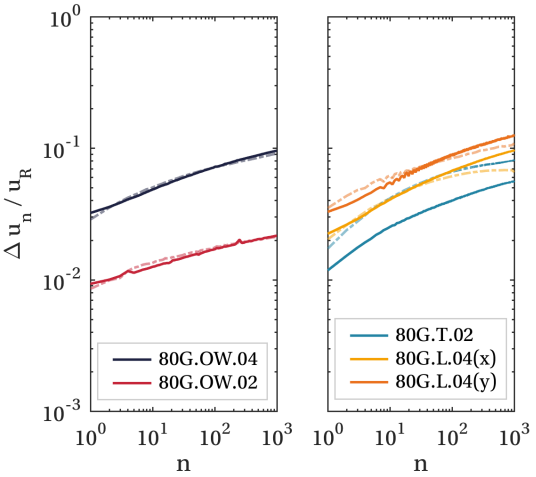

(b) Ratcheting response

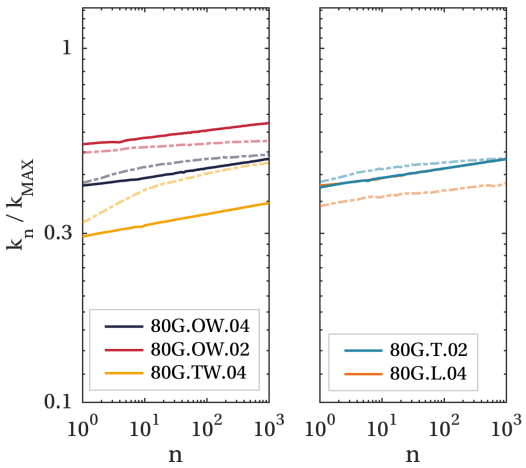

(c) Secant stiffening

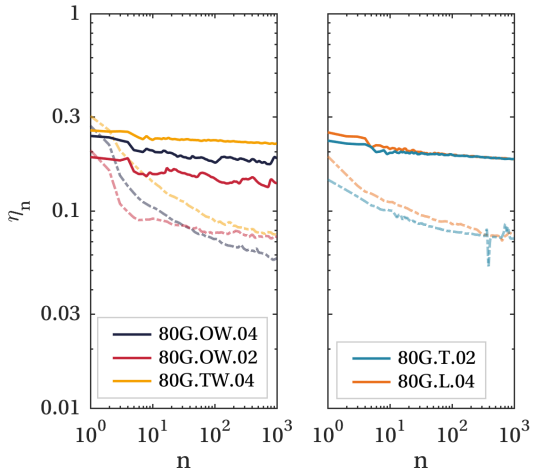

(d) Evolution of energy loss factor

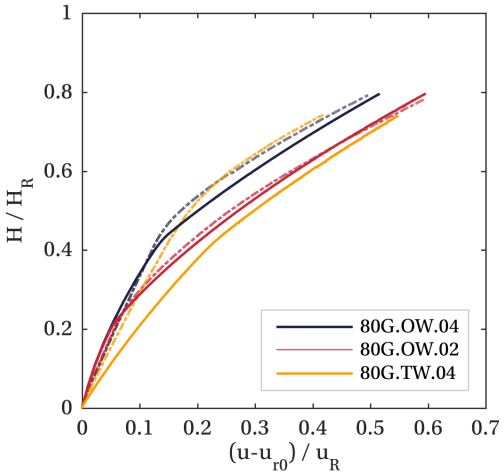

(e) Post-cyclic reloading

Figure 7.21: Computation of regular cyclic responses for UWA 80g dataset using ratcheting models
(*E.g.* — model computations, ---- experimental data)

capture the significant increase in ratcheting observed under fan-type loading at greater spread angles. The OU datasets also highlight the inability of the models to capture the increase in ratcheting that tends to be observed under partial 2-way loading.

The evolution of secant stiffness k_n under unidirectional, 1-way loading is captured reasonably well across the datasets. However, there is some variation in the magnitude of secant stiffness — which will also depend on the monotonic calibration — for the UWA $1g$ and OU very loose datasets. Under multidirectional (T-shape, L-shape and moderate fan-type) loading, the evolution of secant stiffness is generally captured as well as under unidirectional loading, while the stiffness evolution under 2-way and partial 2-way loading is often underestimated.

The magnitude and evolution of the energy loss factor η_n under unidirectional and multidirectional loading is captured very well for the UWA $1g$ dataset, reasonably well for the UWA $9g$ dataset and overestimated for the UWA $80g$ dataset. This trend is at odds with the increasing accuracy of the computed ratcheting and stiffness values for the UWA datasets as stress-level increases, and suggests that evolution of the energy loss factor may not be wholly explained by evolution of secant stiffness and ratcheting. For the OU datasets, energy loss factor is significantly and systematically underestimated where the experimental data is distorted by transducer friction contributions (at high cycle number and low cyclic amplitude). This represents a limitation of the experimental data, rather than the numerical model.

The post-cyclic reloading responses are captured approximately for the UWA $1g$ dataset and reasonably well for the remaining four datasets. However, the inferred capacity on reloading tends to be underestimated where secant stiffness evolution is underestimated (often under 2-way or partial 2-way loading).

Together, Figures 7.17 to 7.21 demonstrate the ability of the calibrated ratcheting models to capture ratcheting, evolution of stiffness and (in some cases) energy loss factor under unidirectional and multidirectional (perpendicular and moderate fan-type) cyclic loading at various cyclic amplitudes, in three sand densities and at multiple stress-levels. Distortion of Masing behaviour is limited and the post-cyclic reloading

responses are captured with reasonable success. The accuracy of the computations may also be improved by optimisation of the evolution function parameters.

The ability of the models to capture the response to perpendicular cyclic loading builds confidence in the bi-directional ratcheting model formulation. However, model development is necessary to capture the increase in ratcheting and stiffening under fan-type loading where $\Phi > 30°$. The models are also unable to capture the full impact of load asymmetry: ratcheting under partial 2-way loading is underestimated and stiffness evolution under 2-way and partial 2-way loading is often underestimated. This is of concern as much of the loading experienced by a monopile is expected to be partial 2-way (see *e.g.* Figure 5.6, Section 5.3.5). Development of a model which better captures the impact of load asymmetry would therefore be of great value.

7.5.7 Computation of response to storm loading

Figures 7.22 and 7.23 present computations for two example multidirectional storms using the ratcheting model presented in Section 7.5.2 with the evolution functions outlined in Section 7.5.4. The results for both the OU very loose and dense datasets are presented, in terms of the moment-rotation ($M - \theta$) response and rotation per cycle on loading (θ_{na}). The corresponding experimental responses are plotted alongside the computations for comparison, and the results are presented in the dominant loading direction (x) only. The computations used the same backbone parameters (K_m, H_m, Section 7.4.3) and evolution function parameters (Section 7.5.5) used to compute the regular cyclic loading responses in Section 7.5.6. The storm responses did not inform model calibration, but the responses were known at the time of model computation; the computations are therefore Class C1 predictions (Lambe, 1973).

In general, the computations capture the key features of the monopile response to storm loading: ratcheting is observed during application of small-amplitude cyclic loading but the response is dominated by large load events. The peak rotations are predicted particularly accurately in all cases. However, the OU very loose computations over-predict the rotation per cycle on loading (θ_{na}) for both tests, principally because the rotation accumulated across the peak load cycle (at $n \approx 1000$) is significantly over-predicted. This behaviour is related to the poor prediction of the hysteresis loop

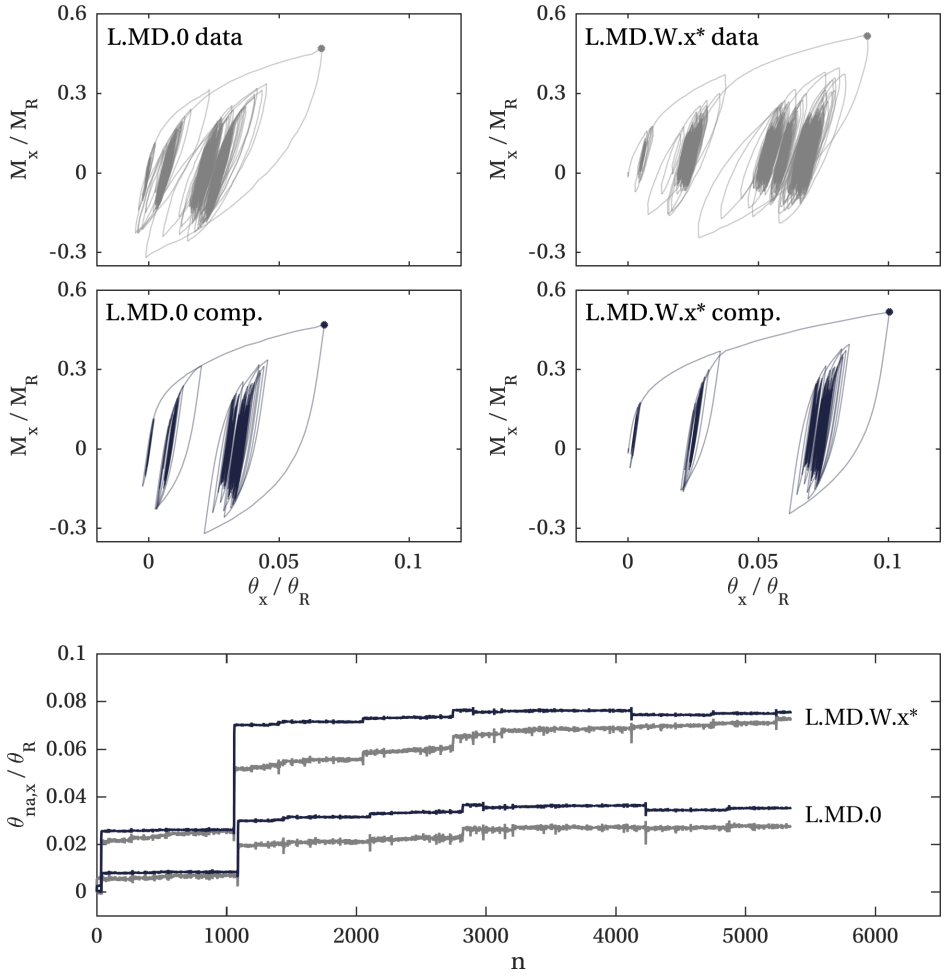

Figure 7.22: Computation of example storm responses for OU very loose dataset
* First half of test L.MD.W.x presented (— model computations, — experimental data, • peak load response)

shape, which is also observed in computation of the unidirectional hysteretic response for the OU very loose dataset (Figure 7.17a). The hysteretic response and evolution of θ_{na} can be better predicted by reducing the evolution of K_m (*e.g.* with $m_k = 0.01$), however, this would be at odds with the observed increase in secant stiffness under regular cyclic loading.

The hysteresis loop shapes are predicted more accurately for the OU dense computations, as too are the accumulated rotations across the peak loads (at $n \approx 750$). However, the rate of ratcheting under small amplitude cycling is slightly under-predicted, causing an under-prediction of the rotation per cycle on loading (θ_{na}) across the tests. This behaviour can also be observed in the OU very loose computations, and may be explained by the inability of the presented models to

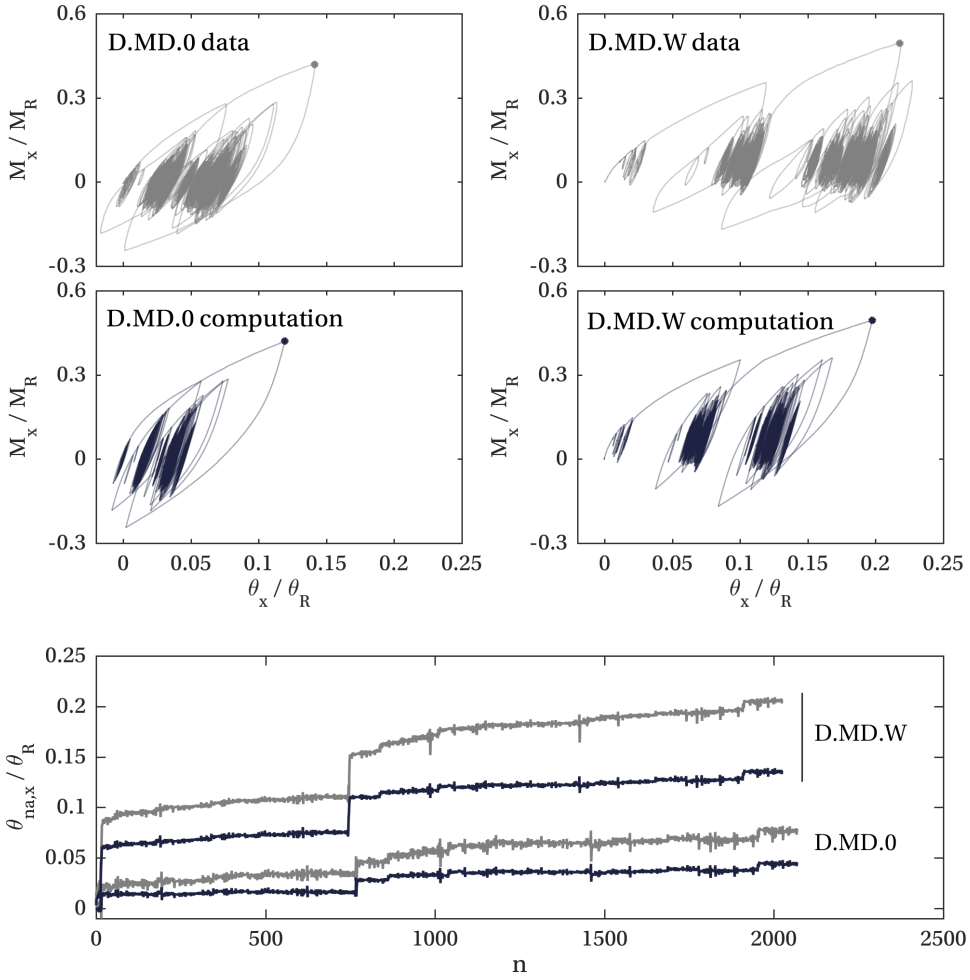

Figure 7.23: Computation of example storm responses for OU dense dataset (— model computations, — experimental data, • peak load response)

capture the increase in ratcheting under partial 2-way loading, which constitutes the majority of the loading in these example storms.

7.6 Prediction of prototype-scale response to storm loading

In this Section, a prototype-scale model is developed to allow exploration of the response of a monopile to storm loading at prototype-scale. This brief study reflects the overall aim of the coordinated programme of research to which this thesis contributes: to develop practical design methods to capture the response of full-scale monopiles to realistic cyclic lateral loading.

7.6.1 Generation of prototype-scale model

A prototype-scale ratcheting model is generated here by scaling the bi-directional ratcheting model (Section 7.5.2) for the UWA 80g dataset using the dimensionless framework presented by Leblanc *et al.* (2010a). An equivalent prototype-scale kinematic hardening model (Section 7.4.2) is also generated for comparison. The models are scaled to represent a prototype monopile with diameter 6.9 m and $L/D = 4$; the same size prototype was used to scale down the prototype-scale DeRisk loads to laboratory-scale for application in dense sand (see Section 5.3.4). There is confidence in the use of the dimensionless framework of Leblanc *et al.* (2010a) to account for the impact of foundation size and stress-level on the monotonic response (Kelly *et al.* (2006); Section 6.4.1), but the framework does not account for the impact of stress-level on ratcheting and stiffness evolution revealed in Chapter 6. The dimensionless framework is therefore used to scale the UWA 80g backbone curve, while the evolution function parameters calibrated to the UWA 80g dataset are used directly at prototype-scale (for the ratcheting model), given that the prototype-scale stress-level is close to that simulated in the UWA 80g tests.

Scale	Pile diameter D [m]	Pile length L [m]	Unit weight γ' [kN/m^3]	Normalised reference stress-level σ'_{REF}/p_a
UWA 80g	0.042	0.170	$17 \times 80 = 1360$	1.60
Prototype	6.9	27.6	7.12	1.36

Table 7.5: Parameters used for scaling UWA 80g models to prototype-scale

The laboratory- and prototype-scale parameters necessary for scaling the backbone curve are summarised in Table 7.5. The prototype-scale unit weight was determined by matching ϕ'_p between laboratory- and prototype-scale using the relations presented by Bolton (1987); the prototype soil is assumed to be saturated. The scaling factors on horizontal load f_H and pile displacement f_u are determined from the expressions presented in Table 3.4, Section 3.4.3. Employing the values in Table 7.5, the scaling factors become:

$$f_H = H_P/H_L = 22.67 \times 10^3 \tag{7.74}$$

$$f_u = u_P/u_L = 151.5 \tag{7.75}$$

Table 7.6 summarises the resulting prototype-scale backbone parameters, where the backbone is defined by a power-law (Equation 7.27). The prototype-scale parameters K_m and H_m are then obtained using Equations 7.25 and 7.26.

$\sigma_R = H_R$	$\varepsilon_R = u_R$	E_i	P_p
13.53 MN	2.70 m	33.04 MN/m	1.82

Table 7.6: Prototype-scale backbone curve parameters (backbone defined by a power-law, Equation 7.27)

7.6.2 Response to storm loading

Figure 7.24 presents the response of the prototype-scale models to an example storm. The responses are presented in the dominant loading direction (x) only, in terms of the load-displacement ($H-u$) response at $\tilde{e} = h/L = 2.5$ and the pile displacement per cycle on loading (u_{na}). The loading was derived from the DeRisk wave basin tests (described in Section 5.3) and corresponds to a multidirectional sea-state with a 100-year return period acting on a 7 m diameter cylinder, with additional constant wind loading (MD.W). The kinematic hardening and ratcheting models predict very similar pile displacement at peak load (≈ 1.8 m), approximately corresponding to $1.16°$ pile rotation (assuming the model monopile used for the UWA 80g tests was perfectly rigid). These displacements are towards the upper limit of what may be tolerated in ULS design, but are not unrealistic.

For both models, the hysteretic responses are more linear than observed under equivalent loading for the OU very loose and dense datasets, given the higher stress-level. For the ratcheting computation, the linearity of the cyclic response, coupled with evolution parameters which capture the (lower) rate of ratcheting at approximately prototype-scale stress-level, leads to prediction of negligible ratcheting between peak load cycles. However, the ratcheting model does predict greater accumulation of pile displacement across the peak load cycles than the kinematic hardening model. Some stiffening can be observed in the hysteretic response computed using the ratcheting model, although the change in loop shape is not significant.

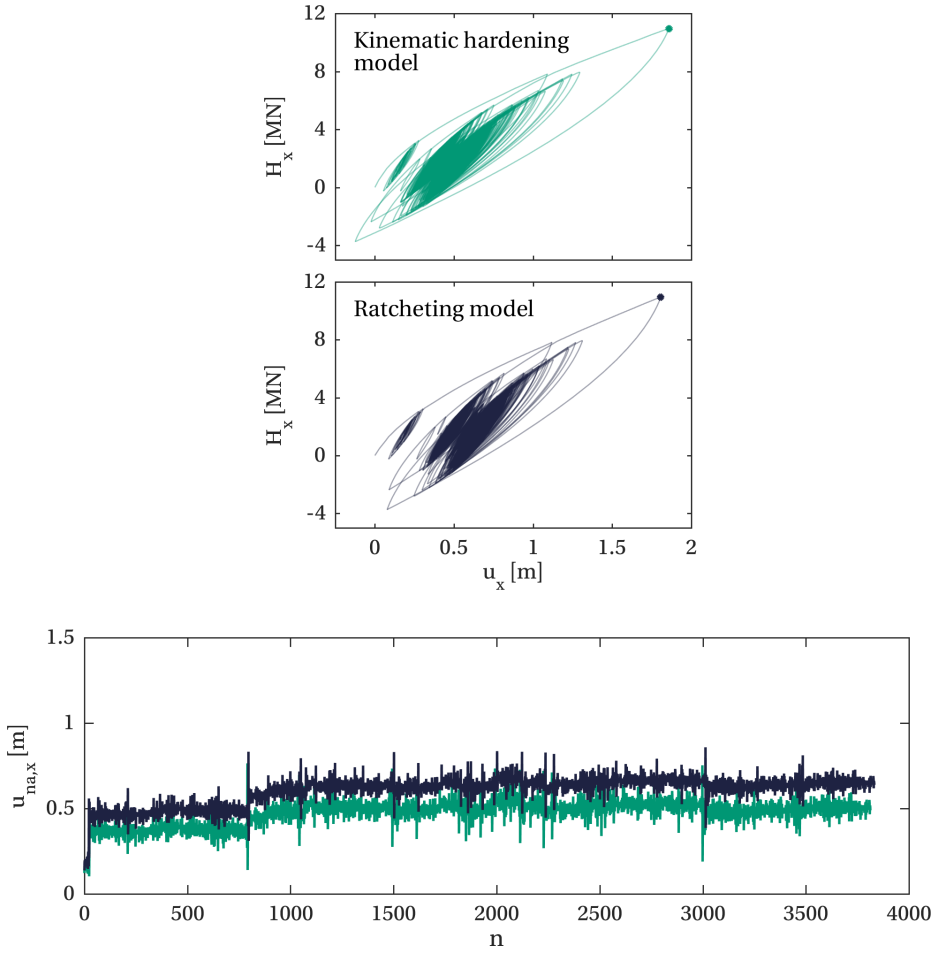

Figure 7.24: Computation of response of prototype-scale monopile to example storm (MD.W) (— kinematic hardening model, — ratcheting model, • response to peak load)

These computations suggests that a kinematic hardening model may approximately capture the peak response and hysteretic response over a short storm, but may underestimate the accumulation of pile displacement. Although the difference in the pile displacement computed using the two models is small for the short (6 hour) storm computed here, the contribution from ratcheting may become large over the $20 - 25$ year lifetime of the structure.

These computations demonstrate how numerical models, informed by experimental testing, can be used to explore prototype-scale responses when coupled with appropriate scaling techniques. However, validation of the scaling techniques (particularly the use of evolution function parameters calibrated to centrifuge tests at approximate prototype stress-level) through *e.g.* large-scale field testing may be necessary before such scaled models can be applied with confidence for full-scale

design.

7.7 Summary

	Key behaviour	Capturing key behaviour
1	The monopile exhibits a non-linear monotonic response.	Underlying kinematic hardening model is able to capture any monotonically increasing non-linear response.
2	The extended Masing rules are approximately adhered to during the first few loading cycles.	Underlying kinematic hardening model adheres to extended Masing rules, evolution functions and parameters chosen to minimise distortion of Masing rules.
3	Ratcheting occurs i) under biased cyclic loading and ii) in the direction of the mean load.	The ratcheting strain increment occurs in the direction of the incremental applied load (Equations 7.41 and 7.56).
4	Ratcheting evolves as a power-law with cycle number.	Evolution function for R (Equation 7.66) evolves as a power-law with hardening parameter β at large β.
5	The magnitude of ratcheting increases as a power-law with cyclic amplitude (for constant ζ_c).	The magnitude of R (Equation 7.66) varies as a power-law with incremental load magnitude.
6	Load asymmetry (ζ_c) affects the shape, rate and therefore magnitude of ratcheting.	Behaviour not fully captured: more ratcheting observed than predicted.
7	Secant stiffening occurs under cyclic loading and evolves logarithmically or as a power-law, depending on the load asymmetry.	Evolution function for K_m captures power-law increase in local K_m at large β_m, but impact of load asymmetry not captured.
8	The cyclic response is broadly independent of the cyclic loading direction, relative to the mean load direction.	Evolution of R and K_m depend on hardening parameter β (Equation 7.61) which is direction-independent.
9	Multidirectional fan-type loading can lead to greater ratcheting and stiffening than unidirectional loading.	Behaviour not fully captured: more ratcheting and stiffening observed than predicted.
10	The inferred capacity on post-cyclic reloading is equal to or greater than the monotonic capacity.	Evolution function for K_m can capture power-law increase in all (global) K_m at large β.

Table 7.7: Description of whether and how the key behaviours observed experimentally are captured with the presented ratcheting models

This Chapter has demonstrated the ability of constitutive models in the HARM framework to capture many key features of the response of a monopile to complex cyclic lateral loading in dry sand. Multi-surface kinematic hardening models were able

to capture the hysteretic response for the first few cycles of loading, but ratcheting models were necessary to capture the high-cycle response. Both unidirectional and bi-directional models were presented, formulated as rate-independent, series models and implemented as macro (single-element) models.

New evolution functions were proposed to capture the evolution of ratcheting and stiffness under cyclic loading. These functions avoid significant distortion of the Masing rules, are able to capture the post-cyclic reloading response and are calibrated with parameters which all have an interpretable impact on the computed cyclic response. The evolution functions are applicable to equivalent rate-dependent and parallel models, and are expected to be suitable for application in 1D Winkler models.

The ratcheting models were calibrated to the monotonic responses and the ratcheting and stiffening behaviour under regular, unidirectional, 1-way cyclic loading for five datasets (OU very loose, OU dense, UWA $1g$, UWA $9g$ and UWA $80g$). Computation of the cyclic response under a variety of regular cyclic loadings demonstrates the ability of the models to capture the majority of the key behaviours outlined in Table 7.1. Table 7.7 summarises whether and how each of the key behaviours are captured. A key limitation is the inability of the models to capture the full impact of load asymmetry and multidirectional fan-type loading (for $\Phi > 30°$) on the cyclic response.

The bi-directional ratcheting model, calibrated to regular, unidirectional, 1-way data, was also shown to capture the key features of the response to realistic, irregular, multi-amplitude and multidirectional storm loading. This result builds confidence in the use of models developed in the HARM framework for design in realistic loading scenarios. Models were also scaled to explore the potential response at prototype-scale, reflecting the overall aim of this research.

The development of practical calibration methods for the evolution function parameters, derived from standard element testing results, is essential if these models are to be used for design. Balaam (2020) is exploring the correlation between parameters calibrated to cyclic element tests using a single-element model and parameters calibrated to the response of monopile systems using a 1D Winkler model.

There is confidence that correlations between these parameters can be observed, given the similarity in the cyclic response observed in element tests and in model pile tests in similar soils (Truong *et al.*, 2019).

Chapter 8

Conclusions

8.1 Introduction

This thesis has explored the response of monopile foundations in sand to complex cyclic lateral loading through physical modelling. Regular cyclic loading tests allowed systematic investigation of monopile behaviour, while the application of storm loading and exploration of stress-level effects has provided insight into the response under realistic loading and at full-scale. The physical modelling data has also facilitated demonstration of the ability of models in the HARM framework to capture key features of the monopile response to complex cyclic lateral loading. Summary sections at the end of each Chapter have presented detailed conclusions; this Chapter distils the key contributions and implications for design, and makes suggestions for future work.

8.2 Key contributions

Development of novel laboratory apparatus for 1*g* monopile testing

New laboratory apparatus was developed to apply complex lateral loading to a model monopile. The loading and pile measurement apparatus, with associated *Labview* software, is capable of applying continuously varying, multi-amplitude and multidirectional loading under accurate load control, and was used to perform the 60 $1g$ tests at OU presented in Chapters 3, 4 and 5.

Regular cyclic loading response at 1*g*

Regular cyclic loading tests at $1g$ in very loose and dense sand revealed i) approximate adherence to the extended Masing rules over the first few loading cycles (Section 4.3),

ii) accumulation of pile rotation (ratcheting) under many cycles of biased loading (*e.g.* Section 4.4.1), and iii) evolution of the hysteretic response (characterised in terms of secant stiffness and energy loss factor) under many cycles of general cyclic loading (*e.g.* Sections 4.4.2 and 4.4.3), consistent with previous studies (*e.g.* Abadie, 2015). The results also highlighted the significant impact of load amplitude and load asymmetry.

Novel perpendicular multidirectional tests revealed that ratcheting occurs in the direction of mean load and that the cyclic response is insensitive to cyclic loading direction (Section 4.6.1), with implications for numerical modelling (Section 7.2). Meanwhile, spread fan-type loading tests demonstrated that an increase in ratcheting and secant stiffening is possible under multidirectional loading, compared to equivalent unidirectional loading (Section 4.6.2).

The post-cyclic reloading responses showed no decrease in capacity relative to the monotonic response, at odds with the conventional cyclic degradation approach (Section 4.7). In general, the behaviour in very loose and dense sand was qualitatively similar.

Application of realistic storm loading at 1*g*

Irregular, multi-amplitude and multidirectional storm loading was derived from wave tank tests performed as part of the DeRisk project (Section 5.2); careful processing of the loading data was necessary, particularly to ensure structural dynamic effects were accounted for. Application of these realistic loading signals to the model monopile led to behaviour consistent with that observed under regular cyclic loading, and highlighted the dominance of large load events (Section 5.4). The results suggested that, for a short storm, peak monopile rotation may be approximated by the monotonic response.

Investigating the effect of stress-level

Exploration of stress-level effects — through 21 monotonic, unidirectional and multidirectional cyclic loading tests — revealed qualitatively similar responses at g-levels from $1g$ to $80g$, building confidence in the applicability of observations made at $1g$ to full-scale. However, a logarithmic reduction in the exponents controlling the rate of ratcheting and secant stiffness evolution with stress-level was observed

(Sections 6.5.2 and 6.5.3). This suggests that the effects of cyclic loading will be significantly less pronounced at full-scale than observed in small-scale $1g$ physical modelling. These results help inform comparison of behaviour observed at different stress-levels, and support the dimensionless framework proposed by Leblanc *et al.* (2010a) for scaling of the monotonic response of the monopile (Section 6.4.1).

Modelling the response of a monopile to complex cyclic loading

Together, the physical modelling results facilitated demonstration of the ability of models in the HARM framework to capture key features of the monopile response to complex cyclic loading in (dry) sand at multiple stress-levels and in various densities, following calibration to regular, unidirectional data. Multi-surface kinematic hardening models were able to approximate the hysteretic response (Section 7.4.4), but ratcheting models were necessary to capture ratcheting and evolution of hysteresis loop shape under many cycles (Section 7.5.6).

The physical modelling results also informed new functions for capturing the evolution of ratcheting and hysteresis loop shape (Section 7.5.4). In particular, these functions limit distortion of Masing behaviour and improve the ability to capture the post-cyclic reloading response, analogous to the ULS response.

8.3 Key implications for design

Approximating the response to large loads

The monotonic response is likely to provide a conservative estimate for monopile rotation under ULS loading for drained conditions (Section 4.7 and 6.5.5), given that the inferred post-cyclic capacity on reloading was found to be equal to or greater than the monotonic capacity. The monotonic response may also be used to approximate the peak foundation rotation during a short storm (Section 5.5).

Assessment of loading conditions

Greater ratcheting and stiffening behaviour was observed under partial 2-way loading and spread multidirectional loading (Chapter 4). This highlights the need to accurately assess loading asymmetry and directionality before conducting cyclic design for monopile foundations.

Considering stress-level effects

The logarithmic reduction in the exponents controlling ratcheting and stiffening rate with stress-level (Sections 6.5.2 and 6.5.3) suggests that cyclic loading effects will be less pronounced at full-scale than observed in small-scale $1g$ physical modelling. As a result, direct application of empirical functions for ratcheting and evolution of stiffness with cycle number, derived from small-scale $1g$ physical modelling (*e.g.* Leblanc *et al.*, 2010a), are not recommended for full-scale design, although the expressions for ratcheting are likely to be conservative.

Modelling the cyclic response

Multi-surface kinematic hardening models may be appropriate for some dynamic design calculations (Section 7.4), but ratcheting models are necessary for predicting permanent monopile rotation and the effects of cyclic loading on foundation strength and stiffness. Models in the HARM framework are able to capture many aspects of the response to complex cyclic loading, but development of practical calibration methods for the evolution functions and parameters is required (Section 7.5). Accurate prediction of the monotonic response is a pre-requisite for models in the HARM framework (Section 7.4.3), and cyclic design in general.

Noting the stress-level effects discussed above, for preliminary full-scale cyclic design in sand, the evolution functions and parameters for the UWA $80g$ dataset might be employed, as this dataset most closely represents full-scale stress-levels. The limitations of the presented models to fully capture the impact of load asymmetry and spread multidirectional loading should, however, be considered.

8.4 Future work

Physical modelling

The physical modelling presented herein simulated fully-drained conditions, which may not be representative of field conditions (Section 3.2.2). Exploration of pore-pressure accumulation and the effect on the cyclic response under partial drainage conditions, in soils of representative permeability and under realistic loading rates,

would therefore be of great value. Exploration of the monopile response under complex cyclic loading in cohesive and layered soils would also complement this work.

Monopiles in the field are exposed to lateral loading with continuously varying loading eccentricity (Section 1.2.1), but a single loading eccentricity was used for the physical modelling presented herein. It would therefore be of interest to explore the effect of loading eccentricity, across a representative range, on the monotonic and cyclic response.

Exploration of stress-level effects

In exploration of stress-level effects in Chapter 6, a constant dimensional reference pile displacement u_R was employed (Section 6.5.1). As a result, the linearity of the responses (at a given normalised load) varied with stress-level. Although this variation in linearity may be interpreted as a stress-level effect, complementary insight into the effect of stress-level may be gained by elimination of the variation in linearity through selection of a dimensionless reference parameter *e.g.* $\tilde{u}_R$, following the dimensionless framework of Leblanc *et al.* (2010a). Ideally, a future study into stress-level effects would involve tests at a number of cyclic amplitudes such that the results could be interpreted in terms of i) a constant dimensional reference parameter *e.g.* u_R, and ii) a constant dimensionless reference parameter *e.g.* $\tilde{u}_R$, which minimises the variation in response linearity.

The centrifuge study presented herein was limited to simulation of monopiles 5.7 m in diameter (Section 6.1). Extension of this study to simulate prototype monopiles with diameters of 8–10 m would build confidence in the applicability of the presented trends at full-scale. Future testing may also consider using a driven installation method.

Loading investigations

Chapter 4 showed how spread multidirectional loading can lead to greater ratcheting and stiffening than equivalent unidirectional loading; for example, accumulated rotation after 1000 cycles was found to approximately double with a $90°$ half internal spread angle (Section 4.6.2). However, application of example multidirectional storm loading in Chapter 5 showed only a small impact of multidirectionality (Sections 5.4.3

and 5.4.4). Future work may investigate typical distributions of cyclic load direction in detail, to provide more informed inputs for physical and numerical modelling. Further exploration of typical distributions of cyclic load amplitude and asymmetry would also be of value.

Numerical modelling

Although able to capture many of the key features of the monopile response to complex cyclic loading, the models in the HARM framework presented in Chapter 7 are unable to capture fully the effect of load asymmetry and spread multidirectional loading. Refinement of the models to capture these effects is likely to be important, but must be informed by further investigations into typical loading (discussed above). This work employed a series, rate-independent model, but future work might explore other model variants.

The development of practical calibration methods for models in the HARM framework will also be essential if these models are to be used in design. Mapping between parameters calibrated to cyclic element tests and parameters calibrated to the response of monopile systems (using 1D Winker models) may be possible. Alternatively, element testing may inform calibration of 3D FE models, from which parameters for 1D Winkler models may be obtained. Validation of these models and associated calibration methods against *e.g.* large-scale responses in natural deposits may also be necessary to build confidence in their application for design.

Pragmatic cyclic design

The computed response of a prototype-scale monopile to realistic storm loading (Figure 7.24, Section 7.6) exhibited negligible ratcheting between peak load events, illustrating the potential combined effects of i) the reduction in ratcheting and evolution of hysteresis loop shape at large-scale stress-levels, and ii) the dominance of large amplitude loads in controlling the rotation response under multi-amplitude loading. Future work could therefore explore the extent to which the ratcheting response can be approximated by computation of the response to only the largest load events (following the work of Abadie, 2017).

8.5 Overview

As conservatism in the monotonic design of monopile foundations reduces, OWTs are developed at sites with more demanding environmental conditions, and lifetime extension is considered, the cyclic design of monopile foundations is increasingly critical. However, no commonly accepted design methods exist for predicting the response of monopiles to cyclic lateral loading. This thesis forms part of a coordinated programme of research at Oxford University which aims to understand monopile performance and develop practical cyclic design methods for the next generation of monopiles. Through laboratory-scale physical modelling, this thesis has provided important insights into the response of monopile foundations in sand under regular and complex — irregular, multi-amplitude and multidirectional — cyclic loading. These insights inform monopile design and, in particular, build confidence in the use of models in the HARM framework for the design of monopiles under realistic loading and at full-scale.

References

Aasen, S., Page, A. M., Skau, K. S., and Nygaard, T. A. (2017). "Effect of foundation modelling on the fatigue lifetime of a monopile-based offshore wind turbine". *Wind Energy Science* 2, pp. 361–376. DOI: 10.5194/wes-2-361-2017.

Abadie, C. N. (2015). "Cyclic Lateral Loading of Monopile Foundations in Cohesionless Soils". DPhil thesis, University of Oxford.

Abadie, C. N. (2017). *Personal communication*.

Abadie, C. N., Byrne, B. W., and Levy-Paing, S. (2015). "Model pile response to multi-amplitude cyclic lateral loading in cohesionless soils". *Proceedings of the 3rd International Symposium on Frontiers in Offshore Geotechnics (ISFOG)*. Oslo, Norway, pp. 681–686.

Abadie, C. N., Houlsby, G. T., and Byrne, B. W. (2019a). "A method for calibration of the Hyperplastic Accelerated Ratcheting Model (HARM)". *Computers and Geotechnics* 112, pp. 370–385. DOI: 10.1016/j.compgeo.2019.04.017.

Abadie, C. N., Byrne, B. W., and Houlsby, G. T. (2019b). "Rigid pile response to cyclic lateral loading: laboratory tests". *Géotechnique* 69.10, pp. 863–876. DOI: 10.1680/jgeot.16.P.325.

Achmus, M., Abdel-Rahman, K., and Kuo, Y. S. (2007). "Numerical Modelling of Large Diameter Steel Piles under Monotonic and Cyclic Horizontal Loading". *Proceedings of the 10th International Symposium on Numerical Models in Geomechanics (NUMOG)*. Rhodes, Greece.

Achmus, M., Kuo, Y. S., and Abdel-Rahman, K. (2009). "Behavior of monopile foundations under cyclic lateral load". *Computers and Geotechnics* 36.5, pp. 725–735. DOI: 10.1016/j.compgeo.2008.12.003.

Achmus, M., Albiker, J., and Abdel-Rahman, K. (2011). "Investigations on the behavior of large diameter piles under cyclic lateral loading". *Proceedings of the 2nd International Symposium on Frontiers in Offshore Geotechnics (ISFOG)*. Perth, Australia, pp. 471–476.

Adcock, T. A. A. and Taylor, P. H. (2009). "Estimating ocean wave directional spreading from an Eulerian surface elevation time history". *Proceedings of the Royal Society A* 465, pp. 3361–3381. DOI: 10.1098/rspa.2009.0031.

Albiker, J., Achmus, M., Frick, D., and Flindt, F. (2017). "1g Model Tests on the Displacement Accumulation of Large-Diameter Piles Under Cyclic Lateral Loading". *Geotechnical Testing Journal* 40.2, pp. 173–184. DOI: 10.1520/GTJ20160102.

Alderlieste, E. A., Dijkstra, J., and van Tol, A. F. (2011). "Experimental investigation into pile diameter effects of laterally loaded monopiles". *Proceedings of the 30th International Conference on Ocean, Offshore and Arctic Engineering (OMAE)*, pp. 985–990.

Altaee, A. and Fellenius, B. H. (1994). "Physical modeling in sand". *Canadian Geotechnical Journal* 31.3, pp. 420–431. DOI: 10.1139/t94-049.

Andersen, K. H. (2015). "Cyclic soil parameters for offshore foundation design". *Proceedings of the 3rd International Symposium on Frontiers in Offshore Geotechnics (ISFOG)*. Oslo, Norway, pp. 3–82.

API (2011). *Geotechnical and Foundation Design Considerations ANSI/API RP 2GEO*. 1st Ed.

Arany, L., Bhattacharya, S., Macdonald, J. H. G., and Hogan, S. J. (2016). "Closed form solution of Eigen frequency of monopile supported offshore wind turbines in deeper waters incorporating stiffness of substructure and SSI". *Soil Dynamics and Earthquake Engineering* 83, pp. 18–32. DOI: 10.1016/j.soildyn.2015.12.011.

Arany, L., Bhattacharya, S., Macdonald, J., and Hogan, S. J. (2017). "Design of monopiles for offshore wind turbines in 10 steps". *Soil Dynamics and Earthquake Engineering* 92, pp. 126–152. DOI: 10.1016/j.soildyn.2016.09.024.

Arshad, M. and O'Kelly, B. C. (2017). "Model Studies on Monopile Behavior under Long-Term Repeated Lateral Loading". *International Journal of Geomechanics* 17.1. DOI: 10.1061/(ASCE)GM.1943-5622.0000679.

Bachynski, E. E., Kristiansen, T., and Thys, M. (2017). "Experimental and numerical investigations of monopile ringing in irregular finite-depth water waves". *Applied Ocean Research* 68, pp. 154–170. DOI: 10.1016/j.apor.2017.08.011.

Balaam, T. D. (2020). "Calibration of cyclic loading models for monopile foundations". Forthcoming DPhil thesis, University of Oxford.

Balaam, T. D., Houlsby, G. T., Page, A. M., Jostad, H. P., and Byrne, B. W. (2020). "Predictions of multi-amplitude laboratory tests using hyperplasticity models". *Forthcoming Proceedings of the 4th International Symposium on Frontiers in Offshore Geotechnics (ISFOG)*. Austin, USA.

Bayton, S. M., Black, J. A., and Klinkvort, R. T. (2018). "Centrifuge modelling of long term cyclic lateral loading on monopiles". *Proceedings of the 9th International Conference on Physical Modelling in Geotechnics (ICPMG)*. London, UK, pp. 689–694.

Beuckelaers, W. J. A. P. (2017). "Numerical Modelling of Laterally Loaded Piles for Offshore Wind Turbines". DPhil thesis, University of Oxford.

Beuckelaers, W. J. A. P., Houlsby, G. T., and Burd, H. J. (2018). "A comparison of the series and parallel Masing-Iwan model in 2D". *Proceedings of the 9th European Conference on Numerical Methods in Geotechnical Engineering (NUMGE)*. Porto, Portugal.

Bhattacharya, S. (2014). "Challenges in Design of Foundations for Offshore Wind Turbines". *Engineering & Technology Reference, IET*, pp. 1–9. DOI: 10.1049/etr.2014.0041.

Bierbooms, W. (2003). "Wind and wave conditions, DOWEC (Dutch Offshore Wind Energy Converter Project)". Technical Report, Delft University of Technology.

Blaker, Ø., Lunne, T., Vestgården, T., Krogh, L., Thomsen, N. V., Powell, J . J. M., and Wallace, C. F. (2015). "Method dependency for determining maximum and minimum dry unit weights of sands". *Proceedings of the Third International Symposium on Frontiers in Offshore Geotechnics (ISFOG)*. Oslo, Norway, pp. 1159–1166.

Bolton, M. D. (1986). "The strength and dilatancy of sands". *Géotechnique* 36.1, pp. 65–78. DOI: 10.1680/geot.1986.36.1.65.

Bolton, M. D. (1987). "Reply to discussion on: The strength and dilatancy of sands, Bolton (1986)". *Géotechnique* 37.2, pp. 219 –226. DOI: 10.1680/geot.1987.37.2.219.

Bredmose, H., Dixen, M., Ghadirian, A., Larsen, T. J., Schløer, S., Andersen, S. J., Wang, S., Bingham, H. B., Lindberg, O., Christensen, E. D., Vested, M. H., Carstensen, S., Engsig-Karup, A. P., Petersen, O. S., Hansen, H. F., Mariegaard, J. S., Taylor, P. H., Adcock, T. A. A., Obhrai, C., Gudmestad, O. T., Tarp-Johansen, N. J., Meyer, C. P.,

Krokstad, J. R., Suja-Thauvin, L., and Hanson, T. D. (2016). "DeRisk - Accurate Prediction of ULS Wave Loads. Outlook and First Results". *Energy Procedia* 94, pp. 379–387. DOI: 10.1016/j.egypro.2016.09.197.

British Standard (1990). *Soils for civil engineering purposes BS 1377-4 : 1990*.

British Standard (1998). *Testing Concrete BS 1881 : Part 131 : 1998*.

Brodersen, M. L., Bjørke, A., and Høgsberg, J. (2017). "Active tuned mass damper for damping of offshore wind turbine vibrations". *Wind Energy* 20, pp. 783–796. DOI: 10.1002/we.2063.

Broms, B. B. (1964). "Lateral Resistance of Piles in Cohesionless Soils". *ASCE Journal of Soil Mechanics and Foundation Division* 90, pp. 123–156.

Burd, H. J., Taborda, D. M. G., Zdravković, L., Abadie, C. N., Byrne, B. W., Houlsby, G. T., Gavin, K., Igoe, D., Jardine, R. J., Martin, C. M., McAdam, R. A., Pedro, A. M. G., and Potts, D. M. (2019). "PISA Design Model for Monopiles for Offshore Wind Turbines: Application to a Marine Sand". *Submitted*.

Byrne, B. W. (2000). "Investigations of suction caissons in dense sand". DPhil thesis, University of Oxford.

Byrne, B. W. (2014). "Laboratory scale modelling for offshore geotechnical problems". *Proceedings of the 8th International Conference on Physical Modelling in Geotechnics (ICPMG)*. Perth, Australia, pp. 61–74.

Byrne, B. W. and Houlsby, G. T. (2005). "Investigating 6 degree-of-freedom loading on shallow foundations". *Proceedings of the International Symposium on Frontiers in Offshore Geotechnics (ISFOG)*. Perth, Australia, pp. 477–482.

Byrne, B. W. and Houlsby, G. T. (2010). "Development of a Multi-Axis Loading System for the Testing of Shallow Foundations". *Unpublished report*.

Byrne, B. W., McAdam, R., Burd, H. J., Houlsby, G. T., Martin, C. M., Zdravkovic, L., Taborda, D. M. G., Potts, D. M., Jardine, R. J., Sideri, M., Schroeder, F. C., Gavin, K., Doherty, P., Igoe, D., Muir Wood, A., Kallehave, D., and Skov Gretlund, J. (2015). "New design methods for large diameter piles under lateral loading for offshore wind applications". *Proceedings of the 3rd International Symposium on Frontiers in Offshore Geotechnics (ISFOG)*. Oslo, Norway, pp. 705–710.

Byrne, B. W., McAdam, R. A., Burd, H. J., Houlsby, G. T., Martin, C. M., Beuckelaers, W. J. A. P., Zdravković, L., Taborda, D. M. G., Potts, D. M., Jardine, R. J., Ushev, E., Liu, T., Abadias, D., Gavin, K., Igoe, D., Doherty, P., Skov Gretlund, J., Pache, S., and Plummer, M. A. L. (2017). "PISA: New design method for offshore wind turbine monopiles". *Proceedings of the 8th International Conference on Offshore Site Investigation and Geotechnics (SUT OSIG)*. London, UK, pp. 142–161.

Cannon, M (2012). *Introduction to Control Theory*. Lecture Notes for A2 Engineering Science course, Oxford University.

Carbon Trust (2014). *New project underway using vibration to install monopiles to reduce costs of offshore wind energy*. URL: https://www.carbontrust.com/news/2014/04/new-project-underway-vibration-to-install-monopiles-reduce-costs-offshore-wind-energy/.

Carbon Trust (2019). *Blue Pilot*. URL: https://www.carbontrust.com/offshore-wind/owa/demonstration/blue-pilot/.

Chakraborty, T. and Salgado, R. (2010). "Dilatancy and Shear Strength of Sand at Low Confining Pressures". *Journal of Geotechnical and Geoenvironmental Engineering* 136.1, pp. 527–532. DOI: 10.1061/(ASCE)GT.1943-5606.0000237.

Chow, S. H., Roy, A., Herduin, M., Heins, E., Bienen, B., O'Loughlin, C. D., Gaudin, C., and Cassidy, M. J. (2018). "Characterisation of UWA superfine silica sand". Internal report, The University of Western Australia.

Cox, W. R., Reese, L. C., and Grubbs, B. R. (1974). "Field Testing of Laterally Loaded Piles In Sand". *Proceedings of the Offshore Technology Conference (OTC)*. Houston, Texas, pp. 459–464. DOI: 10.4043/2079-MS.

Cuéllar, P., Georgi, S., Baeßler, M., and Rücker, W. (2012). "On the quasi-static granular convective flow and sand densification around pile foundations under cyclic lateral loading". *Granular Matter* 14.1, pp. 11–25. DOI: 10.1007/s10035-011-0305-0.

Cui, L. and Bhattacharya, S. (2016). "Soil-monopile interactions for offshore wind turbines". *Proceedings of the Institution of Civil Engineers - Engineering and Computational Mechanics* 169.4, pp. 171–182. DOI: 10.1680/jencm.16.00006.

Dewoolkar, M. M., Pak, R. Y. S., and Ko, H.-Y. (1999). "Centrifuge modelling of models of seismic effects on saturated earth structures". *Géotechnique* 49.2, pp. 247–266. DOI: 10.1680/geot.1999.49.2.247.

DNV GL (2016). *Support structures for wind turbines DNVGL-ST-0126*.

Doherty, P. and Gavin, K (2012). "Laterally loaded monopile design for offshore wind farms". *Proceedings of the Institution of Civil Engineers - Energy* 165.1, pp. 7–17. DOI: 10.1680/ener.11.00003.

Duan, N., Xu, X., and Cheng, Y. P. (2017). "Distinct-element analysis of an offshore wind turbine monopile under cyclic lateral load". *Geotechnical Engineering* 170.6, pp. 517–533. DOI: 10.1680/jgeen.16.00171.

Dührkop, J. and Grabe, J. (2008). "Monopilegründungen von Offshore-windenergieanlagen - Zum Einfluss Einer Veränderlichen Zyklischen Lastangriffsrichtung". *Bautechnik* 85.5, pp. 317–321. DOI: 10.1002/bate.200810024.

EWEA (2009). *The Economics of Wind Energy*. Ed. by S. Krohn.

EWEA (2015). "EWEA report on COP21 outcome". URL: https://windeurope.org/wp-content/uploads/files/policy/topics/climate-change/EWEA-report-on-Paris-Agreement.pdf.

Garnier, J. (2013). "Advances in lateral cyclic pile design : Contribution of the SOLCYP project". *Proceedings of the 18th International Conference on Soil Mechanics and Geotechnical Engineering (TC 209 Workshop, Design for cyclic loading: Piles and other foundations)*. Paris, France, pp. 59–68.

Gaudin, C., Loughlin, C. D. O., and Breen, J. (2018). "A new 240 g-tonne geotechnical centrifuge at the University of Western Australia". *Proceedings of the 9th International Conference on Physical Modelling in Geotechnics (ICPMG)*. London, UK, pp. 501–506.

GE Renewable Energy (2019). *Haliade-X Offshore Wind Turbine Platform*. URL: https://www.ge.com/renewableenergy/wind-energy/turbines/haliade-x-offshore-turbine.

Geotechdata (2013). *Soil elastic Young's modulus*. URL: http://www.geotechdata.info/parameter/soil-young's-modulus.html.

Green, E. I. (1955). "The story of Q". *American Scientist* 43, pp. 584–594.

Gui, M. W., Bolton, M. D., Garnier, J., Corte, J. F., Bagge, G., Laue, J., and Renzi, R. (1998). "Guidelines for cone penetration tests in sand". *Proceedings of the International Conference on Centrifuge Modelling (Centrifuge 98)*. Rotterdam, The Netherlands, pp. 155–160.

Hardin, B. O. (1965). "Dynamic versus static shear modulus for dry sand". *Materials Research and Standards* 5.5, pp. 232–235.

Herduin, M. (2019). "Multi-directional loading on shared anchors for offshore renewable energy: Definition and preliminary investigation into soil behaviour and anchor performance". PhD Thesis, The University of Western Australia. DOI: 10.26182/5d2fd93d88ce7.

Houlsby, G. T. (1981). "A study of plasticity theories and their applicability to soils". PhD Thesis, University of Cambridge.

Houlsby, G. T. and Puzrin, A. M. (2006). *Principles of Hyperplasticity: An Approach to Plasticity Theory Based on Thermodynamic Principles*. Springer-Verlag.

Houlsby, G. T., Abadie, C. N., Beuckelaers, W. J. A. P., and Byrne, B. W. (2017). "A model for nonlinear hysteretic and ratcheting behaviour". *International Journal of Solids and Structures* 120, pp. 67 –80. DOI: 10.1016/j.ijsolstr.2017.04.031.

IEA (2017). *World Energy Outlook 2017*. URL: https://www.iea.org/weo2017.

Inman, D. J. (2014). *Engineering vibration*. 4th ed. Pearson. Chap. 2.

IRENA (2017). *Electricity storage and renewables: costs and markets to 2030*. URL: https://www.irena.org/publications/2017/Oct/Electricity-storage-and-renewables-costs-and-markets.

Iwan, W. D. (1967). "On a Class of Models for the Yielding Behavior of Continuous and Composite Systems". *Journal of Applied Mechanics* 34.3. DOI: 10.1115/1.3607751.

Jeanjean, P., Zhang, Y., Zakeri, A., Andersen, K. H., Gilbert, K., and Senanayake, A. I. M. J. (2017). "A framework for monotonic p-y curves in clays". *Proceedings of the 8th International Conference on Offshore Site Investigation and Geotechnics (SUT OSIG)*. London, UK, pp. 108–141.

Kelly, R. B., Byrne, B. W., and Houlsby, G. T. (2006). "A comparison of field and laboratory tests of caisson foundations in sand and clay". *Géotechnique* 56.9, pp. 617–626. DOI: 10.1680/geot.2006.56.9.617.

Kementzetzidis, E., Corciulo, S., Versteijlen, W. G., and Pisanò, F. (2019). "Geotechnical aspects of offshore wind turbine dynamics from 3D non-linear soil-structure simulations". *Soil Dynamics and Earthquake Engineering* 120, pp. 181–199. DOI: 10.1016/j.soildyn.2019.01.037.

Klinkvort, R. and Hededal, O. (2013). "Lateral response of monopile supporting an offshore wind turbine". *Proceedings of the Institution of Civil Engineers - Geotechnical Engineering* 166.2, pp. 147–158. DOI: 10.1680/geng.12.00033.

Klinkvort, R., Springman, S., and Hededal, O. (2013). "Scaling issues in centrifuge modelling of monopiles". *International Journal of Physical Modelling in Geotechnics* 13.2, pp. 38–50. DOI: 10.1680/ijpmg.12.00010.

Klinkvort, R. T. (2012). "Centrifuge modelling of drained lateral pile-soil response". PhD Thesis, DTU.

Koukoura, C. (2014). "Validated Loads Prediction Models for Offshore Wind Turbines for Enhanced Component Reliability". PhD Thesis, DTU.

Kramer, S. L. (1996). *Geotechnical Earthquake Engineering*. Prentice Hall.

Kucuk, S. and Bingul, Z. (2006). "Robot Kinematics: Forward and Inverse Kinematic". *Industrial Robotics: Theory, Modelling and Control*. Ed. by S. Cubero. IntechOpen. DOI: 10.5772/44.

Lambe, T. W. (1973). "Predictions in soil engineering". *Géotechnique* 23.2, pp. 149–202. DOI: 10.1680/geot.1973.23.2.151.

Lazarevic, Z. (1997). "Feasibility of a Stewart Platform with Fixed Actuators as a Platform for CABG Surgery Device". Master's Thesis, Columbia University.

Leblanc, C., Houlsby, G. T., and Byrne, B. W. (2010a). "Response of stiff piles in sand to long-term cyclic lateral loading". *Géotechnique* 60.2, pp. 79–90. DOI: 10.1680/geot.7.00196.

Leblanc, C., Byrne, B. W., and Houlsby, G. T. (2010b). "Response of stiff piles to random two-way lateral loading". *Géotechnique* 60.9, pp. 715–721. DOI: 10.1680/geot.09.T.011.

Li, S., Zhang, Y., and Jostad, H. P. (2019). "Drainage conditions around monopiles in sand". *Applied Ocean Research* 86, pp. 111–116. DOI: 10.1016/j.apor.2019.01.024.

Li, Z., Haigh, S. K., and Bolton, M. D. (2010). "Centrifuge modelling of mono-pile under cyclic lateral loads". *Proceedings of the 7th International Conference on Physical Modelling in Geotechnics (ICPMG)*. Zurich, Switzerland, pp. 965–970. DOI: 10.1680/ijpmg.2010.10.2.47.

Little, R. L. and Briaud, J.-L. (1988). "Full scale cyclic lateral load tests on six single piles in sand". *Miscellaneous Paper GL-88-27, Geotechnical Div., Texas A&M University*.

Long, J. H. and Vanneste, G. (1994). "Effects of Cyclic Lateral Loads on Piles in Sand". *Journal of Geotechnical Engineering* 120.1, pp. 225–244. DOI: 10.1061/(ASCE)0733-9410(1994)120:1(225).

Løvholt, F., Madshus, C., and Andersen, K. H. (2020). "Intrinsic Soil Damping from Cyclic Laboratory Tests with Average Strain Development". *Geotechnical Testing Journal* 43.1. DOI: 10.1520/GTJ20170411.

Lunne, T. (2012). "The Fourth James K. Mitchell Lecture: The CPT in offshore soil investigations - a historic perspective". *Geomechanics and Geoengineering* 7.2, pp. 75–101. DOI: 10.1080/17486025.2011.640712.

Manceau, S., McLean, R., Sia, A., and Soares, M. (2019). "Application of the Findings of the PISA Joint Industry Project in the Design of Monopile Foundations for a North Sea Wind Farm". *Proceedings of the Offshore Technology Conference (OTC)*. Houston, Texas.

Masing, G. (1926). "Eiganspannungen und verfestigung beim messing". *Proceedings of the 2nd International Congress of Applied Mechanics*.

Mayall, R. O. (2019). "Monopile response to scour and scour protection". DEng thesis, University of Oxford.

Mayall, R. O., McAdam, R. A., Whitehouse, R. J. S., Burd, H. J., Byrne, B. W., Heald, S. G., Sheil, B. B., and Slater, P. L. (2019). "Flume tank testing of offshore wind turbine dynamics with foundation scour and scour protection". *Submitted*.

Mrŏz, Z, Norris, V. A., and Zienkiewicz, O. C. (1978). "An isotropic hardening model for soils and its application to cyclic loading". *International Journal for Numerical and Analytical Methods in Geomechanics* 2, pp. 203–221.

Murchison, J. M. and O'Neill, M. W. (1984). "Evaluation of p-y relations in cohesionless soils". *Proceedings of the ASCE symposium on analysis and design of pile foundations*. San Francisco, USA, pp. 174 –191.

Nguyen-Sy, L. and Houlsby, G. T. (2005). "The theoretical modelling of a suction caisson foundation using hyperplasticity theory". *Proceedings of the International Symposium on Frontiers in Offshore Geotechnics (ISFOG)*. Perth, Australia, pp. 417–423.

Nicolai, G. (2017). "Cyclic behaviour of laterally loaded monopiles in sand supporting offshore wind turbines". PhD Thesis, Aalbog University.

Nicolai, G. and Ibsen, L. B. (2014). "Small-Scale Testing of Cyclic Laterally Loaded Monopiles in Dense Saturated Sand". *Journal of Ocean and Wind Energy* 1.4, pp. 240–245.

Nicolai, G., O'Loughlin, C. D., White, D. J., Cassidy, M. J., and Ibsen, L. B. (2017a). "Centrifuge study with PIV analysis of monopiles in dense sand under cyclic lateral loading". DCE Technical Report No. 206, Deprtment of Civil Engineering, Aalborg University.

Nicolai, G., Ibsen, L. B., O'Loughlin, C. D., and White, D. J. (2017b). "Quantifying the increase in lateral capacity of monopiles in sand due to cyclic loading". *Géotechnique Letters* 7.3, pp. 1–8. DOI: 10.1680/jgele.16.00187.

Niemann, C., Reul, O., Tian, Y., O'Loughlin, C. D., and Cassidy, M. J. (2018). "Centrifuge tests on the response of piles under cyclic lateral 1-way and 2-way loading". *Proceedings of the 9th International Conference on Physical Modelling in Geotechnics (ICPMG)*. London, UK, pp. 731–736.

Niemunis, A. and Herle, I. (1997). "Hypoplastic model for cohesionless soils with elastic strain range". *Mechanics of Cohesive-Frictional Materials* 2, pp. 279–299.

Niemunis, A., Wichtmann, T., and Triantafyllidis, Th. (2005). "A high-cycle accumulation model for sand". *Computers and Geotechnics* 32.4, pp. 245–263. DOI: 10.1016/j.compgeo.2005.03.002.

Osman, A. S. and Randolph, M. F. (2012). "Analytical Solution for the Consolidation around a Laterally Loaded Pile". *International Journal of Geomechanics* 12.3, pp. 199–208. DOI: 10.1061/(ASCE)GM.1943-5622.0000123.

Ovesen, N. K. (1975). "Centrifugal testing applied to bearing capacity problems of footings on sand". *Géotechnique* 25.2, pp. 394–401. DOI: 10.1680/geot.1975.25.2.394.

Oztoprak, S. and Bolton, M. D. (2013). "Stiffness of sands through a laboratory test database". *Géotechnique* 63.1, pp. 54–70. DOI: 10.1680/geot.10.P.078.

Page, A. M., Grimstad, G., Eiksund, G. R., and Jostad, H. P. (2018). "A macro-element pile foundation model for integrated analyses of monopile-based offshore wind turbines". *Ocean Engineering* 167, pp. 23–35. DOI: 10.1016/j.oceaneng.2018.08.019.

Page, A. M., Næss, V., De Vaal, J. B., Eiksund, G. R., and Nygaard, T. A. (2019). "Impact of foundation modelling in offshore wind turbines: comparison between simulations and field data". *Marine Structures* 64, pp. 379–400. DOI: 10.1016/j.marstruc.2018.11.010.

Peralta, P (2010). "Investigations on the Behaviour of Large Diameter Piles under Long-Term Lateral Cyclic Loading in Cohesionless Soil". PhD thesis, Leibniz Universitat Hannover.

Peralta, P., Ballard, J. C., Rattley, M., and Erbrich, C. E. (2017). "Dynamic and cyclic pile-soil response curves for monopile design". *Proceedings of the 8th International Conference on Offshore Site Investigation and Geotechnics (SUT OSIG)*. London, UK, pp. 1054–1061.

Poulos, H. G. and Hull, T. S. (1989). "The role of analytical geomechanics in foundation engineering". *Proceedings of the ASCE Foundation Engineering Congress (Foundation Engineering: Current Principals and Practices)*. Evanston, US.

Prévost, J. (1977). "Mathematical modelling of monotonic and cyclic undrained clay behaviour". *International Journal for Numerical and Analytical Methods in Geomechanics* 1, pp. 195–216. DOI: 10.1002/nag.1610010206.

Puzrin, A. M. and Shiran, A. (2000). "Effects of the constitutive relationship on seismic response of soils . Part I . Constitutive modeling of cyclic behavior of soils". *Soil Dynamics and Earthquake Engineering* 19.5, pp. 305–318. DOI: 10.1016/S0267-7261(00)00027-0.

Pyke, R. (1979). "Nonlinear soil models for irregular cyclic loadings". *Journal of the Geotechnical Division, Proceedings of the ASCE* 105.6, pp. 715–726.

Rad, N. S. and Tumay, M. T. (1987). "Factors Affecting Sand Specimen Preparation By Raining". *Geotechnical Testing Journal* 10.1, pp. 31–37. DOI: 10.1520/GTJ10136J.

Ramberg, W. and Osgood, W. R. (1943). "Description of stress-strain curves by three parameters (Technical Note 902)". National Advisory Committee For Aeronautics, Washington, US.

Randolph, M. F. (2018). "Potential Damage to Steel Pipe Piles During Installation". *IPA News Letter* 3.1, pp. 3–10.

Reese, L. C. and Van Impe, W. (2011). *Single piles and pile groups under lateral loading*. 2nd ed. CRC Press/Balkema.

Reese, L. C., Cox, W. R., and Koop, F. D. (1974). "Analysis of Laterally Loaded Piles in Sand". *Proceedings of the Offshore Technology Conference (OTC)*. Houston, Texas, pp. 473–483. DOI: 10.4043/2080-MS.

Renewable UK (2019). *Wind Energy*. URL: https://www.renewableuk.com/page/WindEnergy.

Roy, A., Chow, S., O'Loughlin, C. D., and Randolph, M. F. (2019). "Effect of stress history and shallow embedment on centrifuge cone penetration tests in sand". *Proceedings of the 39th International Conference on Ocean, Offshore and Arctic Engineering (OMAE)*. Glasgow, Scotland.

Rudolph, C. and Grabe, J. (2013). "Untersuchungen zu zyklisch horizontal belasteten Pfählen bei veränderlicher Lastrichtung". *Geotechnik* 36.2, pp. 90–95. DOI: 10.1002/gete.201200025.

Rudolph, C., Grabe, J., and Bienen, B. (2014a). "Drift of piles subjected to cyclic lateral loading from a varying direction: system vs. soil element behaviour". *Proceedings of 33rd International Conference on Ocean, Offshore and Arctic Engineering (OMAE)*. San Francisco, USA.

Rudolph, C., Bienen, B., and Grabe, J. (2014b). "Effect of variation of the loading direction on the displacement accumulation of large-diameter piles under cyclic lateral loading in sand". *Canadian Geotechnical Journal* 51.10, pp. 1196–1206. DOI: 10.1139/cgj-2013-0438.

Schnaid, F. (1990). "A study of the cone-pressuremeter test in sand". DPhil thesis, University of Oxford.

Schofield, A. N. (1980). "Cambridge Geotechnical Centrifuge Operations". *Géotechnique* 30.3, pp. 227–268. DOI: 10.1680/geot.1980.30.3.227.

Schroeder, F. C., Merritt, A. S., Sørensen, K. W., Muir Wood, A., Thilsted, C. L., and Potts, D. M. (2015). "Predicting monopile behaviour for the Gode Wind offshore wind farm". *Proceedings of the 3rd International Symposium on Frontiers in Offshore Geotechnics (ISFOG)*. Oslo, Norway, pp. 735–740.

Skau, K. S., Grimstad, G., Page, A. M., Eiksund, G. R., and Jostad, H. P. (2018). "A macro-element for integrated time domain analyses representing bucket foundations for offshore wind turbines". *Marine Structures* 59, pp. 158–178. DOI: 10.1016/j.marstruc.2018.01.011.

Sørensen, S. P. H., Augustesen, A. H., Leth, C. T., Østergaard, M. U., and Møller, M. (2017). "Consequences of p-y curve selection for monopile design for offshore wind turbines". *Proceedings of the 8th International Conference on Offshore Site Investigation and Geotechnics (SUT OSIG)*. London, UK, pp. 1062–1069.

Su, D., Wu, W. L., Du, Z. Y., and Yan, W. M. (2014). "Cyclic Degradation of a Multidirectionally Laterally Loaded Rigid Single Pile Model in Compacted Clay". *Journal of Geotechnical and Geoenvironmental Engineering* 140.5. DOI: 10.1061/(ASCE)GT.1943-5606.0001084.

Taborda, D. M. G., Potts, D. M., and Zdravković, L. (2016). "On the assessment of energy dissipated through hysteresis in finite element analysis". *Computers and Geotechnics* 71, pp. 180–194. DOI: 10.1016/j.compgeo.2015.09.001.

Tatsuoka, F. (1987). "Discussion on: The strength and dilatancy of sands, Bolton (1986)". *Géotechnique* 37.2, pp. 219–226. DOI: 10.1680/geot.1987.37.2.219.

Truong, P., Lehane, B. M., Zania, V., and Klinkvort, R. T. (2019). "Empirical approach based on centrifuge testing for cyclic deformations of laterally loaded piles in sand". *Géotechnique* 69.2, pp. 133–145. DOI: 10.1680/jgeot.17.p.203.

Uesugi, M. and Kishida, H. (1986). "Frictional resistance at yield between dry sand and mild steel". *Soils and foundations* 26.4, pp. 139 –149. DOI: 10.3208/sandf1972.26.4_139.

United Nations (2015). "Paris Agreement". Framework Convention on Climate Change.

University of Strathclyde (2015). *XL Monopiles*. URL: http://www.esru.strath.ac.uk/EandE/Web{_}sites/14-15/XL{_}Monopiles/technical.html.

Van Vledder, G. Ph. (2013). "On Wind-Wave Misalignment, Directional Spreading and Wave Loads". *Proceedings of the 32rd International Conference on Ocean, Offshore and Arctic Engineering (OMAE)*. Nantes, France. DOI: 10.1115/OMAE2013-11393.

Villalobos, F. (2006). "Model Testing of Foundations for Offshore Wind Turbines". DPhil thesis, University of Oxford.

Wang, S. (2018). "Assessment of offshore wind turbines in extreme weather conditions". PhD Thesis, DTU Wind Energy.

White, J. R. F. (2020). "A laboratory investigation into the behaviour of sand at low confining stresses". Forthcoming DPhil thesis, University of Oxford.

Wichtmann, T., Triantafyllidis, T., Chrisopoulos, S., and Zachert, H. (2017). "Prediction of Long-Term Deformations of Offshore Wind Power Plant Foundations Using Engineer-Oriented Models Based on the High Cycle Accumulation Model". *International Journal of Offshore and Polar Engineering* 27.4, pp. 346–356. DOI: 10.17736/ijope.2017.fv05.

Wind Europe (2017). "Wind energy in Europe: Scenarios for 2030". URL: https://windeurope.org/wp-content/uploads/files/about-wind/reports/Wind-energy-in-Europe-Scenarios-for-2030.pdf.

Wind Europe (2018). "Offshore Wind in Europe: Key trends and statistics 2017". URL: https://windeurope.org/wp-content/uploads/files/about-wind/statistics/WindEurope-Annual-Offshore-Statistics-2017.pdf.

Wind Europe (2019). "Offshore Wind in Europe: Key trends and statistics 2018". URL: https://windeurope.org/about-wind/statistics/offshore/european-offshore-wind-industry-key-trends-statistics-2018/.

Wind Turbine Models (2015). "Vestas V164-8.0". URL: https://en.wind-turbine-models.com/turbines/318-vestas-v164-8.0.

Windindustrie in Deutschland (2016). *1300 tonnes – world´s largest monopile moved on self-propelled transporters*. URL: https://www.windindustrie-in-deutschland.de/fachartikel/1300-tonnes-worlds-largest-monopole-moved-on-self-propelled-transporters/trackback/.

Windpower (2019). *Vattenfall proves offshore wind can be profitable without subsidies*. URL: https://www.windpowerengineering.com/business-news-projects/vattenfall-proves-offshore-wind-can-be-profitable-without-subsidies/.

Zhang, Y., Andersen, K. H., Klinkvort, R. T., Jostad, H. P., Sivasithamparam, N., Boylan, N. P., and Langford, T. (2016). "Monotonic and Cyclic p-y Curves for Clay Based on Soil Performance Observed in Laboratory Element Tests". *Proceedings of the Offshore Technology Conference (OTC)*. Houston, Texas. DOI: 10.4043/26942-MS.

Zhao, Y., Gafar, K., Elshafie, M. Z. E. B., Deeks, A. D., Knappett, J. A., and Madabhushi, S. P. G. (2006). "Calibration and use of a new automatic sand pourer". *Proceedings of the 6th International Conference on Physical Modelling in Geotechnics (ICPMG)*. Hong Kong, pp. 265 –270.

Zhu, F. Y., O'Loughlin, C. D., Bienen, B., Cassidy, M. J., and Morgan, N. (2017). "The response of suction caissons to long-term lateral cyclic loading in single-layer and layered seabeds". *Géotechnique* 67.11, pp. 1–13. DOI: 10.1680/jgeot.17.P.129.

Ziegler, H. (1977). *An Introduction to Thermomechanics*. 2nd ed. North-Holland, Amsterdam.